

Application of poly-Si on oxide junctions as one or both polarities of high-efficiency IBC solar cells

Von der Fakultät für Elektrotechnik und Informatik
der Gottfried Wilhelm Leibniz Universität Hannover

zur Erlangung des akademischen Grades
Doktorin der Naturwissenschaft
Dr. rer. nat.

genehmigte Dissertation von

M. Sc. Christina Hollemann geb. Klamt
geboren am 23.10.1991 in Hildesheim

Erscheinungsjahr 2023

Referent: Prof. Dr. Robby Peibst

Korreferent: Prof. Dr. Jan Schmidt

Korreferent: Prof. Dr. Stefan Glunz

Tag der Disputation: 10.11.2022

Zusammenfassung

Diese Arbeit befasst sich mit der Anwendung von passivierenden Kontakten, genauer gesagt POLO-Kontakten, welche durch ihre hervorragende passivierende Wirkung die Selektivität der Ladungsträger an den Metallkontakten und so die Effizienz von Solarzellen über das heutzutage übliche Niveau hinaus steigern können. Diese poly-Si basierten Kontakte, zumeist TOPCon genannt, etablieren sich zurzeit in der industriellen Solarzellenfertigung. Allerdings gibt es noch einige offene Fragen bezüglich ihrer Funktionsweise und der optimalen Herstellung.

Der erste Teil der Arbeit ist auf die sogenannte POLO²-IBC Zelle fokussiert, mit der, unter Mitarbeit der Autorin dieser Arbeit, 2018 ein Rekordwirkungsgrad von 26.1 % für *p*-Typ Material erzielt werden konnte. Mit einer Fläche von 4 cm² und sehr komplexen Strukturierungsprozessen ist diese rückseitig kontaktierte Zelle zwar keine industriell relevante Zelle, sie zeigt aber das große Potenzial der POLO-Kontakte. Eine Besonderheit dieser Zelle ist die durchgängigen Schichten von dünnem Oxid und darüberliegendem poly-Si, welche den sogenannten „poly-Si on oxide“ (POLO) Kontakt bilden. Die elektronensammelnden und löchersammelnden Kontakte, die durch Dotierung mittels Ionenimplantation hergestellt werden, sind nur durch schmale intrinsische POLO-Bereiche voneinander getrennt.

Ein umfassendes Monitoring des Herstellungsprozesses und eine Simulationsstudie zeigen, dass das Potenzial dieses Zelltyps mit 26.1 % noch nicht gänzlich ausgeschöpft ist. Der Vergleich mit einem hochohmigen Basismaterial zeigt darüber hinaus die deutlich höhere Anfälligkeit der Passivierung bei abnehmender Dotierung, so dass trotz höherer intrinsischer Rekombination das verwendete 1.3 Ω cm-Material als besser geeignet identifiziert wird.

Die Trennung der *p*⁺ und *n*⁺ Kontakt durch den undotierten Bereich erweist sich als elegante Lösung, die jedoch nur unter bestimmten Voraussetzungen funktioniert. Die Diffusion von Dotierstoffen aus den *n*⁺- und *p*⁺-Bereichen in den intrinsischen Bereich verbessert die dort ansonsten schlechte Passivierqualität. Gleichzeitig nimmt damit jedoch der nicht gewollte Rekombinationsstrom zwischen den Kontakten zu, sodass die Wahl der geeigneten Breite von imenser Bedeutung ist. Durch das gewonnene Verständnis der Funktionsweise sind im Weiteren auch weniger aufwendige Strukturierungen denkbar.

Um den Sprung von der Laborzelle zur industriellen Anwendung zu schaffen, ist jedoch die Stabilität gegen über dem Feuerschritt zur Kontaktformierung mit den gängigen Siebdruckpasten unerlässlich. Obwohl die POLO-Kontakte alleine durch ihren Herstellungsprozess beweisen, dass sie hohen Temperaturen mit guter Passivierqualität standhalten, führt das Feuern ohne Deckschicht zu einer Verschlechterung. Im zweiten Teil dieser Arbeit kann gezeigt werden, dass dieses Verhalten vermutlich auf die um zwei Größenordnungen größeren Aufheiz- und Abkühlraten in Kombination mit thermischen Spannungen zurückzuführen ist und dass der Degradation mithilfe von wasserstoffreichen dielektrischen Schichten entgegengewirkt werden kann. Zu viel Wasserstoff kann sich hier jedoch negativ auswirken. Für die typischen Feuertemperaturen von um die 800 °C zeigt ein Stapel aus $\text{Al}_2\text{O}_3/\text{SiN}_y$ auf dem POLO-Kontakt die besten Ergebnisse.

Im letzten Abschnitt der Arbeit kann der Einsatz eines n^+ POLO-Kontaktes in einer siebgedruckten, sogenannten POLO-IBC Zelle mit einer Effizienz von 23.92 % erfolgreich demonstriert werden. Dabei kommt die hervorragende Passivierqualität von 0.2 fA/cm^2 der n^+ POLO-Kontakte zum Tragen, die mittels der $\text{Al}_2\text{O}_3/\text{SiN}_y$ Schichten erhalten werden kann. Insgesamt hat diese Arbeit dazu beigetragen, passivierende Kontakte von hocheffizienten POLO²-IBC-Laborzellen auf das vielversprechende industrietaugliche POLO-IBC-Zellenkonzept zu übertragen.

Abstract

This work deals with the application of passivating contacts, specifically POLO contacts, which can increase the selectivity of the charge carriers at the metal contacts and thus the efficiency due to their excellent passivating effect. These poly-Si based contacts, also called TOPCon, are just establishing themselves in industrial solar cell manufacturing. However, there are still some open questions regarding their operation and optimal fabrication.

The first part of the paper is focused on the so-called POLO²-IBC cell, with which Felix Hasse's team, with the collaboration of the author of this thesis, was able to achieve a record efficiency of 26.1 % for *p*-type material in 2018. With an area of 4 cm² and very complex patterning processes, this back-contacted record cell is not an industrially relevant cell, but it demonstrates the great potential of POLO contacts. A distinctive feature of this cell is the continuous layers of thin oxide and overlying poly-Si that form the so-called „poly-Si on oxide“ (POLO) junctions. The electron-collecting and hole-collecting contacts, fabricated by doping via ion implantation, are separated only by narrow intrinsic POLO regions.

Extensive monitoring of the fabrication process and a simulation study show that the potential of this cell type with 26.1 % has not yet been fully exploited. Furthermore, the comparison with a high resistivity base material shows the significantly higher susceptibility of the passivation quality with decreasing doping concentration, so that despite higher intrinsic recombination, the used 1.3 Ω cm material is identified as more suitable.

Separating the *p*⁺ and *n*⁺ contact through the undoped region proves to be an elegant solution, which, however, only works under certain conditions. Diffusion of dopants from the *n*⁺ and *p*⁺ regions into the intrinsic region improves the otherwise poor passivation quality there. At the same time, however, this increases the unwanted recombination current between the contacts, so the choice of the appropriate width is of immense importance. With the understanding of the working principle gained, less complex structuring is conceivable in the future.

However, in order to make the leap from the laboratory cell to industrial application, stability against the firing step for contact formation with common screen printing pastes is essential. Although the POLO contacts prove by their manufacturing pro-

cess alone that they can withstand high temperatures with very good passivation quality, firing without a capping layer leads to deterioration of the passivation quality. In the second experimental part of this work, it is shown that this behavior is probably due to the two orders of magnitude higher heating and cooling rates in combination with thermal stresses. However, the degradation can be counteracted with the help of hydrogen rich dielectric layers. Nevertheless, it is shown, that too much hydrogen can also have a negative effect here. For typical firing temperatures of around 800 °C, a stack of Al₂O₃/SiN_y layers yields the best results.

In the last section of this work, the use of a *n*⁺POLO contact in a screen-printed POLO-IBC cell can be successfully demonstrated with an efficiency of 23.92 %. The excellent passivation quality of 0.2 fA/cm², which can be obtained using Al₂O₃/SiN_y stack to cap the *n*⁺POLO junction, plays an important role here. Overall, this work has helped to transfer passivating contacts from high-efficiency POLO²-IBC laboratory cells to the promising POLO-IBC cell concept suitable for industrial applications.

Schlagwörter: Passivierende Kontakte, polykristallines Silizium, POLO-Kontakte, Rückkontaktsolarzellen, Feuerstabilität

Keywords: passivating contacts, polycrystalline silicon, POLO contacts, IBC solar cells, firing stability

Contents

1	Introduction	1
1.1	Outline	3
2	Theory and State-of-the-Art	5
2.1	Working principle of solar cells	5
2.2	Selectivity	10
2.3	Working principle of passivating contacts	12
2.4	Poly-Si on oxide junctions	13
2.4.1	Processing	13
2.4.2	Application in back contact solar cells	15
2.4.3	From laboratory to industrial solar cells	16
2.4.4	Firing stability	17
3	Characterization and simulation methods	19
3.1	Current-voltage measurements	19
3.2	Quasi-steady-state photoconductance and photoconductance decay techniques	19
3.3	Infrared lifetime mapping	23
3.4	Time-resolved photoluminescence	27
3.5	Fourier-transform infrared spectroscopy	28
3.6	Time of flight secondary ion mass spectrometry	30
3.7	High-frequency capacitance- and conductance-voltage measurements	32
3.8	MarcoPOLO model	38
3.9	Free energy loss analysis	39
4	IBC solar cells with POLO junctions for both polarities	41
4.1	Cell structure and processing	42
4.1.1	Solar cells	43

4.1.2	Test structures	47
4.2	Analysis of loss mechanisms	47
4.2.1	Monitoring of cell parameters during processing	48
4.2.2	Free Energy Loss Analysis	54
4.2.3	Quantification of process-induced degradation and (<i>i</i>) poly-Si region passivation quality	56
4.2.4	Summary and discussion of Section 4.2	62
4.3	Investigation of the working principle of the $p^+(i)n^+$ back contact structure	64
4.3.1	Impact of the poor passivation quality of <i>i</i> POLO junctions on the cell performance	64
4.3.2	Density of pinholes and their impact on the passivation of <i>i</i> POLO junctions	67
4.3.3	Comparison of large area and small area, embedded (<i>i</i>) poly-Si regions	70
4.3.4	Lateral interdiffusion of dopants in the embedded (<i>i</i>)POLO regions	71
4.3.5	<i>J-V</i> characteristics of poly-Si $p^+(i)n^+$ structures	75
4.3.6	Influence of (<i>i</i>) poly-Si region width and annealing temperature	77
4.3.7	Influence of hydrogenation on the (<i>i</i>)POLO region	79
4.3.8	Summary and discussion of Section 4.3	82
4.4	Summary and implications of Chapter 4	85
5	Firing stability of n^+POLO junctions	89
5.1	Experimental details	90
5.1.1	Sample preparation	90
5.1.2	The firing process	94
5.2	Firing stability of uncapped n^+ POLO junctions	95
5.2.1	Recombination current density	95
5.2.2	Interface state density	98
5.2.3	Variation of the conveyor belt speed	102
5.2.4	Thermal expansion at the c-Si/SiO _x /poly-Si interface	106
5.2.5	Summary and discussion of Section 5.2	107
5.3	Influence of different hydrogen-containing capping layers	109
5.3.1	SiN _y capping layer	109

5.3.2	Post-firing annealing	114
5.3.3	Al ₂ O ₃ capping layer	115
5.3.4	Al ₂ O ₃ /SiN _y capping layer stack	117
5.3.5	Interface state density	118
5.3.6	Summary and discussion of Section 5.3	119
5.4	Changes in hydrogen concentration and defect state density due to firing	122
5.4.1	Evolution of recombination current density and hydrogen concentration with firing temperature	123
5.4.2	Comparison of integrated hydrogen concentrations and defect state densities at the interface	129
5.4.3	Summary and discussion of Section 5.4	132
5.5	Summary and implication of Chapter 5	133
6	IBC solar cells with POLO junctions for one polarity	137
6.1	Cell structure and processing	137
6.2	Analysis of loss mechanisms	139
6.2.1	Evaluation of J - V results of different split groups	139
6.2.2	Free Energy Loss Analysis	146
6.3	Summary and implications of Chapter 6	147
7	Summary	149
	Bibliography	xv
	Lebenslauf	xlvi

1 Introduction

Already in 1824, J. Fourier [1] explained the greenhouse effect of the global atmosphere and found out that different gases in the atmosphere warm the climate. In 1860, Tyndall [2] discovered that mainly water vapor and CO₂ are responsible for this effect. From the end of the 19th century, human influence on the earth's temperature was discussed, and the first calculations on the correlation between the CO₂ concentration and the global temperature were made [3], [4]. However, at that time, a temperature increase of 2 °C that would be induced by a doubling of the CO₂ concentration in the atmosphere, as calculated by G. S. Callendar in 1938, was mainly associated with positive expectations, e.g., the prevention of another ice age.

About 20 years later, scientific evidence solidified that human-made climate change and the resulting temperature rise threaten the very foundations of human life [5], [6]. Moreover, the latest Intergovernmental Panel on Climate Change (IPCC) report from 2022 clarifies that „Any further delay in concerted global action will miss a brief and rapidly closing window to secure a liveable future“[7]. In particular, so-called tipping points that make climate change impacts irreversible at certain points of global warming [8] make short-term action urgently necessary. Therefore, the entire energy, industry, and agriculture sectors must be decarbonized as quickly as possible.

Fortunately, the primary conditions for this major transition are in place, as technologies that enable power and heat generation from renewable sources are available on an industrial scale. The two most important technologies for the transition are solar and wind energy. After Russel Ohl had laid the foundation in 1939 with the discovery of the *pn*-junction [9], the cornerstone for solar energy was laid in 1953 at Bell Company when Chapin, Fuller, and Pearson [10] developed the first silicon-based solar cell, which had an efficiency of 6%. Over the years, knowledge of the harmful effects of fossil fuels has expanded the application of photovoltaics (PV) beyond island systems in remote locations and space travel to an available renewable

1 Introduction

energy source, providing an essential building block for the transition of the energy system to renewable energy sources.

Today, silicon solar cells dominate the world's PV market, and more than 770 GW of PV capacity are installed worldwide [11]. This breakthrough has been possible because the average efficiencies of PV modules have increased significantly over the last ten years from 15 % to over 20 % and, at the same time, module prices have dropped by 93 % to about 0.20 € per W_{peak} today [12]. As a result, ground-mounted PV systems achieved a levelized cost of electricity (LCOE) of fewer than six cents per kWh in Germany in 2021, making them the cheapest form of on-site electricity generation. Nevertheless, substantial efforts are still needed.

Studies, which consider the necessary development in Germany, indicate that an increase of the PV capacity from today 59 GW to 200 to 550 GW is necessary to become climate neutral by 2045 [13]. To not exceed the German CO₂ budget for meeting the 1.5 °C path, an even more significant increase to 590 GW by 2035 is needed [14].

The current leading technology in PV are passivated emitter and rear cells (PERC), which made tremendous improvements in the last decade but are finally reaching their efficiency limit. However, as the next step in the evolutionary improvement of silicon solar cells, using poly-Si on oxide (POLO) junctions has become a promising approach [15], [16]. A continued efficiency increase will further reduce the LCOE and thus further increase its commercial viability.

This thesis analyzes the integration of POLO passivating contacts in an interdigitated back-contact solar cell with a world record certified efficiency of 26.1 % for *p*-type cells in great detail. Moreover, the next step to implement them into industrial-relevant solar cell concepts is supported by analyzing the stability of these contacts toward a „firing“ step. This short high temperature process is needed for the industrial metallization technique of screen printing, which is currently applied to over 90 % of the silicon solar cell market share [17]. Finally, the successful application of an *n*⁺POLO junction in a screen-printed POLO-IBC cell with 23.92 % is shown and analyzed.

1.1 Outline

This work consists of the three main experimental Chapters 4, 5, and 6, supplemented by a theoretical introduction and a description of the characterization methods used.

Chapter 2 briefly presents the working principle of solar cells and passivating contacts focusing and poly-Si on oxide junctions. Moreover, it gives an overview of the current state-of-the-art efficiencies reached by implementing POLO junctions into solar cells and improving the firing stability by applying hydrogen-containing capping layers.

Chapter 3 introduces the primary measurement methods used in this work.

Chapter 4 presents an investigation of process-induced degradation and intrinsic loss channels of POLO²-IBC cells. Furthermore, the working principle of separating the two poly-Si contact polarities by an intrinsic poly-Si gap region is investigated.

Chapter 5 investigates the firing stability of POLO junctions, which is essential for successfully transferring POLO junctions into industrial solar cells. The degradation of uncapped POLO junctions and the firing stability improvement using different hydrogen-containing capping layers are analyzed.

Chapter 6 demonstrates the implementation of n^+ POLO contacts into industry-relevant POLO-IBC solar cells. Moreover, comparing simulations and measurements of cells with varying parameters gives insight into further pathways for improvement.

2 Theory and State-of-the-Art

This chapter starts with a short introduction to the working principle of solar cells and their current-voltage characteristic. Subsequently, it focuses on passivating contacts and, in particular, discusses poly-Si on oxide junctions denoted POLO junctions in the following. First, the group of passivating contacts is classified. Then their mode of operation and historical development are briefly described. Finally, an overview of the current state of research is given.

2.1 Working principle of solar cells

Generally, a solar cell is a semiconductor device that converts thermal energy from incident light into electrical energy. The absorption of light and the associated conversion of thermal energy into chemical energy initially creates excess electrons and holes, which in turn can be extracted from the solar cell to a greater or lesser extent in the form of electrical energy, depending on the efficiency of the solar cell.

For a semiconductor in thermal equilibrium, the occupation probability for holes and electrons of a state with energy E can be described by the Fermi-Dirac distribution. Under the condition that $E - E_F > 3k_B T$, the electron and hole concentration (n_0 and p_0) in equilibrium can be approximated by the Boltzmann distribution, which results in

$$n_0 = N_C \exp\left(\frac{E_F - E_C}{k_B T}\right) \text{ for electrons and} \quad (2.1)$$

$$p_0 = N_V \exp\left(\frac{E_V - E_F}{k_B T}\right) \text{ for holes,} \quad (2.2)$$

where N_C and N_V are the effective state densities of the conduction and valence band, E_F is the Fermi energy, k_B is the Boltzmann constant and T the temperature.

Combining equations 2.1 and 2.2 gives

$$n_0 p_0 = N_C N_V \exp\left(\frac{E_V - E_C}{k_B T}\right) = n_i^2, \quad (2.3)$$

$$(2.4)$$

where n_i is the intrinsic charge carrier concentration of $\approx 1 \times 10^{10} \text{ cm}^{-3}$ for silicon at 300 K, which is a material property, however, slightly influenced by temperature and doping density due to band gap narrowing [18], [19]. From equations 2.1 and 2.2 it follows that the product of the equilibrium electron and hole densities depends only on the band gap $E_V - E_C = E_G$ and thus remains constant independent of the doping.

If a semiconductor is illuminated, it is thus brought out of thermal equilibrium with its environment. Photons with energies above the band gap generate additional free charge carriers in the semiconductor. The additional electrons Δn in the conduction band and holes Δp in the valence band lead to a splitting of the Fermi level E_F into two quasi-Fermi levels. The quasi-Fermi level of the holes E_{Fp} moves closer to the valence band as the hole concentration p increases, and the quasi-Fermi level of the electrons E_{Fn} moves closer to the conduction band due to an increased electron concentration n . The distribution of these free electrons and holes can also be described by means of the Fermi-Dirac, respectively Boltzmann statistic:

$$n = n_0 + \Delta n = N_C \exp\left(\frac{E_{Fn} - E_C}{k_B T}\right) \quad (2.5)$$

$$p = p_0 + \Delta p = N_V \exp\left(\frac{E_V - E_{Fp}}{k_B T}\right). \quad (2.6)$$

From the conservation of charge carriers, it follows that $\Delta n = \Delta p$ and thus

$$np = (n_0 + \Delta n)(p_0 + \Delta n) = n_i^2 \exp\left(\frac{E_{Fn} - E_{Fp}}{k_B T}\right), \quad (2.7)$$

with $E_{Fn} - E_{Fp} = \Delta E_F = qV_{\text{impl}}$, where q is the elementary charge and V_{impl} is the implied voltage.

How many free charge carriers generated by illumination with a generation rate G can be extracted from a solar cell depends on how many can be extracted before recombining. The J - V characteristic thus results from generation rate G minus

recombination rate R of the free charge carriers. This gives

$$J(V) = \underbrace{qWG}_{J_{\text{gen}}} - qWR(qV), \quad (2.8)$$

where W is the thickness of the solar cell, and J_{gen} is the photo-generated current density. Furthermore, it is assumed here that $V = V_{\text{impl}}$, which means that the implied voltage can be extracted completely.

The recombination of charge carriers in silicon solar cells is induced by different processes, which additionally depend on the quasi-Fermi level splitting. In general, however, the recombination rate can be described by $R = \frac{\Delta n}{\tau_{\text{eff}}}$, where τ_{eff} is the effective charge carrier lifetime, i.e., the mean time until their recombination.

Under the condition that $\Delta n = \Delta p \ll N_A$, which corresponds to a low-level injection condition in a p -type doped material, it follows that

$$\Delta n \approx \frac{n_i^2}{N_A} \left[\exp\left(\frac{qV}{k_B T}\right) - 1 \right]. \quad (2.9)$$

Assuming an ideal solar cell under low-level injection conditions, with constant τ_{eff} and a spatially uniform quasi-Fermi level splitting across the absorber, this results in

$$J(V) = J_{\text{gen}} - \underbrace{qd \frac{n_i^2}{\tau N_A}}_{J_{01}} \left[\exp\left(\frac{qV}{k_B T}\right) - 1 \right], \quad (2.10)$$

where J_{01} is the recombination current density (prefactor). This J - V characteristic corresponds to the simplest, ideal form of a solar cell J - V characteristic; the so-called one-diode model. However, the recombination rate R has different individual components due to different recombination mechanisms. The effective lifetime τ_{eff} is thus defined as

$$\frac{1}{\tau_{\text{eff}}} = \frac{1}{\underbrace{\tau_{\text{intr}}}_{\tau_{\text{bulk}}}} + \frac{1}{\tau_{\text{SRH}}} + \frac{1}{\tau_{\text{surf}}}, \quad (2.11)$$

where the intrinsic lifetime τ_{intr} is determined by two intrinsic recombination paths in crystalline silicon, band-to-band, also called radiative recombination and Auger recombination [20], [21]. The Shockley-Read-Hall (SRH) lifetime τ_{SRH} depends on recombination over defect states present in the bulk of the measured sample, and τ_{surf}

is the lifetime due to SRH recombination at the surface. Contrary to the intrinsic recombination mechanisms, SRH recombination can be prevented by the passivation of the existing defect states. In particular, the passivation of the defect-rich surfaces and interfaces to the contacts is of special importance.

If one considers the individual recombination mechanisms in detail, different so-called ideality factors m result, which enter in the J - V characteristic as follows.

$$J(V) = J_{\text{gen}} - J_{01} \left[\exp \left(\frac{qV}{m k_B T} \right) - 1 \right] \quad (2.12)$$

The radiative recombination involves one electron and one hole, and the recombination rate is given by

$$\begin{aligned} R_{\text{rad}} &= R_{\text{rad},0} n_i^2 \left(\frac{np}{n_i^2} - 1 \right) \\ &= R_{\text{rad},0} \left[\exp \left(\frac{qV}{k_B T} \right) - 1 \right], \end{aligned} \quad (2.13)$$

which gives an ideality factor of $m = 1$.

For Auger recombination, the three charge carriers involved result in different ideality factors for high and low-level injection. SRH recombination involves defect states in the bulk or at the surface, and here, too, an ideality factor deviates between high- and low-level injection conditions. The corresponding ideality factors are listed in Table 2.1.

Table 2.1: Ideality factors of different recombination mechanisms.

Recombination type	Ideality factor	
	Low-level injection	High-level injection
Radiative recombination	1	1
Auger recombination	1	2/3
SRH recombination	1	2

To account for these further recombination mechanisms, a two-diode model is often used to describe actual solar cells, which takes into account a second recombination current density with m_2 and J_{02} :

$$J_{\text{rec}}(V) = J_{01} \left[\exp \left(\frac{qV}{m_1 k_B T} \right) - 1 \right] + J_{02} \left[\exp \left(\frac{qV}{m_2 k_B T} \right) - 1 \right]. \quad (2.14)$$

Another difference between an ideal and a real solar cell is that a series resistance $R_s > 0$, and a shunt resistance $R_{sh} < \infty$ have to be considered. The J - V characteristic of the double diode model thus as well includes R_s and R_{sh} :

$$J(V) = J_{\text{gen}} - J_{01} \left[\exp \left(\frac{q(V + JR_s)}{m_1 k_B T} \right) - 1 \right] - J_{02} \left[\exp \left(\frac{q(V + JR_s)}{m_2 k_B T} \right) - 1 \right] - \frac{V + JR_s}{R_{sh}}. \quad (2.15)$$

Measuring the J - V characteristic of solar cells makes it possible to obtain information about the solar cell performance. In addition to the output at the maximum power point (MPP) and the efficiency η of energy conversion, values such as the short circuit current J_{sc} , the open-circuit voltage V_{oc} and the fill factor FF , as well as shunt and series resistance R_{sh} and R_s , provide information about different loss mechanisms of the measured solar cell.

The most important parameters for interpreting the J - V characteristic are given in the following.

- The **short-circuit current density** J_{sc} is the maximum current, which flows in the external circuit when the solar cell is short-circuited. Its value gives, among others, information about the optical properties of the solar cell.
- The **open circuit voltage** V_{oc} is the maximum voltage available from a solar cell when operated at open circuit condition, i.e., $J(V) = 0$. From this condition, it follows that :

$$V_{oc} = \frac{nk_B T}{q} \ln \left(\frac{J_{\text{gen}}}{J_0} + 1 \right). \quad (2.16)$$

V_{oc} is a measure of the recombination behavior of the solar cell and is typically given for an illumination of one sun.

The implied open-circuit voltage iV_{oc} refers to the separation of the quasi-Fermi levels under a fixed illumination and $J(V) = 0$, which can be written as $iV_{oc} = \frac{k_B T}{q} \ln \left(\frac{pn}{n_{i,\text{eff}}^2} \right)$ (see equation 2.7) and determined from lifetime measurements at an injection condition corresponding to 1 sun illumination.

- The **maximum power point** MPP characterizes the optimal operating point

at which the maximum power is extracted from the solar cell,

$$P_{\text{mpp}} = J_{\text{mpp}} V_{\text{mpp}}. \quad (2.17)$$

- The **fill factor** FF is defined as the ratio of the maximum power P_{MPP} from the solar cell to the product of V_{oc} and J_{sc} ,

$$FF = \frac{J_{\text{MPP}} V_{\text{MPP}}}{J_{\text{oc}} V_{\text{oc}}}. \quad (2.18)$$

- The **efficiency** η is defined as the ratio of power output from the solar cell to power input P_{in} ,

$$\eta = \frac{P_{\text{out}}}{P_{\text{in}}} = \frac{J_{\text{sc}} V_{\text{oc}} FF}{P_{\text{in}}}. \quad (2.19)$$

Under STC $P_{\text{in}} = 100 \text{ mW/cm}^2$.

- The **series resistance** R_{s} is caused by the ohmic resistance of the semiconductor material, the contact resistance between the semiconductor and the metal contacts, and the ohmic resistance in the contacts.
- The **shunt resistance** R_{sh} is caused by local disturbances of the pn junction and short circuits, for example, at the edge of the solar cell.

2.2 Selectivity

To extract the charge carriers, solar cells need two contact types, one of which mainly extracting the electrons and the other primarily the holes. The major challenge in solar cell optimization is to passivate these contacts as well as possible and make them selectively accessible for one charge carrier type without significant resistive losses.

The currents of charge carriers within the semiconductor are given by

$$J_{\text{n}} = \mu_{\text{n}} n \frac{\partial}{\partial x} E_{\text{Fn}} \quad (2.20)$$

$$J_{\text{p}} = \mu_{\text{p}} p \frac{\partial}{\partial x} E_{\text{Fp}}, \quad (2.21)$$

are thus driven by the gradients in quasi-Fermi energy and are also proportional to the conductivity. Therefore, the enhancement of a selective current toward the contacts implemented inside the cell is possible by changing the mobilities μ_n , μ_p and the charge carrier concentrations (n, p) in the vicinity of the contacts [22]. The simplest and, therefore, the standard solution is to implement a pn junction through doping.

These desired differences between the efficient transport of one charge carrier and the blocking of the other can be expressed by the ratio of the majority carrier resistance ρ_M to the minority carrier resistance ρ_m . Brendel and Peibst [23] suggested this figure of merit, called selectivity S :

$$S = \frac{\rho_m}{\rho_M}. \quad (2.22)$$

For the case of diode-like contacts, as is the case with the samples studied in this work, ρ_m is derived from the slope of the voltage-dependent recombination current at $V = 0$ and thus is described by

$$\rho_m = \frac{k_B T}{q f_c J_0} \quad (2.23)$$

and ρ_M is determined by the resistive loss for majority charge carriers over the passivating junction to the metal contact ρ_c ,

$$\rho_M = \frac{\rho_c}{f_c}. \quad (2.24)$$

This yields the selectivity

$$S = \frac{k_B T}{q J_0 \rho_c}, \quad (2.25)$$

which is quantified by the two relatively easy measurable parameters, contact resistance ρ_c and recombination current density J_0 . Both must be reduced to increase the conversion efficiency. Thus, this figure of merit allows a direct comparison of S of different contact schemes with a single number.

2.3 Working principle of passivating contacts

The POLO junctions belong to the group of so-called passivating contacts, which in recent times particularly have contributed to efficiency improvements [24]–[26] beyond cells with classical diffused pn junctions. The classical dopant-diffused crystalline silicon (c-Si) solar cells use strong doping of the near-surface layer of the c-Si wafer for contact selectivity. This high doping reduces the density and, thus, the conductivity of one of the charge carrier types (electrons or holes) at the interface to the metal contacts [22]. This prevents most but not all of the respective minority charge carriers from reaching the recombination sites at the interfaces. However, there are some limitations to this passivation method. The parasitic free-carrier absorption (FCA) increases with doping density and thus induces a loss in the generated current. Moreover, the Auger recombination of generated excess charge carriers in the doped c-Si region also increases with increasing doping levels. These two effects eventually lead to a limitation of dopant-diffused c-Si cells.

However, good passivation is needed because an unpassivated direct contact between metal and c-Si absorber leads to severe recombination losses due to the high defect density at the metal/c-Si interface. Thus, the c-Si is not directly metalized when using passivating contacts, but a passivating layer is inserted between the absorber and the metal layer. For this purpose, silicon dioxide or amorphous silicon, which are well-established for surface passivation, are typically used.

To achieve good contact passivation, however, the applied layers do not only need to passivate the c-Si surface but also prevent the minority charge carriers from reaching the highly defective metal interface. At the same time, the majority of charge carriers must reach these contacts with as low as possible resistive losses. This charge carrier separation can be achieved in several ways. Here doping of, for example, an additional poly-Si (POLO junctions) or a-Si (heterojunctions) layer is used to create a pn or high-low junction to the absorber. At the same time, research is being done on so-called dopant-free contacts, which apply metal oxides such as titanium oxide TiO_x [27], [28], molybdenum oxide MoO_x [29], [30] and tungsten oxide WO_x [30], [31] or organic materials as PEDOT:PSS [32]–[34].

Another aspect that needs to be considered is optical loss due to free carrier absorption. Doped poly-Si and especially doped a-Si layers lead to increasing losses in J_{sc} with increasing layer thickness when applied to the front side of the cells. In the

case of a-Si, additional transparent conductive oxide (TCO) layers are usually used in conjunction with a very thin doped a-Si layer to reduce reflection and provide lateral conductivity. However, this implies the necessity for using rare and expensive materials.

2.4 Poly-Si on oxide junctions

Poly-Si on oxide junctions has been an active field of research in c-Si photovoltaics since 2013 due to their promising properties. However, they were applied already in 1975 when they were investigated in the field of bipolar junction transistors [35]. In 1980, the first promising experiments with poly-Si junctions in silicon solar cells were done [36], [37]. However, the breakthrough which provoked active international research was only initiated in 2013 through the work of Römer et al. [38] and Feldmann et al.[39]. Since then, many researchers have been working on understanding and optimizing POLO junctions and bringing them into industrial production. This process has been picking up speed in recent years, [16], [40]–[46] so that POLO junctions are now a promising candidate to be brought into large-scale industrial production in the next few years. Companies are already ramping up corresponding production lines [47]–[49].

2.4.1 Processing

As the name implies, POLO junctions consist of a thin interfacial oxide with a poly-Si layer on top. Various methods, such as wet-chemical oxides [38], [50]–[53], thermal oxide growth [54]–[56] and plasma oxides [57], [58] have proven suitable for the preparation of the interfacial oxide. The targeted SiO_x thicknesses are typically in the range of 1 to 3 nm.

Also, for the deposition of the a-Si or a-Si:C layer, which is later crystallized to poly-Si, different methods such as low-pressure chemical vapor deposition (LPCVD) [52]–[54], [59], [60], atmospheric pressure chemical vapor deposition (APCVD) [61], plasma-enhanced chemical vapor deposition (PECVD) [39], [52], [60], [62] and even sputtering can be used [63], [64]. The high-level doping can either be introduced directly during deposition (in situ) or afterward by ion implantation or diffusion

(ex-situ). The poly-Si thickness is typically between 20 nm and several 100 nm.

The deposition is followed by an annealing step at a temperature between 800 to 1050 °C. The optimum annealing temperature is determined by factors such as the oxide thickness and stability. During annealing, rearrangement processes occur at the $\text{SiO}_x/\text{c-Si}$ interface [56], [65], which, depending on the oxide properties and the temperature, can anneal defects at the interface, present after a-Si deposition, or introduce new defects, and also lead to the formation of pinholes inside the oxide layer [66], [67]. A-Si layers are crystallized during this process, while a-Si:C layers used by ISE and EPFL [68], [69] mainly stay amorphous. Also, forming poly-Si/ SiO_x contacts during a single firing step instead of a long high-temperature anneal followed by hydrogenation has shown to achieve good passivating quality [70].

The transport efficiency of the majority carriers to the metal contacts through the POLO junction and its dominant mechanism is significantly influenced by the oxide properties and the annealing parameters. The two occurring mechanisms for carrier transport are tunneling and the transport through local pinholes in the interfacial oxide. Depending on the oxide thickness, stability, and the annealing temperature, one or the other mechanism predominates [66], [71]–[73]. However, both mechanisms, tunneling, and pinholes enable high junction selectivity [73].

Moreover, the annealing process influences the density of defect states D_{it} at the $\text{SiO}_x/\text{c-Si}$ interface. At the same time, diffusion of dopants (especially strong for boron) from the poly-Si into the wafer occurs, leading to the interface's passivation. In the case of an annealing temperature too low for a specific oxide, the contact resistance would stay too high. Furthermore, defects and dangling bonds present at the interface after a-Si deposition would also not sufficiently be annealed, and not enough passivation due to in-diffused doping would be generated. However, suppose the opposite case of a too-high temperature; the in-diffusion would be too strong. Thus the advantage over the PERC cell of a lower doping density at the c-Si surface would be lost due to massive in-diffusion of dopants from the poly-Si. Moreover, after annealing at a certain temperature, the interfacial oxide is no longer sufficiently intact, leading to an increased number of recombination sites at the interface to the highly defective poly-Si. In general, for optimizing the selectivity of POLO junctions, the choice of the oxide and the corresponding adjustment of the annealing process is crucial. If this process is optimized, excellent J_0 values can be achieved directly after annealing. With n -type POLO junctions (n^+ POLO)

and p -type POLO junctions (p^+ POLO) J_0 values of down to (0.5 ± 0.3) fA/cm² and (3.3 ± 0.7) fA/cm² respectively can be reached [60], [74]–[76].

Since SiO_x films have long been used for surface passivation of solar cells, it was well known that introduced hydrogen can reduce the defect density at the c-Si/SiO_x interface by passivating dangling bonds [77]. For this purpose, hydrogen-containing layers like Al₂O₃ and SiN_y can be used, which in combination with annealing at 400 to 450 °C or a firing step, release hydrogen, which diffuses to the SiO_x interface. This method has also been shown to improve the passivation quality of poly-Si junctions. In various experiments, hydrogen was introduced into poly-Si junctions by depositing a hydrogen-rich layer such as SiN_y [59], [78]–[80] or Al₂O₃ [81], [82] and subsequent annealing at about 400 °C or a firing step. Improved J_0 values have been achieved for both n^+ POLO and p^+ POLO junctions. The n^+ POLO, however, showed slightly worse J_0 values after firing, in contrast to the p^+ POLO junctions, which benefit from both annealing and firing. The better the interface is passivated beforehand, the less improvement the hydrogen treatment brings. However, in particular, less stable wet-chemical oxides benefit strongly from this treatment.

2.4.2 Application in back contact solar cells

As mentioned before, applying POLO junctions on the front side of the cells results in significant losses due to FCA. An approach to, nevertheless, replace both contact polarities with POLO junctions are therefore interdigitated back-contacted (IBC) solar cells, where both contacts are placed on the rear side of the cell.

Various groups have thus developed IBC cell concepts with POLO junctions [28], [41], [43], [83]–[86]. A challenge that arises from the one-sided contacting is the structuring of the rear side and the separation of the n^+ POLO and p^+ POLO junctions. If the contacts are in direct contact, strong recombination occurs, as evidenced by low V_{oc} , shunt resistances R_{sh} and FF values [38], [83], [85], [86]. Therefore, different concepts were implemented, separating the contacts by a trench or an intrinsic poly-Si region. Local doping of the poly-Si was implemented by photolithography [28], [85], [86] or masked ion implantation [84]. At ISFH, Haase et al. [25] were able to set a world record for p -type cells at an efficiency of 26.1%. The author of this thesis was involved in this work, and in chapter 4 of this thesis, the corresponding cells and their working principle are deeply investigated. The focus here is on

understanding the working principle of contact separation by an intrinsic poly-Si region.

2.4.3 From laboratory to industrial solar cells

The PERC technology currently dominates the solar cell market. Cells with a p -type base, a phosphor emitter on the front side, and local alloyed Al p^+ -type (Al- p^+) contacts on the rear side have the largest share. The comparatively simple process flow and the constant progress in efficiency improvements are its recipes for success. In 2020, PERC had a market share of 80 % [87]. However, the potential is predicted to be exhausted in the next few years due to enhanced recombination in the emitter region.

In order to successfully step in here and implement the advantages of POLO junctions, a simple process flow is essential. A possible concept for this is a both-side contacted cell concept, in which a POLO junction only replaces the contact on the rear. The so-called tunnel oxide passivated contact (TOPCon) cell is a common cell concept with n^+ POLO junctions. This cell is an n -type cell with a n^+ POLO junction on the rear and boron diffused emitter on the front side [39], [88], which is already transferred to industrially more relevant cells by various research groups [78], [89], [90]. In the meantime, companies are even exceeding 25 % on full area cells with fired screen-printed metallization [15], [16].

In order to transfer the successful concept of the POLO²-IBC cell to an industrially relevant cell concept, some adaptations are necessary [91]. One goal of the thus developed POLO-IBC concept [92], [93] is to remain as close as possible to the manufacturing process of the PERC technology, which will make a conversion of the process lines more straightforward, cost-effective, and therefore attractive. Thus POLO-IBC cells use a p -type wafer, and the Al- p^+ contacts of the PERC cell are also maintained. For the POLO-IBC structure, emitter fingers with n^+ POLO junctions are inserted between the Al- p^+ fingers. Thus the limiting phosphor emitter on the front side is replaced by a n^+ POLO passivating contact on the rear. The POLO-IBC cells thus exploit the high selectivity of a large-area n^+ POLO junction and a small-area Al- p^+ contact. The latter is a standard process for PERC cells [94] and can be cost-effectively formed during the metallization process, avoiding expensive Ag metallization.

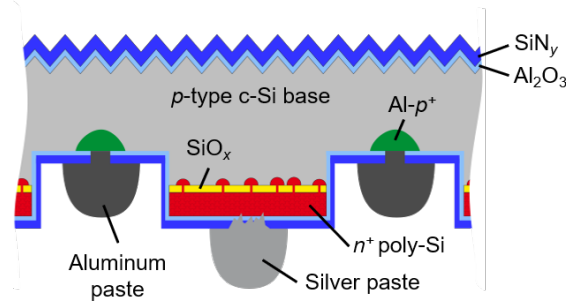


Figure 2.1: Schematic drawing of the POLO-IBC cell structure.

However, the transition to screen-printed metallization is only possible because POLO junctions are more stable at higher temperatures than, for example, silicon heterojunction (SHJ) solar cells. Unlike SHJ technologies, these contacts can withstand temperatures exceeding $300\text{ }^{\circ}\text{C}$. This enables metallization by screen printing and firing at high temperatures, which is the established manufacturing process in industrial silicon solar cell production with a market share of 98% [17]. This feature thus makes TOPCon and other cell concepts like POLO-IBC and POLO-BJ especially attractive.

2.4.4 Firing stability

The advantage of POLO junctions and similar junction schemes compared to other competitors is their thermal stability which facilitates compatibility with standard mainstream high-temperature screen-print metallization [92], [95], mandatory for a cost-efficient industrial-relevant metalization. This short high-temperature „firing“ process step typically uses temperatures between $700\text{ }^{\circ}\text{C}$ and $900\text{ }^{\circ}\text{C}$ and is needed for the printed metal paste to form a contact to the solar cell.

However, several groups have reported degradation of the passivation quality in metalized and also non-metalized regions for n^+ POLO junctions after firing [78], [95], [96]. Therefore, optimizing the metal pastes to avoid the metal spiking through the POLO junction [60], [95], [97] became a field of research. Although no issue might have been expected from firing since the thermal budget of the previously performed anneal is significantly higher than that of the firing step, the former results showed that firing indeed could harm the passivation quality of especially

n^+ POLO junctions. Thus the mitigation of firing-induced degradation on the non-metalized regions also moved into research focus [58], [78], [96], [98]–[109].

Researchers from ECN [78], [96] showed that with a SiN_y capping layer as a hydrogen source J_0 values increased from 2 fA/cm^2 before firing to 4 to 20 fA/cm^2 after firing. Using a stack of $\text{Al}_2\text{O}_3/\text{SiN}_y$ or even $\text{Al}_2\text{O}_3/\text{SiN}_y/\text{Al}_2\text{O}_3$, the passivation quality after firing was improved to about 1 fA/cm^2 . These investigations showed that the hydrogenation of the interface is highly important to maintaining the excellent passivation of n^+ POLO junctions after firing and that there is potential here to enhance the performance of POLO junctions further. Thus, since 2020, several papers [100]–[103] have been published dealing with the impact of hydrogen-containing capping layers on the firing stability. One of the first [100] and two others have been generated as part of this work. In the meantime, it has become apparent that the firing stability of POLO junctions depends on various factors, including the oxide growth method [104], [109], the poly-Si deposition method (PECVD, LPCVD) [58], [109] and the doping type of the poly-Si layers [60], [96], [98], [101], [110]. In addition, besides the POLO junctions themselves, the choice of the capping layer is of crucial importance. As already shown by Mewe et al. [96], $\text{Al}_2\text{O}_3/\text{SiN}_y$ stacks seem to work particularly well. However, since the additional deposition of an Al_2O_3 layer is an expensive process from an industrial point of view, the optimization of passivation with a single layer of SiN_y is an aim of the research. Besides the variation of the SiN_y deposition equipment and techniques [104], [109], which leads to significant differences, also the variation of the refractive index shows to influence the achieved passivation quality [102], [109], [111].

An in-depth analysis of the firing stability of LPCVD deposited n^+ POLO junctions is done in chapter 5 of this work. On the one hand, the question is raised why the passivation quality deteriorates at all due to firing. On the other hand, the reason why different hydrogen capping layers achieve significantly different results after firing is inquired.

3 Characterization and simulation methods

3.1 Current-voltage measurements

To make J - V characteristics comparable, standard test conditions (STC) have been specified that prescribe an AMG1.5 spectrum with an irradiance of 100 mW/cm^2 under vertical illumination and a temperature of $25 \text{ }^\circ\text{C}$. The J - V characteristics shown in this work are measured using the LOANA solar cell characterization system from pvtools. Here instead of an AMG1.5 spectrum, an infrared LED array is used, calibrated before each series of measurements using a reference cell measured under STC at ISFH CalTeC.

3.2 Quasi-steady-state photoconductance and photoconductance decay techniques

Determining the effective minority charge carrier lifetime τ_{eff} (from here briefly "lifetime") as a function of the excess charge carrier density Δn is an essential method for evaluating the quality of unmetallized solar cell precursors, which can be quickly done with the Sinton Instruments WCT-120 lifetime tester [112]. This device determines the time-dependent conductivity of the tested samples averaged over an area of approx. 250 mm^2 using an inductively coupled coil below the sample, as can be seen in Figure 3.1.

Under the conditions of a homogeneous photogeneration of excess charge carriers and a small recombination activity at the surface, the photogenerated conductance

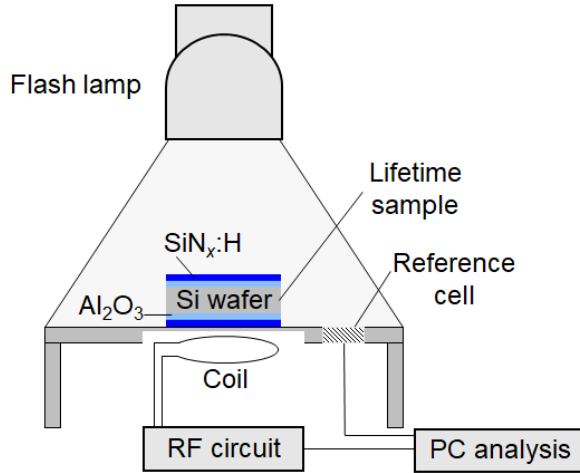


Figure 3.1: Schematic drawing of the WCT-120 setup used in this work. This figure is taken from [113].

is given by

$$\Delta\sigma \approx qW(\mu_n + \mu_p)\Delta n_{\text{avg}}, \quad (3.1)$$

where W is the sample thickness and μ_p and μ_n are the electron and hole mobilities. Thus, to determine Δn , the only required quantities are the thickness of the sample W and the base doping N_{dop} , which is required to calculate the electron and hole mobilities [114].

To determine the lifetime, one can use two different methods or a combination of these two depending on the absolute value of the lifetime. One method is the Quasi-Steady-State Photoconductance (QSSPC) measurement, during which a flashlight illuminates the sample with a long decay time of approximately 2.1 ms, which generates excess charge carriers in the sample. The time-dependent illumination intensity is monitored via a calibrated reference solar cell while the coil monitors the illumination-induced photoconductance of the sample under test. To obtain the effective lifetime τ_{eff} , additionally, to the time-resolved Δn , the generation rate $G(t)$ is needed.

$$R(t) = \frac{\Delta n}{\tau_{\text{eff}}} = G(t) - \frac{\partial \Delta n}{\partial t} \quad (3.2)$$

The generation rate $G(t)$ is given by the photogenerated current density J_{gen} determined by the reference solar cell (see Figure 3.1) and the optical factor f_{opt} accounting for the optical properties of the sample. Inserting these into equation 3.2

3.2 Quasi-steady-state photoconductance and photoconductance decay techniques

yields:

$$\tau_{\text{eff,QSSPC}} = \frac{\Delta n}{\frac{J_{\text{gen}} f_{\text{opt}}}{qW} - \frac{\partial \Delta n}{\partial t}}. \quad (3.3)$$

For the case that $\tau_{\text{eff}} \ll t_{\text{decay}}$ the term $\frac{\partial \Delta n}{\partial t}$ can be neglected. However, the equation 3.3 is applied in the full form for intermediate lifetimes.

The second method, the photoconductance decay method (PCD), is a transient technique and works with the decay in conductivity of a sample after illumination with a short flash. When the decay time of the illumination about 30 μs is significantly shorter than the effective lifetime, the generation rate can be neglected, which yields the following simplified equation:

$$\tau_{\text{eff,PCD}} = -\frac{\Delta n}{\frac{\partial \Delta n}{\partial t}}. \quad (3.4)$$

This equation is independent of the optical properties of the measured sample. However, to full fill the condition of a lifetime $\tau_{\text{eff}} \gg t_{\text{decay}}$, in this work, this method is only used when $\tau_{\text{eff}} > 800 \mu\text{s}$.

Recombination current density

The recombination at the surface τ_{surf} is typically quantified by a surface recombination current density J_0 defined by

$$J_{\text{rec,surf}} = \frac{qW \Delta n}{\tau_{\text{surf}}} = J_0 \left(\frac{np}{n_{\text{i,eff}}^2} - 1 \right). \quad (3.5)$$

For samples where the surface region is always in low injection due to, e.g., highly doped poly-Si contacts with in-diffusion of dopants, as in this work, the surface recombination current density J_0 can be extracted from the $\tau_{\text{eff}}(\Delta n)$ data obtained by the QSSPC or PCD measurements with the method of Kane and Swanson [115]. For this method J_0 is approximated as follows:

$$J_0 = \frac{qW n_{\text{i,eff}}^2}{\tau_{\text{surf}} (N_{\text{dop}} + \Delta n)}. \quad (3.6)$$

To obtain J_0 the slope over Δn of the equation

$$\frac{1}{\tau_{\text{eff}}} - \frac{1}{\tau_{\text{intr}}} = \frac{1}{\tau_{\text{SRH}}} + J_0 \frac{2(N_{\text{dop}} + \Delta n)}{qWn_{i,\text{eff}}^2}. \quad (3.7)$$

is evaluated in high injection, where τ_{SRH} is injection independent and $\Delta n + N_{\text{dop}}$ can be approximated by Δn . If a linear relationship between $\frac{1}{\tau_{\text{eff}}} - \frac{1}{\tau_{\text{intr}}}(\Delta n)$ is obtained, J_0 can be determined.

In this work, the described simplifying approach is applied, using corrected lifetimes provided by the Sinton lifetime tester spreadsheet, taking into account an injection-dependent $n_{i,\text{eff}}$ [116], [117] due to bandgap narrowing in the base substrate [118] and applying the model for τ_{intr} by Richter et al. [20]. To meet the applied assumptions, this method is only applied to either high-quality float-Zone material or high impedance Czochralski (Cz) grown material (20 Ω cm), leading to high injection conditions being reached during the lifetime measurement.

Surface recombination velocity

Apart from the recombination current density J_0 an additional parameter called the effective surface recombination velocity (S_{eff}) is used to specify the surface recombination. S_{eff} is defined as the recombination rate R_{surf} (number of charge carriers recombining at the surface [$\text{cm}^{-2}\text{s}^{-1}$]) per excess charge carrier density Δn [cm^{-3}] at the surface, which gives a unit of cm/s. Enhanced recombination at the surface reduces Δn at the surface, and thus a gradient towards the surface develops. This gradient, in turn, leads to a diffusion of minority charge carriers toward the surface. The diffusion constant of the minority carriers is thus limiting the recombination at the surface. The surface recombination velocity S_{eff} can be expressed as

$$S_{\text{eff}} = \sqrt{D \left(\frac{1}{\tau_{\text{eff}}} - \frac{1}{\tau_{\text{bulk}}} \right)} \tan \left[\frac{W}{2} \sqrt{\frac{W}{2} \left(\frac{1}{\tau_{\text{eff}}} - \frac{1}{\tau_{\text{bulk}}} \right)} \right] \quad (3.8)$$

[119] where D is the minority charge carrier diffusion constant.

3.3 Infrared lifetime mapping

Infrared lifetime mapping is used for measuring the spatially resolved effective carrier lifetime, which, in contrast to QSSPC and PCD measurements, can also be applied to structured and metalized samples. Figure 3.2 shows the setup required for an ILM measurement.

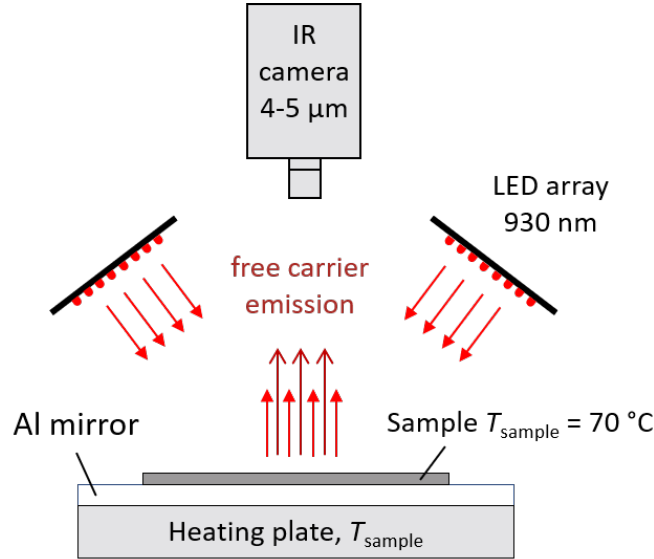


Figure 3.2: Schematic drawing of the ILM setup used in this work.

In silicon, free charge carriers can absorb and emit radiation with energy below the bandgap. During this process, the charge carriers change between two states within a continuous band of allowed energy states. The absorption coefficient for the FCA, α_{fc} is directly proportional to the density of free charge carriers Δn as only one type of charge carrier (either an electron in the conduction band or a hole in the valence band) is involved,

$$\alpha_{fc} \propto \Delta n. \quad (3.9)$$

According to the law of detailed balance and Kirchoffs law, they have to emit the same amount of power they absorb at thermal equilibrium. Therefore in equilibrium the absorption coefficient has to be equal to the emission coefficients ($\alpha_{fc} = \epsilon_{fc}$). The linear dependence of the free carrier emission (FCE) and FCA on Δn is the basis for a quantitative determination of the charge carrier density from measurements of FCE and FCA [120].

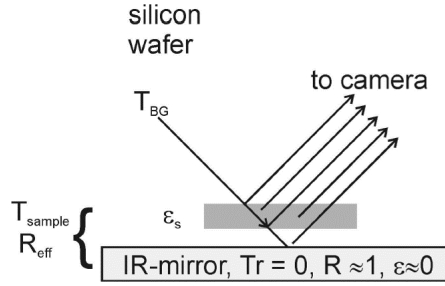


Figure 3.3: Sketch of IR radiation paths in the setup used, taken from [121].

For the ILM measurement, an infrared (IR) mirror is placed between the heating plate and the sample in the setup used in this work, which is shown in Figure 3.2. Thus, the measured signal only consists of the IR radiation emitted by the sample and a background signal that is emitted above the sample and reflected at the sample's surface or the IR mirror (see Figure 3.3). The sample is heated to 70 °C, enhancing the FCE in the sample and thus improving the signal-to-noise ratio to the surroundings. A modulated LED array with a wavelength of 930 nm illuminates the sample to generate excess charge carriers using a step-like illumination function with a period length of 25 ms. The sample's time- and spatial-resolved FCE is measured with an IR camera during an integration time of 400 μ s. A schematic generation rate $G(t)$ and $\Delta n(t)$ during one measurement period are shown in Figure 3.4.

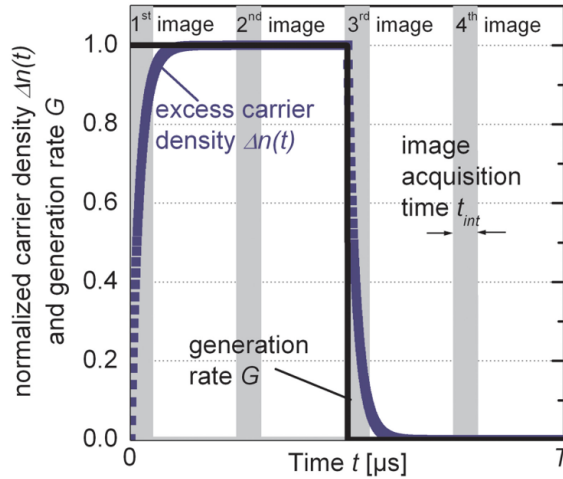


Figure 3.4: Schematic of the generation rate $G(t)$ excess carrier density $\Delta n(t)$ and image acquisition during one measurement period of length T , taken from [122].

As the FCE is proportional to the density of free charge carriers, the signal is a spatially resolved measure of the excess charge carrier density Δn , which is described by the continuity equation

$$\frac{d}{dt}\Delta n(t) = G - \frac{\Delta n(t)}{\tau_{\text{eff}}}. \quad (3.10)$$

Assuming a mono exponential rise and decay it develops as follows after switching on and off the illumination:

$$\Delta n(t) = G\tau_{\text{eff}} \begin{cases} \left[1 - \exp\left(-\frac{t}{\tau_{\text{eff}}}\right)\right] & 0 < t < T/2 \\ \left[\exp\left(-\frac{t-T/2}{\tau_{\text{eff}}}\right)\right] & T/2 < t < T. \end{cases} \quad (3.11)$$

To determine Δn and τ_{eff} from the measured signal, either a calibration is necessary, or the dynamic ILM method must be applied as it is done in this work. The dynamic ILM measurement uses the time-dependence of the charge carrier density Δn after switching on/off the excitation light to derive τ_{eff} . Therefore, four images are taken during one illumination period, as shown in Figure 3.4. The first image (S_1) is taken shortly after switching on the illumination, the second (S_2) after steady-state under illumination is reached, the third (S_3) immediately after the illumination is switched off, and the fourth (S_4) after the steady-state without illumination is reached. The carrier lifetime can then be derived from the ratio of the steady-state signal (S_2) under illumination and the signal directly after switching on or off the excitation source (S_1 or S_3). The fourth image (S_4) is used to subtract the background signal.

Moreover, the setup applies a lock-in analysis technique to reduce the signal-to-noise ratio. For this purpose, all four images are needed. Therefore, cosine-correlated and sine-correlated images are calculated using the four measured images:

$$S_{\text{sin}} = S_2 - S_4 \quad (3.12)$$

$$S_{\text{cos}} = S_1 - S_3. \quad (3.13)$$

which are used to compute a phase image according to lock-in theory [123, Chap-

ter 2.2]:

$$\Phi = \arctan\left(\frac{S_{\cos}}{S_{\sin}}\right) \quad (3.14)$$

$$= \arctan\left(\frac{t_{\text{int}} - 2\tau_{\text{eff}} \left[1 - \exp\left(-\frac{t_{\text{int}}}{\tau_{\text{eff}}}\right)\right]}{t_{\text{int}} - 2\tau_{\text{eff}} \left[\exp\left(-\frac{T}{4\tau_{\text{eff}}}\right) - \exp\left(-\frac{T + 4t_{\text{int}}}{4\tau_{\text{eff}}}\right)\right]}\right). \quad (3.15)$$

This gives an expression 3.15 that only depends on the known integration time t_{int} , lock-in period time T and the effective lifetime τ_{eff} . Using this expression, a look-up table is generated, which allows determining τ_{eff} for every pixel in the phase image and thus generating a lifetime image without further information about the sample. Moreover, an injection-dependent measurement of $\tau_{\text{eff}}(\Delta n)$ is possible by varying the illumination intensity.

In addition to the advantages mentioned above of the dynamic ILM method, some disadvantages must be considered. On the one hand, blurring occurs due to the diffusion of charge carriers and internal optical reflections. Especially areas with low lifetimes are thus overestimated [121]. Another factor that can lead to an overestimation of the lifetime are injection-dependent lifetimes since the assumption that is made of a mono-exponential development of Δn assumes an injection-independent lifetime. In low-injection, where injection-dependent lifetimes occur due to SRH recombination, it essentially averages back out as both the rising signal as well as the falling signal are affected [121, p. 69-74]. In the case of a high-injection condition where the Auger recombination provides for an injection dependency, a severe overestimation of the lifetime by the dynamic ILM method was shown by Herlufsen [124, p. 84-87]. However, for highly doped wafer material ($1.5 \Omega \text{ cm}$), according to Herlufsen, this effect only occurs for injection levels above $1 \times 10^{17} \text{ cm}^{-3}$.

Implied pseudo- J - V data

To compare the process-induced degradation with J - V values of finalized solar cells as in Section 4.2, it is helpful to calculate implied J - V parameters from the measured lifetimes. For this purpose, Δn can be computed using the reflectivity R at 930 nm and the sample thickness W , the illumination intensity I_{suns} in suns and the photon

flux ϕ

$$\Delta n = \frac{\tau_{\text{eff}} I_{\text{suns}} \phi (1 - R)}{W}. \quad (3.16)$$

With this, the recombination current density J_{rec} can be calculated using the expression

$$J_{\text{rec}} = \frac{qW\Delta n}{\tau_{\text{eff}}}. \quad (3.17)$$

With the implied open-circuit voltages iV_{oc} calculated from

$$iV_{\text{oc}} = \frac{k_{\text{B}} T}{q} \ln \left(\frac{np}{n_i^2} \right) = \frac{k_{\text{B}} T}{q} \ln \left(\frac{\Delta n^2 + \Delta n \left(\frac{n_i^2}{N_{\text{dop}}} + N_{\text{dop}} \right) + n_i^2}{n_i^2} \right) \quad (3.18)$$

and assuming a reasonable J_{sc} value, as determined by J - V or J_{sc} - V_{oc} measurements on optical identical samples, the respective iV_{oc} at one sun, the implied pseudo- FF (ip FF) and implied pseudo-efficiency ip η can be determined. The same procedure is used for the $\tau_{\text{eff}}(\Delta n)$ curves determined with PCD and QSSPC measurements.

3.4 Time-resolved photoluminescence

Photoluminescence (PL) measurement methods make use of the radiative band-to-band recombination mechanism in semiconductors. The radiative band-to-band recombination describes the direct recombination of an electron from the conduction band with a hole from the valence band. The energy difference between the electron and the hole is emitted as a photon of corresponding energy, which can be detected by a camera. Since the process simultaneously involves both electrons and holes, the recombination rate depends on both types of charge carriers. Thus, the radiative recombination rate is [125] :

$$R_{\text{rad}} \propto np \propto \Delta n N_{\text{dop}} + \Delta n^2 \quad (3.19)$$

Time-Resolved Photoluminescence (TRPL) is a method for studying the decay of Δn after an excitation pulse. In this work, the samples are excited by a mode-locked Titanium-sapphire laser with 80 MHz pulse rate and a wavelength of 780 nm. The spot size is adjusted to about 1 mm for optimal signal yield. The streak camera

mechanism uses a multiplier-channel plate (MCP). An electric field alternating with a high frequency deflects the electrons generated by the MCP and a charge-coupled device (CCD) detects them using a phosphorescent filter enabling picosecond time resolution. The resulting time-resolved signal S_{PL} of the excitation and decay process can be fitted by an exponential decay function according to equation 3.10 which gives the following expression for the decay of Δn after an excitation pulse

$$\Delta n(t) = G \tau_{\text{eff}} \exp\left(-\frac{t}{\tau_{\text{eff}}}\right) \quad (3.20)$$

$$\text{and thus } S_{\text{PL}} = A \exp\left(-\frac{2t}{\tau_{\text{eff}}}\right), \quad (3.21)$$

where A is the amplitude. If multiple lifetime components are involved, they can be fitted by a sum of exponential functions.

3.5 Fourier-transform infrared spectroscopy

Infrared spectroscopy uses a thermal source to generate infrared light over a wide range of wavelengths of 2.5 to 25 μm directed through an interferometer onto the sample under investigation. A beam splitter divides the light beam into two paths: one with a fixed mirror and the other with a movable mirror. After reflection from the respective mirrors, both beams interfere with each other, and the resulting beam passes through the sample. Subsequently, its intensity is measured by a detector, as shown in Figure 3.5.

During the measurement, the movable mirror is shifted, which leads to a varying time delay between the two interfering beams. The resulting measured signal thus is the autocorrelation function of the transmitted signal, which gives the intensity as a function of the time delay between the interfering beams. Subsequent Fourier transformation (FT) according to the Wiener-Khinchin-Theorem yields the energy spectrum, i.e., the intensity as a function of wavenumber $\tilde{\nu} = 1/\lambda$.

Light of wavelengths characteristic of a material is absorbed by it. These are wavelengths whose frequency corresponds to the resonance frequency, i.e., the vibration frequency of a molecular vibration mode. Moreover, a prerequisite for excitation by IR radiation is that the dynamic dipole moment changes during the vibration. As described by the Beer-Lambert law, the light intensity decreases exponentially when

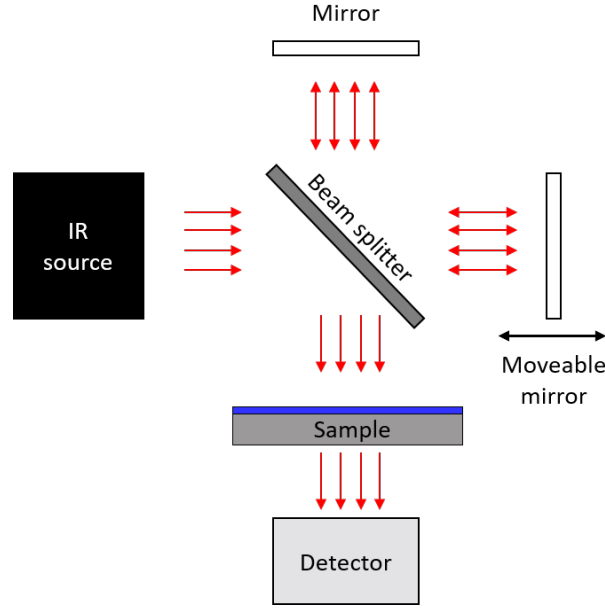


Figure 3.5: Schematic drawing of a Fourier-transform infrared spectroscopy (FTIR) setup.

traveling through a sample. Therefore, the light intensity can be described as

$$S_{\text{FTIR}}(\tilde{\nu}) = S_{\text{IR},0}(\tilde{\nu}) \exp(-\alpha(\tilde{\nu}) W) \quad (3.22)$$

$$\text{and thus } \alpha(\tilde{\nu}) = \frac{\ln \left(\frac{S_{\text{FTIR}}(\tilde{\nu})}{S_{\text{FTIR},0}(\tilde{\nu})} \right)}{W}, \quad (3.23)$$

where α is the absorption coefficient, $\tilde{\nu}$ the wavenumber and W the thickness of the respective film.

The transmittance $T = S_{\text{FTIR}}/S_{\text{FTIR},0}$ is determined from the ratio of a measurement with the layer under investigation on a substrate and a measurement of the bare substrate. The absorption A is then given by $A = 1 - T - R$, where R is the reflectance. The wavelengths absorbed in the respective sample thus can be seen as characteristic peaks in the resulting absorption spectra.

In this work, atomic bonds within silicon nitride films with their characteristic absorption peaks (see Figure 3.6) are investigated to determine the concentration of hydrogen-containing bonds and, thereby, the total hydrogen concentration $[\text{H}]$ within

Table 3.1: Silicon nitride absorption peak locations and calibration constants c taken from [126].

Bonds	Wave number $\tilde{\nu}$ [cm ⁻¹]	IR absorption cross section K [cm ⁻¹]
Si-N	880	2.1×10^{16}
Si-N	1070	2.1×10^{16}
Si-H	2200	5.9×10^{16}
N-H	3320	8.2×10^{16}

the film. The concentration of the atomic bonds is determined using [126]

$$[X - Y] = K([X - Y]) \int \alpha(\tilde{\nu}) d\tilde{\nu} \quad (3.24)$$

where K is the IR absorption cross-section needed to calibrate the measured areas under the absorption peaks, given in Table 3.1 and taken from [126]. The spectra were subjected to background correction, baseline fitting, and deconvolution of absorption peaks before determining the areas under the absorption peaks. An example is shown in Figure 3.6.

The hydrogen fraction H in the silicon nitride films is defined as [127]

$$H = \frac{[Si - H] + [N - H]}{[Si - H] + [N - H] + [Si - N]} \quad (3.25)$$

under the assumption of neglecting [Si-Si], [N-N], and [H-H] bonds, which holds for nearly stoichiometric films as measured in this work.

3.6 Time of flight secondary ion mass spectrometry

During Time of Flight Secondary Ion Mass Spectrometry (ToF-SIMS), a sample is bombarded with primary ions (e.g., O₂⁺, Cs⁺, Bi⁺). This produces charged particles (secondary ions) that can be separated according to their mass, employing a time-of-flight mass analysis. As particles of different masses reach different velocities at the same accelerating voltage, the accelerated particles travel a certain distance in the analyzer and reach the detector with different time delays. This method achieves a very high spectral mass resolution and provides an accurate image of the sample

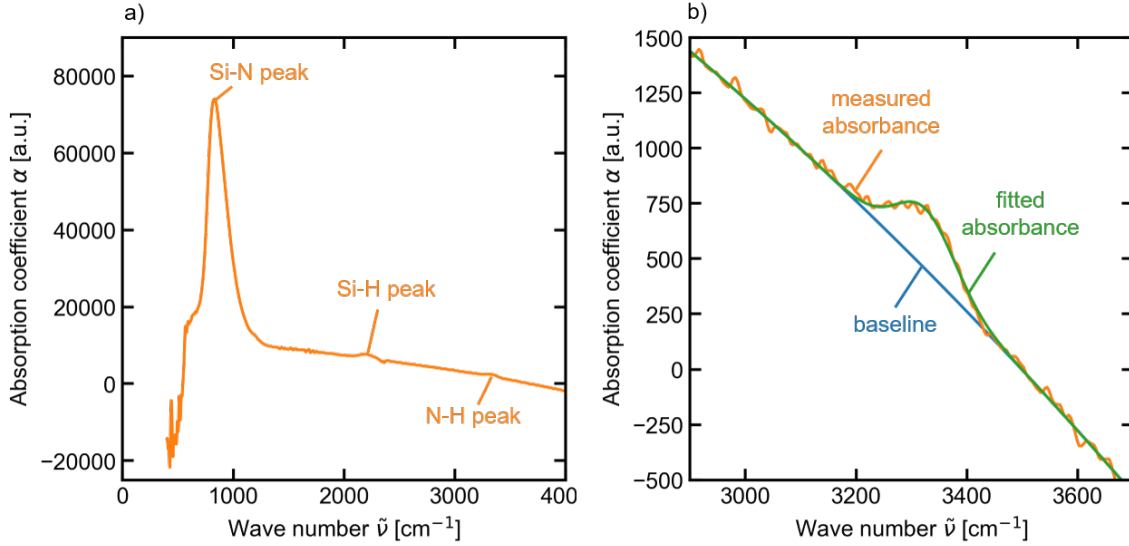


Figure 3.6: (a) Absorption coefficient α of a c-Si sample coated with hydrogen-rich silicon nitride. The marked absorption peaks related to silicon-nitrogen, silicon-hydrogen and to nitrogen-hydrogen bonds. (b) Absorption spectrum zoomed-in on the N-H peak with fitted baseline and absorption peak.

surface and composition. In this work, the ToF-SIMS analyses are performed using ION-TOF TOF-SIMS V spectrometers.

Lateral and depth-resolved analysis of doping elements in the $p^+(i)n^+$ poly-Si region in Section 4.3.4 is done at different sample positions in depth profiling mode using the sputter sources Cs^+ (at 1 keV) and O_2^+ (at 1 keV) for negative and positive ion mode, respectively. The sputter area is set to $220 \times 200 \mu\text{m}^2$ and the target area is set between $80 \times 80 \mu\text{m}^2$ up to $150 \times 150 \mu\text{m}^2$. For quantification of the B^+ and P^+/P^- ion intensities, the relative sensitivity factors (RSFs) with respect to the Si^+/Si^- intensity are used. The primary sputter gun is Bi^+ (at 25 keV, bunched mode). For the analysis in Section 5.4.1 a 30 keV Bi^+ beam with a pulsed beam current of 1 pA is used, and sputtering is performed with both 1 keV and 3 keV sputter gun energies, and at 10 and 40 A beam current, respectively. The resulting profiles are quantified using implanted Si standards and thus are not accurate for the Al_2O_3 and SiN_y layers.

3.7 High-frequency capacitance- and conductance-voltage measurements

By Capacitance-Voltage ($C-V$) measurements, it is possible to determine various parameters of semiconductor devices as doping density, interface trap density, and oxide thickness. In the simplest case of an ideal Schottky diode, the principle is based on the relationship between the applied voltage and the capacitance of the space charge region in the semiconductor C_s , determined by its width W corresponding to a plate capacitor:

$$C_s = \frac{\epsilon_{\text{Si}}\epsilon_0 A_c}{W}, \quad (3.26)$$

where ϵ_0 and ϵ_{Si} are the permittivities of vacuum, and silicon, respectively, and A_c is the contact area. By applying an external voltage, the width of the depletion region can be manipulated. In reverse bias, the width increases, and accordingly, the capacitance of the depletion region decreases. The dependence of the depletion width and the capacitance upon the applied voltage thus provides information on the semiconductor's internal characteristics, such as its doping profile.

The samples investigated in this work are POLO junction samples, although in this case, the oxide is thermally grown and significantly thicker ($d_{ox} = 10$ nm) than in typical POLO junctions. This is necessary to suppress leakage currents through the oxide, negatively affecting the measurement. Their structure is shown in Figure 5.3. Due to the thick oxide and the high doping density inside the poly-Si, these samples can be treated according to the metal oxide semiconductor (MOS) structure theory.

High frequency $C-V$ measurements enable the determination of the interface state density D_{it} at the oxide interface as a function of the energetic position in the bandgap. A cascade probe station with an Agilent 4294A impedance analyzer is used for the following measurements. The D_{it} is determined by following the conductance method described by Nicollian et al. [128] and Brews et al. [129]. During the conductance measurements, a small high-frequency alternating current (AC) voltage added to the direct current (DC) gate voltage V_g moves the band edge alternately toward and away from the Fermi level leading to a change in surface potential. If the frequency of the AC voltage is low, the potential changes slowly, and the traps that move from above to below the Fermi level (or vice versa) can respond directly

3.7 High-frequency capacitance- and conductance-voltage measurements

with emitting or trapping of charge carriers. However, if the frequency increases, the traps lag behind, and a difference ΔE between the surface energy and the mean energy of traps develops. Thus an energy loss occurs when a charge carrier is captured/emitted by a trap with lower/higher energy than the surface energy. This energy loss can be measured as frequency-dependent parallel conductance G_p as the voltage source of the setup supplies the lost energy. Moreover, it can be directly seen as a frequency dispersion in the C - V curves shown in Figure 3.7(a).

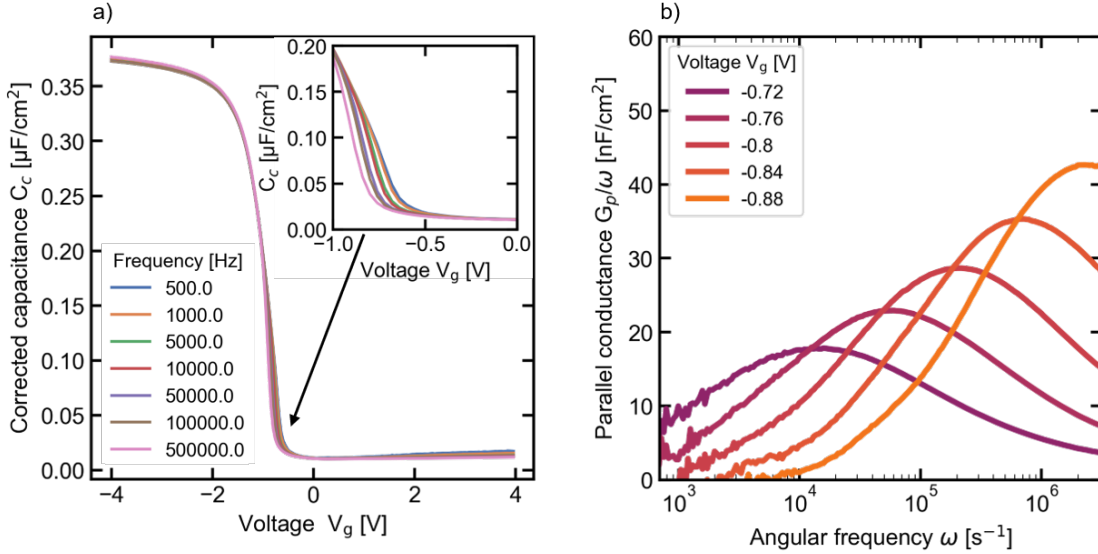


Figure 3.7: (a) Corrected capacitance C_c as a function of voltage V_g for samples measured at different frequencies between 0.5 kHz and 0.5 MHz. The inset shows the lower part of the curve between depletion and inversion where a frequency dispersion can be seen. (b) Parallel conductance G_p over angular frequency ω as a function of the logarithmic angular frequency for different voltages V_g . This figure is adapted from Figure 4 in Ref. [104].

Figures 3.8(a)-(d) show the corresponding electrical equivalent circuits considered for the measurement and evaluation. The circuit (a) shows the circuit based on which the measured admittance $Y = G_m + i\omega C_m$ is initially evaluated, (b) shows a MOS capacitor equivalent circuit including an oxide capacitance C_{ox} and a parallel conductance element G_p accounting for the interface states and (c) additionally to (b) includes a series resistance element accounting for the series resistance of the semiconductor (c-Si). Circuit (d) shows an equivalent circuit in strong accumulation, which is used to determine R_s and C_{ox} .

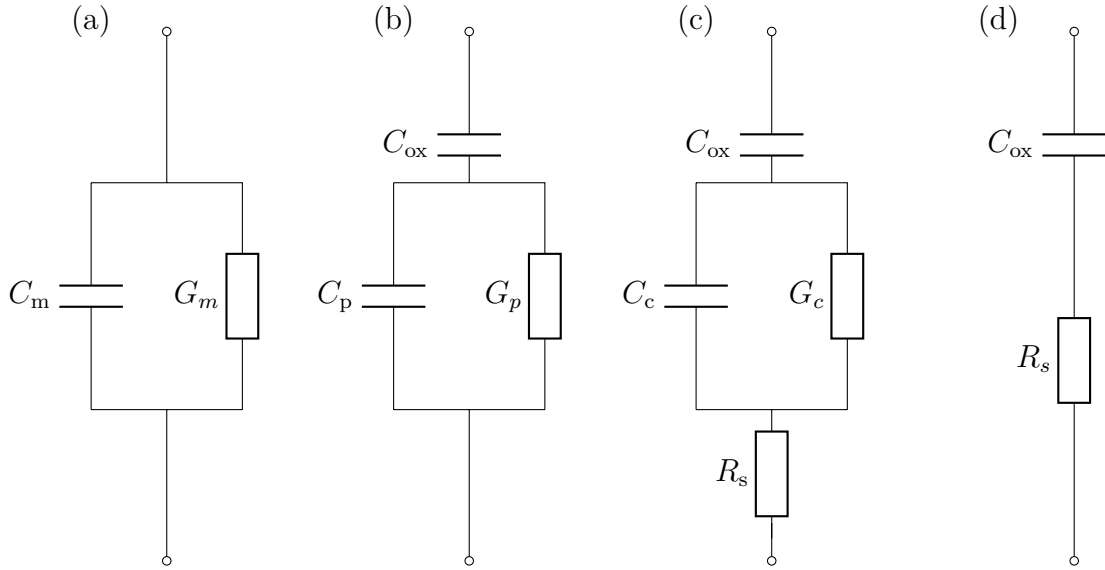


Figure 3.8: Electrical equivalent circuits with the resistive and capacitive contributions of MOS capacitors utilized for measurement and evaluation. (a) Measurement circuit; (b) equivalent circuit of ideal MOS including effects of D_{it} and (c) additionally including the semiconductor series resistance R_s ; (d) simplified equivalent circuit in strong accumulation.

The frequencies used for the high-frequency measurements range of 0.5 to 500 kHz, and the DC bias voltage is swept from accumulation to inversion condition. In accumulation, a strong deviation between capacitances with increasing frequency is observed. However, one constant value corresponding to the oxide capacitance C_{ox} is expected for all frequencies. This behavior suggests that the equivalent circuit models shown in Figure 3.8(a) and (b) are inappropriate for extracting the capacitance from the measured impedance. The measurements are affected by additional frequency-dependent effects, probably the series resistance R_s of the substrate. Thus a series resistance R_s , probably induced by the substrate resistance, is included in the equivalent circuit (see Figure 3.8(c)). To determine R_s , the frequency-dependent admittance in strong accumulation is determined, where the equivalent circuit can be simplified as shown in 3.8(d). With the thus determined values G_{ma} and C_{ma} the series resistance $R_s(\omega)$ and the oxide capacitance C_{ox} can be calculated [130,

p.222-224]:

$$R_s = \frac{G_{ma}}{G_{ma}^2 + \omega C_{ma}^2} \quad (3.27)$$

$$C_{ox} = C_{ma} \left(1 + \left(\frac{G_{ma}}{\omega C_{ma}} \right)^2 \right). \quad (3.28)$$

With this the corrected capacitance C_c and parallel conductance G_c corresponding to the equivalent circuit in Figure 3.8(c) are calculated [130, p.224], which are used for the further evaluation. This correction is applied to all data sets. With the corrected values G_c and C_c , the parallel conductance

$$\frac{G_p}{\omega} = \frac{\omega \cdot C_{ox}^2 \cdot G_c}{(G_c^2 + \omega^2 (C_{ox} - C_c)^2)} \quad (3.29)$$

is calculated. From the peak of the function G_p/ω versus $\log(\omega)$ (see Figure 3.7) the interface state density D_{it} at one energetic position for each gate voltage can be determined. To obtain D_{it} as a function of V_g , further G_p/ω measurements are performed with sweeps of frequency from 500 Hz to 0.5 MHz for different fixed gate voltages in depletion and weak inversion conditions (-0.6 to -0.9 V).

The following equation is used to calculate the D_{it} [130, p.216]

$$D_{it} = \frac{[G_p/\omega]_{peak}}{q \cdot A \cdot f_D(\sigma_s)}, \quad (3.30)$$

where f_D is a correction factor that accounts for the effect of a spatial non-uniform surface potential. This variation of the surface potential can be described by a Gaussian distribution with standard deviation σ_s around the mean value of the surface potential ψ_s . For the calculation of the correction factor f_D , the standard deviation σ_s of the G_p/ω curve is required. Instead of a direct determination via a Gaussian fit, it can also be deduced from the ratio of $G_p/\omega(n \cdot \omega_{peak})/G_p/\omega(\omega_{peak})$ where n is chosen to be 5 or 1/5 so that $n \cdot \omega_{peak}$ is within the reliable measurement range as proposed by Nicollian et al. [128], [130]. The function $f_D(\sigma_s)$ is calculated numerically following [130, p.216] and is shown in Figure 3.9.

To determine the position of the Fermi level at each operating point V_g , which indicates the position of the interface states in the bandgap, the $\phi_s - V_g$ relationship is determined, where ϕ_s is the surface band bending. For this purpose, the high-

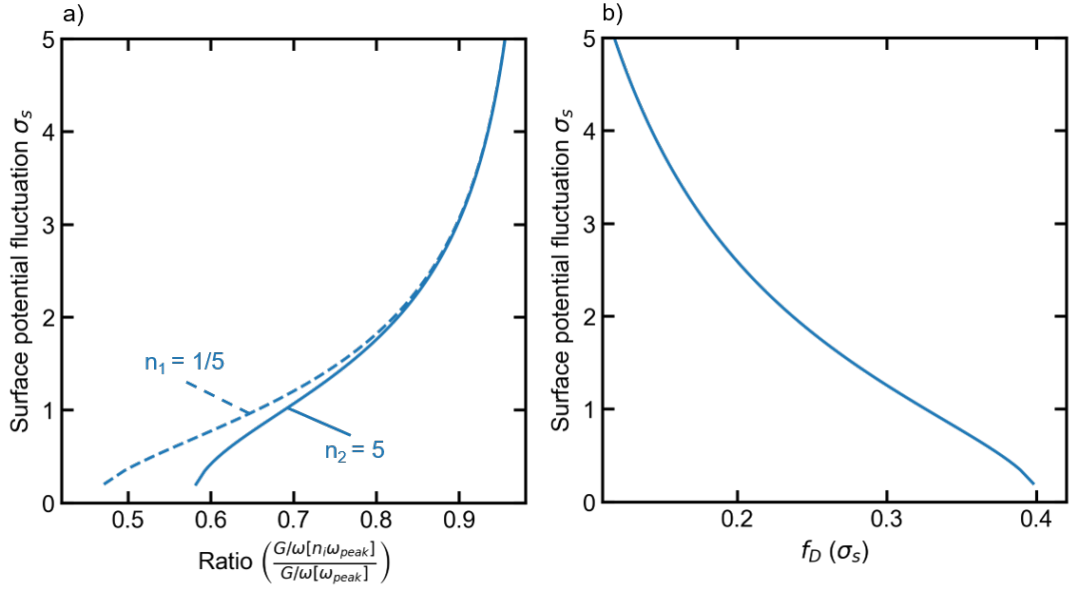


Figure 3.9: (a) Surface potential fluctuation σ_s as a function of the Ratio $\left(\frac{G/\omega[n_i\omega_{peak}]}{G/\omega[\omega_{peak}]}\right)$. (b) Correction factor f_D as a function of σ_s .

frequency method developed by Terman [131] is applied as described by Nicollian et al. [130]. The capacitance measurements described above are measured at sufficiently high frequencies so that the interface traps do not follow the AC gate voltage. The D_{it} thus does not contribute to the high-frequency capacitance C_{HF} which can be described by

$$C_{HF} = \frac{C_s C_{ox}}{C_s + C_{ox}}, \quad (3.31)$$

where C_s is the semiconductor capacitance. Even though the defect states do not follow the high-frequency AC voltage, they do follow the slow change in V_g , which is swept from accumulation to inversion. In the case of present defects at the interface, additionally to the depletion layer charge, the occupancy of the defect states has to be changed with changing voltage, which leads to a stretch-out along the V_g axis. Therefore, any ϕ_s from a calculated theoretical $C_{HF}(\phi_s)$ curve corresponds to V_g at $C_{HF,experimental}(V_g) = C_{HF,theoretical}(\phi)$. Thus the correlation ϕ_s - V_g is calculated from the comparison between the measured and the theoretical high-frequency C - V curves, as shown in figure 3.10.

The theoretical high-frequency capacitance is calculated based on the one-dimensional

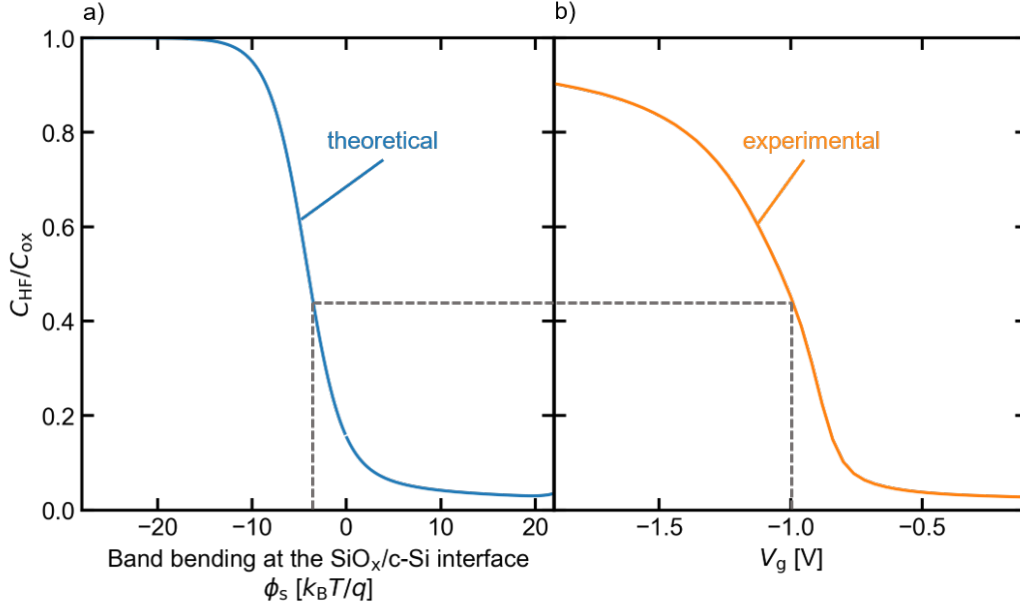


Figure 3.10: (a) Theoretical high-frequency capacitance as a function of the band bending at the $\text{SiO}_x/\text{c-Si}$ interface ϕ_s and (b) experimental high-frequency capacitance as a function of the applied Voltage V_g .

Poisson equation (for p -type c-Si):

$$\frac{\phi(x)^2}{dx^2} = -\frac{\rho(x)}{\epsilon_0 \epsilon_{Si}} \quad (3.32)$$

$$= -\frac{q}{\epsilon_0 \epsilon_{Si}} (p(x) - N_A - n(x) + n_{i,\text{eff}}^2/N_A) \quad (3.33)$$

$$= -\frac{q}{\epsilon_0 \epsilon_{Si}} \left[N_A \left(\exp\left(-\frac{q\phi}{k_B T}\right) - 1 \right) - \frac{n_{i,\text{eff}}^2}{N_A} \left(\exp\left(\frac{q\phi}{k_B T}\right) - 1 \right) \right] \quad (3.34)$$

The first integration of equation 3.32 gives the electric field F_s at the surface:

$$F_s = -\left. \frac{d\phi}{dx} \right|_{x=0} \quad (3.35)$$

$$= \sqrt{\frac{2k_B T N_A}{\epsilon_0 \epsilon_{Si}} \left[\left(\exp\left(-\frac{q\phi_s}{k_B T}\right) + \frac{q\phi_s}{k_B T} - 1 \right) - \frac{n_{i,\text{eff}}^2}{N_A^2} \left(\exp\left(\frac{q\phi_s}{k_B T}\right) - \frac{q\phi_s}{k_B T} - 1 \right) \right]} \quad (3.36)$$

Applying Gauss' theorem yields the following expression for the total charge density

in the semiconductor:

$$Q_s = -\epsilon_0\epsilon_{\text{Si}}F_s(\phi_s), \quad (3.37)$$

which results in the following equation for the high-frequency capacitance

$$C_s = -\frac{dQ_s}{d\phi_s} = -\epsilon_0\epsilon_{\text{Si}}\frac{d}{d\phi_s}\left.\frac{d\phi}{dx}\right|_{x=0} \quad (3.38)$$

$$= 2\epsilon_0\epsilon_{\text{Si}}\sqrt{\frac{q^2N_A}{k_B T}}\left[1 - \exp\left(\frac{q\phi_s}{k_B T}\right) + \frac{n_{i,\text{eff}}^2}{N_A^2}\left(\left[\exp\left(\frac{q\phi_s}{k_B T}\right) - 1\right]\frac{\Delta}{\Delta + 1}\right)\right]F_s^{-1} \quad (3.39)$$

$$\text{with } \Delta \approx \frac{F_s(\phi_s)}{\exp\left(\frac{q\phi_s}{k_B T}\right) - 1}\left[\int_0^{\phi_s} d\phi \frac{\exp\left(\frac{q\phi}{k_B T}\right) - \exp\left(\frac{-q\phi}{k_B T}\right) - 2\phi}{F_s^3(\phi)} - 1\right], \quad (3.40)$$

which is calculated for the known doping concentration N_A and oxide thickness d_{ox} .

3.8 MarcoPOLO model

Due to high leakage currents, the C - V method described above 3.7 cannot be applied to samples with thin and, therefore, leaky oxide, as in typical POLO junctions. Therefore, for these junctions, the MarcoPOLO model by Folchert et al. [73] is used to determine an upper estimate for the density of defect states $D_{\text{it,max}}$ from injection-dependent lifetime measurements. The MarcoPOLO model is a semi-analytic model that self-consistently solves the Poisson equation in the poly-Si/SiO_x/c-Si structure to determine the surface band-bending. In this model, the D_{it} at the SiO_x/c-Si interface is treated as a recombination zone, which may also contain a charge that affects the band bending, as known from the detailed metal-insulator-semiconductor modeling [132]. This defect density D_{it} , doping density $N_{\text{dop,poly}}$ in the poly-Si layer, maximum doping concentration $N_{\text{dop,c-Si}}$ in c-Si (example in Figure 5.6) and oxide thickness d_{ox} are used to consistently characterize the surface recombination and tunneling currents of electron- and hole-collecting poly-Si/SiO_x/c-Si junctions [73], [133].

The recombination parameter J_{0s} at the maximum of the diffusion profile is calculated using the defect density D_{it} at the SiO_x/c-Si interface and the maximum dopant concentration $N_{\text{dop,c-Si}}$. In addition to this surface recombination, expressed

by J_{0s} , Auger recombination occurs within the diffused region. The sum of the two recombination paths is calculated using the software EDNA2 [134]. Therefore, the calculated surface recombination parameter J_{0s} from the MarcoPOLO model and the doping concentration determined from measured ECV profiles are used to calculate the Auger recombination.

For this D_{it} calculation, the following assumptions are made:

- the defect density is the only interface charge of the junction
- recombination at sites where the oxide is locally broken up (pinholes) [66], [135] is negligible
- recombination via point defects in the diffusion profiles is negligible.

Under these assumptions, the only remaining recombination pathway is via defect states at the SiO/c-Si interface, making the resulting $D_{it,max}$ values mark the upper limit for the actual defect density. A detailed explanation and derivation can be found in Ref.[136].

3.9 Free energy loss analysis

For the simulation of the POLO²-IBC and POLO-IBC cells and, in particular, for the breakdown of its loss channels via a free energy loss analysis (FELA) [137], the simulation softwares Quokka2 [138], [139] and Quokka3 [140] are used. These numerically solve the 1D/2D/3D charge carrier transport in a quasi-neutral silicon device. Therefore the conductive boundaries model [141] accounts for the diffusion of surface dopants. Near-surface regions are, thus, not modeled in detail but as a conductive boundary via their sheet resistance and recombination current density. Employing the conductive boundary model allows simulations on short timescales with easily measurable cell parameters.

The implemented FELA quantifies the losses due to free energy dissipation in each loss channel when the cell is operated at the maximum power point. Therefore, the electrical power is considered a rate of free enthalpy \dot{F} since it is free of entropy. The rate of free enthalpy \dot{F} is given by the terminal charge current J_Q times the terminal voltage U . To analyze the local free energy in different parts of the cell, the

3 Characterization and simulation methods

local charge current densities and the local voltages, e.g., the local quasi-Fermi level splitting, must be considered. The output parameters of the unit cell simulation performed by the Quokka software are local currents, conductivities, and Fermi levels. These parameters allow the determination of the rate of loss of free energy density \dot{f} in the different parts of the cell due to the recombination and transport of holes and electrons at the surfaces and in the base. This allows a comparison of the recombination and transport losses in the same power density units mW/cm^2 and thus identifies the main loss channels of the cell.

4 IBC solar cells with POLO junctions for both polarities

This chapter describes the fabrication and investigates loss mechanisms of IBC solar cells with POLO junctions for both contact polarities, called POLO²-IBC solar cell, first presented in reference [83], which have been further optimized [85], [142], reaching a record efficiency of 26.1% [25]. These losses include degradation occurring during cell manufacturing and electrical losses due to the base doping and perimeter losses. Moreover, the recombination behavior within the lateral $p^+(i)n^+$ junction, created by a nominal intrinsic poly-Si (i poly-Si) region placed between the n^+ poly-Si and p^+ poly-Si fingers on the rear of the cell, is analyzed in depth.

This chapter is based on the peer-reviewed journal papers „26.1 %-efficient POLO-IBC cells: Quantification of electrical and optical loss mechanisms“, by C. Hollemann, F. Haase, S. Schäfer, J. Krügener, R. Brendel, and R. Peibst published in Progress in Photovoltaics: Research and Applications in 2019 [143] and „Separating the two polarities of the POLO contacts of an 26.1 %-efficient IBC solar cell“, by C. Hollemann, F. Haase, M. Rienäcker, V. Barnscheidt, J. Krügener, N. Folchert, R. Brendel, S. Richter, S. Großer, E. Sauter, J. Hübner, M. Oestreich, and R. Peibst published in Scientific Reports in 2020 [144].

Section 4.2 is based on the peer-reviewed paper [143]. Felix Haase and Robby Peibst developed and optimized the cell process, which was continued to be enhance under the participation of the author of this thesis. The author of this work performed the cell monitoring via ILM measurements, its analysis, and the cell simulations.

Section 4.3 is based on the peer-reviewed paper [144]. The author of this work performed the PCD measurements and S_{eff} calculation. Nils Folchert simulated the

band structure of the (*i*)POLO junctions. Manuel Stratmann did the selective etching of the poly-Si, and he and Bettina Wolpensinger took the SEM images. Robby Peibst did the calculations using the Fischer model. The ToF-SIMS measurements were performed by Susanne Richter working in the team of Stefan Großer „c-Si-Defect diagnostics“ at Fraunhofer Center for Silicon Photovoltaics. The author did the analysis of these results and calculated the diffusion coefficients. Annika Raugewitz did the ECV measurements. Felix Haase did the cell simulation. The J - V measurements on $p^+(i)n^+$ test structures were done by Verena Barnscheidt and analyzed by her and the author of this work. The author determined the implied efficiencies of cells with varying (*i*) poly-Si region width. The time-resolved PL measurements were done by Eduard Sauter and Jens Hübner from the group „Spin and charge carrier dynamics of complex semiconductor nanostructures“ of Michael Oestreich at the Institute for Solid-State Physics at Leibniz University Hannover. The author of this thesis interpreted the results regarding the impact on the working principle of the IBC cell with (*i*) poly-Si regions separating the n^+ and p^+ poly-Si fingers.

4.1 Cell structure and processing

In this section, the fabrication process of 20 mm × 20 mm POLO²-IBC cells is described. Figure 4.1(a) shows the structure of these POLO²-IBC solar cells with an (*i*) poly-Si region between the p^+ poly-Si and n^+ poly-Si fingers on the rear side of the cell. In addition, the processing of test structures with $p^+(i)n^+$ POLO junctions of different (*i*) poly-Si region widths is described, which are used for the electrical characterization of the $p^+(i)n^+$ junctions.

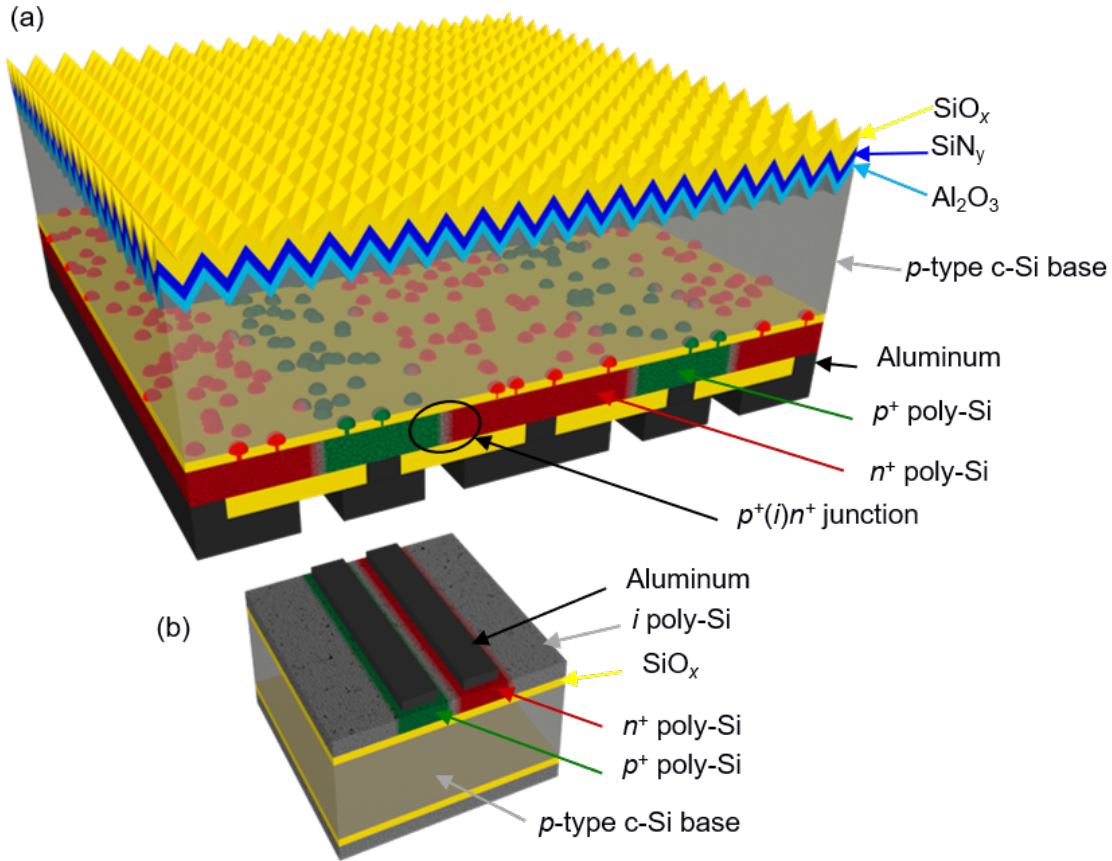


Figure 4.1: (a) Schematic illustration of an POLO²-IBC solar cell with n^+ poly-Si and p^+ poly-Si contact fingers separated by a nominal intrinsic poly-Si region. (b) Sketch of a $p^+(i)n^+$ test structure. This figure is reprinted from Figure 1 in Ref. [144].

4.1.1 Solar cells

The cell process flow, shown in Figure 4.2, is performed and compared on three wafer types in this work. These are p -type Float Zone (FZ) wafers with a resistivity of $1.3 \Omega \text{ cm}$ or $80 \Omega \text{ cm}$ and n -type Czochralski (Cz) wafers with a resistivity of $2 \Omega \text{ cm}$. The p -type wafers have a thickness of $300 \mu\text{m}$, and the n -type wafers have a thickness of $250 \mu\text{m}$.

All samples undergo a saw damage etch and a Radio Corporation of America (RCA) cleaning sequence. Then the process starts with the growth of a wet thermal oxide which is used as an etching barrier for the adjustment marks that are subsequently defined by photolithography and etched in KOH. After the oxide is removed in 40%

HF and the samples are cleaned again by the RCA cleaning sequence, a thermal interfacial oxide layer of 2.2 nm-thickness is grown onto the wafer (Figure 4.2(b)). The oxide is then covered with a 225 nm-thick LPCVD intrinsic a-Si layer (c) grown at 550 °C. Local doping is achieved by masked ion implantation of boron and phosphorous into the a-Si layer on the rear side. Therefore photolithography is used to generate photoresist implant barriers that guarantee high accuracy and are designed to leave an intrinsic poly-Si gap between the n^+ poly-Si and p^+ poly-Si fingers (d). The finger pitches are 300 μm or 450 μm , while the (i) poly-Si gaps have a width of 20 μm or 30 μm , unless otherwise stated. Seven 4 cm² cells are processed on each wafer.

In a tube furnace, the a-Si is crystallized and its surface oxidized during a high-temperature wet oxidation step at 900 °C for 30 min. During the oxidation, the thickness of the n^+ poly-Si layers decreases to (115 \pm 10) nm while the p^+ poly-Si thickness decreases to (150 \pm 10) nm. A subsequent tube furnace process at 1035 °C for 1 h under N₂ atmosphere breaks up the interfacial oxide layer forming the POLO contacts followed by an impurity gettering step at 550 °C for 1 h, also in N₂ atmosphere [145], [146] (e).

Hydrogen is introduced to the poly-Si/SiO_x/c-Si interface on the rear side via an 80 nm thick a-Si:H rich SiN_y layer with a refractive index of 2.8 that is deposited on the rear on top of the oxide and a subsequent annealing step in N₂ atmosphere at 425 °C for 30 min (f). Afterward, we remove the SiO_x on the front side via a one-side HF process, the poly-Si layer via a KOH etch and texturize the front side using a KOH-based solution (g). The SiN_y layer on the rear is selectively removed in phosphoric acid (h). We define the contact areas by laser contact openings (LCO) [25] on the rear side, introduced by a layer-selective laser ablation process [147] with a wavelength of $\lambda = 355$ nm and a pulse length of 9 ps that does not compromise the POLO junction's passivation quality underneath (i). This laser ablation is followed by an RCA cleaning sequence.

A 20 nm thick atomically deposited (ALD) Al₂O₃ layer is deposited to passivate the front surface, followed by a forming gas annealing step at 425 °C for 30 minutes. The Al₂O₃ then capped by a plasma-enhanced chemical vapor deposited (PECVD) 54 nm thick SiN_y layer with $n = 1.9$ and an 72 nm SiO_x layer again followed by an annealing step at 425 °C for 30 min in N₂ atmosphere (j). Finally, the rear side of the cell is metalized by an evaporated aluminum layer covered with a sputtered

80 nm SiO_x layer (k). Again, we use a laser to pattern the SiO_x (l), which serves as an etching mask to separate the metal fingers by a 10 s wet-chemical etching step using a solution of phosphoric, nitric and acetic acid at 70°C [25] (m).

Moreover, we process some $\text{POLO}^2\text{-IBC}$ cells on $160\ \mu\text{m}$ thick $1.5\ \Omega\text{cm}$ boron doped p -type Cz material using a wet-chemical interfacial oxide grown in an ozone-based solution. This POLO junction with a thinner and less stable oxide requires a lower annealing and break-up temperature of 860°C . Apart from the oxidation and the annealing step, those cells see the same process flow described above. In addition, we fabricate reference wafers with full-area n -type doped, p -type doped, and intrinsic POLO contacts using the same front-end process. For further information about the cell geometry, please refer to Table 4.1.

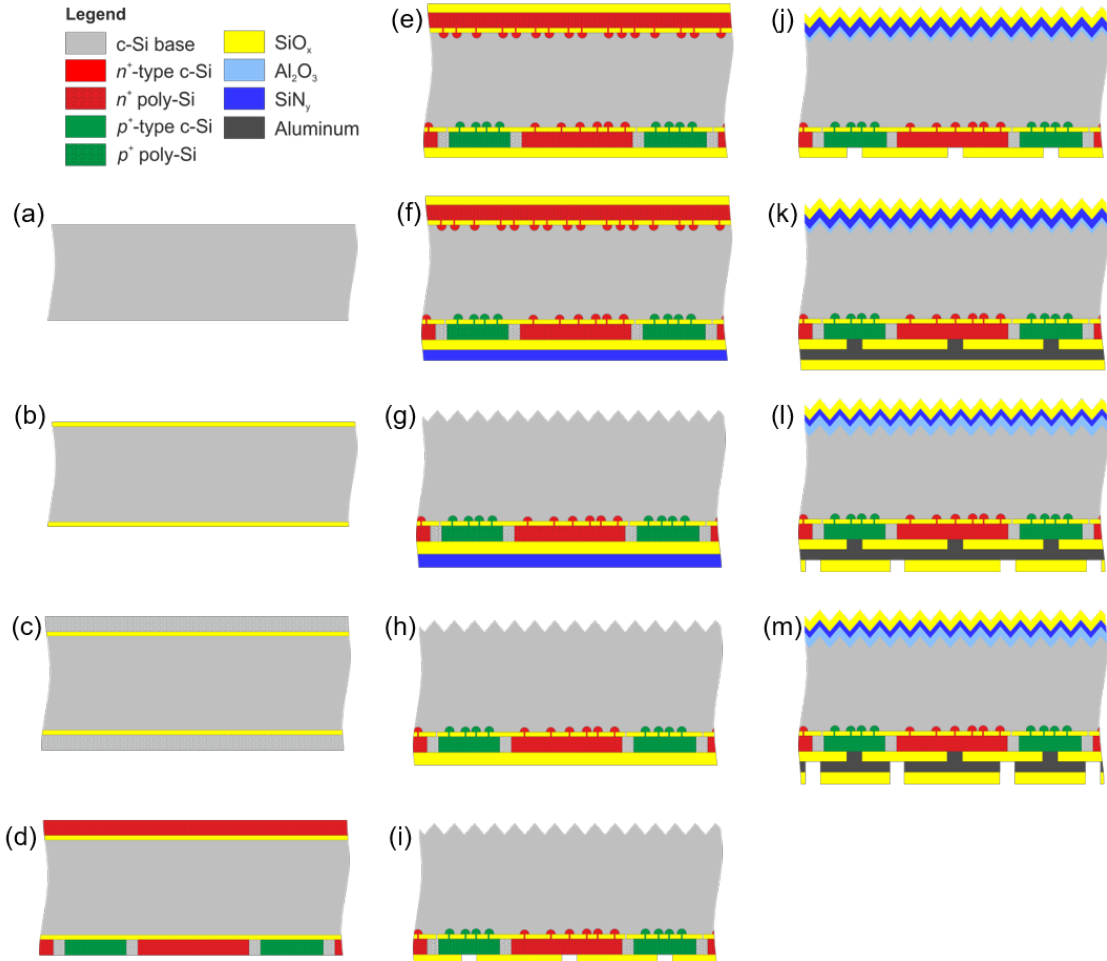


Figure 4.2: Schematic cross-sections of the $\text{POLO}^2\text{-IBC}$ solar cell at different steps during the process sequence.

Table 4.1: Input parameters for the solar cell simulations. This table is reprinted from Table 1 in [143].

Cell name	p-1.3	p-80	n-2
Bulk doping type	<i>p</i> -type		<i>n</i> -type
Bulk ρ_{bulk} [$\Omega \text{ cm}$]	1.3	80	2
Bulk N_{dop} , [cm^{-3}]	1.1×10^{16}	1.7×10^{14}	2.4×10^{15}
Cell thickness [μm]	290		240
Photogeneration [mA/cm^2]	43.29		43.13
Bulk $\tau_{\text{SRH,bulk}}$ [ms]	100[145]		
Front surface S_{front} [cm s^{-1}]	0.1 to 100		
Rear gap $S_{i\text{-region}}$ [cm s^{-1}]	0.1 to 100		
<i>n</i> ⁺ POLO junction $J_{0,n^+\text{POLO}}$ [fA/cm^2]	4		
<i>p</i> ⁺ POLO junction $J_{0,p^+\text{POLO}}$ [fA/cm^2]	10		
<i>n</i> ⁺ POLO junction $\rho_{c,n^+\text{POLO}}$ [$\text{m}\Omega \text{ cm}^2$]	0.6		
<i>p</i> ⁺ POLO junction $\rho_{c,p^+\text{POLO}}$ [$\text{m}\Omega \text{ cm}^2$]	0.2		
<i>n</i> ⁺ POLO junction width [μm]	270		
<i>p</i> ⁺ POLO junction width [μm]	120		
Nominal (<i>i</i>)POLO junction width d_{gap} [μm]	30		
Finger pitch [μm]	450		
Contact line width [μm]	7		
Mobility model	Klassen[114]		

4.1.2 Test structures

Figure 4.1(b) shows the test samples' structures prepared for the poly-Si $p^+(i)n^+$ diode investigation. The preparation starts with a 180 μm -thick n -type Cz Si wafer, onto which we thermally grow a 100 nm thick oxide to avoid any carrier transport through the wafer. This is followed by an LPCVD-deposited intrinsic a-Si layer. We locally implant phosphorous and boron, patterned in two steps by a masking layer of SiO_x patterned by inkjet printed hot melt wax. Since this method leads to wavy edges, variations of up to 10 μm per edge occur. The resulting structures yield 6 mm long $p^+(i)n^+$ diodes with 1 mm wide p^+ poly-Si and n^+ poly-Si regions. The width of the intrinsic region between p^+ poly-Si and n^+ poly-Si areas is nominally varied between $d_{\text{gap}} = 0 \mu\text{m}$ and 380 μm . Upon ion implantation, the samples are annealed under oxidizing atmosphere for 30 min (900 $^\circ\text{C}$ plateau), which is followed by 1 h inert annealing at 1050 $^\circ\text{C}$. One-half of the wafers, like the cells, are hydrogenated by an a-Si:H-rich SiN_y layer followed by a 30 min annealing step at 425 $^\circ\text{C}$. Finally, aluminum is deposited on the samples, and the contacts are separated in a wet-chemical etch bath with a patterned SiO_x layer as an etching barrier.

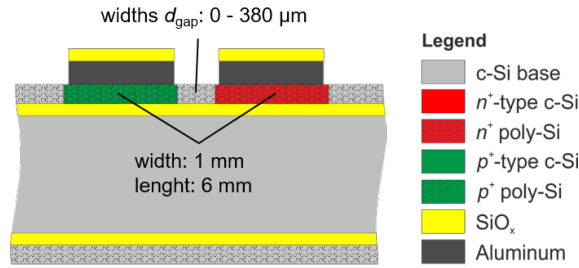


Figure 4.3: Schematic cross-sections of the $p^+(i)n^+$ test structures.

4.2 Analysis of loss mechanisms

To improve solar cell efficiencies, it is essential to monitor the manufacturing process. The data obtained from this monitoring helps to identify processes and loss mechanisms that cause substantial degradation. This section's main objective is to investigate degradation during processing in the optimized process flow, which enabled a record cell with an efficiency of 26.1%, and the influence of the base material. Furthermore, edge losses and series resistances are quantified, and a Free

Energy Loss Analysis (FELA) is carried out. This section is based on the peer-reviewed paper [143].

4.2.1 Monitoring of cell parameters during processing

Figure 4.5 shows implied and measured J - V parameters after various process steps for cells processed on three differently doped base materials. To obtain the implied pseudo- J - V parameters from lifetime measurement results that allow a comparison of ILM and J - V measurements, we need to estimate a value for J_{sc} . We must assume that J_{sc} decreases during the process, but the extent is, however, difficult to determine. Therefore, we set the J_{sc} to the value we measure with the masked J - V measurement on the finalized cell, which provides a lower bound on the actual J_{sc} values during the process. Table 4.2 gives an overview of the characterization methods and the included losses for the various process steps. The first three data points on the x-axis show the implied pseudo-efficiency after different process steps until the completion of the cell, which are determined from ILM measurements. The first data point presents the state after junction formation and hydrogenation (step f in Figure 4.2). This state is also where the recombination current densities of the n^+ POLO and p^+ POLO junction are determined on reference wafers for the simulations shown in section 4.2.3. The second data point shows the state after contact opening (step j), and the third state is measured after the finalization of the cell. Those three values are measured while illuminating the entire cell wafer containing seven 4 cm^2 cells, i.e., in an unmasked state.

Due to the relatively small active cell area, losses from recombination in the perimeter region significantly harm these cells. The perimeter region is illuminated during measurements without a mask, and charge carriers are also generated outside the active cell area. When a mask is used to ensure that only the cell area is illuminated, no charge carriers are generated outside the cell area, and a large gradient of charge carrier density arises. This gradient induces a carrier flow from the cell area into the perimeter region. Thus, the charge carrier density inside the cell is reduced, leading to reduced implied V_{oc} and J values. This effect is described in more detail in Haase et al. [85]. However, it should be noted here that the cells examined in that paper were still affected by poorer passivation in the rear perimeter region, in contrast to the cells in this work, which are passivated by p^+ poly-Si in the perime-

ter region. To estimate the perimeter losses and isolate them from the loss due to series resistance implied in the J - V measurements, we perform an unmasked and masked ILM measurement of the finalized cells and compare them to the masked J_{sc} - V_{oc} and J - V values. Here, the masked ILM and J_{sc} - V_{oc} measurements should ideally match exactly according to theory. As seen in Figure 4.4, the two curves for the cell on p -type $1.3 \Omega \text{ cm}$ materials indeed match quite well. In particular, the V_{oc} matches precisely. For the other two materials, a slight overestimation of V_{oc} by the data from ILM can be seen. The possible reasons for that will be discussed in the following discussion of Figure 4.5. Overall, however, the comparison shows that the implied pseudo J - V data from ILM measurements allow a reasonable evaluation of process-induced degradation.

Table 4.2: Overview of the applied measurement methods in the different monitoring steps.

Process state	Characterization method	Perimeter region	Excluded losses
after hydrogenation (f)	ILM	unmasked	perimeter loss, R_s
after contact opening (j)	ILM	unmasked	perimeter loss, R_s
finalized cell (m)	ILM	unmasked	perimeter loss, R_s
finalized cell (m)	ILM	masked	R_s
finalized cell (m)	J_{sc} - V_{oc}	masked	R_s
finalized cell (m)	J - V	masked	-

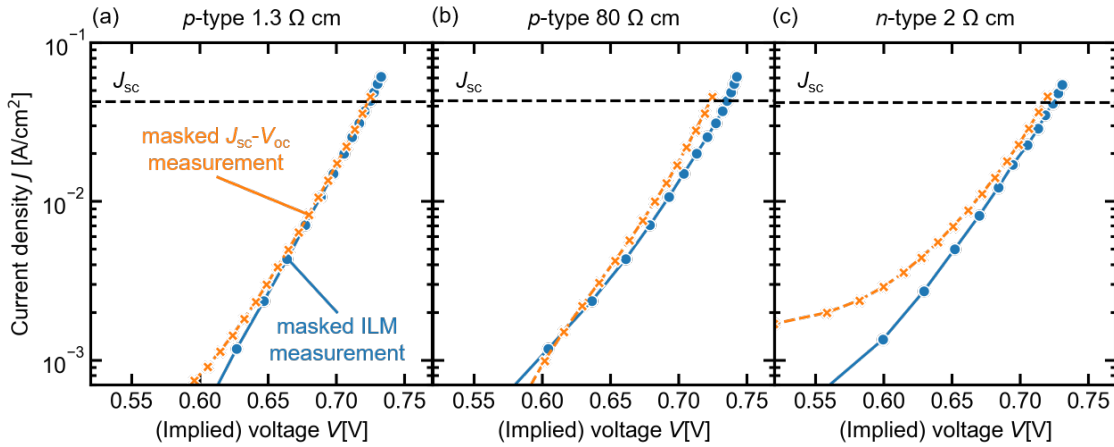


Figure 4.4: Implied (pseudo-) and measured J_{sc} - V_{oc} curves of finalized cells on (a) $1.3 \Omega \text{ cm}$ p -type (b) $80 \Omega \text{ cm}$ p -type and (c) $2 \Omega \text{ cm}$ n -type material. The cells are measured in the ILM setup and in the J - V setup as J_{sc} - V_{oc} curves both with a mask.

4 IBC solar cells with POLO junctions for both polarities

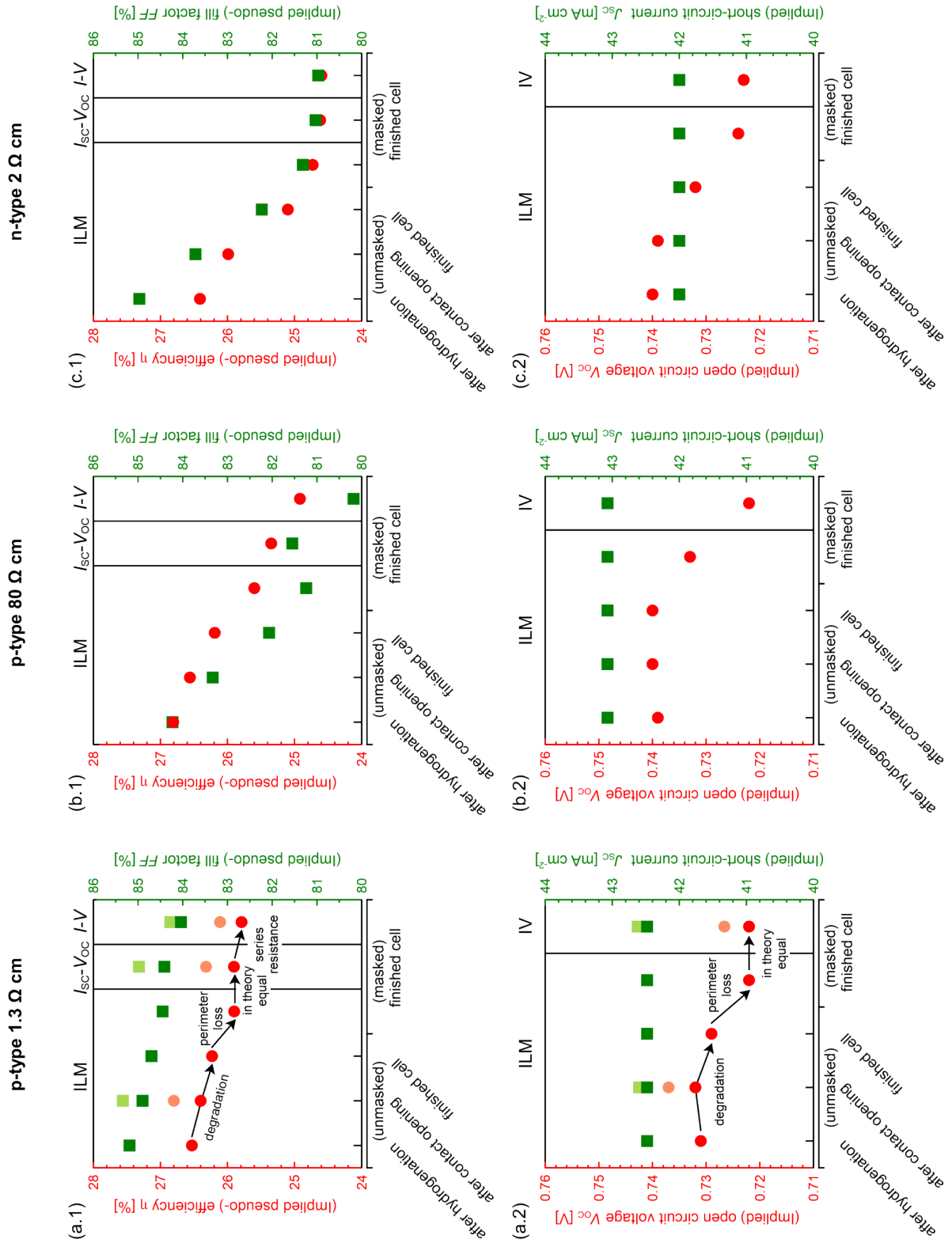


Figure 4.5: (Next Page.)

Figure 4.5: (Previous page.) Implied and measured J - V parameters of the three cells at different stages during the cell process. The ILM measurements are partly carried out with and without a mask, whereas the J_{sc} - V_{oc} and J - V measurements are only carried out with a masked perimeter region. The bright symbols in (a.1) and (a.2) originate from the record cell, which was not measured in every state for preserving reasons. This figure is reprinted from Figure 2 in [143].

Table 4.3: J - V parameters of the best cells. This table is reprinted from Table 2 in [143].

Cell name	p-1.3	p-80	n-2
η [%]	26.1	24.9	24.6
V_{oc} [mV]	727	722	723
J_{sc} [cm^2]	42.6	43.1	42.0
FF [%]	84.3	80.2	81.0
R_s [$\Omega \text{ cm}^2$]	0.16	0.28	0.01
R_{sh} [$\text{M}\Omega \text{ cm}^2$]	10.0	4.8	0.002

The J - V parameters of the best-finalized cell of each group are shown in Table 4.3. Figure 4.5(a.1) shows the (implied pseudo-) efficiency and the (implied pseudo-) fill factor of the $1.3 \Omega \text{ cm}$ p -type (p-1.3) cell. For conservation reasons, the best solar cell, later measured to have a record efficiency of 26.1 %, is not measured in each state (bright symbols). Therefore, we also show a nominal identical cell (dark symbols) with slightly lower J - V parameters to observe the degradation curve and the perimeter loss. The implied pseudo efficiency of this cell after hydrogenation is measured to be 26.5 %. It decreases slightly after front side processing, contact opening and separation and is 26.3 % for the finalized cell in the unmasked and 26.0 % in the masked configuration. Thus, the efficiency loss due to perimeter recombination amounts to 0.3 %_{abs}.

The entire processing of the front side of the cell takes place between the first ILM measurement „after hydrogenation“ and the second measurement „after contact opening“. First, the front side is textured, then contact opening takes place, and the front side is provided with a double anti-reflection coating. Afterward, the LCOs are shot into the oxide on the rear side. In [25], a detailed study of different wavelengths, laser powers, and poly-Si thicknesses was performed for both n - and p^+ POLO junctions. Thus a damage-free LCO process was identified on symmetric

test structures with POLO junctions on both sides. On the cell wafers, the front side is, however, textured and passivated with an $\text{Al}_2\text{O}_3/\text{SiN}_y/\text{SiO}_x$ stack. Therefore, it is reasonable to assume that the reason for losses occurring is more likely to be on the front side of the cell. However, no losses are observed in V_{oc} for this step while the FF is affected. The subsequent metallization process and primarily the contact separation, which consists of a laser process and a subsequent wet-chemical etching step, lead to a degradation in FF and V_{oc} . Here the wet-chemical Al etching step might have damaged the front side passivation.

The J_{sc} - V_{oc} measurement, which also provides the pseudo-efficiency in the masked state and is performed to verify the method, gives a pseudo efficiency of 25.9 %, which agrees well with the ILM measurement of 26.0 %. The final J - V measurement gives an efficiency of 25.8 % resulting in a loss of 0.1 %_{abs} induced by a series resistance of $0.07 \Omega \text{ cm}^2$. After contact opening, the record cell shows an implied pseudo efficiency of 26.8 %. The completed cell shows a pseudo efficiency of 26.3 % and an efficiency of 26.1 % resulting from a slightly higher efficiency loss of 0.2 %_{abs} due to a series resistance of $0.16 \Omega \text{ cm}^2$. The J - V curve of this cell, measured at ISFH CalTeC, is shown in Figure 4.6.

Figure 4.5(b) shows the J - V parameters of the cell on p -type, $80 \Omega \text{ cm}$ material (p-80). The implied pseudo efficiency after hydrogenation starts at a higher value of 26.8 %, identical to that of the record cell on $1.3 \Omega \text{ cm}$ material after contact opening. The observed degradation for the p-80 cell of 0.6 %_{abs} in efficiency is larger than the corresponding degradation of the p-1.3 cell (0.2 %_{abs}).

The implied pseudo efficiency drops to a value of 26.2 % after completed processing, measured in an unmasked state and 25.6 % in a masked state. This decrease in implied pseudo-efficiency is mainly due to a loss in the implied pseudo-fill factor, while the implied open-circuit voltage is less affected. Crosschecking with the J_{sc} - V_{oc} measurement shows differences in the pseudo-efficiencies, the pseudo-fill factors, and especially in the open-circuit voltages. The pseudo efficiency of 25.3 % determined with the masked J_{sc} - V_{oc} measurement is 0.3 %_{abs} lower than the value from the masked ILM measurement. The largest difference occurs with V_{oc} . Here, the ILM measurement overestimates V_{oc} by 0.011 V. Overestimation of τ_{eff} by the dynamic ILM method is a known artifact due to injection-dependent lifetimes [121], [124]. The injection level, at which V_{oc} is determined, is $>1 \times 10^{15} \text{ cm}^{-3}$ for the weakly doped p-80 material in contrast to the other two materials, which are already in high

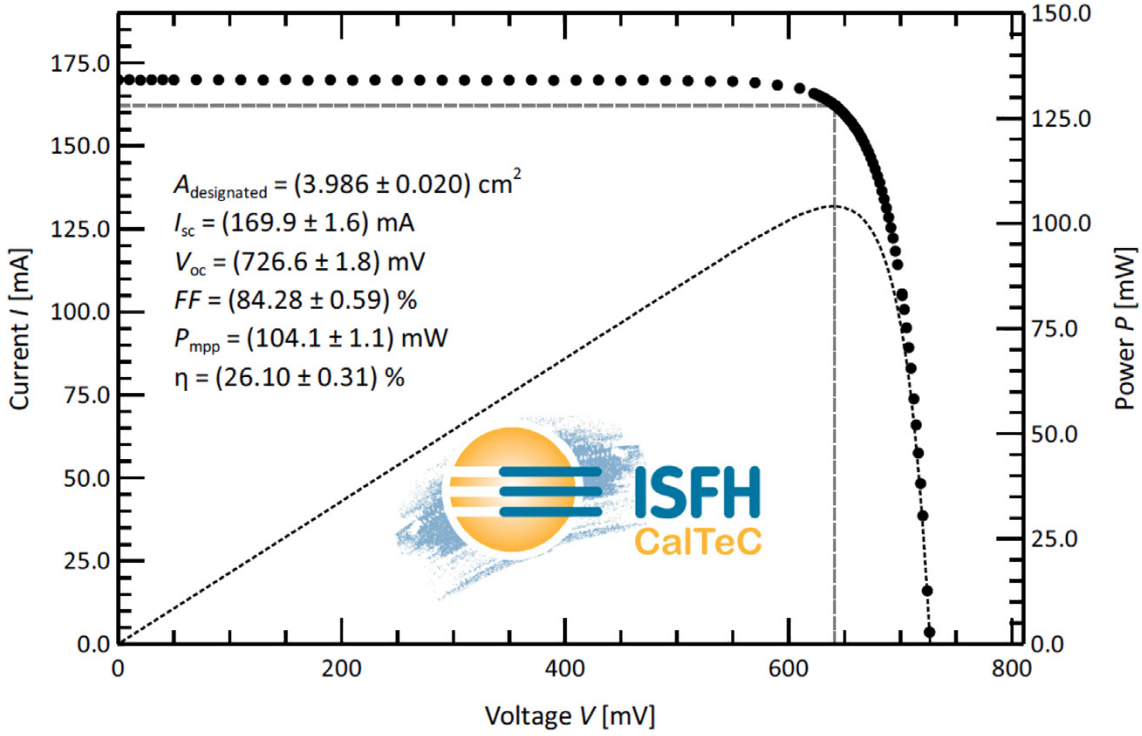


Figure 4.6: Light J - V curve and power in dependence of the voltage of the POLO²-IBC cell measured at the ISO 17025-accredited Calibration and Test Center, ISFH CalTeC. The power conversion efficiency of the POLO²-IBC-IBC cell is $(26.10 \pm 0.31) \%$. This figure is reprinted from [25].

injection, where the Auger recombination leads to a steep gradient in the lifetime. Herlufsen [124, p. 84 - 87] has shown that this can lead to a significant overestimation of the lifetime by the dynamic ILM method. However, this effect was simulated only for material with $N_{\text{dop}} = 1 \times 10^{16} \text{ cm}^{-3}$ where a significant error occurs only for $\Delta n > 1 \times 10^{17} \text{ cm}^{-3}$. It is, however, possible that this effect affects the p-80 material already for $\Delta n > 1 \times 10^{15} \text{ cm}^{-3}$ and can thus explain the overestimation of the iV_{oc} values. This overestimation of V_{oc} also leads to slightly underestimating the implied pseudo-fill factor by the ILM method. However, the lifetime and hence the implied recombination current is not affected at MPP. Compared to the p-1.3 cells, the p-80 cell exhibits a larger efficiency loss of $0.4\%_{\text{abs}}$ due to series resistance, which is $0.27 \Omega \text{ cm}^2$. Process-induced degradation is also observed for this cell type, especially in the FF . As mentioned above, however, the low doping of the base probably leads to a significant overestimation in V_{oc} , so a possible degradation might be superimposed here.

Figure 4.5(c) shows the J - V parameters of the cell on n -type, $2 \Omega \text{ cm}$ material (n-2).

Again process-induced degradation leads to a decrease of the implied pseudo efficiency from 26.4% after hydrogenation to 26.0% after the contact opening. The decrease of implied pseudo-efficiency during the final process step to 25.1% is particularly strong. The two (implied) pseudo-efficiencies measured on the finalized cell in the masked state by ILM and J_{sc} - V_{oc} differ by only about 0.1%_{abs}. The series resistance of $0.01 \Omega \text{ cm}^2$ causes an efficiency loss that is smaller than 0.1%_{abs}. The overall poorer performance of these cells can be attributed to several reasons. Firstly, the material with 240 μm is thinner than the wafers of the p -type cells with 290 μm . Secondly, the structure of the p^+ and n^+ POLO on the backside was not adapted for these cells. Thus, the emitter area fraction is only 27% instead of 60%. Furthermore, last but not least, the metal contacts are separated between the n^+ and (i) poly-Si regions independent of the base doping. Therefore, in the case of the n -type base, the emitter metallization overlaps with the (i) poly-Si region. In the case of the n -type base, this leads to shunt currents through the leaky SiO_x on the rear side ($R_{sh} = 1800 \Omega \text{ cm}^2$). Thus, separating the n^+ poly-Si and the intrinsic poly-Si region would have been advantageous for the n-2 cell to minimize shunting.

4.2.2 Free Energy Loss Analysis

A Free Energy Loss Analysis [137] is carried out to compare the loss mechanisms found in the previous subsection with recombination and transport loss contributions to the total energy losses of the cell. Therefore a front surface recombination velocity S_{front} and a recombination velocity at the interface between the c -Si and the nominal (i) poly-Si region $S_{i\text{-region}}$ need to be estimated. On symmetrical precursors with symmetrical front side passivation (textured and passivated with Al_2O_3 and SiN_y), S_{front} values between 0.3 and 2 cm/s are measured. On precursors with full-area (i)POLO junctions, S values of > 100 cm/s are measured. However, due to the actually achieved high efficiencies, $S_{i\text{-region}}$ must be much smaller in the narrow (i) poly-Si regions of the cell. An exact determination of the passivation quality in the narrow (i) poly-Si areas is difficult and will be considered more closely in the next chapter.

Under the assumption of an excellent passivation S_{front} is set to 0.1 cm/s and $S_{i\text{-region}}$ to 10 cm/s for the FELA shown in Figure 4.7, which gives the different loss channel contribution for the three wafer materials. Since only the unit cell is simulated, edge

losses and possible series resistances due to finger line resistances are not included here.

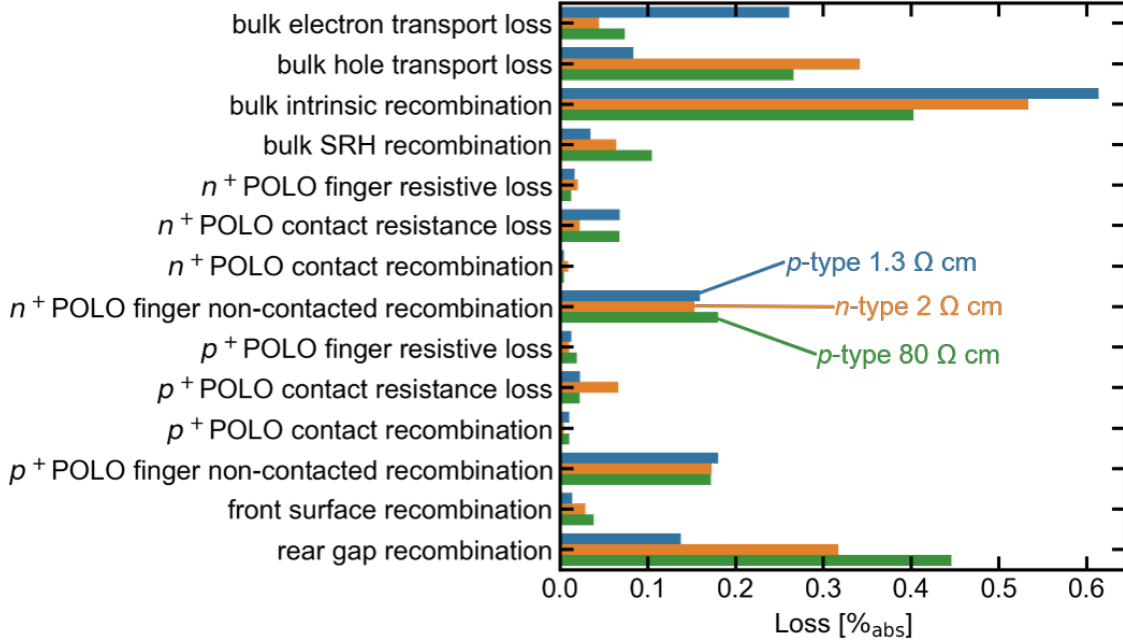


Figure 4.7: FELA analysis of the three cells according to a Quokka simulation assuming $S_{\text{front}} = 0.1 \text{ cm/s}$ and $S_{i\text{-region}} = 10 \text{ cm/s}$. The losses due to recombination and resistance are given in $\%_{\text{abs}}$. This figure is adapted from Figure 3 in [143].

A large part of the loss that limits the cell efficiency is intrinsic bulk recombination or doping-dependent Auger recombination. The cells on p-1.3 material lose about $0.6\%_{\text{abs}}$ efficiency compared to $0.4\%_{\text{abs}}$ on p-80 material. The loss of n -type cells is in between with $0.53\%_{\text{abs}}$. Rear gap recombination behaves inversely to intrinsic bulk recombination concerning base doping. Here, the p-1.3 material performs best with only $0.13\%_{\text{abs}}$ loss, whereas the p-80 material loses $0.38\%_{\text{abs}}$. This severe loss for the lower doped materials matches the observed higher sensitivity to degradation during fabrication. Adding up the rear gap recombination and the intrinsic bulk recombination shows that the p-1.3 has an overall advantage of $0.15\%_{\text{abs}}$ over the other two materials. Since this FELA is based on very low $S_{i\text{-region}}$ values, an even more significant advantage for more highly doped material can be expected for a less than excellent passivation.

Other large losses are hole and electron bulk resistive losses. The two p -type base materials perform very similarly overall. Both losses give a total of $0.34\%_{\text{abs}}$. In the case of the p-1.3 cell, the minority carrier resistivity leads to large losses. In

the p-80 case, the ratio between electron and hole-related resistive losses is reversed, and here the greater losses occur due to majority charge carriers (holes). Thus an optimization might be possible by slightly increasing the base finger area fraction. The n -type cell performs about 0.05 %_{abs} worse than the other two. However, this can be attributed to the adverse ratio of emitter and base areas, as the doping of the fingers is not switched due to the changed base doping. An improvement can thus be expected by swapping the fingers' polarity.

All in all, the p-1.3 cell performs best. The simulated efficiency potential of the p-1.3 cell is highest with 27.01 % followed by the p-80 cell with an efficiency potential of 26.83 %. The n-2 cell has an efficiency potential of only 26.49 % due to a lower J_{sc} value (see Figure 4.8). This can be attributed to the lower cell thickness in addition to the other effects described above.

4.2.3 Quantification of process-induced degradation and (i) poly-Si region passivation quality

Unit cell simulations

In the following, simulations of the POLO²-IBC cells are performed. For all three base materials, we simulate efficiency, fill factor, short circuit current density, and open-circuit voltage of a unit cell as a function of the surface recombination velocity at the front side S_{front} and at the interface between the c-Si bulk and the nominal (i) poly-Si region at the rear $S_{i\text{-region}}$. These unit cell simulations based on the parameters given in Table 4.1 do not account for perimeter recombination as it occurs on the cell level during the masked J - V measurement. Moreover, a possible impact of the line resistance of the Al fingers is not included. To enable a comparison between measurements and simulations, all simulated parameters are corrected by the perimeter loss. In other words, we subtract the respective perimeter recombination losses determined from the difference between the masked and unmasked ILM measurements from the simulated values for each cell separately.

Figure 4.8 shows the resulting J - V parameters as contour plots as a function of the front and (i) poly-Si region SRV, which are varied between 0.1 to 100 cm/s. The three cells show similar performance in the area of S_{front} and $S_{i\text{-region}}$ of 0.1 to

1 cm/s. All four main J - V parameters decrease with increasing surface recombination velocity. However, the decrease is less severe for an increasing $S_{i\text{-region}}$ since the (*i*) poly-Si region covers only 13.3% of the surface compared to the entire front surface. In particular, the J_{sc} is greatly reduced by increased front surface recombination velocity since carriers generated next to the front side recombine there and do not reach the contacts on the rear anymore. J_{sc} of cell n-2 additionally suffers more from electrical shading since it has only 27% instead of 60% of the rear surface covered by an emitter region. With an emitter coverage of 60%, a simulation with $S_{\text{front}} = 1$ cm/s and $S_{i\text{-region}} = 10$ cm/s shows a 0.1 mA cm^{-2} higher short circuit current density. This could be achieved by adjusting the doping pattern, which is the same here as in the p -type cells.

The open-circuit voltage, fill factor, and consequently, the efficiency decreases more sharply with increasing surface recombination velocity for the cells with lower bulk-doping concentration. This is particularly strong for the p-80 cell and a significant result, indicating the higher vulnerability of cells with a low-doped bulk concerning surface passivation degradation.

4 IBC solar cells with POLO junctions for both polarities

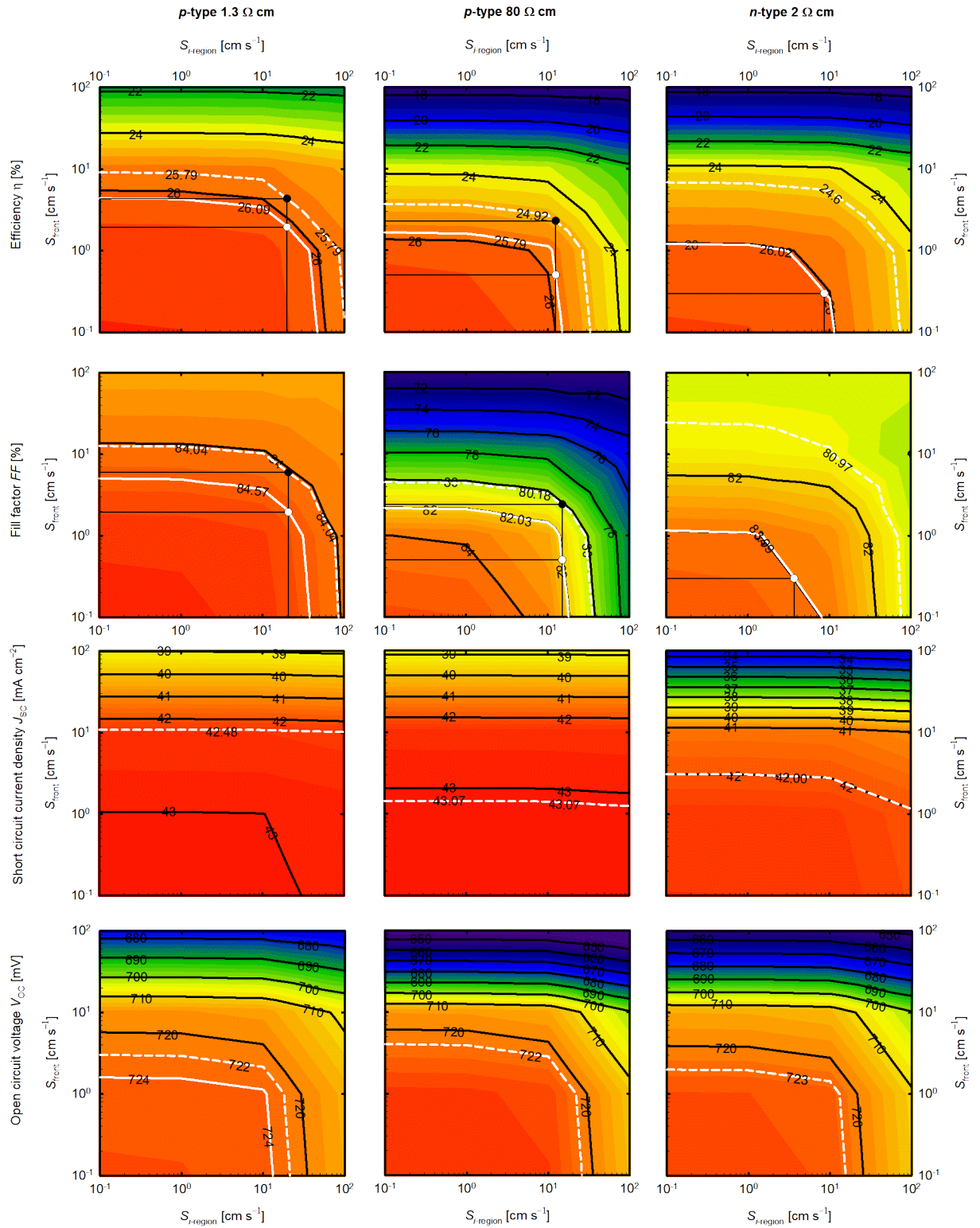


Figure 4.8: (Next page.)

Figure 4.8: (Previous page.) The contour plots show the efficiencies, fill factors, short-circuit currents, and open-circuit voltages of the three cells as a function of S_{front} and $S_{i\text{-region}}$. The experimentally determined loss due to perimeter recombination is subtracted from the unit cell simulation results to enable a comparison to the experimental data. The dashed white contour lines show the measured J - V parameters of the finalized cells (including losses from series resistance, perimeter recombination, and process-induced degradation). The solid white lines show the implied J - V parameters as determined by ILM in the state after hydrogenation of the POLO contacts, reduced by the series resistance loss (difference $J_{\text{sc}}-V_{\text{oc}}/J$ - V) and the perimeter loss (difference masked/unmasked ILM) for each cell. Consequently, the different positions of the solid and dashed white contour lines originate from the process-induced degradation of the surface passivation quality. This figure is reprinted from Figure 4 in Ref. [143].

Comparison to results from process monitoring

In the following, the simulations of the POLO²-IBC cells are compared to the findings obtained through process monitoring. This way, the surface recombination velocity of the nominal (i) poly-Si region and the increase in front surface recombination velocity during the back-end processing, i.e., processing of the front side and rear side metallization, can be quantified.

In addition to the simulation results in Figure 4.8, also measurement results are marked to enable a direct comparison. To quantify the process-induced degradation during back-end processing, we need to compare the J - V parameters measured on finalized, masked cells with the implied pseudo J - V parameters obtained by ILM after the hydrogenation step (see step (f) in Figure 4.2). Since the latter measurements are performed without a mask, they do not include perimeter recombination or series resistance losses. We, hence, subtract the perimeter losses (difference unmasked/masked ILM) and the series resistance losses (difference $J_{\text{sc}}-V_{\text{oc}}$ and J - V) from the implied pseudo J - V parameters measured after hydrogenation. The reduced implied pseudo J - V parameters at this stage – before any process-induced degradation – are illustrated as white solid lines in Figure 4.8. The white dashed lines show the as-measured J - V parameters of the finalized cells. Thus, these two lines differ only in the process-induced degradation of the surface passivation.

Furthermore, we are using these white contour lines to estimate the surface recombination velocity $S_{i\text{-region}}$ in the nominal intrinsic region. This value is difficult to

access by other means due to the width-dependent doping due to interdiffusion and the narrow width of 30 μm of the regions. Since each contour line represents numerous S_{front} and $S_{i\text{-region}}$ value combinations, a reference point for S_{front} is needed to conclude on $S_{i\text{-region}}$. The front surface recombination velocity determined from J_0 values of full-area reference wafers with n^+ POLO junctions as present on the front side before back-end processing gives this reference point (white dots in Figure 4.8).

p-1.3 cells

The p-1.3 cell shows a lower efficiency loss due to process-induced degradation than the other cells. This observation is consistent with the loss analysis, revealing a comparatively lower sensitivity to a decrease in surface recombination velocity S_{front} . This is also true for the fill factor and the open-circuit voltage, which depend less on S_{front} than for the other cell types.

$S_{\text{front}, n\text{POLO}}$ refers to the state (f) in Figure 4.2 before the front site processing and is (1.95 ± 0.65) cm/s determined on the full area n^+ POLO reference wafers (white dots). Combining this reference point with the efficiency contour line of 26.09% gives an estimate of the surface recombination velocity $S_{i\text{-region}}$ in the range of about 20 cm/s in the state before any process-induced degradation (white dot in the upper left graph in Figure 4.8 and Table 4.4).

The J - V parameters after completion of the cell, shown by the white dashed contour line, are all reduced compared to the values in the state after hydrogenation. We attribute this reduction primarily to a deterioration in front surface passivation, as described in 4.2.1. Nevertheless, degradation of the interface passivation of the nominal intrinsic poly-Si region is possible. However, assuming that the back-end processing only affects the front surface passivation, an estimation for the final front surface recombination velocity can be obtained (black point) and yields a value of $S_{\text{front}, \text{finalized}} = 4.4$ cm/s (shown in Table 4.4).

Simulation of the fill factor reveals a similar $S_{i\text{-region}}$ value of 21 cm/s and a surface recombination velocity of the finalized cell of $S_{\text{front}, \text{finalized}} = 5$ to 7 cm/s. Since the J_{sc} of the p-1.3 cell is almost independent of $S_{i\text{-region}}$, the surface recombination velocity of the finalized cell can be approximated to be $S_{\text{front}, \text{finalized}} = 10$ cm/s.

The open-circuit voltage of this cell is so high that it does not meet the measured

values of $S_{\text{front, nPOLO}}$. However, the maximum of $S_{i\text{-region}}$ is 13 cm/s, which is well below the values determined from the other three parameters. Finding the reason for this needs further investigation.

p-80 cells

Although the unit-cell simulation gives the highest efficiency for the p-80 cell, it only has an implied efficiency of 25.79%, starting on a lower level than the p-1.3 cell. This can be attributed to the larger perimeter recombination loss of 0.6%_{abs} and series resistance loss of 0.4%_{abs}. The simulation and the measured data show a strong correlation with the surface recombination velocity and, thus, a distinct loss in the efficiency and the fill factor.

$S_{\text{front, nPOLO}}$ determined on the associated reference wafer is (0.5 ± 0.1) cm/s, and so the simulation of the efficiency gives an estimation for $S_{i\text{-region}}$ of about 13 cm/s. The $S_{\text{front, finalized}}$ of the finalized cell can be estimated to be about 2.3 cm/s using the efficiency simulation. The fill factor gives very similar values of $S_{i\text{-region}} = 15$ cm/s and $S_{\text{front, finalized}} = 2.4$ cm/s for the finalized cell. The front surface recombination velocity of the finalized cell determined from the short circuit current is $S_{\text{front, finalized}} = 1.3$ cm/s, which is slightly lower than the values determined from the simulation. As mentioned above, the open-circuit voltage is also overestimated by the ILM method and is thus out of the simulated range.

Overall, assuming that the degradation during the process only affects the passivation of the front surface, the recombination velocity of the front surface increases from about 0.5 ± 0.1 to an upper estimate of (2.4 ± 0.1) cm/s.

n-2 cells

The n-type cell starts from an equally reduced pseudo efficiency level of 26.04% compared to the p-1.3 cell. Furthermore, the ILM method overestimated the implied open-circuit voltage for this bulk material, and this cell is suffering from a shunting issue that affects the (implied pseudo) fill factor.

The front surface recombination velocity determined on the related reference wafer is (0.3 ± 0.1) cm/s, giving a $S_{i\text{-region}}$ value of 9 cm/s from evaluation of the efficiency

Table 4.4: S_{front} and $S_{i\text{-region}}$ values determined by the comparison of simulation and experiment. This table is reprinted from Table 3 in Ref. [143].

Cell name	p-1.3	p-80
$S_{\text{front, nPOLO}}$ [cm s^{-1}]	1.95 ± 0.65	0.5 ± 0.1
$S_{\text{front, finalized}}$ [cm s^{-1}]	4.4 to 10	1.3 to 2.3
$S_{i\text{-region}}$ [cm s^{-1}]	20 to 21	13 to 15

simulation results and a value of 4 cm/s for the fill factor. Both values are smaller than those obtained on the p -type wafers, but they are probably less reliable due to the shortcomings of this cell.

4.2.4 Summary and discussion of Section 4.2

The best-reached efficiency of 26.1 % [25], independently confirmed at ISFH CalTeC, of the best POLO²-IBC solar cell on 1.3 Ω cm p -type material was the second-highest reported efficiency in 2018 for Si single-junction cells (in terms of team ranking) and is still the current world record on p -type Si material. By performing a systematic process monitoring by ILM measurements of POLO²-IBC cells on three different base materials (1.3 and 80 Ω cm p -type and 2 Ω cm n -type), we reveal their different behavior and thus suitability for achieving highest energy conversion efficiencies.

The analysis of process-induced degradation shows that the efficiency potential of the POLO²-IBC cell is not fully exploited yet. Process induced degradation accounts for 0.3 %_{abs}, 0.6 %_{abs} and 1.3 %_{abs} for the p-1.3, p-80 and n-2 cells respectively. Reasons for the degradation of the passivation quality are assumed to be the damaging of the front side passivation by the LCO process and the wet-chemical contact separation process, as well as Al spiking through the oxide and producing shunts in the (*i*) poly-Si region.

We suspect that in the case of the p-80 cell, the stronger degradation is caused by the lower resistivity, which leads to a higher injection condition at MPP and, thus, a stronger sensitivity to surface recombination. Here the implied pseudo-FF is mainly responsible for the loss in efficiency while the V_{oc} remains almost constant. However, it should be noted that the comparison between ILM and J - V measurement of the finalized cells shows that the ILM measurement significantly overestimates the V_{oc} .

This considerable degradation makes up for the initially higher potential of the p-80 cell compared to the p-1.3 cell.

In the case of the n -type cell, the even greater degradation is suspected to be induced by electrical shading due to an adverse ratio of base and emitter area fractions. Moreover, the metal contact fingers of all three cells, independent of the base doping type, are separated between the n^+ poly-Si and the nominal intrinsic poly-Si region (see Figures 4.2(l) and (m)). Therefore the emitter metallization overlaps with the (i) poly-Si region in the case of the n -type base, which leads to shunting currents through the leaky SiO_x on the rear side ($R_{\text{sh}} = 1800 \Omega\text{cm}^2$). Thus, separating the n^+ poly-Si and the intrinsic poly-Si region would enable higher efficiencies.

Perimeter recombination also leads to a significant loss in efficiency for all three cells. With 0.6%, the loss of the p-80 cell is in comparison to 0.3%_{abs} (p-1.3) and 0.4%_{abs} (n-2) particularly pronounced. Due to the lower doping in the p-80 material, mobility and lifetime (due to lower Auger recombination) are increased, leading to an increased effective diffusion length L_{eff} . These larger L_{eff} values, in turn, lead to a larger current into the edge regions and thus to higher losses [142].

The series resistances of the cells also differ significantly with 0.1 to 0.2%_{abs}, 0.4%_{abs} and 0.02%_{abs} for the p-1.3, p-80 and n-2 cells respectively.

Finally efficiencies of 26.1% and 24.9% on a 1.3 Ωcm and 80 Ωcm p -type FZ wafer and 24.6% on a 2 Ωcm n -type Cz wafer respectively are reached. The subsequent FELA also shows the same qualitative trend between these cell types, although the simulated difference between the p-1.3 and p-80 cells is significantly smaller. In particular, poorer passivated surfaces than assumed in the simulation probably play a major role here. Altogether, the low-resistance p -type material is thus the most suitable of the three groups. At the same time, the n -type cell could be significantly improved by flipping the finger doping type.

By comparing the ILM and J - V measurements with a finite element simulation, we determine the surface recombination velocity in the nominal intrinsic poly-Si region in the range of 12 to 21 cm/s. Using the same approach, we analyze the increase of the front surface recombination velocity during cell processing from 2 to 10 cm/s for the 1.3 Ωcm and from 0.5 to 2.3 cm/s for the 80 Ωcm . This, in turn, leads to the finding that cells fabricated on lowly-doped bulk material are more vulnerable to process-induced degradation of the surface passivation, which is

particularly important for establishing a robust, industrially relevant cell process.

4.3 Investigation of the working principle of the $p^+(i)n^+$ back contact structure

This section investigates the $p^+(i)n^+$ poly-Si contact structure on the rear of the POLO²-IBC cells, which implements a separation of the n^+ and p^+ poly-Si fingers by a nominally intrinsic poly-Si region. The effect of the intrinsic region on the rear side passivation and the recombination current across the diode is analyzed. These charge carrier separating regions are a simple method to avoid a lateral p^+n^+ poly-Si junction between the base and emitter poly-Si fingers, which would lead to high recombination currents if they were not isolated from each other [83], [84], [86], [148].

This section is based on the peer-reviewed paper [144] to which other groups have contributed. The time-resolved PL measurements were done by E. Sauter and J. Hübner from the group „Spin and charge carrier dynamics of complex semiconductor nanostructures“ of M. Oestrich at the Institute for Solid-State Physics at Leibniz University Hannover. The ToF-SIMS measurements were performed by S. Richter, working in the team of S. Großer „c-Si-Defect diagnostics“ at Fraunhofer Center for Silicon Photovoltaics.

4.3.1 Impact of the poor passivation quality of i POLO junctions on the cell performance

The i poly-Si region itself negatively influences the passivation at the oxide interface to the wafer, as a field effect passivation is not present. To estimate the impact of an i poly-Si region on the rear surface passivation quality, we measure the carrier lifetimes using the PCD method on symmetric reference samples with full-area p^+ POLO, n^+ POLO, and i POLO junctions processed in this cell batch. Table 4.5 shows a lifetime of only 9 μs at the MPP in the i POLO sample while the two samples with doped POLO junctions have effective lifetimes of 1400 μs and 3300 μs , respectively.

4.3 Investigation of the working principle of the $p^+(i)n^+$ back contact structure

Table 4.5: Effective lifetimes measured on symmetric full area reference wafers with i POLO, n^+ - and p^+ POLO junctions after hydrogenation. This table is reprinted from Table 1 in Ref. [144]. This figure is reprinted from Figure 6 in Ref. [144].

Reference sample	τ_{eff} at MPP of the cell [ms]
i POLO	0.009
p^+ POLO	1.392
n^+ POLO	3.289

To determine the influence of the poor lifetime on the cell performance, we simulate the unit cell of our POLO²-IBC solar cells. The simulations are performed using Quokka2 [138], [139], which employs our conductive boundary model [141]. For this simulation, we first calculate the injection-dependent surface recombination velocity, S_{eff} , from the injection-dependent lifetime τ_{eff} measured on the i POLO sample, assuming a bulk Shockley-Read-Hall lifetime of 100 ms.

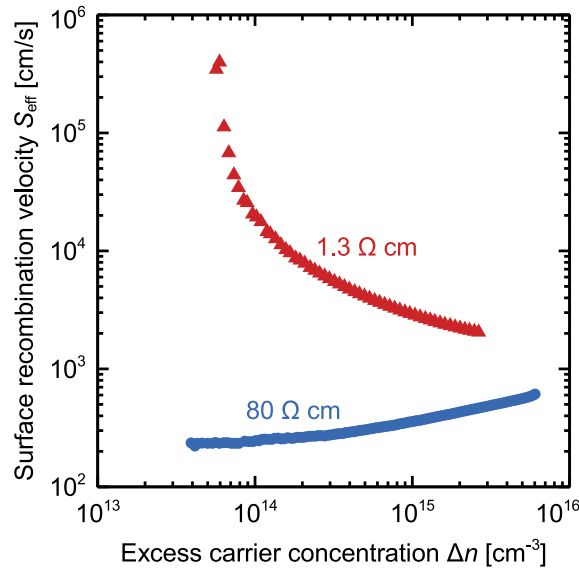


Figure 4.9: Surface recombination velocity S_{eff} as a function of the excess carrier concentration and the resistivity of p -type silicon wafers with symmetric i POLO junctions. This figure is reprinted from Figure 5 in Ref. [144].

Figure 4.9 shows the S_{eff} values of the i POLO reference samples on $1.3 \Omega \text{ cm}$ and $80 \Omega \text{ cm}$ material. We observe a decreasing SRV with decreasing doping level, as has also been shown for bare thermally oxidized p -type wafers [77]. This effect can be explained by positive fixed oxide charges Q_f that do not depend on the wafer

resistivity. These charges cause a depletion at the surface in lightly doped p -type Si wafers, resulting in high S_{eff} values. The depletion evolves toward inversion with decreasing doping level and thus lower S_{eff} values for the lowly doped $80\ \Omega\ \text{cm}$ material. As shown in Figure 4.10 for the $1.3\ \Omega\ \text{cm}$ material, the depletion condition is enhanced when intrinsic poly-Si is applied on top of the oxide, leading to stronger recombination, which occurs in an intermediate region between depletion and inversion and therefore, even higher S_{eff} values. The corresponding band diagram in equilibrium (see Figure 4.10) for the $1.3\ \Omega\ \text{cm}$ material has been calculated with the semiconductor module of Comsol Multiphysics, using the common models for numerical device simulations of solar cells [149] and assuming a fixed charge density of $5 \times 10^{10}\ \text{cm}^{-2}$ adjacent to the silicon wafer.

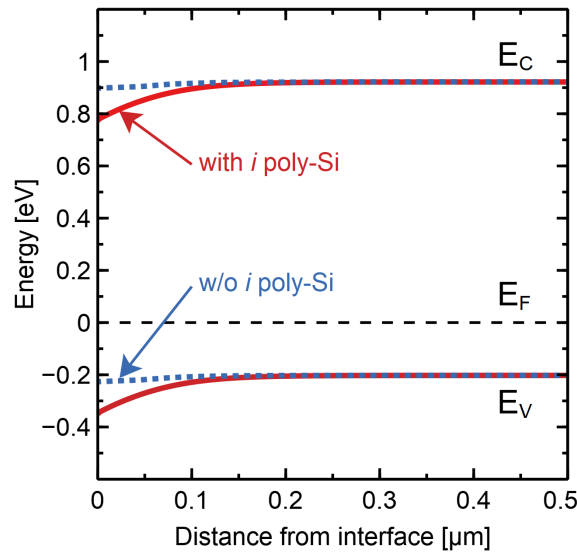


Figure 4.10: Band diagram of an $1.3\ \Omega\ \text{cm}$ sample in equilibrium at the interface to the silicon oxide with and without i poly-Si on top. The figure is reprinted from Figure 6 in Ref.[144]

For the simulation of a p - 1.3 POLO²-IBC cell, the calculated injection dependent S_{eff} values for the i POLO areas, and all the other simulation parameters from Table 4.1 are taken. The simulation shows that the (i)POLO junctions with a width of $d_{\text{gap}} = 30\ \mu\text{m}$, covering 13.3% of the rear side area, would limit the efficiency potential to 14.9%. However, 26.1% efficiency is achieved with this cell structure. The discrepancy between the simulated efficiency of 14.9% and the actual measured efficiency of 26.1% hints toward a significant difference between the S_{eff} value of the

(i)POLO regions in the cell and the i POLO test structures, used here for the S_{eff} calculation.

4.3.2 Density of pinholes and their impact on the passivation of i POLO junctions

Determining the areal densities of the pinholes helps to understand whether the high recombination activity at the c-Si/SiO_x/ i poly-Si interface is caused exclusively by the moderate chemical passivation of SiO_x on p -type Si [77] or possibly also by the formation of pinholes [66], [67], [135], [150] in the interfacial oxide. We use the selective etching method developed by Tetzlaff et al. [67] followed by scanning electron microscopy (SEM) examination to determine the pinhole areal densities that are listed in Table 4.6. Differences between the p^+ POLO, n^+ POLO and i POLO junctions and etching times can be seen. However, the base doping does not affect the areal density of the pinholes.

Table 4.6: Etch pit areal density (EPD) in the interface oxide of a p^+ , n^+ and i POLO junction after appropriate etching times. This table is reprinted from Table 2 in Ref. [144].

Junction	Resistivity	EPD	J_0	Etching time
i POLO	1.3	$(2.6 \pm 0.1) \times 10^6$	2900	5
i POLO	80	$(2.8 \pm 0.2) \times 10^6$	540	5
n^+ POLO	80	$(1.0 \pm 0.6) \times 10^8$	6	1
p^+ POLO	80	$(1.96 \pm 0.09) \times 10^7$	5	5

Figure 4.11 shows SEM images of the n^+ POLO, p^+ POLO and i POLO samples etched for 5 min and the n^+ POLO sample etched for 1 min. Figure 4.11(a) of the n^+ POLO sample etched for 5 min shows that the etch pits have reached a size that is so large, that several of them touch each other. Thus, an evaluation of these images would underestimate the etch pit density. Therefore, an appropriate etch time is chosen for each sample. To eliminate the influence of local differences in the etch pit density, we examine an area of $1000 \mu\text{m}^2$ for each sample. The n^+ POLO contact contains the largest etch pit areal density of $(1.0 \pm 0.6) \times 10^8 \text{ cm}^{-2}$ (etch time 1 min). The p^+ POLO sample has a lower etch pit density of $(1.96 \pm 0.09) \times 10^7 \text{ cm}^{-2}$ and

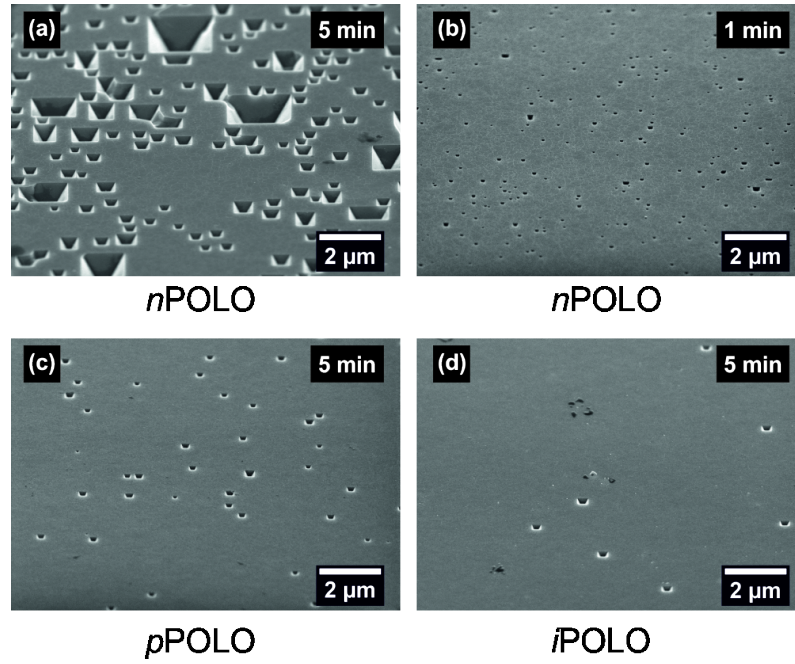


Figure 4.11: SEM images of full area reference samples on $80 \Omega \text{ cm}$ p -type wafers after etching with 15% TMAH at 80°C . The samples are tilted to 31° out of the vertical position. In figure (a), after etching for 5 min the etch pit are so wide that they are growing into one another, which would falsify the areal density. Thus, we chose a shorter etching time of 1 min (b) for the evaluation of this sample. In figures (c) and (d), the etching time of 5 min is appropriate for determining the pinhole areal density. This figure is reprinted from Figure 7 in Ref. [144].

the i POLO samples shows the lowest etch pit density of $(2.8 \pm 0.2) \times 10^6 \text{ cm}^{-2}$ on an $80 \Omega \text{ cm}$ wafer and $(2.6 \pm 0.1) \times 10^6 \text{ cm}^{-2}$ on a $1.3 \Omega \text{ cm}$ wafer.

Figure 4.12 shows an SEM image of a $p^+(i)n^+$ junction on a cell wafer. This image confirms that the differences in etch pit density between those regions are also present inside the cell structures. However, the etch pit size differs here from the full-area samples. In the p^+ poly-Si region, there are extensive etch pits of up to $3 \mu\text{m}$ size, which do not occur in the full-area p^+ POLO samples. Furthermore, the reason for the accumulation of etch pits at the interface with the n^+ POLO region is unclear.

Concerning the pinhole current transport picture, doping of the poly-Si is essential to introduce carrier selectivity [22], [23]. Intrinsic domains, therefore, do not exhibit carrier selectivity and thus allow strong recombination at the interface. However, the i POLO sample exhibits considerably fewer etch pits than the doped POLO

4.3 Investigation of the working principle of the $p^+(i)n^+$ back contact structure

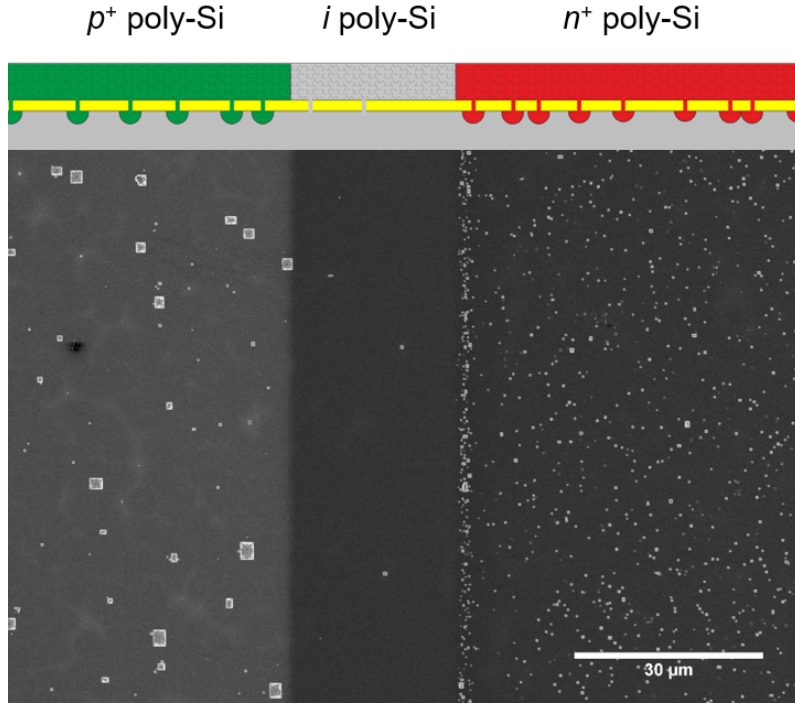


Figure 4.12: SEM images of cell wafer on $1.3 \Omega \text{ cm}$ p -type material after etching with 15 % TMAH at $80 \text{ }^\circ\text{C}$ for 4 min. This figure is adapted from Figure 8 in Ref. [144].

samples. However, the recombination activity at the still present pinholes will be larger than for the p^+ POLO and n^+ POLO junctions due to the lack of asymmetry of electron and hole concentrations and thus leads to a negligible carrier selectivity. To estimate the recombination activity of the pinhole, we calculate the recombination current density as a function of the areal density of the pinholes using the Fischer model [66], [151]. We assume a pinhole radius r_{pin} of 2 nm following the transmission electron microscope (TEM) studies performed by Tetzlaff et al. [67] and Peibst et al. [66]. Here, we consider recombination in the pinholes only, i.e., we assume a surface recombination velocity of zero for the passivated regions and $S_{0,\text{pinhole}} = 1 \times 10^7 \text{ cm/s}$ within the pinholes.

Figure 4.13 shows that the simulated recombination current density as a function of the pinhole areal density (lines) decreases with the doping concentration and decreasing pinhole areal density. The measured recombination current density J_0 of the $80 \Omega \text{ cm}$ sample (blue star) is only slightly higher than the simulated value. The simulated recombination current density of the $1.3 \Omega \text{ cm}$ sample (red star) is about

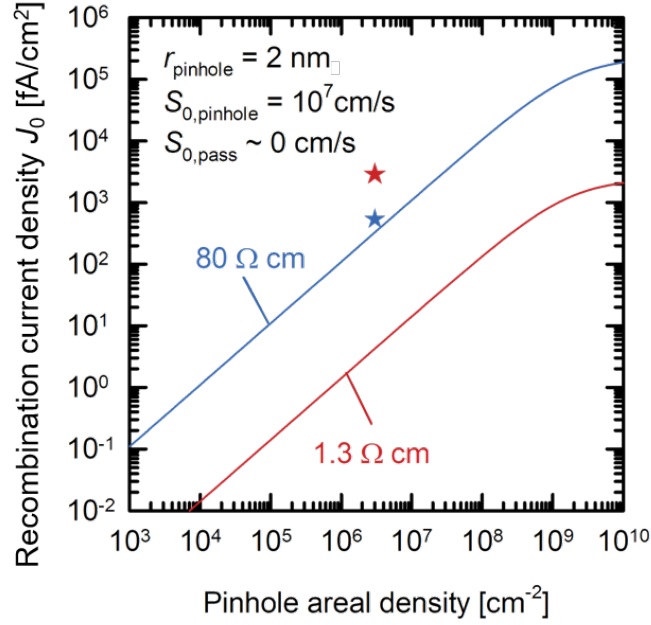


Figure 4.13: Recombination current density as a function of the pinhole areal density determined using the given parameters together with the Fischer model. [151]. The blue and red lines present the two p -type base materials used for the cells and the reference wafers. The stars indicate the recombination current densities calculated from the measured lifetimes and the respective measured pinhole areal densities. This figure is reprinted from Figure 9 in Ref. [144].

three orders of magnitude higher. Thus, recombination at the interface clearly dominates in the $1.3\ \Omega\ \text{cm}$ sample and is at least as large as the recombination in the pinholes in the $80\ \Omega\ \text{cm}$ sample.

4.3.3 Comparison of large area and small area, embedded

(i) poly-Si regions

To track down the apparent contradiction between the actual and the simulated efficiency, based on the S_{eff} values of the full-area i POLO reference samples, we take a spatially resolved ILM image of cell precursors in the pre-metallization state (see Figure 4.14). The image shows low lifetimes and thus high SRV in four large i poly-Si regions. However, the cell regions containing interdigitated p^+ POLO and n^+ POLO finger structure with either $20\ \mu\text{m}$ or $30\ \mu\text{m}$ nominal (i) poly-Si regions show the

4.3 Investigation of the working principle of the $p^+(i)n^+$ back contact structure

highest lifetimes across the wafer. These high lifetimes in the cell areas indicate that the small-area (i) poly-Si regions embedded between the n and p^+ poly-Si fingers are qualitatively different from the four large area i poly-Si areas.

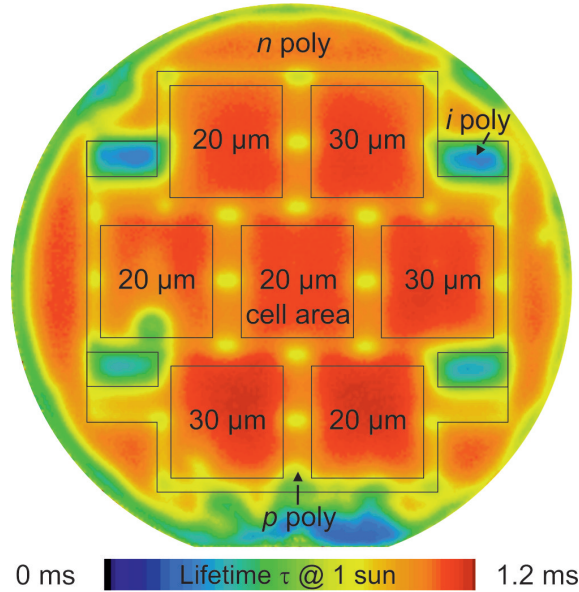


Figure 4.14: Spatially resolved carrier lifetime of a cell at 1 sun illumination measured by the ILM method. The active cell areas of the seven solar cells are marked with squares, and the value inside gives the nominal width of the intrinsic region. The rear side area between the cells is passivated with p^+ poly-Si. Four smaller regions with low lifetimes are i poly-Si regions. This figure is reprinted from Figure 10 in Ref. [144].

Interdiffusion of the dopants into the initially intrinsic embedded regions during the high-temperature treatment (1035 °C for 1 h) of the POLO contacts could explain this result. The fact that the diffusion coefficients D of boron and especially phosphorous in poly-Si are about four orders of magnitude higher than the corresponding values in crystalline Si (at $T = 1050$ °C of $D_{\text{P}} = 1.4 \times 10^{-9}$ cm²/s [152] and $D_{\text{B}} = 6.3 \times 10^{-12}$ cm²/s [153]), supports this hypothesis.

4.3.4 Lateral interdiffusion of dopants in the embedded (i)POLO regions

We conduct lateral and depth-dependent ToF-SIMS measurements on a solar cell precursor after annealing at 1035 °C that exhibits 30 μm-wide nominal (i) poly-Si

regions to clarify whether lateral diffusion indeed is responsible for the improved lifetime in the cell area (see Figure 4.15).

The lateral and depth-dependent measurement shown in Figure 4.15(a) is performed over a volume with an area of $150 \times 150 \mu\text{m}^2$ and a depth of about 314 nm. The summed dopant concentration over the entire $150 \times 150 \mu\text{m}^2$ surface area in the x and y direction and to a depth of 100 nm into the wafer is shown in Figure 4.15(b). The measurement reveals an average phosphorous concentration of $5 \times 10^{20} \text{cm}^{-3}$ in the n^+ poly-Si region and a boron concentration of $4 \times 10^{19} \text{cm}^{-3}$ in the p^+ poly-Si regions. An error function decay in dopant concentrations from the adjacent regions is observed in the region that was originally undoped before the annealing step. The boron concentration decreases more rapidly with distance from the p^+ poly-Si region, yielding a diffusion coefficient of about $(8 \pm 2) \times 10^{-11} \text{cm}^2/\text{s}$. The phosphorous diffuses much further, resulting in a fitted diffusion coefficient of $(2 \pm 1) \times 10^{-10} \text{cm}^2/\text{s}$. The boron and phosphorous concentration curves intersect at a distance of 24 μm from the n^+ poly-Si region and a distance of 4 μm from the p^+ poly-Si region at a concentration of $2 \times 10^{19} \text{cm}^{-3}$.

Moreover, vertical Electrochemical Capacitance-Voltage (ECV) measurements, as shown in figures 4.15(c) and (d), are carried out to enable a comparison of vertical SIMS and ECV measurements. The vertical boron concentration and electrically active boron concentration, respectively, as measured by a ToF-SIMS and an ECV, are shown in Figure 4.15(c). Both techniques yield a mean concentration of $(4 \pm 1) \times 10^{19} \text{cm}^{-3}$. However, the mean vertical phosphorous concentration in Figure 4.15(d) differs by about a factor of two between the ECV and the vertical ToF-SIMS measurement with values of $2.5 \times 10^{20} \text{cm}^{-3}$ and $6 \times 10^{20} \text{cm}^{-3}$. This comparison shows significantly more phosphorus in the poly-Si than is activated during annealing. The active phosphorus concentration of $2.5 \times 10^{20} \text{cm}^{-3}$ here most likely corresponds to the active solubility limit, which depends on the annealing temperature [154]. Furthermore, the depths of the profiles and, thus, the apparent thicknesses of the poly-Si layers do not match well. The more accurate method here is clearly the SIMS measurement, especially since the depth of the etch craters was not determined after the ECV measurement, and the given depth is, therefore, only a rough estimate.

In addition, the phosphorous profile from the ToF-SIMS measurement shows a prominent peak at 120 nm depth from the surface, consistent with the position of

4.3 Investigation of the working principle of the $p^+(i)n^+$ back contact structure

the interfacial oxide. This finding may have different origins. We suspect that at least part of the higher signal is due to the high oxygen content in the SiO_x layer. In the positive ionization mode, oxygen is known to lead to an increased signal and thus overestimation of the dopant concentration. The uncertainty of the P concentration is higher than that of B [155] because the ^{31}P signal is superimposed by the signal of the $^{30}\text{Si}^1\text{H}$ molecule. In addition to these artifacts, actual accumulation of dopants at the SiO_x interface, which thus become electrically inactive, is possible. An 80-fold higher segregation coefficient at the interface of Si and SiO_x of P fits the significantly prominent peak compared to B [156].

These measured lateral doping profiles in Figure 4.15(b) can explain the improved passivation quality of the nominally (*i*) poly-Si regions compared to large and thus actually *i* poly-Si regions on the same wafer. The recombination at the c-Si/ SiO_x interface is reduced by introducing a certain band bending, and pinhole recombination is reduced by the formation of a *pn* junction in the vicinity of the pinholes [135], [157]. In the regions where the poly-Si is *p*-type doped, an accumulation of holes and, thus, a reduction of the electron concentration occurs on the c-Si side of the interfacial oxide. In the regions where the poly-Si is *n*-type doped, interdiffusion of phosphorous into the c-Si leads to an increase in electron concentrations and a reduction of the hole concentration on the c-Si side of the interface. In both regions, the effective c-Si/ SiO_x interface recombination is lower than in large area *i* poly-Si regions, where the c-Si side of the interfacial oxide is depleted, and both carrier types are present in similar concentrations.

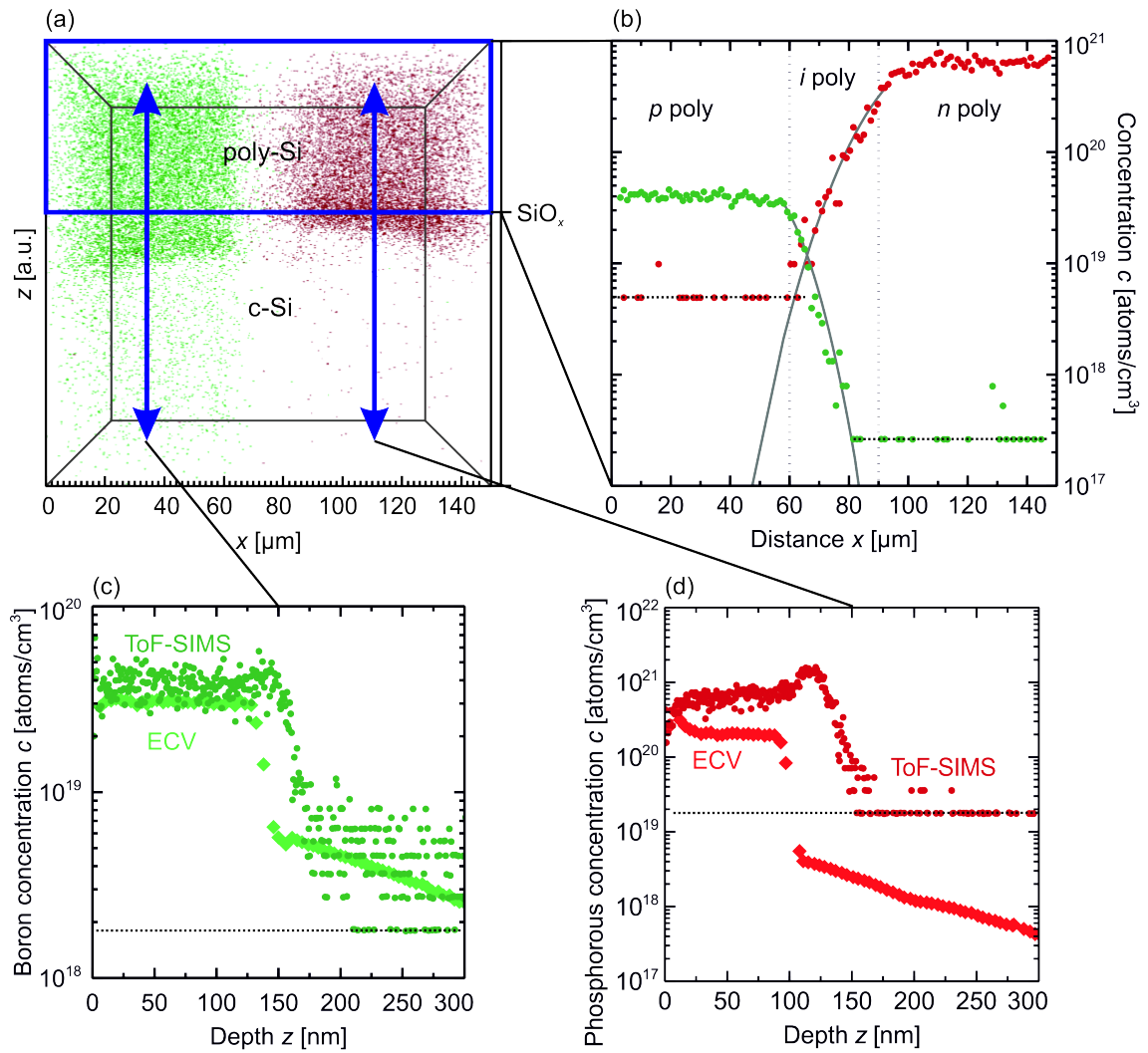


Figure 4.15: ToF-SIMS analysis of a $p^+(i)n^+$ structure in a solar cell precursor. (a) 3D point diagram of the spatially resolved dopant concentrations of boron and phosphorous in a volume with an area of $150 \times 150 \mu\text{m}^2$ and a depth of 314 nm. (b) Summed doping concentration over the volume in Figure (a) above a depth of 100 nm. The solid gray lines show error function fits to the data in the formally intrinsic region to quantify the interdiffusion. (c),(d) Depth profiles of the boron and phosphorous concentration determined by ToF-SIMS and ECV measurements. The difference in position in the z -direction of the decrease of the dopant concentrations needs to be investigated further. Black dotted lines mark the resolution limits of the different TOF-SIMS measurements. This figure is reprinted from Figure 11 in Ref. [144].

4.3.5 J - V characteristics of poly-Si $p^+(i)n^+$ structures

Since a separation of the p^+ and n^+ poly-Si regions is necessary, as shown by the previous investigations [83], the needed width of the initially intrinsic region is systematically investigated in the next step. The aim is to determine the width of the process window and a possible optimum outside the previously selected range of 25 and 30 μm wide (i) poly-Si regions.

Figure 4.16(a) shows the current-voltage characteristics of $p^+(i)n^+$ poly-Si samples. The structure of these samples is shown in Figure 4.1(b) and consists of poly-Si $p^+(i)n^+$ diodes with different nominal widths of the intrinsic region. Plotted is the absolute current density that would occur in a POLO²-IBC cell due to its lateral poly-Si $p^+(i)n^+$ junction area $A_{\text{pin, cell}}$ to enable a comparison between the measured dark I - V current $I_{\text{meas, test}}$ and the total recombination current density $J_{\text{rec, cell}}$ of the POLO²-IBC solar cell. The vertical $p^+(i)n^+$ junction area in the test structures is $A_{\text{pin, test}} = 9 \times 10^{-6} \text{ cm}^2$ as the length of the structures is $l_{\text{test}} = 0.6 \text{ cm}$ and the poly-Si thickness is $d_{\text{poly}} = 150 \text{ nm}$. The solar cells have a finger pitch of 450 μm and thus $n_{\text{fingers}} = 44$ fingers of one polarity, a poly-Si thickness of $d_{\text{poly}} = 150 \text{ nm}$ and a cell area of $A_{\text{cell area}} = 4 \text{ cm}^2$ and thus contain a lateral $p^+(i)n^+$ junction area of $A_{\text{pin, cell}} = 2.67 \times 10^{-3} \text{ cm}^2$.

$$A_{\text{pin, test}} = d_{\text{poly}} \cdot l_{\text{test}} = 9 \times 10^{-6} \text{ cm}^2 \quad (4.1)$$

$$J_{\text{rec, pin}} = \frac{I_{\text{meas, test}}}{A_{\text{pin, test}}} = \frac{I_{\text{meas, test}}}{9 \times 10^{-6} \text{ cm}^2} \quad (4.2)$$

$$A_{\text{pin, cell}} = d_{\text{poly}} \cdot l_{\text{cell}} \cdot 2n_{\text{fingers}} = 2.67 \times 10^{-3} \text{ cm}^2 \quad (4.3)$$

$$J_{\text{rec, cell}} = J_{\text{rec, pin}} \cdot \frac{A_{\text{pin, cell}}}{A_{\text{cell}}} = J_{\text{rec, pin}} \cdot 6.67 \times 10^{-4} \quad (4.4)$$

This gives factor of $a_{\text{pin to cell}} = 6.67 \times 10^{-4}$ for the measured dark current per $p^+(i)n^+$ area J_{pin} compared to the current density $J_{\text{rec, cell}}$ of an POLO²-IBC solar cell due to its lateral $p^+(i)n^+$ area.

The poly-Si p^+n^+ diode (zero-width of intrinsic region) shows a very high current density of up to $J_{0 \mu\text{m}} = 60 \text{ mA/cm}^2$ at a voltage of 0.64 V (V_{MPP} of the best measured final solar cell) again confirming the necessity of the intrinsic region.

Regarding small (i) poly-Si regions of nominally up to 25 μm and 30 μm the cur-

4 IBC solar cells with POLO junctions for both polarities

rent per cell area at V_{MPP} decreases about 2 to 3 orders of magnitude to $J_{25\mu\text{m}} = 0.2\text{ mA/cm}^2$ and $J_{30\mu\text{m}} = 0.03\text{ mA/cm}^2$ at V_{MPP} while the diode-like behavior remains.

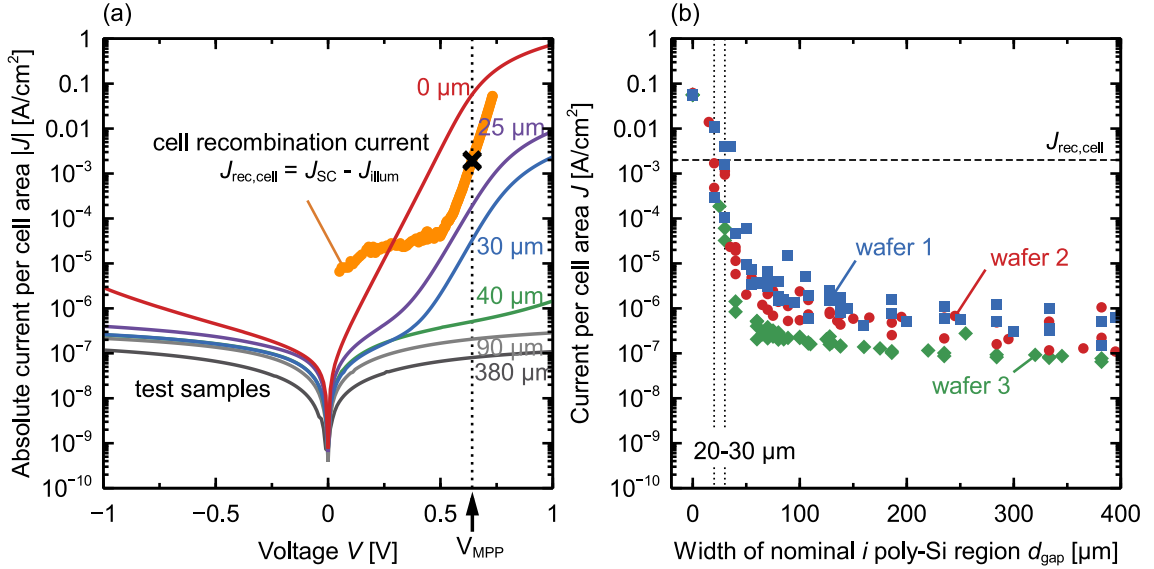


Figure 4.16: J - V analysis of the $p^+(i)n^+$ test structures. (a) J - V curves of $p^+(i)n^+$ diodes with different widths of the (i) poly-Si region. The MPP and $J_{\text{rec, cell}}$ refer to the record solar cell with a 30 μm -wide intrinsic region. (b) Current per cell area J through the $p^+(i)n^+$ diodes at a voltage of 0.64 V (representative for the maximum power point of our solar cells) as a function of the designated width of the intrinsic region. The different colors indicate three identical test structures on different wafers. This figure is reprinted from Figure 4 in Ref. [144].

In the range between nominally 30 μm and 40 μm both, the absolute value of the current density and the shape of the J - V curve change drastically. The asymmetrical diode behavior changes to a symmetric one. The current density decreases by about two orders of magnitude to a value of $5 \times 10^{-7}\text{ A/cm}^2$ at V_{MPP} . The current density continues to decrease with further enlargements of the nominal (i) poly-Si region up to 380 μm . J - V curves of samples with d_{gap} of 90 μm or more do not show a rectifying behavior.

Besides the J - V curves of the test structures, Figure 4.16(a) also shows the MPP of the best fully processed solar cells at 0.641 V and 40.6 mA/cm². Moreover, the total recombination current density $J_{\text{rec, cell}} = J_{\text{sc}} - J_{\text{gen}}$ of this cell is calculated from the difference between the short circuit current density J_{sc} and the current density at one sun illumination J_{gen} and applied bias voltage. Comparing this to the recombination

4.3 Investigation of the working principle of the $p^+(i)n^+$ back contact structure

current through the nominal (i) poly-Si region, we conclude that a nominal width of 30 μm is sufficient to reduce the latter to a level where it no longer significantly affects the cell performance anymore.

In Figure 4.16(a), only some selected representative curves can be shown. However, having in mind the deviations in width of up to 10 μm that occur due to the inkjet-printed masks, it is necessary also to get an overview of all measured samples, given in Figure 4.16(b). Here, for all measured samples, the current per cell area through the $p^+(i)n^+$ test structures, at 0.64 V, as a function of the nominal width of the (i) poly-Si region, is shown. From 20 μm to 40 μm , the current density decreases sharply. A clear correlation between the recombination current and the nominal (i) poly-Si region width can be seen. Most data points for diodes with d_{gap} between 20 μm and 30 μm are smaller than the total recombination current density $J_{\text{rec, cell}}$ of the record cell [25]. These widths very well correspond to the nominally 30 μm -wide (i) poly-Si region of the record cell. The recombination current across the $p^+(i)n^+$ junction thus does not limit the cell's total recombination current.

4.3.6 Influence of (i) poly-Si region width and annealing temperature

The two opposing recombination pathways, the recombination through the $p^+(i)n^+$ poly-Si junction and recombination at the (i) poly-Si/SiO_x/c-Si interface, and the study in section 4.3 give reason to believe that there is an optimum in (i) poly-Si region width. To find this optimal width for our cell process, we process cell precursors with a larger range of d_{gap} from 5 to 40 μm . In addition to cells on p-1.3 material processed according to the process flow shown in Figure 4.2, we also process 1.5 Ωcm cells on p -type Cz material with a wet-chemically grown interfacial oxide. These samples require a lower annealing and break-up temperature of 860 $^\circ\text{C}$, at which we expect the interdiffusion to be noticeably weaker.

The implied pseudo efficiencies results determined from ILM measurements shown in Figure 4.17 scatter strongly. We attribute this to a significant variation in lifetimes that we observe across the wafers, which thus influences the cell efficiencies. Moreover, the absolute implied pseudo efficiency achieved in the state after hydrogenation (step h in Figure 4.2) on the FZ wafer strongly lag behind the previously

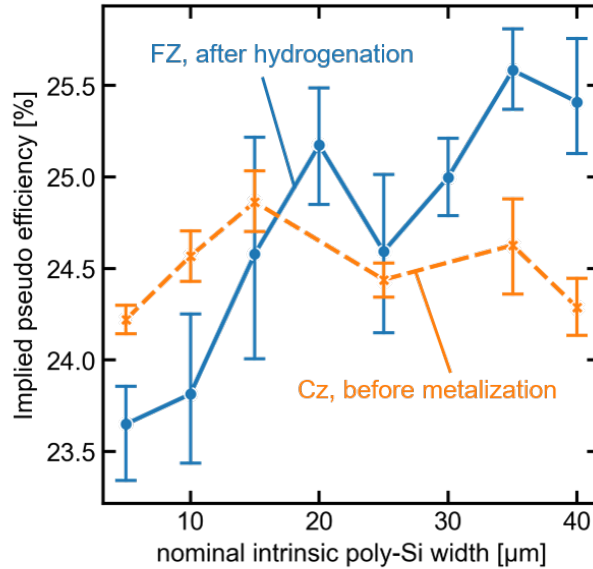


Figure 4.17: Implied pseudo efficiency as a function of the nominal (*i*) poly-Si region width for two different types of samples. The orange data points represent POLO²-IBC cells on Cz material with a wet-chemical interfacial oxide that were annealed at 860 °C. The blue data points show the results of POLO²-IBC cells on FZ material with a thermally grown interfacial oxide annealed at 1035 °C.

achieved implied efficiency due to a contamination issue. Nevertheless, it can be said that for the FZ samples (*i*) poly-Si region, widths of 5 to 10 μm are leading to a significantly lower implied pseudo efficiency than wider (*i*) poly-Si regions, as already indicated by the results in the previous section. These (*i*) poly-Si regions are too small to sufficiently suppress recombination within the poly-Si due to the very high doping levels of above 1×10^{20} P atoms/ cm^{-3} across the whole nominally intrinsic region. The cells with larger d_{gap} values show higher pseudo-implied efficiencies with a positive trend toward larger d_{gap} values up to 35 μm . Up to a width of $d_{\text{gap}} = 40 \mu\text{m}$ the doping concentration should still be well above 1×10^{18} atom/ cm^{-3} . With somewhat wider (*i*) poly-Si regions, slightly better results could possibly be achieved.

The Cz cells annealed at 860 °C, which were measured before metalization (step j in Figure 4.2) and without having seen any boron-oxygen deactivation process show even lower values but yield the expected trend. Due to the weaker interdiffusion, the doping in smaller gaps remains low enough to achieve a high resistivity. This

4.3 Investigation of the working principle of the $p^+(i)n^+$ back contact structure

behavior is reflected in the smaller optimal width of 15 μm . Above a width of 15 μm , the effective lifetimes already start to decrease again. This can be attributed to increasing recombination at the c-Si/SiO_x interface due to insufficient doping within the nominal (*i*) poly-Si region. This means that such a low annealing temperature of 860 °C leads to a rather small process window for an optimal width.

4.3.7 Influence of hydrogenation on the (*i*)POLO region

POLO junctions can profit strongly from introducing hydrogen into the poly-Si layer and to the interface, [82], [148] because hydrogen can passivate defects in the poly-Si layers, at grain boundaries, and the c-Si/SiO_x/poly-Si interface. For the passivation quality of a classical POLO junction, the passivation of defects at the interface to the wafer is particularly important. In the case of the lateral n^+/p^+ poly-Si junction, the passivation quality inside the poly-Si, where the grain boundaries are causing additional defect levels, should also be reduced to an acceptable level known from mono-crystalline Si. If this could be achieved by efficient hydrogenation, no further steps would be required to electrically separate the n^+ poly-Si and p^+ poly-Si fingers. As the SiO_x oxide grown during annealing on the poly-Si is needed for structuring reasons during the POLO²-IBC process flow, the hydrogenation is performed with a hydrogen-rich PECVD SiN_y layer on top of the SiO_x, which probably only introduces very little hydrogen. To investigate if enhanced hydrogenation might yield an advantage, a sample is hydrogenated by the deposition of a hydrogen-rich PECVD SiN_y layer directly onto a 180 nm-thick intrinsic poly-Si.

To determine the effective carrier lifetime inside the poly-Si, τ_{eff} , hydrogenated and non-hydrogenated poly-Si samples are subjected to time-resolved PL measurements. Therefore *i* poly-Si samples are prepared by starting with a quartz glass substrate onto which a 30 nm-thick SiN_y layer is deposited, followed by a 160 nm a-Si layer that is subsequently crystallized to poly-Si. In addition, one part of the samples are hydrogenated via a-Si:H rich SiN_y layer and annealed at 425 °C for 30 min. The resulting time-resolved signal of the excitation and decay process is shown in Figure 4.18.

Here, a clear difference in the decay behavior of the two samples becomes apparent. A bi-exponential fit is suitable for describing this behavior, resulting in the following two components given in Table 4.7. The first and faster lifetime component, i.e., the

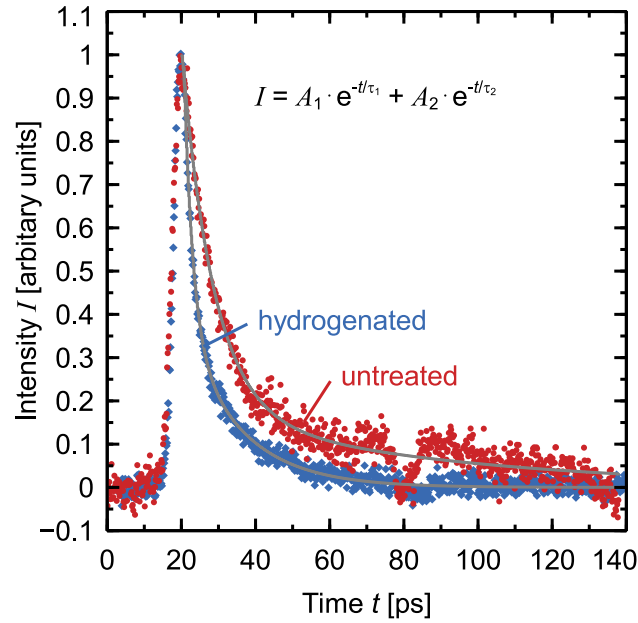


Figure 4.18: Time-dependent photoluminescence signal of a poly-Si layer on a glass substrate due to excitation with an 80 MHz Titanium-Sapphire Laser with a wavelength of 780 nm. The red circles show the signal of a non-hydrogenated sample, and the blue circles show the signal of a hydrogenated sample. The solid gray lines indicate the fitted bi-exponential functions. This figure is reprinted from Figure 2 in Ref. [144].

lifetime inside poly-Si, determined by the time-resolved PL method, changes from 8.2 to 2.4 ps due to the hydrogen treatment. This decreasing lifetime implies that the amount of recombination active defect states inside the poly-Si layers is not reduced by hydrogenation. Besides the short-lifetime component, a second component is determined from the PL signal. As shown in Table 4.7, this long-lived component is also reduced after the hydrogen treatment. A possible explanation for the decreasing lifetimes due to hydrogenation could be the passivation of defect-states that rather cause trapping of charge carriers than recombination.

Such an influence of hydrogenation on the properties of poly-Si was first shown by Seager et al.[158]. He demonstrated a significant reduction of the grain boundary state density and, thus, grain boundary potential barrier by showing an increased conductance over a grain boundary potential barrier in a poly-Si sample due to hydrogen treatment. These grain boundary states are known to be trapping states which can explain the measurement results shown in Figure 4.18.

4.3 Investigation of the working principle of the $p^+(i)n^+$ back contact structure

Table 4.7: Bi-exponential fit parameters of the time-dependent photoluminescence signal of an intrinsic poly-Si layer on a glass substrate shown in Figure 4.18.

Sample	fast component		slow component	
	A_1	τ_1 [ps]	A_2	τ_2 [ps]
untreated	0.25 ± 0.03	8.2 ± 0.3	9.9 ± 0.8	65 ± 5
hydrogenated	$(4 \pm 1) \times 10^3$	2.37 ± 0.08	1.47 ± 0.09	15.0 ± 0.4

Regarding the resistivity of the $p^+(i)n^+$ junctions, we perform dark J - V measurements of hydrogenated and non-hydrogenated $p^+(i)n^+$ diodes having a nominal width of above $50 \mu\text{m}$ as shown in section 4.3.2. Here an increase of the dark J - V current, i.e., recombination current density due to the hydrogen treatment, is observed (Figure 4.19). In agreement with the reduced lifetime, probably trapping states at the grain boundaries rather than recombination active defects are passivated by the introduced hydrogen. By this, the trapping of charge carriers in these states is reduced, reducing the potential barriers at the grain boundaries. Thus, an unwanted decrease in resistivity is induced.

These experiments show that hydrogen passivation is not a solution to reduce the recombination current over the n^+ / p^+ poly-Si junctions. Thus, separating the n^+ / p^+ poly-Si fingers by a large enough intrinsic region can not be circumvented.

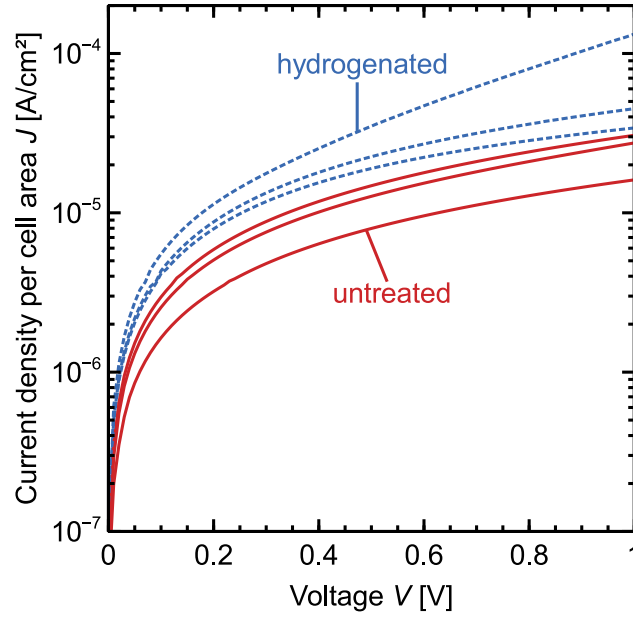


Figure 4.19: Dark- J - V -curves of $p^+(i)n^+$ diode structures with a width of $50\ \mu\text{m}$ of (i) poly-Si region. The measured current per lateral $p^+(i)n^+$ area is multiplied by $a_{\text{pin to cell}}$ to get the current per cell area J_{cell} . The dotted lines show results of hydrogenated samples, and the solid lines show samples that have not received a hydrogen treatment. This figure is reprinted from Figure 3 in Ref. [144].

4.3.8 Summary and discussion of Section 4.3

The key findings of the working principle of the $p^+(i)n^+$ back contact structures and their influence on the cell performance, presented in this section, are:

- The poor passivation quality of i POLO junctions determined on whole-area references would limit the efficiency of a POLO²-IBC cell with $30\ \mu\text{m}$ -wide i poly-Si regions to 14.9% as determined by a numerical simulation. However, the best-measured efficiency is 26.1%.
- Compared to n^+ POLO and p^+ POLO junctions, the pinhole areal density of i POLO junctions is reduced by two, respectively, one order of magnitude. The nevertheless poor passivation quality on $1.3\ \Omega\ \text{cm}$ material is mainly caused by recombination at the intact c-Si/SiO_x interface.
- A comparison of large i POLO areas and the cell areas with 13.3% i POLO area fraction based on an ILM measurement shows that the cell areas exhibit excellent lifetime in contrast to the large i POLO areas.

4.3 Investigation of the working principle of the $p^+(i)n^+$ back contact structure

- SIMS measurements show that the annealing of the POLO junctions leads to a strong interdiffusion of the dopants. This leads to a doping density of more than 1×10^{19} atoms/cm⁻³ in the formerly intrinsic region and, thus, to a drastic improvement of the passivation quality at the c-Si/SiO_x interface.
- The recombination current of a poly-Si $p^+(i)n^+$ diode is drastically reduced when increasing the nominal (i) poly-Si region from 0 to 50 μm . A width of 30 to 40 μm is sufficient to reduce the recombination current so that it is not limiting the total recombination current of the presented POLO²-IBC cells.
- A lower annealing temperature leads to a lower sufficient width of the (i) poly-Si region.
- An enhanced hydrogenation does not improve the lifetime inside poly-Si but leads to an increased recombination current in $p^+(i)n^+$ poly-Si structures. However, the passivation quality of p^+ POLO and n^+ POLO junctions is improved by hydrogenation.

As shown by Rienäcker et al. [83], pn junctions inside the highly defective poly-Si layer are responsible for a detrimental recombination behavior. The theoretically simplest solution would be to passivate the defects responsible for recombination and thus get closer to the recombination level in c-Si. Such an improvement would significantly increase the poly-Si lifetime, which we determined by time-resolved PL measurements on poly-Si samples with and without applied hydrogenation. These, however, do not show the desired effect of an increasing lifetime, but even a decreasing lifetime which lies in the range of 2 to 8 ps and thus nine orders of magnitude lower than the effective lifetime of the solar cells shown in section 4.2. Thus, the parasitic recombination cannot be reduced to an acceptable level known from c-Si by hydrogen treatment. Therefore, further measures are required to electrically separate the n^+ poly-Si and p^+ poly-Si fingers. Implementing an (i) poly-Si region, which we pursue, is the most straightforward way to achieve this from a process point of view.

To optimize the POLO²-IBC cell with $p^+(i)n^+$ structure on the rear side, both the recombination current at the c-Si/SiO_x interface ($J_{\text{rec, POLO}}$) and the recombination current $J_{\text{rec, pin}}$ across the $p^+(i)n^+$ diode in the poly-Si must be reduced. Therefore, a trade-off is necessary: On the one hand, the (i) poly-Si region must be kept as narrow as possible due to its poor passivation quality to reduce $J_{\text{rec, POLO}}$. On the

other hand, a certain width is necessary to reduce the $J_{\text{rec, pin}}$ to a level that does not limit the cell performance.

Different factors, such as hydrogenation and interdiffusion of dopants, influence these recombination pathways. The occurring interdiffusion leads to doping of more than $1 \times 10^{19} \text{ atom/cm}^{-3}$ in a formerly intrinsic region with a width of $30 \mu\text{m}$. As this doping introduces a certain selectivity to the (*i*)POLO junction, the $J_{\text{rec, POLO}}$, which for p-1.3 samples is mainly influenced by recombination at the c-Si/SiO_x interface rather than pinhole recombination, is significantly reduced. This is clearly seen by comparing full-area (*i*)POLO samples and lifetime measurements on cell structures, but the direct measurement is impossible. This interdiffusion somewhat weakens the necessity of width reduction for the (*i*) poly-Si region regarding $J_{\text{rec, POLO}}$. With increasing width, however, this effect also decreases again.

The passivation quality of *i*POLO junctions, where the c-Si side of the interface is depleted and both carrier types are present at a similar concentration, is extremely low ($S_{\text{eff}} > 1 \times 10^3 \text{ cm/s}$). Strong hydrogenation can lead to a significant improvement, hereby enhancing the chemical passivation of SiO_x on *p*-type c-Si. However, this is accompanied by hydrogenation of the *i* poly-Si itself, which increases the recombination current of a $p^+(i)n^+$ diode as shown in Figure 4.19. The hydrogenation applied in this work, in which the H-containing layer is deposited on the thick SiO_x layer and not directly on the poly-Si, leads only to weak hydrogenation. Due to the improvement in the passivation quality of the p^+ POLO and n^+ POLO junctions, the slight increase in $J_{\text{rec, pin}}$ is acceptable here.

For $p^+(i)n^+$ junctions, hydrogenated in the same way as the solar cells, J - V measurements in Figure 4.16 indicate a necessary width of minimum $30 \mu\text{m}$ to reduce $J_{\text{rec, pin}}$ well below $J_{\text{rec, cell}}$. The sudden decrease in recombination current density measured on the $p^+(i)n^+$ diodes with increasing width of the (*i*) poly-Si region from $0 \mu\text{m}$ and $50 \mu\text{m}$ (see Figure 4.16(b)) is consistent with the lateral interdiffusion and the strongly doping-dependent resistivity of poly-Si. According to literature [159]–[164] a sharp decrease in resistivity is expected at a doping concentration in the range of 1×10^{18} to $1 \times 10^{19} \text{ atoms/cm}^3$. This is because, with increasing doping concentration, more and more trapping defects at the grain boundaries are occupied by dopants and thus get charged. This leads to an increased potential barrier at the grain boundaries and, thus, to a simultaneous reduction in charge carrier mobility. When the doping increases beyond the grain boundary trap density, the mobility

increases again as the barrier height is reduced. For low doping densities, this results in about 4 to 5 orders of magnitude increased resistivity of poly-Si compared to c-Si [160], [165]. With increasing poly-Si doping density, the resistivity at first only slightly decreases until a threshold doping concentration is reached. Here the resistivity drops about six orders of magnitude. This threshold's actual position depends on the grain boundary trap state density, and thus shifts to higher doping concentration with decreasing grain size [163]. Hartenstein et al. [166] recently directly confirmed the existence of a high-resistivity region within the nominal (*i*) poly-Si region of a $p^+(i)n^+$ poly-Si structure by scanning spreading resistance microscopy.

For the width of the (*i*) poly-Si region, this means that doping just below this threshold should be aimed for, as this at the same time gives an as high as possible doping and thus passivation quality. The annealing temperature, in particular, significantly influences the corresponding width, as seen in Figure 4.17, since it determines both the diffusion strength and the grain size. As it was reported that hydrogenation reduces the grain boundary trap state density, [164], [167] stronger hydrogenation of the samples would probably lead to a shift of the threshold doping to lower doping density and thus would make a larger gap necessary.

4.4 Summary and implications of Chapter 4

In this chapter we presented an experimental and simulation study of the efficiency potential of IBC cells with p^+ and n^+ POLO junctions on different wafer material (1.3 Ω cm *p*-type, 80 Ω cm *p*-type and 2 Ω cm *n*-type c-Si). A distinctive feature of the POLO²-IBC cells is a nominally intrinsic poly-Si region separating the electron-collecting *n*-type poly-Si and the hole-collecting *p*-type poly-Si regions. These charge carrier separating regions are an elegant method to avoid a lateral p^+n^+ poly-Si junction between the base and emitter poly-Si fingers, which we experimentally investigated in detail.

With the described cell concept, we achieve an independently certified efficiency of $(26.10 \pm 0.31)\%$ on *p*-type 1.3 Ω cm wafer material. By systematic process monitoring, using injection-dependent ILM measurements, we show that the efficiency potential has not yet been fully exploited. Series resistance and perimeter recombination are responsible for an efficiency loss of 0.5%_{abs}, and process-induced degra-

dation implies a further loss of $0.2\%_{\text{abs}}$. A FELA reveals that the primary loss channel is intrinsic bulk recombination. Therefore it seems advantageous to use a lower doped material. However, we show experimentally and by simulations that the cells on low-doped material are more susceptible to surface passivation degradation (e.g., $0.6\%_{\text{abs}}$ efficiency loss on the $80\ \Omega\ \text{cm}$ p -type material).

By comparing the experimentally determined and simulated J - V parameters, we also quantify the recombination velocity in the (i) poly-Si region. This quantity is difficult to determine by other methods. $S_{i\text{-region}}$ values between 15 to 21 cm/s are obtained for the cells on p -type material.

The previous discussion referred to the efficiency potential of our cells for a given status of the POLO junction passivation quality (compare Table 4.1). The reasons why the full simulated potential of 27.01% (26.83%) for the $1.3\ \Omega\ \text{cm}$ ($80\ \Omega\ \text{cm}$) p -type material is not fully exploited yet, are, first, processed-induced degradation and, second, perimeter losses. Both aspects are not fundamental and can be addressed by improving the process sequence and using larger cells with higher area to perimeter ratios. Moreover, the passivation quality of the doped POLO junctions obtained in this study and used as an input parameter for the simulation (n^+ POLO $4\ \text{fA}/\text{cm}^2$, p^+ POLO $10\ \text{fA}/\text{cm}^2$) are not excellent and could be further optimized. In previous studies, values down to $0.6\ \text{fA}/\text{cm}^2$ for n^+ POLO junctions and down to $3.8\ \text{fA}/\text{cm}^2$ for p^+ POLO junctions were achieved [66]. Other groups even reported values down to $1\ \text{fA}/\text{cm}^2$ for p^+ POLO after hydrogenation with an optimized firing process [60]. Note that more hydrogenation can probably lead to this improvement in passivation quality. However, it could also reduce the resistance over the $p^+(i)n^+$ poly-Si diode, thus requiring an adjustment of the nominal intrinsic region.

The investigation of the $p^+(i)n^+$ poly-Si junction's working principle shows that different effects must be weighed to achieve optimal properties. The goal of electrically separating the p^+ and n^+ fingers requires a certain width of the (i) poly-Si region so that the recombination current over the $p^+(i)n^+$ junction is reduced to an acceptable level. However, as the width of the (i) poly-Si region increases, the relatively poor passivation in the nominally intrinsic region becomes more important. The average passivation further decreases as the width increases since the average doping becomes weaker and weaker. Moreover, the cell concept benefits from the fact that the dopants are mainly captured in trapping states at the grain boundaries up to a certain doping level. These trapped dopants create a potential barrier and,

thus, a transport limitation for charge carriers inside the poly-Si. This allows for smaller widths of the (*i*) poly-Si regions, which improves surface passivation. The experiments show that at an annealing temperature of 1035 °C, a width of 30 μm is sufficient.

The gained understanding of the $p^+(i)n^+$ junction will further open the way for a simplified fabrication of Si solar cells with efficiencies above 26 %. With this cell concept, high efficiencies can be achieved while avoiding process steps like trench formation and additional dielectric passivation resulting in significantly lower process complexity. A cell structure with a lower full area boron doping of the poly-Si followed by masked phosphorous doping, omitting the initially intrinsic regions, could be used. This would require adjusting the doping concentration to remain below the doping threshold at which recombination across the diode reaches the order of magnitude of a direct n/p -poly-Si junction while avoiding strong recombination at the poly-Si/SiO_x/c-Si interface. This approach, in turn, would open up the possibility of using counter-doping [148], [168] while potentially reducing the need for exact alignment.

A leaner process flow could also be accomplished by combining intrinsic poly-Si deposition with printed doping sources, structured doped glasses, or a masked deposition of in situ doped poly-Si. However, precise alignment is necessary to achieve the appropriate distances between n^+ POLO and p^+ POLO contacts [169], [170], which still needs to be demonstrated.

Another critical step for the simplification of the process flow and, thus, the transition to an industrial cell process with two or even only one poly-Si polarity is metallization. Here, evaporation and the complex contact separation should be replaced by an industrial process such as screen printing [171]. The transition to an industrial-relevant solar cell concept and the firing stability of POLO junctions, which must be provided or improved for this purpose, will be investigated in detail in the next chapter.

5 Firing stability of n^+ POLO junctions

This chapter provides a detailed investigation of the instability of n^+ POLO junctions towards the firing process, suggests possible reasons for the observed behavior, and demonstrates ways to circumvent the loss in passivation quality during firing. The research is based on PCD, $C-V$, and ToF-SIMS measurements of samples with different interfacial oxides, firing experiments with and without different hydrogen-rich capping layers, and varied conveyor belt speeds. These investigations and results are essential for transferring the promising POLO junction to mass production, for which metallization by screen printing followed by a firing process is essential to keep the process flow as close as possible to the current state of the art.

Large parts of the research shown in this chapter have been published in the peer-reviewed paper „Firing stability of tube furnace annealed n-type poly-Si on oxide junctions“, by C. Hollemann, M. Rienäcker, A. Soeriyadi, C. Madumelu, F. Haase, J. Krügener, B. Hallam, R. Brendel, and R. Peibst in Progress in Photovoltaics: Research and Applications in 2021 [104] and „Changes in hydrogen concentration and defect state density at the poly-Si/SiO_x/c-Si interface due to firing“, by C. Hollemann, N. Folchert, S. P. Harvey, P. Stradins, D. L. Young, C. L. Salles de Souza, M. Rienäcker, F. Haase, R. Brendel, and R. Peibst in Solar Energy Materials and Solar Cells in 2021 [105].

Sections 5.2 and 5.3 is based on the paper [104] to which Brett Hallam, Anastasia Soeriyadi, and Chukwuka Madumelu from the University of New South Wales (UNSW) have contributed. Robby Peibst, Felix Haase, Jan Krügener, and the author designed the first experiments, which were developed further by the author. The

author performed and evaluated the PCD and C - V measurements and executed the firing experiments. Nils Folchert did the calculations using the MarcoPOLO model [73] he developed [136]. Martin Rudolf and Chukwuka Madumelu performed the FTIR measurements, and Bettina Wolpensinger took the SEM images. The author evaluated and interpreted the results and developed a hypothesis for understanding them.

Section 5.4 is based on the peer-reviewed paper [105] resulting from a successful collaboration with Steve P. Harvey, Paul Stradins, David L. Young, and Caroline Lima Salles de Souza from the National Renewable Laboratory, Denver, Colorado (NREL). Steve P. Harvey performed the ToF-SIMS measurements. Nils Folchert did the calculations using the MarcoPOLO model. The author designed the experiments and evaluated and interpreted the results. In a discussion with Robby Peibst, Paul Stradins, Steve P. Harvey, and David Young, the author developed a hypothesis for explaining the results.

5.1 Experimental details

This section presents the experimental details of the preparation of the samples used in the following experiments. In addition, the experimental conditions of the firing process are described.

5.1.1 Sample preparation

The samples described in the following are used to characterize the firing stability via PCD, C - V , and SIMS measurements that are carried out in this work. The sample groups described in the following essentially differ in the interfacial oxide and the dielectric capping layers applied.

For all experiments, we prepare symmetrical test samples on p -type (boron-doped) Cz grown silicon, $20\ \Omega\ \text{cm}$ material. This resistivity allows for accurately determining the J_0 values [172]. All samples undergo a KOH-based saw damage removal process and an RCA cleaning sequence. We apply two different interfacial oxides (see Figure

5.1 for an overview of the various groups). On the primary set of samples, a wet-chemical oxide grows using dissolved ozone (O_3) in de-ionized water ($DI-H_2O$). The nominal thickness of (1.5 ± 0.2) nm is measured by ellipsometry on a reference sample. This process is similar to industrial cell sequences like POLO-IBC or POLO-BJ cells [173], [174].

Since classical POLO junctions with thin oxide are not suitable for the characterization by $C-V$ measurements due to emerging high leakage currents, one group of the samples receives a thicker oxide. On this set of samples, a 10 nm thick oxide grows by a dry thermal oxidation in a tube furnace at 900°C for 22 min. This thicker oxide suppresses leakage currents and thus allows the investigation of the $SiO_x/c\text{-Si}$ interface properties by $C-V$ measurements.

All samples are subsequently capped by a 220 nm-thick in situ n -type doped a-Si layer deposited at 580°C by low-pressure chemical vapor deposition (LPCVD). After the a-Si deposition, the samples are annealed and oxidized in a tube furnace for 30 min. Samples with a thermal interfacial oxide are annealed at 880°C . Samples with wet-chemical interfacial oxide are processed in two different batches. They are annealed at either 820°C or 860°C , as indicated in all respective figure captions. Subsequent annealing for 1 h at 550°C in N_2 atmosphere provides gettering of impurities [145], [146] and is applied to all samples. The oxide grown on the poly-Si during oxidation is removed using a 40 % HF solution. Afterward, the poly-Si thickness is about 120 to 140 nm depending on the annealing temperature and, thus, the oxidation rate.

Subsequently, the samples are capped by Al_2O_3 , SiN_y , or Al_2O_3/SiN_y stacks. Two sets of samples are coated with 100 nm-thick SiN_y layers with a refractive index of $n = 2.05$ by microwave-assisted plasma-enhanced chemical vapor deposition (MA-PECVD) or inductively coupled plasma (IC)-PECVD as stated respectively. Another set of samples receives a 10 nm-thick atomic layer deposited (ALD) Al_2O_3 -layer coating and is subsequently annealed at 425°C for 30 min in N_2 atmosphere. An additional set of the samples receives a stack of 10 nm Al_2O_3 plus 100 nm SiN_y from the IC-PECVD tool. Between the Al_2O_3 and the SiN_y deposition these samples are annealed (425°C , 30 min, N_2) if not stated otherwise. It should be noted that the sample sets described above were processed in three different batches.

A further group of samples (see Figure 5.2 for an overview) receives ALD Al_2O_3

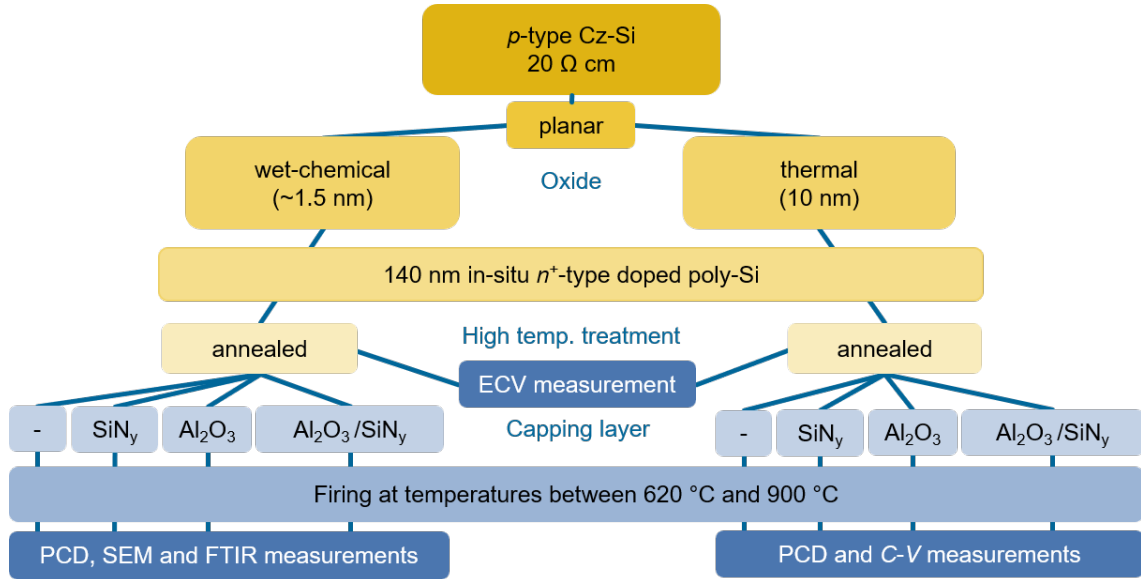


Figure 5.1: Overview of the investigated sample groups. This figure is adapted from Figure 1 in Ref. [104].

layer coatings of different thicknesses between 2 to 15 nm. Unlike the earlier samples, no annealing process is done after the Al_2O_3 deposition. The deposition of a 100 nm-thick SiN_y layer from the MA-PECVD tool follows directly afterward with a refractive index of $n = 2.05$ (chamber temperature of $500\text{ }^\circ\text{C}$). Another difference is that the usually used H_2 process gas is replaced by D_2 gas during SiN_y deposition to incorporate deuterium into the SiN_y layer. Using deuterated SiN_y allows to separate hydrogen from different sources in the layer stack in SIMS and to take advantage of the lower SIMS detection limit for deuterium [175]. The other process gases, ammonia (NH_3) and silane (SiH_4) are not replaced so that both hydrogen and deuterium are present in the SiN_y layers.

C-V-sample preparation

The preparation of samples for C - V measurements, first of all, includes the removal of existing dielectric layers in a 40% HF solution. Samples dedicated for conductance measurements receive full-area thermal evaporation of aluminum to a thickness of $10\text{ }\mu\text{m}$ on the rear side. The other side is locally metalized with thermally evaporated aluminum through a shadow mask with circular pads with a size of about $(0.46 \pm 0.06)\text{ mm}^2$. Finally, on the rear side, laser-fired contacts (LFCs) [176]

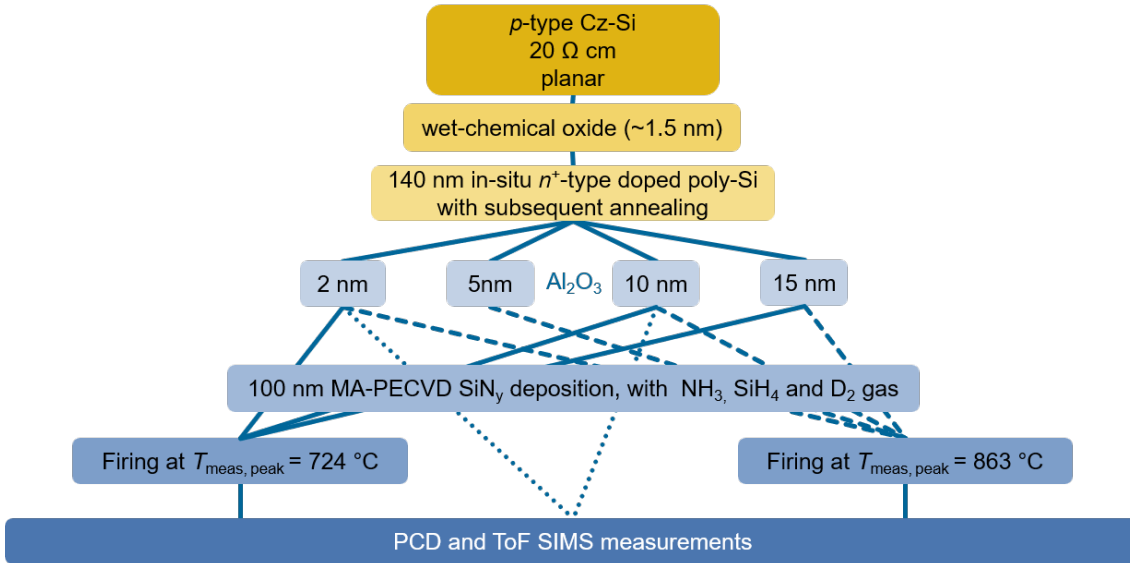


Figure 5.2: Overview of the sample groups investigated with TOF-SIMS to determine the hydrogen content.

provide an ohmic contact from the base to the rear side metallization surpassing the POLO junction. Subsequently, the POLO junction between the pads is removed by reactive ion etching. Figure 5.3 schematically shows the structure of those samples.

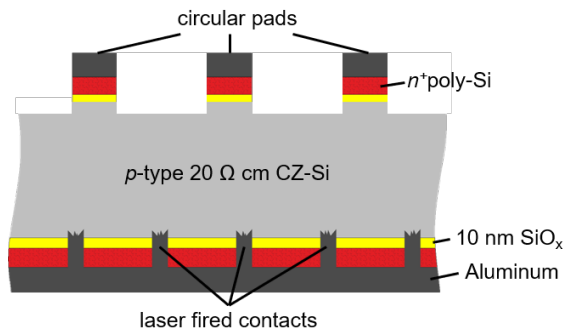


Figure 5.3: Schematic illustration of samples prepared for C - V measurements. This figure is adapted from Figure 3 in Ref. [104].

On two samples, circular pads with areas of 0.09 mm^2 and 0.24 mm^2 are defined by photolithography as a reference to cross-check the adequacy of the metallization through shadow masks. Comparison of C - V measurements of all three pad types provides an uncertainty interval of 0.1 mm^2 for the area of the (standard) pads evaporated through shadow masks.

5.1.2 The firing process

All samples are fired in an industrial infrared conveyor-belt furnace (DO-FF-8.600-300, Centrotherm). The chosen temperature profile is typical for the firing of metallization pastes [177]. During the following experiments, the set peak temperatures ($T_{\text{set,peak}}$) are varied between 620 °C and 900 °C and if not mentioned otherwise a conveyor belt speed (v_{belt}) of 5.6 m/min is used. Figure 5.4 shows three examples of recorded temperature profiles.

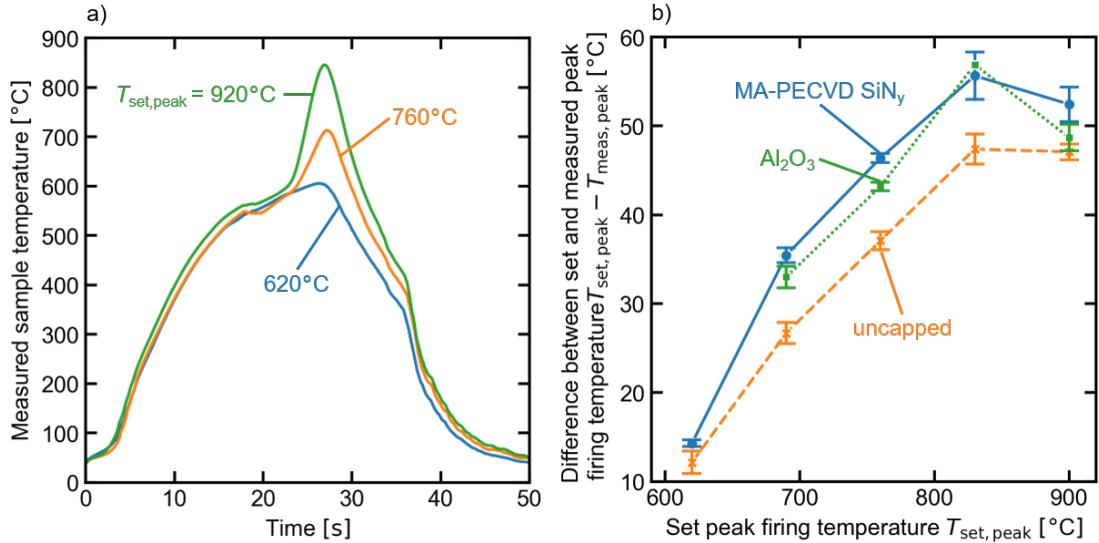


Figure 5.4: (a) Measured wafer temperature profiles during firing of uncapped samples. The temperature is tracked using a DATAPAQ Insight Oven Tracker. (b) Difference between the set and the measured peak temperatures as a function of $T_{\text{set,peak}}$ for samples with different capping layers. The error bars denote the 95 % confidence interval of measurements on three different wafers, respectively. This figure is adapted from Figure 2 in Ref. [104].

Those actual temperature profiles are monitored by fixing a temperature probe on a wafer and connecting it to a DATAPAQ Insight Oven Tracker for data recording. As can be seen from Figure 5.4(b), the actual measured peak temperatures are smaller than the set peak temperatures and depend on the capping layer and the set peak temperature. The difference is increasing from 15 K to about 55 K with increasing $T_{\text{set,peak}}$ from 620 °C to 900 °C for samples capped with Al₂O₃ or SiN_y. For uncapped samples, the actual measured temperature lies about 12 K to 45 K beneath the set peak temperature.

5.2 Firing stability of uncapped n^+ POLO junctions

In this section, the impact of the firing process for contact formation in screen printed cells is investigated for uncapped n^+ POLO samples. Therefore the evolution of the recombination current density and interface state density are analyzed.

5.2.1 Recombination current density

Figure 5.5 shows the recombination current density of samples with (a) an approximately 1.5 nm-thick wet-chemical interfacial oxide and (b) a 10 nm-thick thermally grown oxide, both measured before and after a firing process at different $T_{\text{set,peak}}$. All samples shown here were neither capped by a dielectric layer nor hydrogenated by forming gas anneal. The initial J_0 values after annealing are affected by the two different oxides. While the samples with thin wet-chemical oxide reach acceptable J_0 values of (5 ± 1) fA/cm², the passivation quality of the samples with the thermal oxide is relatively low with J_0 between 20 to 40 fA/cm². One explanation could be the lower in-diffusion of P into the wafer through the thicker oxide, which is observed in ECV measurements, as shown in Figure 5.6. In turn, the strong in-diffusion in the case of the thinner oxide leads to a further reduced minority carrier density at the interface, improving the surface passivation. This passivation could overcompensate for the increase in J_0 due to the increased Auger recombination caused by the in-diffusion. In addition, thicker oxides shield the electric field between the poly-Si and c-Si more strongly and further reduce the field-effect from high poly-Si dopant concentration [136].

The firing negatively influences the passivation quality for both sets of samples, which, however, look different in detail. Figure 5.5 shows the J_0 values of the uncapped samples with (a) the wet-chemical oxide and (b) the thermal oxide. The J_0 values of the wet-chemical oxide samples show a sharp increase with increasing firing temperature. The samples with 10 nm thermal oxide show an even stronger rise in J_0 , which is especially strong for temperatures between 620 to 760 °C. Above this, J_0 saturates at about 1000 fA/cm².

Altogether, uncapped and as annealed n^+ POLO junctions with wet-chemically and thermally grown oxides investigated in this experiment reveal poor stability against

5 Firing stability of n^+ POLO junctions

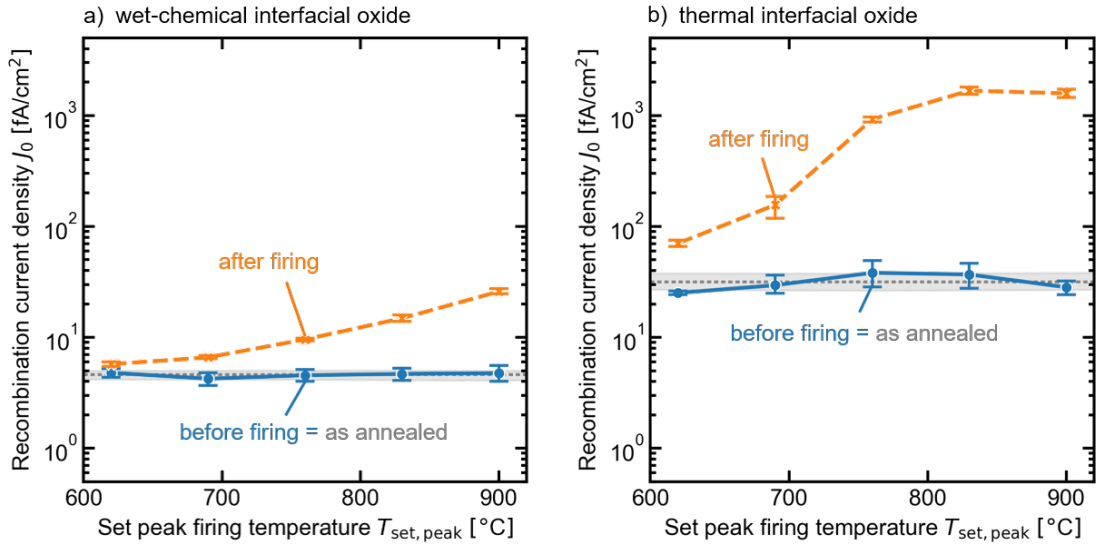


Figure 5.5: Recombination current density J_0 of (a) samples with a 1.5 nm wet-chemical oxide, annealed at 860 °C and (b) a 10 nm thick thermal oxide, annealed at 880 °C. Blue data points are measured before firing, and orange data points are measured after firing. The gray interval depicts the results directly after annealing measured on all samples from the respective set of samples (upper/lower quartile). The error bars denote the 95 % confidence interval of measurements on five different parts of two different wafers, respectively. This figure is reprinted from Figure 5 in Ref. [104].

a commonly used industrial firing process.

As shown in Figure 5.7 the passivation quality can almost be restored by a post-firing annealing at 400 °C in N₂ atmosphere for 30 min. Due to this annealing step J_0 decreases from (160 ± 260) fA/cm² after firing to (11 ± 2) fA/cm² which is in the same order of magnitude as before firing where J_0 is (6 ± 1) fA/cm².

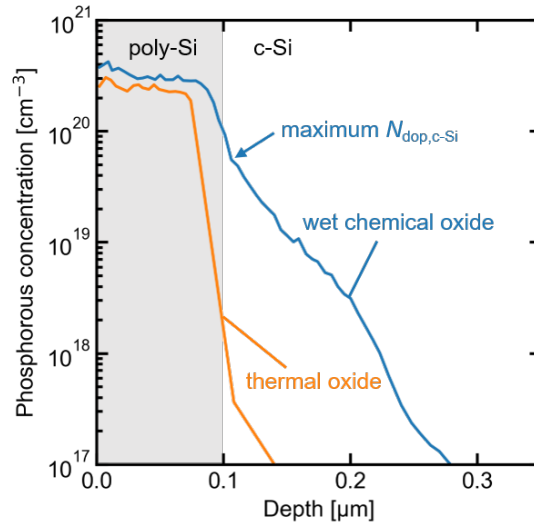


Figure 5.6: ECV profile measurements of n -type POLO samples with a 1.5 nm-thick wet-chemical interfacial oxide annealed at 860 °C and an 10 nm-thick thermal oxide annealed at 880 °C. This figure is adapted from Figure 6 in Ref. [104].

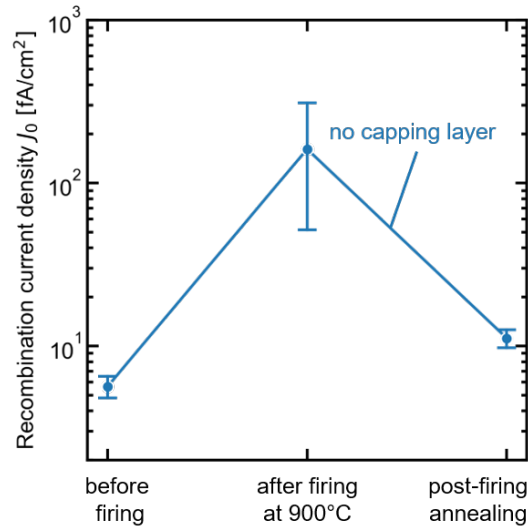


Figure 5.7: Recombination current density J_0 of samples with a thin wet-chemical interfacial oxide, annealed at 820 °C. The samples were measured directly before firing, after firing at $T_{\text{set,peak}} = 900$ °C and finally after a subsequent annealing process at 425 °C for 30 min in N_2 atmosphere. The error bars denote the 95% confidence interval of five measurements on different parts of two wafers, respectively. This figure is adapted from Figure 12 in Ref. [104].

5.2.2 Interface state density

On the samples with the 10 nm-thick thermal oxide, C - V measurements are conducted and analyzed with the conductance method to obtain the interface state density D_{it} at the $\text{SiO}_x/\text{c-Si}$ interface.

Since this method does not allow leakage currents through the oxide, all samples analyzed by this method exhibit a 10 nm-thick thermal oxide. Figure 5.8 shows the parallel conductance G_p/ω as a function of angular frequency ω for different applied gate voltages. The various peaks measured at different applied gate voltages correspond to different energetic positions in the bandgap ($E - E_v$). The height of the peaks increases with increasing D_{it} , indicating an increase in D_{it} with increasing set peak firing temperature from Figure 5.8(a) to (c).

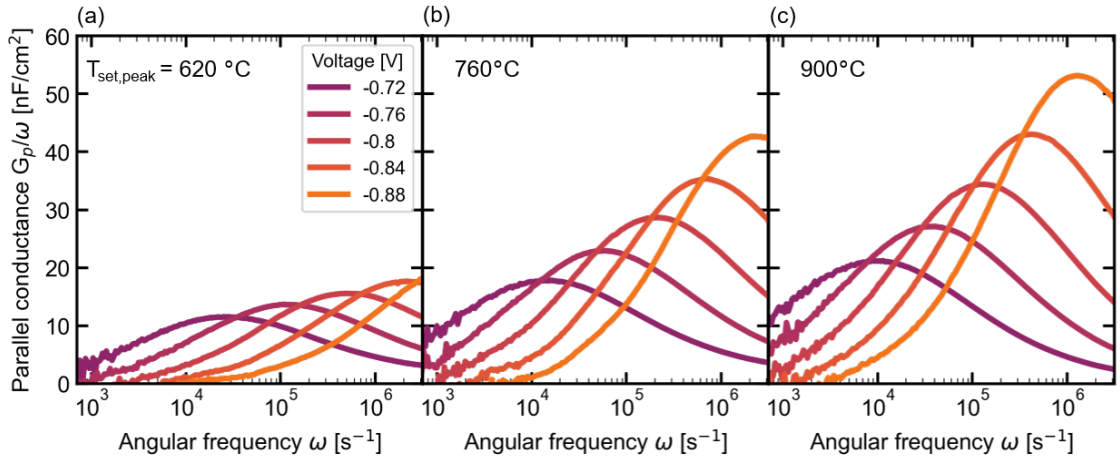


Figure 5.8: Parallel conductance G_p/ω as a function of angular frequency ω for different gate voltages as measured on uncapped samples with a thick thermal oxide fired at (a) 620 °C, (b) 760 °C and (c) 900 °C. This figure is adapted from Figure 13 in Ref. [104].

Figure 5.9(a) shows the D_{it} values from the lower part of the band gap ((0.3 ± 0.1) eV), determined from the C - V measurements, plotted over $T_{set,peak}$. Before firing D_{it} is $(1 \pm 1) \times 10^{11} \text{ cm}^{-2} \text{ eV}^{-1}$ and rise from $(3 \pm 1) \times 10^{11} \text{ cm}^{-2} \text{ eV}^{-1}$ when fired at 620 °C to $(7 \pm 1) \times 10^{11} \text{ cm}^{-2} \text{ eV}^{-1}$ when fired at 900 °C, where the D_{it} shows no saturation behavior in contrast to J_0 (see Figure 5.5(b)). The determined values are a factor of 6 smaller than the values of O’Sullivan et al. [178] measured after firing on samples with just a thermal oxide and no poly-Si.

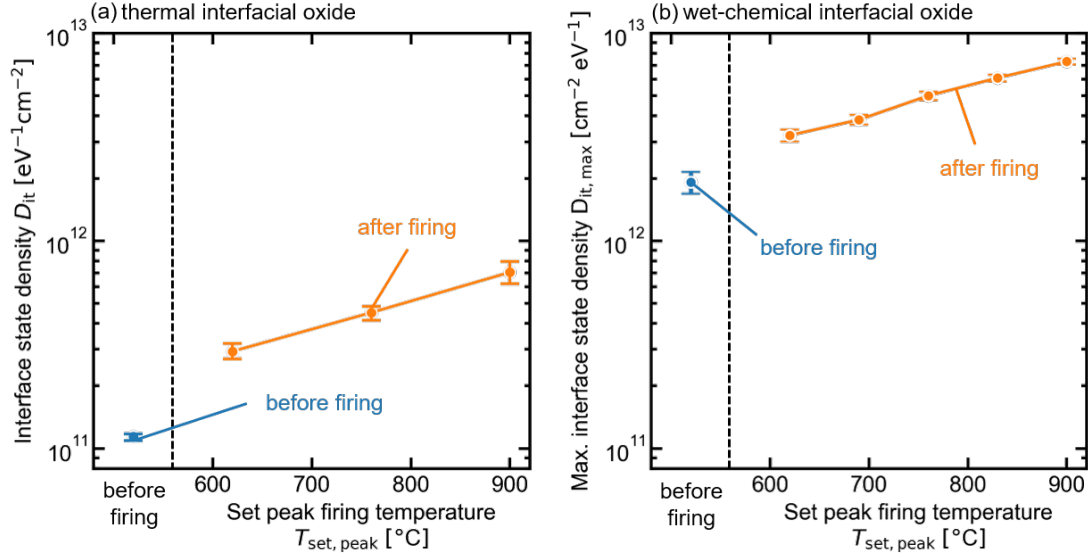


Figure 5.9: Interface state density as a function of firing $T_{\text{set,peak}}$ (a) determined from C - V measurements and (b) deduced from a regression of the MarcoPOLO model to the measured J_0 values using $D_{it,\text{max}}$ as the only free parameter. The error bars in (a) denote the 95 % confidence interval of four measurements on two different wafers, respectively. The error bars in (b) denote the standard deviation of the calculated values determined by a Monte-Carlo analysis.

Samples with wet-chemical oxide show too large leakage currents to deduce the D_{it} from C - V measurements. The defect density of these samples (see Figure 5.9(b)) is instead deduced from a regression of the MarcoPOLO model by Folchert et al. [73] to the measured J_0 values using $D_{it,\text{max}}$ as the only free parameter. Therefore a capture-cross-section of holes of $4.2 \times 10^{-18} \text{ cm}^2$ leading to the same results as the energy-dependent hole capture-cross-sections reported by Aberle et al. [179] is assumed. In addition, a Monte-Carlo simulation with 500 samples per measurement is performed varying the following parameters: the oxide thickness as $d_{\text{ox}} = (1.5 \pm 0.2) \text{ nm}$, the poly-Si doping concentration as $N_{\text{dop,poly}} = (3.0 \pm 0.1) \times 10^{20} \text{ cm}^{-3}$ and the c-Si peak doping concentration as $N_{\text{dop,c-Si}} = (4.4 \pm 1.0) \times 10^{19} \text{ cm}^{-3}$ (see Figure 5.6). The measured J_0 values are varied with a constant uncertainty range of 20%. The resulting mean defect density and standard deviation of the obtained $D_{it,\text{max}}$ values are shown in Figure 5.9(b).

Before firing the interface state density of these as-annealed, uncapped samples is $(2.0 \pm 0.3) \times 10^{12} \text{ cm}^{-2} \text{ eV}^{-1}$. Compared to the samples with a thermal oxide that show D_{it} values of $(1.1 \pm 0.1) \times 10^{11} \text{ cm}^{-2} \text{ eV}^{-1}$, these results are at least one order of

magnitude higher. However, they are consistent with values reported for comparable thin oxides [73], [130]. The strong dopant diffusion into the wafer in these samples provides for passivation. Thus, despite the higher D_{it} , the very low J_0 values are reasonable.

Firing then leads to a substantial increase in D_{it} to about $3 \times 10^{12} \text{ cm}^{-2} \text{ eV}^{-1}$ to $7 \times 10^{12} \text{ cm}^{-2} \text{ eV}^{-1}$, showing an exponential dependence between D_{it} and the set firing temperature. This trend fits the results of the samples with the 10 nm-thick thermally grown interfacial oxide.

The D_{it} of the fired, uncapped n^+ POLO samples increases strongly with the set peak firing temperature. Such dependence has been attributed to the temperature-induced dissociation of hydrogen from $\text{SiO}_x/\text{c-Si}$ interfaces [180], [181]. Dissociation of hydrogen from a bound state that passivates an interface defect to an unbound state that activates the corresponding defect can be described by the following rate equation:

$$\frac{\partial N_{it}}{\partial t} = k \cdot (N_0 - N_{it}(t)) \quad (5.1)$$

where k is the interface defect generation rate. N_0 is the number of the initially “passivated” inactive species at the interface, e.g., Si-H bonds, and $N_{it}(t)$ is the number of electrically active interface states, e.g., dangling Si bonds. With respect to a hydrogen desorption process, the assumption made for this equation is that the amount of free hydrogen at the interface and in the poly-Si is small, which is a reasonable assumption after the previous high-temperature annealing process. Under this assumption, the process is limited only by the forward reaction, i.e., the breaking of Si-H bonds.

Since the recombination current density after annealing/before firing is 30 fA/cm^2 and increases dramatically after firing, we can also assume that the amount of initially broken Si-H bonds $N_{it}(t)$ at the interface is minimal compared to the breaking of bonds during firing. This yields the following equation:

$$\frac{\partial N_{it}}{\partial t} = k \cdot N_0. \quad (5.2)$$

5.2 Firing stability of uncapped n^+ POLO junctions

For a defined annealing time t , the equation can be written as:

$$N_{\text{it}} = k \cdot N_0 \cdot t. \quad (5.3)$$

Thus, the Arrhenius equation gives the rate of a thermally activated process:

$$k = A \cdot \exp\left(\frac{-E_A}{k_B T}\right). \quad (5.4)$$

We further suppose that only one process, e.g., hydrogen dissociation, is responsible for the change in D_{it} . In that case, the change in H concentration at the interface is proportional to the change in the interface state density. Thus, we may write:

$$N_{\text{it}} \propto D_{\text{it}} \propto A \cdot \exp\left(\frac{-E_A}{k_B T}\right) \quad (5.5)$$

so that the slope of the Arrhenius plot of $\ln(D_{\text{it}})$ versus $1/k_B \cdot T$ gives the activation energy of this process.

Figure 5.10 shows an Arrhenius law plot of D_{it} determined (a) by C - V measurements on samples with a thermal oxide and (b) by MarcoPOLO model regressions on samples with a wet-chemical oxide. A good linear fit of the data points is possible and yields an activation energy of (0.30 ± 0.03) eV in Figure 5.10(a) and (0.29 ± 0.01) eV in Figure 5.10(b). This result indicates an underlying thermally activated process that is possibly similar for the two oxides.

However, the energy for spontaneous desorption of hydrogen from $\text{Si}_3 \equiv \text{Si-H}$ in the literature ranges from 1.4 to 2.64 eV [182], [183]. The experimental result of (0.30 ± 0.03) eV is obviously well below these energies.

Moreover, it is questionable if the concentration of Si-H bonds at the $\text{SiO}_x/\text{c-Si}$ interface is still sufficient before firing for a significant increase of D_{it} during firing, because the samples were previously subjected to a much higher thermal budget during annealing. Secondary ion mass spectroscopy (SIMS) measurements showed that most of the hydrogen already diffuses out during high-temperature annealing [182], [184], [185].

Thus, this result supports the hypothesis that another mechanism might be responsible for the increase of D_{it} , and the out-diffusion of hydrogen is not the primary

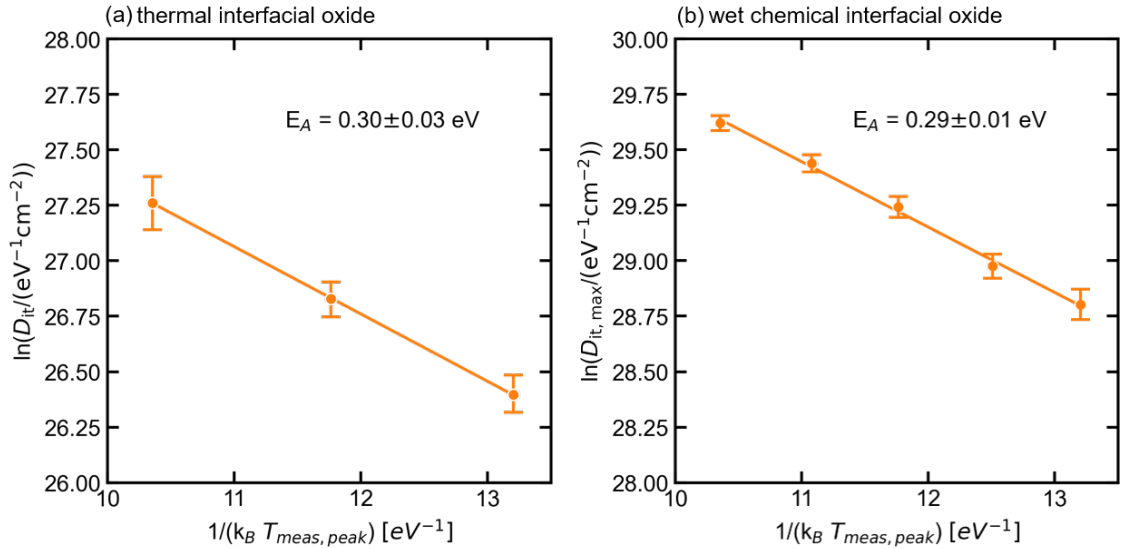


Figure 5.10: Arrhenius plot of the reaction rate for the increase in (a) D_{it} for samples with thermal interfacial oxide determined from C - V measurements and (b) $D_{it,max}$ for samples with wet-chemical interfacial oxide determined using the MarcoPOLO model upon firing at $T_{meas,peak}$. This figure (a) is adapted from Figure 15 in Ref. [104].

defect formation process during the firing of these samples.

As another hypothesis for the increase of D_{it} , the breaking of unstrained Si-O bonds can also not be explained with an activation energy of 0.3 eV [182]. Since the preceding tube furnace annealing step between 820 °C and 880 °C in our case or a dopant diffusion step implies a much higher thermal budget and, at the same time, leads to improved surface passivation, the temperature budget alone cannot be the reason for the observed deterioration of the passivation quality during firing.

Due to the rapid temperature ramp up and cool down, which is orders of magnitude larger during firing than during the annealing process in the tube furnace, the crucial point could, however, be the rate of temperature change.

5.2.3 Variation of the conveyor belt speed

The hypothesis that the rate of temperature change plays an essential role in the passivation's stability against a high-temperature process is tested in an additional experiment. The set peak temperature of the firing furnace is adjusted for four

different belt speeds v_{belt} (2.5, 3.4, 5.6 and 7.2 m/min) so that the same actual peak temperature $T_{\text{meas,peak}}$ is reached for each belt speed. Two experiments of this sort are conducted, one with an actual peak temperature of $T_{\text{meas,peak}} = 724^\circ\text{C}$ and one with a $T_{\text{meas,peak}} = 860^\circ\text{C}$.

In Figures 5.11 the measured temperatures and the temperature change rates as functions of time are shown for the four different v_{belt} . Figure 5.11(a) shows the whole temperature profiles while Figure 5.11(b) shows an excerpt of data above 500°C . For the peak temperature of 724°C , the maximum temperature change rate occurring near the peak temperature changes from $(23 \pm 5) \text{K/s}$ to approx. $(53 \pm 5) \text{K/s}$ with increasing v_{belt} during heating. The minimal temperature change rates of $(-45 \pm 5) \text{K/s}$ and $(-64 \pm 5) \text{K/s}$ are reached during cooling for belt speeds of 2.5 m/min and 7.2 m/min, respectively. At a peak temperature of 863°C , the maximum heating rate at $v_{\text{belt}} = 7.2 \text{m/min}$ is $(120 \pm 5) \text{K/s}$ and the maximum cooling rate is $(-93 \pm 5) \text{K/s}$.

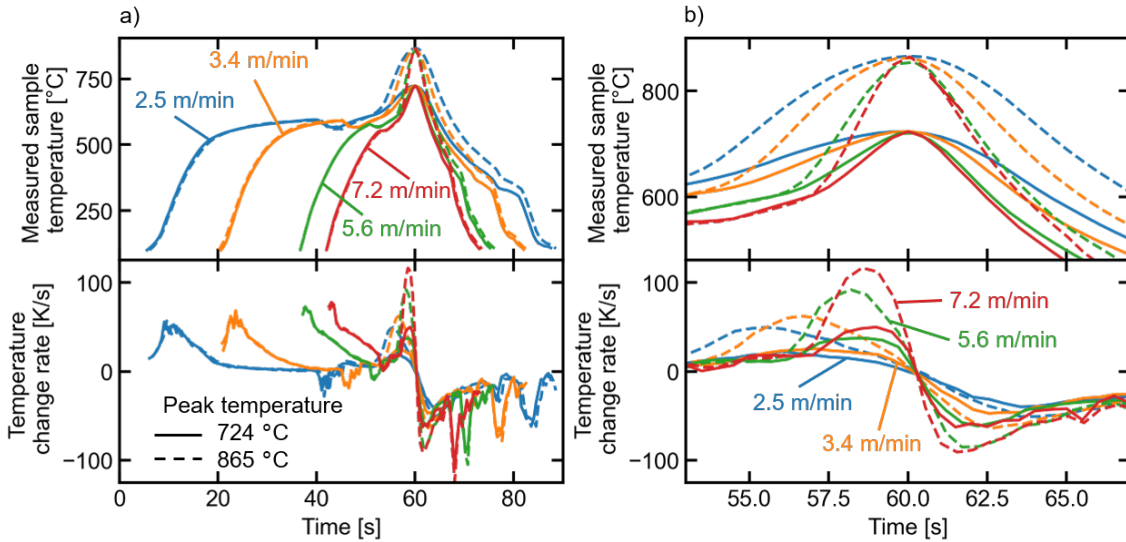


Figure 5.11: Measured sample temperatures (upper half) and respective temperature change rates (lower half) during firing at different conveyor belt speeds and set peak firing temperatures of uncapped POLO samples. The solid lines represent firing with $T_{\text{meas,peak}}$ of 724°C and the dashed lines with $T_{\text{meas,peak}} = 865^\circ\text{C}$.

Figure 5.12 shows the resulting data from PCD measurements. The large error bars originate from large inhomogeneities across the wafer. The samples shown in blue were fired at an actual peak temperature of 724°C . Here the lifetime, iV_{oc} , and J_0 values stay almost constant at the respective positions of the wafer up to

5 Firing stability of n^+ POLO junctions

$v_{\text{belt}} = 5.6$ m/min. For a speed of 7.2 m/min, a strong decrease in the lifetime and iV_{oc} and a simultaneous increase in J_0 to (160 ± 120) fA/cm² is observed. The samples fired at 863 °C show a more continuous trend. As shown in Figure 5.12(a), the lifetime decreases from 0.75 ± 0.30 to 0.35 ± 0.25 ms with increasing belt speed. At the same time, the iV_{oc} decreases from 660 ± 20 to 640 ± 20 mV, and the J_0 increases from 80 ± 40 to 160 ± 100 fA/cm². These results indicate a dependence on the actual peak firing temperature and the belt speed, which are associated with certain temperature change rates. Regarding the heating rates, a decrease of iV_{oc} and τ_{eff} can only be stated at heating rates above (50 ± 5) K/s. For the cooling rates, no such threshold can be found.

This finding supports the hypothesis that the temperature change rate significantly influences surface passivation degradation during firing. Lowering the belt speed can thus mitigate the defect formation process, which is demonstrated by the increase of iV_{oc} with decreasing belt speed in Figure 5.12.

Considering equation 5.3 in terms of this experiment, the time t that the samples experience a temperature close to the peak temperature increases as the belt speed decreases. Since the peak temperature itself is held constant, k should be constant in this case too. This would result in a proportional relationship between D_{it} and t , suggesting an increase in D_{it} with decreasing belt speed. However, as shown in Figure 5.12, the opposite is true, again suggesting that not the thermal budget but the temperature change rate causes an increase of D_{it} during firing.

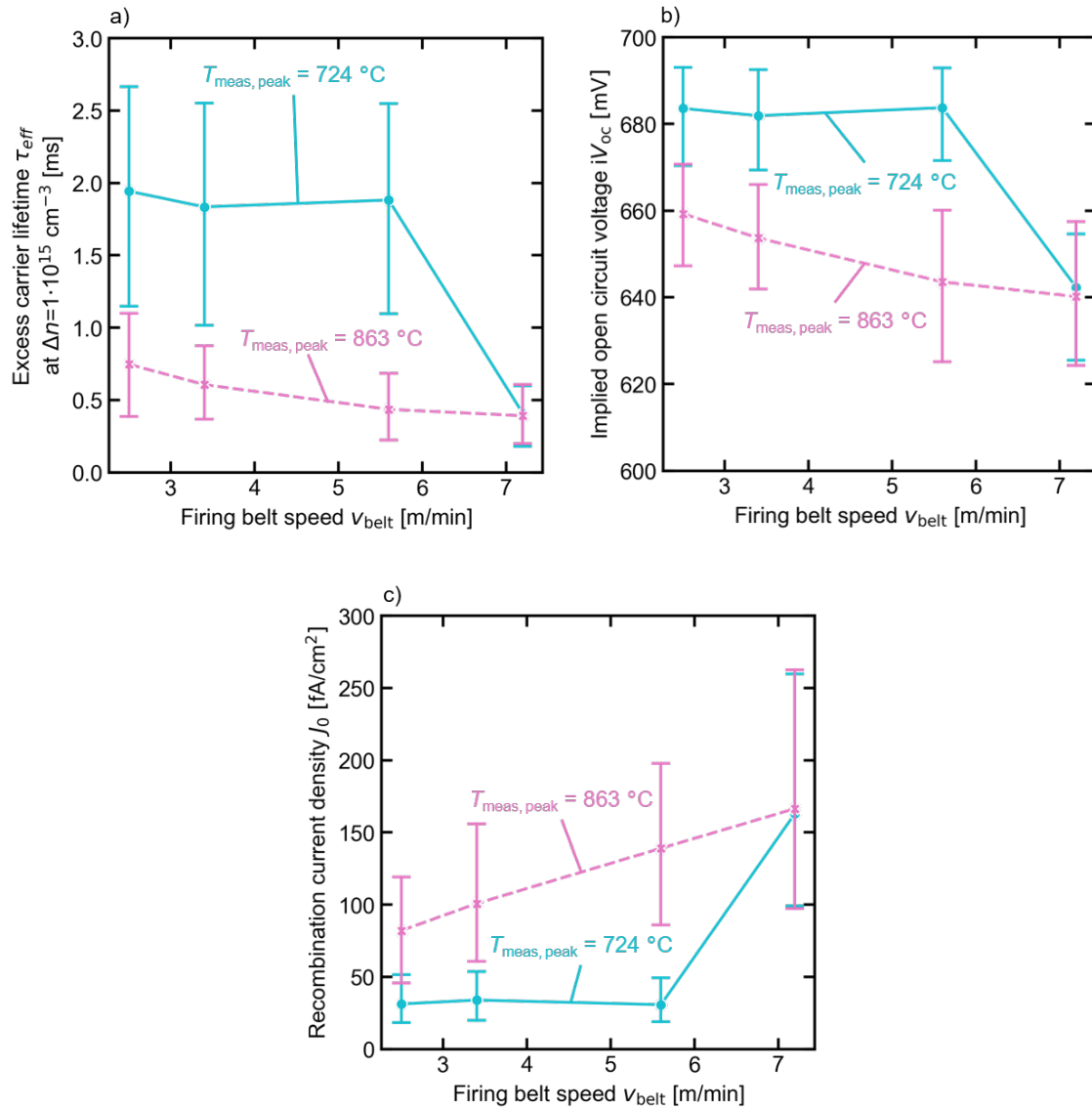


Figure 5.12: (a) Excess carrier lifetime, (b) iV_{oc} and (c) J_0 as a function of the conveyor belt speed for samples with a 1.5 nm wet-chemical oxide, annealed at 820 °C, that are fired at an actual peak temperature of $(724 \pm 5) \text{ }^\circ\text{C}$ (solid lines) or $(863 \pm 5) \text{ }^\circ\text{C}$ (dashed lines). The error bars denote the 95% confidence interval of measurements on five different positions on one (for $T_{\text{meas, peak}} = 724 \text{ }^\circ\text{C}$) or two (for $T_{\text{meas, peak}} = 863 \text{ }^\circ\text{C}$) different wafers, respectively.

5.2.4 Thermal expansion at the c-Si/SiO_x/poly-Si interface

The impact of the temperature change rates on interface defect formation hints toward a mechanical cause of the increase of D_{it} during firing. A possible explanation for the defect formation becomes apparent when looking at the coefficients of thermal expansion (CTE) of the materials involved in the POLO junctions. As shown in Table 5.1, the CTE of c-Si and poly-Si is more than five times as high as the CTE of thermally grown SiO_x. The difference in CTE between SiO_x and c-Si even increases with increasing temperature from $(3.0 \pm 0.5) \times 10^{-6} \text{ K}^{-1}$ at 50 °C to $5.8 \times 10^{-6} \text{ K}^{-1}$ at 850 °C [186]. The value of SiO_x given in Table 5.1 has been reported for a 330 nm thick thermal oxide, which is identical to that of bulk SiO_x ($0.5 \times 10^{-6} \text{ K}^{-1}$ [187]). However, it has to be noted that there is no reported data on how CTE develops for thinner films like the 1.5 nm and 10 nm of the samples under investigation here.

A significant difference in CTE of SiO_x compared to c-Si and poly-Si would, however, lead to thermally induced stress during heating and cooling. Due to the mismatch in CTE, the stress at the interface increases with increasing temperature. In slow processes such as annealing in a tube furnace, the stress is relieved by the viscous flow of the thin oxide, which is possible due to its amorphous nature [188], [189]. However, above a specific temperature change rate, the viscous flow might be too slow to compensate for the stress, so it might be released by breaking strained Si-O bonds. The Si-O bonds will be strained by the forces exerted by the poly-Si and c-Si, and thus a defect formation due to the breaking of Si-O bonds becomes much more likely, as shown by El-Sayed et al. [190].

It should also be mentioned that the type of oxide and the deposition conditions of the poly-Si strongly influence the firing stability. In this work, it is shown that firing samples with 1.5 nm wet-chemically grown oxide leads to a significantly lower increase in J_0 than for samples with 10 nm thermally grown oxide. Kang et al. could also show that the thermal oxide with a thickness of 1.5 nm performed inferior to a 1.4 nm thick chemical oxide [109]. Stöhr et al. [58] moreover observed that samples with PECVD n -type poly-Si and a PECVD SiO_z N_y interfacial oxide show a significantly improved firing stability. In contrast, a comparison of LPCVD and PECVD poly-Si, both with chemically grown interfacial oxide and a SiN_y capping layer by Kang et al. [109], showed a similar increase in J_0 due to firing. Increasing the deposition temperature of LPCVD poly-Si, however, showed to have a negative

Table 5.1: Coefficients of thermal expansion at room temperature from literature.

Materials	Coefficients of thermal expansion [10^{-6} K^{-1}]	References
Bulk c-Si	2.6	[186], [191]
poly-Si film	2.7 to 2.9	[192], [193]
thermal SiO_2 film	0.5	[187]
PECVD $\text{SiO}_x \text{N}_y$ film	-4 to 8	[194]
sputtered $\text{SiO}_x \text{N}_y$ film	-1.2 to 2.4	[195]

effect [109].

Overall, these observations show that the POLO junctions' detailed manufacturing conditions can significantly influence the firing stability. The resulting changes in properties, such as crystallinity and porosity, can influence the respective CTE. Thus, the resulting changes in firing stability could be explained in the framework of the abovementioned hypothesis.

A further amplifying factor for stress at the interface could relate to the high doping of the poly-Si layers and the heating by IR radiation during firing. The high poly-Si doping concentration leads to a substantial FCA of IR radiation and hence stronger heating of the poly-Si layer than the rest of the wafer. This effect could lead to a stronger expansion of the poly-Si film than the c-Si bulk and thus could cause additional stress at the interface. Unfortunately, studying such an effect on the surface temperature is not easily possible due to the small thickness of the poly-Si layer compared to the bulk. However, a significant effect of the level of bulk and emitter doping on the sample temperature reached in an IR furnace was shown by Bende et al. [196].

5.2.5 Summary and discussion of Section 5.2

The key findings of experiments on the firing stability of uncapped poly-Si junctions shown in this section are:

- The passivation quality of uncapped POLO junctions without a hydrogen-containing capping layer is not stable against industrial firing processes.

5 Firing stability of n^+ POLO junctions

- The D_{it} of POLO junctions increases exponentially with the firing temperature between 620 °C and 900 °C.
- The activation energy of this defect formation reaction is too low to account for a possible out-diffusion of hydrogen or directly thermally induced breaking of Si-O bonds.
- Higher belt speeds and a thus higher rates of temperature change negatively affect the passivation quality if a threshold heating rate of 50 K/s is surpassed
- The passivation quality can be significantly improved by post-firing annealing at 400 °C

This chapter shows that the stability toward a firing process is not intrinsically given for poly-Si contacts. Despite the existing stability against high temperatures in general and annealing processes in the furnace in particular, it has been shown in this work and by other authors [79], [96], [103] that firing can deteriorate the passivation quality.

Other groups also observe the emergence of defects during rapid thermal annealing (RTA) processes at c-Si/SiO_x interfaces, such as [178], [189], [197], and also with poly-Si/SiO_x/c-Si junctions [198]. In these papers, the conclusion has been partly drawn that it is probably not a matter of the formation of defects but the dehydrogenation of already present defects. In contrast, Kamgar et al. [198] has shown that it also comes to the formation of defects during RTA when the initially present hydrogen already dissociated during long-term anneals in Ar at 900 °C prior to the RTA process. The above publications on the deterioration of the passivation quality during firing have not considered the influence of mechanical stress. However, a classification of the reported results in the picture of thermal stress-induced defect formation is unfortunately not possible as heating rates have not been reported.

Moreover, it has been shown that the resulting defects are most likely P_{b0} and P_{b1} centers [178], [197], [199], [200]. Due to the measurement method and sample doping, the D_{it} values measured in this work by conductance measurements originate from the lower half of the bandgap. The measured increase in D_{it} values lies between 0.21 eV and 0.35 eV and thus is in the range of the respective peaks of the P_{b0} and P_{b1} defects in the lower part of the bandgap.

Kurachi et al. [189] showed that for a longer RTA process of more than 30 s at

temperatures of above 750 °C, the D_{it} decreases as compared to temperatures below 750 °C where the D_{it} increases. The authors suspect viscous flow during long enough processing and at high enough temperatures to positively affect the D_{it} . Their finding is in accordance with the mitigating effect of lower belt speeds on the formation of defects seen in this work. This again supports the hypothesis that the evolution of D_{it} depends on a combination of the thermal budget and the thermal-mechanical stress within the POLO layer stack during firing.

5.3 Influence of different hydrogen-containing capping layers

Since the importance of hydrogenation for poly-Si passivating contacts has been shown by other groups in the last years [60], [79], [80], [82], [98], [101], [184], [201], this section investigates their temperature-dependent firing stability in combination with different hydrogen-containing capping layers. Therefore, different commonly used dielectric layers are considered. First, the influence of two different SiN_y coatings is compared. Then the capping with an Al_2O_3 layer is investigated, and a stack of $\text{Al}_2\text{O}_3/\text{SiN}_y$ is applied and evaluated.

5.3.1 SiN_y capping layer

Samples with thin wet-chemical oxide

Figure 5.13(a) shows the J_0 values of n^+ POLO samples with POLO-junctions based on a wet-chemical oxide, coated with 100 nm SiN_y with a refractive index of $n = 2.05$ from an IC-PECVD tool. The pre-firing state (denoted as “IC-PECVD SiN_y ,”) was measured after the deposition of SiN_y . Comparison with the state after annealing and before SiN_y deposition (gray dashed line) shows that the deposition of SiN_y in this tool leads to a minor improvement of passivation quality. However, firing at low temperatures up to 760 °C leads to a significant decrease in J_0 . Firing at $T_{\text{set,peak}} = 620$ °C even yields an improvement down to below 1 fA/cm² on the best sample. These samples exhibit an iV_{oc} of 745 mV and an effective lifetime of 8 ms. However, firing at set peak temperatures in the range from 760 °C to 900 °C, where typical

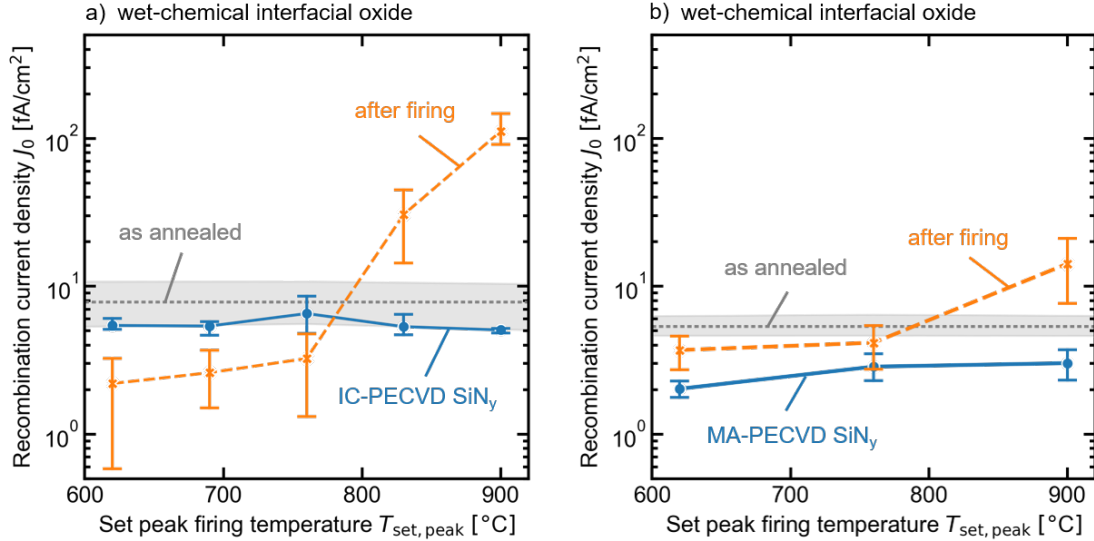


Figure 5.13: Recombination current density J_0 of samples with wet-chemical interfacial oxide, annealed at 820 °C with (a) a 100 nm IC-PECVD SiN_y capping layer or (b) a 100 nm MA-PECVD SiN_y capping layer. The results in Figure (b) are each obtained from two small samples measured at one position. Blue data points are measured before firing, and orange data points are measured after firing. The gray interval depicts the results directly after annealing measured on all samples from the respective set of samples (upper/lower quartile). The error bars in (a) denote the 95 % confidence interval of measurements on one position of three different wafers, respectively. The error bars in (b) denote the 95 % confidence interval of measurements on five different positions on two different wafers, respectively. This figure is adapted from Figure 8 in Ref. [104].

industrial firing processes are performed, results in a drastic increase in J_0 up to 100 fA/cm². Compared to uncapped samples, J_0 is lower at low firing temperatures, but at 830 °C and 900 °C, J_0 significantly exceeds the J_0 values of uncapped samples.

Additional samples are coated with a 100 nm-thick SiN_y layer with $n = 2.05$ from a microwave-assisted (MA) PECVD system. These results are shown in Figure 5.13(b). Here it can be seen from the J_0 values before firing that already the deposition of the SiN_y layer improves the passivation to J_0 values of about 2 to 3 fA/cm². The reason for this could be the higher deposition chamber temperature of about 500 °C in the MA-PECVD system compared to the IC-PECVD system with a deposition temperature of approx. 300 °C. However, already at low firing temperatures, the passivation quality decreases again. At $T_{\text{set,peak}} = 900$ °C, J_0 reaches (14 ± 9) fA/cm² and exceeds the values of about (5.4 ± 0.9) fA/cm² measured after

5.3 Influence of different hydrogen-containing capping layers

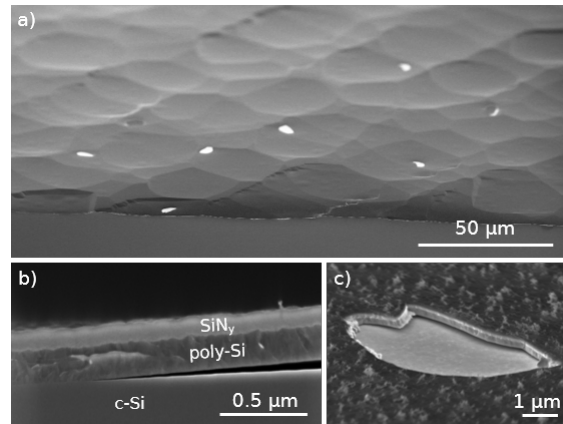


Figure 5.14: SEM images of a poly-Si sample with wet-chemical interfacial oxide and an IC-PECVD SiN_y capping layer fired at 900 °C. (a) shows a tilted overview over the sample surface, b) a cross-sectional view and c) a magnified view on a region with flaked-off POLO junction. This figure is reprinted from Figure 9 in Ref. [104].

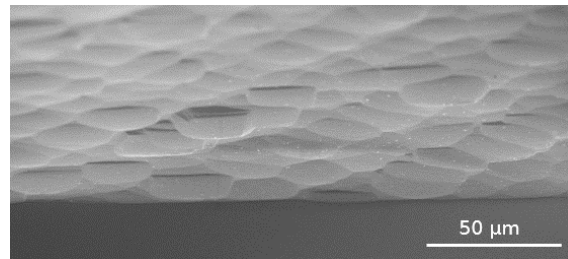


Figure 5.15: SEM images of a poly-Si sample with wet-chemical interfacial oxide and an MA-PECVD SiN_y capping layer fired at 900 °C.

annealing.

The Figures 5.15 and 5.14 show scanning electron microscope (SEM) images of samples with IC- and MA-PECVD SiN_y layers both fired at 900 °C. Figures 5.14(a)-(c) show local delamination of the poly-Si layer from the sample surface together with the IC-PECVD SiN_y layer. In Figure 5.14(c), even a large piece of the POLO junction with a size of about 10 μm² chipped off. In contrast to the group coated with IC-PECVD SiN_y, optical microscope and SEM images of the samples coated with MA-PECVD SiN_y in Figure 5.15 show no visible sign of blistering or interface delamination.

Figure 5.16 shows Fourier-transform infrared spectroscopy (FTIR) measurements of samples with both types of SiN_y capping layers. These results show that the

5 Firing stability of n^+ POLO junctions

IC-PECVD films contain significantly more hydrogen after deposition ($(19 \pm 4)\%$) than the MA-PECVD films ($(5 \pm 1)\%$), which could be the reason why blistering only occurs on the IC-PECVD samples.

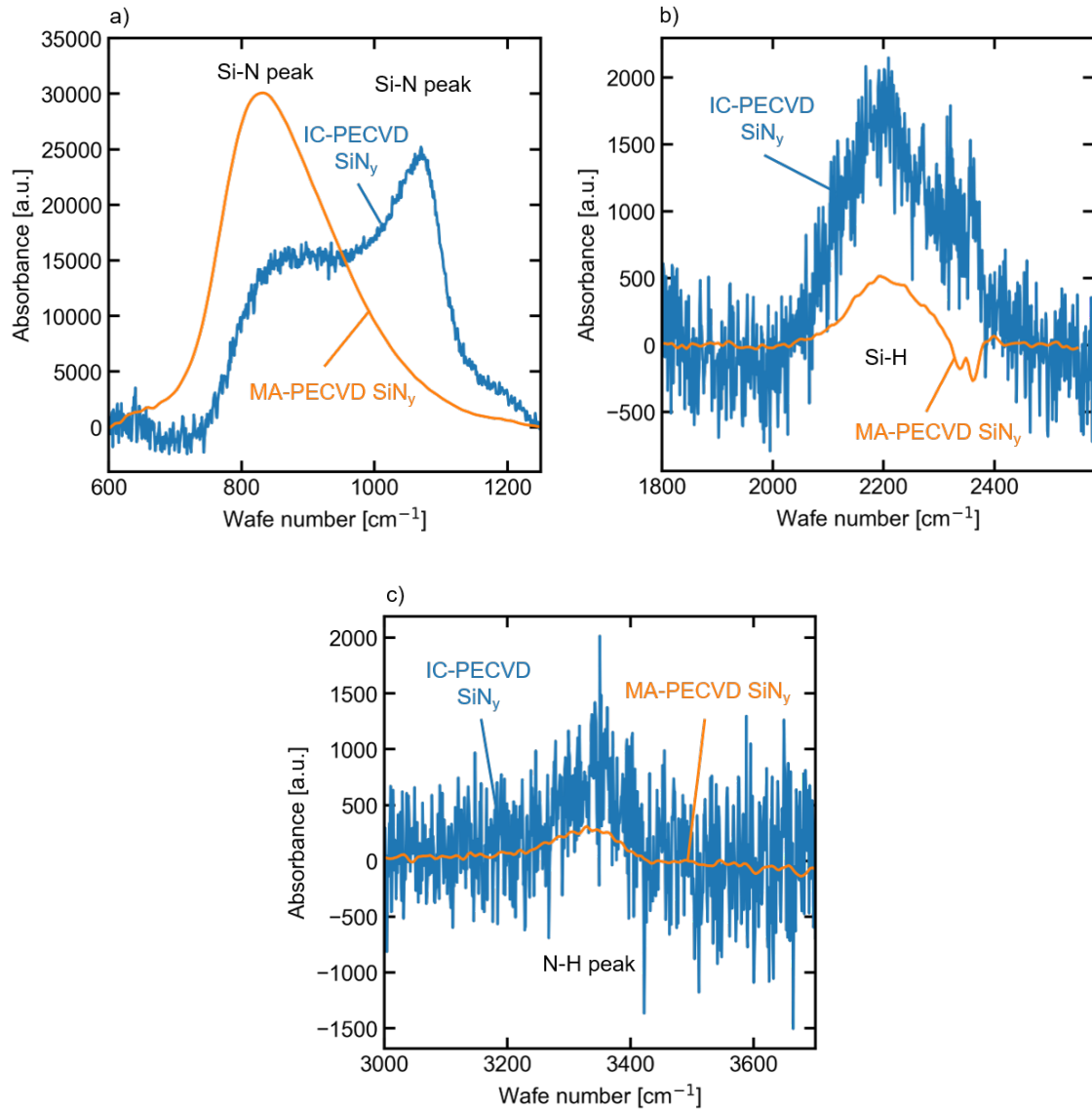


Figure 5.16: FTIR absorbance spectra captured from an n^+ poly-Si/ SiO_x / c -Si sample with an IC-PECVD SiN_y capping layer (blue) and an MA-PECVD SiN_y / c -Si sample (orange). The FTIR spectra are baseline corrected and divided by the FTIR spectra of identical samples without SiN_y layers.

Samples with thick thermal oxide

Figure 5.17(a) shows the J_0 values of n^+ POLO samples with POLO-junctions based on a 10 nm thick thermal oxide, coated with 100 nm SiN_y with a refractive index of $n = 2.05$ from an IC-PECVD tool. The state before firing was measured after the deposition of SiN_y and the state after annealing is measured after annealing/ before SiN_y deposition (gray dashed line). The deposition of SiN_y in this tool does not lead to an improvement of passivation quality. However, firing at $T_{\text{set,peak}} = 620^\circ\text{C}$ leads to an improvement to $J_0 = (9 \pm 2) \text{ fA/cm}^2$. In contrast, firing at set peak temperatures of 760°C and 900°C leads to a drastic increase in J_0 to $(39 \pm 9) \text{ fA/cm}^2$ and $(170 \pm 33) \text{ fA/cm}^2$.

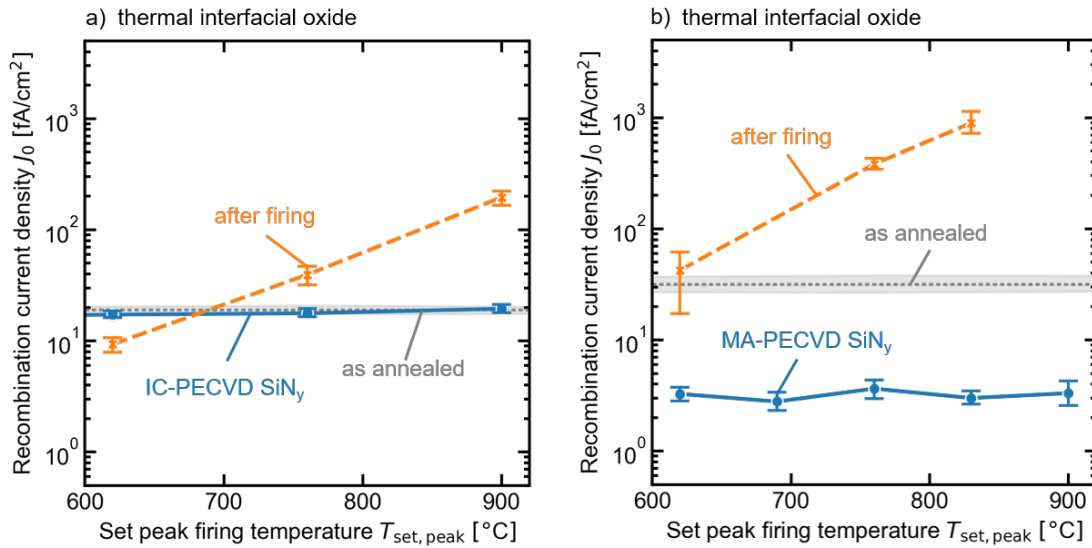


Figure 5.17: Recombination current density J_0 of samples with thermal interfacial oxide, annealed at 880°C with (a) a 100 nm (IC-PECVD) SiN_y capping layer or (b) a 100 nm (MA-PECVD) SiN_y capping layer. Blue data points are measured before firing, and orange data points are measured after firing. The gray interval depicts the results directly after annealing measured on all samples from the respective set of samples (upper/lower quartile). The error bars denote the 95 % confidence interval of measurements on five different positions on two different wafers, respectively.

In contrast, samples with an MA-PECVD SiN_y -layer show a pronounced decrease of J_0 after deposition. Figure 5.17(b) shows J_0 values of $(3 \pm 1) \text{ fA/cm}^2$ for these samples. This behavior is similar to the results in Figure 5.13 with the wet-chemical oxide, although the effect of the MA-PECVD deposition is much stronger on the samples with the thermal oxide.

Contrary to the samples with thin oxide, the J_0 after firing at 760 °C already exceeds the J_0 after annealing for both types of SiN_y . The absolute J_0 level is significantly higher for the group with MA-PECVD SiN_y and reaches $(900 \pm 350) \text{ fA/cm}^2$ already at a firing temperature of 830 °C. Unfortunately, no reliable J_0 values could be determined for the samples fired at 690 °C and 900 °C.

Overall, for both types of SiN_y capping layers, it has been shown that for the firing temperatures of 830 °C and 900 °C, a significant increase in J_0 is observed. However, the question is whether these are the same type of defects also occurring in samples without a capping layer. The presence of hydrogen in the samples with SiN_y capping layer and the blistering observed in some samples suggest that there may be H-induced defects such as platelets.

5.3.2 Post-firing annealing

The following experiment aims to investigate the effect of an annealing process at 425 °C in N_2 atmosphere for 30 min on the J_0 of already fired samples. In Figure 5.18, the J_0 values of samples with and without SiN_y capping layers are compared. The samples with a wet-chemical interfacial oxide fired without a capping layer benefit from the post-firing annealing. In the case of an IC-PECVD SiN_y capping layer, the degradation of the passivation is irreversible, probably due to the intense blistering. However, interestingly for the MA-PECVD- SiN_y samples without visible evidence for blistering, the passivation can also not be recovered by this post-firing anneal. This result supports the hypothesis that in the case of samples with SiN_y capping layers, additional and different types of defects emerge than in those without a dielectric capping layer.

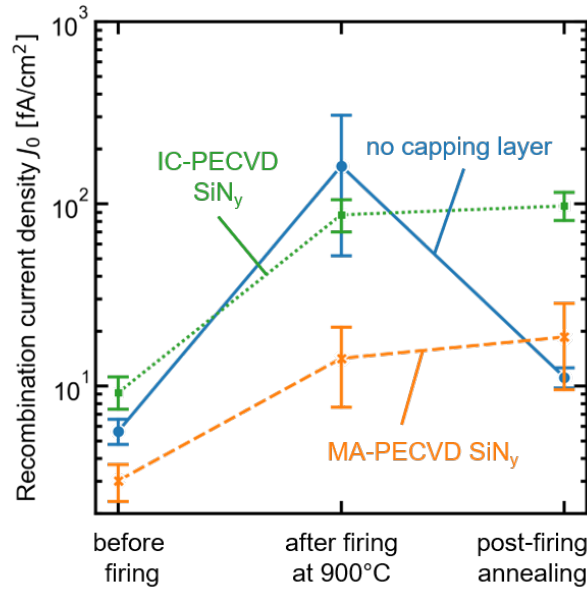


Figure 5.18: Recombination current density J_0 of samples with a thin wet-chemical interfacial oxide, annealed at 820 °C and with different capping layers measured in consecutive process steps. The samples were measured directly before firing, after firing at $T_{\text{set,peak}} = 900$ °C and finally after a subsequent annealing process at 425 °C for 30 min in N_2 atmosphere. The error bars denote the 95 % confidence interval of five measurements on different parts of two wafers, respectively. This figure is reprinted from Figure 12 in Ref. [104].

5.3.3 Al₂O₃ capping layer

Figures 5.19(a) and (b) show the recombination current density of samples coated with ALD Al₂O₃ and annealed at 425 °C in N_2 atmosphere for 30 min before being fired. The samples shown in Figure 5.19(a) exhibit a thin wet-chemical oxide and in Figure 5.19(b) it is a thick thermal oxide. In this section, Al₂O₃ deposition always includes a subsequent annealing process (425 °C, 30 min, N_2).

Comparing the states “as annealed” and “Al₂O₃ + N_2 anneal” in Figure 5.19(a), a relatively small improvement of the J_0 values can be seen. However, quite a large variation occurred depending on the position on the wafers indicated by the large error bars. The firing process results in a slight increase of J_0 . After firing at $T_{\text{set,peak}} = 900$ °C, a moderate increase from 4 to 7 ± 4 fA/cm² is measured.

Figure 5.19(b) shows J_0 after annealing, Al₂O₃ deposition, and firing of samples with a 10 nm thick thermal oxide. A significant improvement of J_0 from 30 fA/cm²

5 Firing stability of n^+ POLO junctions

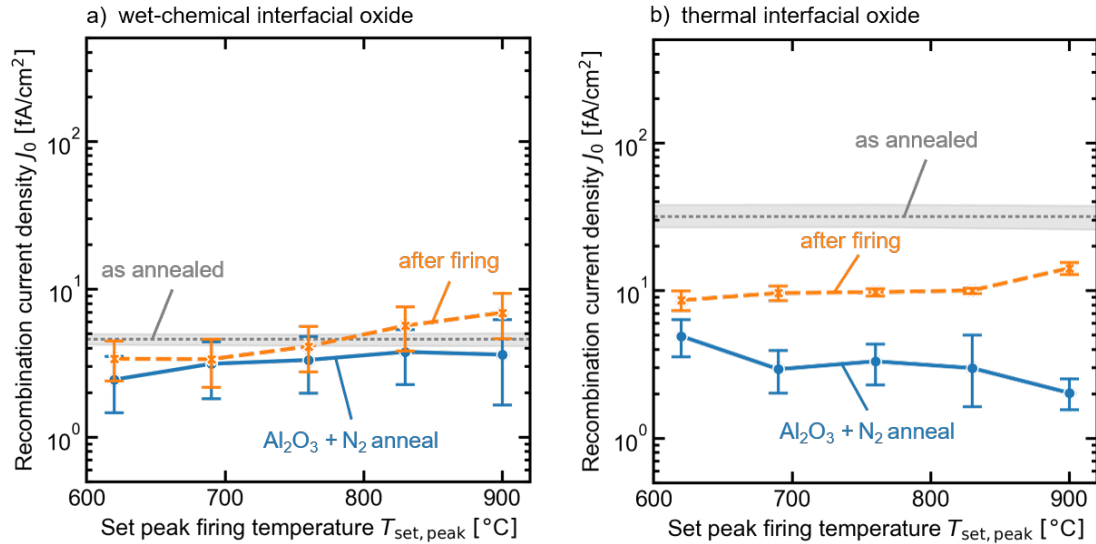


Figure 5.19: Recombination current density J_0 of samples with (a) a wet-chemical interfacial oxide, annealed at 860°C and (b) a thermal oxide, annealed at 880°C both coated with a $10\text{ nm Al}_2\text{O}_3$ layer. Blue data points are measured before firing, and orange data points are measured after firing. The gray interval depicts the results directly after annealing measured on all samples from the respective set of samples (upper/lower quartile). The error bars denote the 95% confidence interval of measurements on five different positions on two different wafers, respectively. This figure is reprinted from Figure 10 in Ref. [104].

to $(3 \pm 2)\text{ fA/cm}^2$ after Al_2O_3 deposition + N_2 anneal is evident. The subsequent firing partly takes back this improvement. In contrast to samples with wet-chemical oxide, it seems that the surface passivation has improved more for these samples upon hydrogenation. The same trend for thermal oxides has been observed before for samples with MA-PECVD SiN_y . One explanation could be more sensitive surface recombination in these samples to the chemical passivation due to the absence of in-diffusion of dopants from the poly-Si layer and a reduction of the band bending in the c-Si due to the increased voltage drop across the thicker interfacial oxide. Firing leads to a deterioration of surface passivation quality to about $(9 \pm 3)\text{ fA/cm}^2$. However, this value is constant from 620°C to 830°C and increases only to $(14 \pm 2)\text{ fA/cm}^2$ at 900°C .

Altogether, it can be said that Al_2O_3 significantly improves the firing stability. However, the improvement previously achieved by Al_2O_3 deposition and annealing is not maintained. Optical microscope images of these samples do not show any sign of blistering.

5.3.4 $\text{Al}_2\text{O}_3/\text{SiN}_y$ capping layer stack

The J_0 values of samples coated with a stack of Al_2O_3 and SiN_y layers are shown in Figure 5.20(a) and (b). The results in Figure 5.20(a) show the J_0 values of samples with a wet-chemical oxide after annealing, after deposition of the layer stack, and after firing. After deposition of the layer stack, excellent passivation quality with J_0 -values of 0.8 to 2.5 fA/cm^2 are reached. This significantly improves the passivation quality compared to 4 fA/cm^2 before the deposition of the $\text{Al}_2\text{O}_3/\text{SiN}_y$ stack. The firing process causes a slight degradation, which increases with increasing firing temperature but remains below 4 fA/cm^2 even at 900 °C. Both the optical microscope images and the good J_0 values indicate that blisters do not occur within this stack.

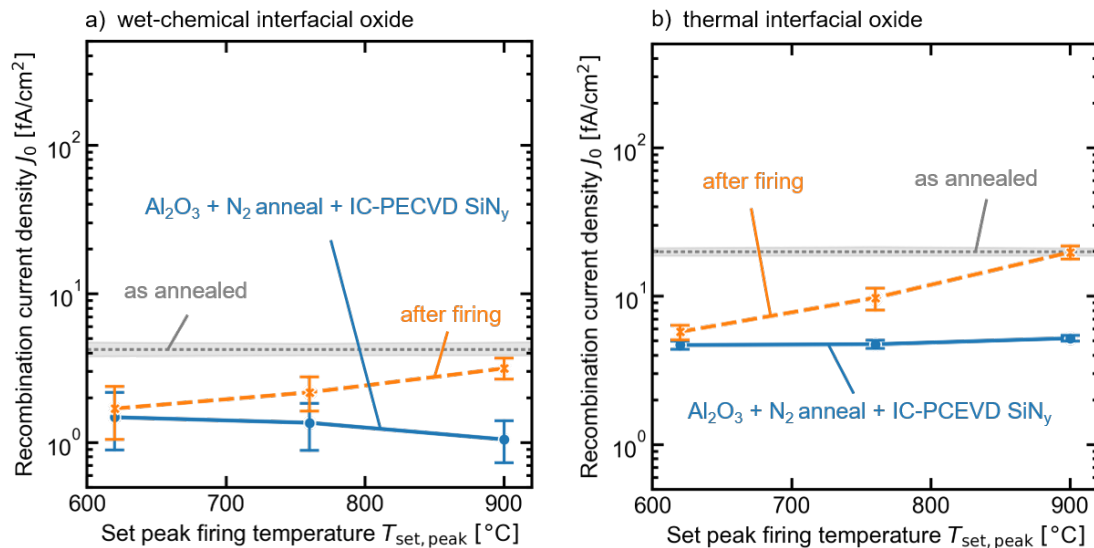


Figure 5.20: Recombination current density of samples with (a) thin wet-chemical oxide, annealed at 860 °C or (b) with thermal oxide, annealed at 880 °C both capped with an $\text{Al}_2\text{O}_3/\text{SiN}_y$ stack measured before (blue) and after (orange) firing. The gray interval depicts the results directly after annealing measured on all samples from the respective set of samples (upper/lower quartile). The error bars denote the 95% confidence interval of measurements on five different positions on two different wafers, respectively. This figure is reprinted from Figure 11 in Ref. [104].

The samples containing a thick thermal oxide in Figure 5.20(b) show qualitatively very similar behavior at a higher J_0 level. After firing at 900 °C J_0 values of about 20 fA/cm^2 are determined.

Concerning the achievement of an acceptable passivation quality with these POLO junctions after firing, deposition of a double layer stack of Al_2O_3 and SiN_y prior to firing is a successful strategy.

5.3.5 Interface state density

The interface state density of samples with thick thermal oxide and capping layers is measured by C - V measurements as in the previous Section 5.2.2. Figure 5.21 shows the D_{it} values plotted over the set peak firing temperatures for samples with no capping layer, a SiN_y or a $\text{Al}_2\text{O}_3/\text{SiN}_y$ capping layer before and after firing. On one set of uncapped samples, D_{it} is measured after an additional SiN_y deposition and low temperature anneal at 425°C for 30 min after firing. Before firing and without a dielectric capping layer the D_{it} values lie at about $1.1 \times 10^{11} \text{ cm}^{-2} \text{ eV}^{-1}$ (orange marker). The deposition of an IC-PECVD SiN_y layer reduces the D_{it} down to $(9 \pm 3) \times 10^9 \text{ cm}^{-2} \text{ eV}^{-1}$ (green marker). This is an excellent value in comparison with reported D_{it} values of bare c-Si/ SiO_x interfaces [185], [202], [203].

The D_{it} values of uncapped samples rise from $3 \times 10^{11} \text{ cm}^{-2} \text{ eV}^{-1}$ when fired at 620°C to $1 \times 10^{12} \text{ cm}^{-2} \text{ eV}^{-1}$ when fired at 900°C , where the D_{it} shows no saturation in contrast to the J_0 values (cf. Figure 5.5(b)). A post-firing treatment with MA-PECVD SiN_y plus an annealing step (425°C , 30 min, N_2) of additional samples previously fired without a capping layer achieves a much lower and also relatively constant D_{it} of about $(8 \pm 2) \times 10^{10} \text{ cm}^{-2} \text{ eV}^{-1}$ shown in red.

The D_{it} of the samples with SiN_y also increases significantly due to firing about one order of magnitude from $(9 \pm 3) \times 10^9$ to $2 \times 10^{11} \text{ cm}^{-2} \text{ eV}^{-1}$ (green markers) in accordance with the J_0 results (see Figure 5.17). The samples that received a stack of Al_2O_3 and SiN_y before firing show a D_{it} of about $(10 \pm 3) \times 10^{10} \text{ cm}^{-2} \text{ eV}^{-1}$ (blue markers), which remains nearly constant over the entire temperature range and is consistent with the J_0 results of the wet-chemical oxide samples.

Overall, the evolution of the D_{it} values with firing temperature is in accordance with the PCD measurements shown above for all sets of samples.

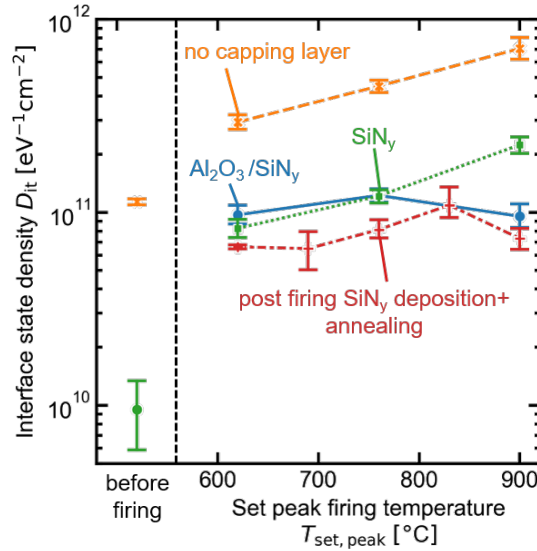


Figure 5.21: Interface state density as a function of set peak firing temperature. Some wafers are fired without a capping layer (orange symbols). The SiN_y layers of the samples coated before firing was deposited by an IC-PECVD tool (green and blue symbols). The post-firing SiN_y deposition is done with an MA-PECVD tool (red symbols). The error bars denote the 95 % confidence interval of measurements on at least three different positions on a sample, respectively. This figure is reprinted from Figure 14 in Ref. [104].

5.3.6 Summary and discussion of Section 5.3

The key findings of the evolution of recombination parameters J_0 and defect densities D_{it} of samples with hydrogen-containing capping layers, presented in this section, are:

- Hydrogen containing capping layers as SiN_y , Al_2O_3 and a stack of Al_2O_3 and SiN_y improve the firing stability of POLO junctions up to a set peak firing temperature of 760 °C
- The capping layer deposition processes or subsequent annealing at 425 °C can also significantly reduce the J_0 before firing. Samples with thick thermal oxide benefit more strongly.
- Firing at 900 °C of samples capped with SiN_y causes a deterioration of J_0 . Samples with a thin oxide capped with IC-PECVD SiN_y suffer from blistering.
- Capping with Al_2O_3 or Al_2O_3/SiN_y leads to J_0 values below 20 fA/cm² even

after firing at 900 °C for both oxide types.

- Best results of 2.2 fA/cm² are reached on samples with a thin oxide and a stack of Al₂O₃ and SiN_y after firing at $T_{\text{set,peak}} = 900$ °C.
- D_{it} values determined from samples with 10 nm thermal oxide show qualitatively similar behavior to the J_0 values of samples from both oxide groups.
- Post-firing annealing of samples with SiN_y (fired at $T_{\text{set,peak}} = 900$ °C) does not lead to any improvement in the J_0 in contrast to uncapped samples, where J_0 is reduced by order of magnitude.

This chapter shows that hydrogen-containing capping layers significantly improve the firing stability of the passivation quality. This advantage, however, depends strongly on the layers used. The two different SiN_y layers applied in this work hint toward the importance of the hydrogen content. Blistering of samples with IC-PECVD SiN_y indicates that too much hydrogen at the interface leads not only to the passivation of existing defects but can also be harmful, depending on the hydrogen concentration and firing temperature. The origin of surface recombination in these samples is believed to differ from that of the uncapped samples as the defects cannot be healed in a post-annealing process, which is possible for uncapped samples. This indicates that in the IC-PECVD SiN_y capped samples sufficient hydrogen is probably present during and after firing to passivate the firing-induced defects. However the additional defects induced by the blistering can not be passivated by the excess hydrogen probably in-diffused during the post-firing annealing. Thus no improvement is taking place.

This same qualitative behavior is also seen for samples with MA-PECVD SiN_y layers. However, the reason is believed to be different. These samples show a clear improvement in passivation quality already after SiN_y deposition. This suggests that during deposition, which takes place at a higher chamber temperature of 500 °C, there is already a significant H diffusion into the sample. The main effusion temperature was shown to increase with increasing SiN_y deposition temperature in the literature [204]. This might lead to the situation that, in the case of MA-PECVD SiN_y as opposed to IC-PECVD SiN_y during firing, less H is diffusing into the poly-Si so that not all firing-induced defects can be passivated. This would explain the rising J_0 during firing. The observed post-firing annealing behavior of no improvement in J_0 could also be explained by a higher main effusion temperature as the selected

5.3 Influence of different hydrogen-containing capping layers

temperature of 425 °C might have been too low to ensure further hydrogen diffusion from the MA-PECVD SiN_y layer. Although this is believed to be the more likely cause, considering the findings of other groups in literature, the opposite case of excess H leading to enhanced recombination, as supposed for the IC-PECVD SiN_y, cannot be ruled out either.

Steinhauser et al.[102] showed 2020, and others confirmed [109], [111] a decrease in J_0 after firing with SiN_y capping layers with increasing refractive index. They stated that the amount of introduced hydrogen increases with an increasing refractive index, which is beneficial for the passivation quality. This fits the results of Bredemeier et al. [205] who has shown that the amount of hydrogen introduced to the sample increases with increasing refractive index n between 1.9 and 2.4. However, the results of this work showed that the SiN_y deposition method also plays a crucial role. Comparing two layers with a refractive index of 2.05 from different tools yields different results. Despite the relatively low refractive index, these experiments lead to the assumption that at least in one case (IC-PECVD SiN_y), sufficient or possibly too much H is in-diffused here. These results, however, fit the results of Kang et al., who also used different equipment for SiN_y deposition (batch-type Centrotherm, a Roth and Rau AK400, and an Oxford PlasmaLab 100 PECVD tool) and as well obtained significantly different results in firing stability [103].

If a 10 nm Al₂O₃ layer is introduced between poly-Si and SiN_y instead of a sole IC-PECVD SiN_y layer, the behavior of the passivation quality changes massively. The J_0 increases only slightly with the firing temperature and remains below the initial level after annealing even up to the firing temperature of $T_{\text{set,peak}} = 900$ °C. These results agree well with that of other groups. Already in 2018, Mewe et al. [96] showed a positive effect of Al₂O₃/SiN_y capping layers over Al₂O₃ single layers, and Kang et al. [103], [108] and Polzin et al. [107] confirmed this trend.

It has been shown by Dingemans et al. [206] that Al₂O₃ releases H over a wide temperature range starting at 400 °C to more than 715 °C. This explains why the samples with Al₂O₃/SiN_y stack show a significant improvement in passivation quality already after SiN_y deposition, which takes place at a chamber temperature between 300 °C and 500 °C. The releasing of H moreover strongly depends on the microstructure of the Al₂O₃ layer which is determined by the preparation method and its process parameters such as deposition temperature [206], [207]. Furthermore, the Al₂O₃ acts as an efficient barrier for the diffusion of H, which limits the

in-diffusion of H from the SiN_y and the out-diffusion of already introduced H [208], [209]. This H regulating effect could be the crucial difference to the SiN_y single layers, which is also hypothesized by Polzin et al. [107]. The beneficial effect of Al_2O_3 layers is thus probably its hydrogen-regulating effect. However, Truong et al. [184] also suggested in 2020 that the hydrogen driven in from Al_2O_3 layers could have a different form (molecular/atomic) than that from SiN_y layers. This hypothesis arose from measurement results showing an increase in iV_{oc} for both samples with Al_2O_3 plus a forming gas anneal (FGA) and $\text{SiN}_y + \text{FGA}$, respectively. However, an a-Si:H peak in the PL spectrum only appeared for the samples hydrogenated with a SiN_y layer. Thus there could also be a connection between the form of hydrogen introduced with the formation of hydrogen-induced defects. However, the absence of the a-Si:H peak after $\text{Al}_2\text{O}_3 + \text{FGA}$ could also be due to a smaller amount of in-diffused H.

Overall, the results obtained agree with those of other groups and show a large room for optimization in the choice of the capping layer and the layer properties, as the ability of dielectric layers to release H strongly depends on the microstructure of the layer. To investigate this further, the next chapter will focus on the generated hydrogen concentration at the c-Si/ SiO_x /poly-Si interface.

5.4 Changes in hydrogen concentration and defect state density due to firing

In this chapter, the relationship between the hydrogen concentration at the c-Si/ SiO_x /poly-Si interface and the J_0 and D_{it} values is investigated to find a possible explanation for the behavior found in the previous chapter. Therefore, the surface passivation stability of n^+ POLO junctions upon firing, with a stack of $\text{Al}_2\text{O}_3/\text{SiN}_y$ capping layers at two firing temperatures and varying Al_2O_3 layer thickness, is studied to achieve different hydrogen concentrations at the interface and examine their influence on the surface passivation.

5.4.1 Evolution of recombination current density and hydrogen concentration with firing temperature

To examine the correlation between the hydrogen content at the interface and the passivation quality, different n^+ POLO sample groups with $\text{Al}_2\text{O}_3/\text{SiN}_y$ stacks are investigated in detail in the following.

Firing at 724 °C

Figure 5.22 shows J_0 and D_{it} values of samples before and after deposition of the $\text{Al}_2\text{O}_3/\text{SiN}_y$ stacks and firing at a $T_{\text{set,peak}} = 724^\circ\text{C}$, for which no blistering is expected from previous experiments and also not visible in optical microscope images. The resulting D_{it} needs to be interpreted as the maximum defect density $D_{it,\text{max}}$ at the $\text{SiO}_x/\text{c-Si}$ interface as they are deduced from a regression of the MarcoPOLO by Folchert et al. [73] model to the measured J_0 values using $D_{it,\text{max}}$ as the only free parameter. Therefore a capture-cross-section of holes of $4.2 \times 10^{-18} \text{ cm}^2$ is assumed. Moreover, a Monte-Carlo analysis with 500 samples per measurement is performed in which the following parameters are varied: the oxide thickness as $d_{\text{ox}} = (1.5 \pm 0.2) \text{ nm}$, the poly-Si doping concentration as $N_{\text{dop,poly}} = (3.0 \pm 0.1) \times 10^{20} \text{ cm}^{-3}$ and the c-Si peak doping concentration as $N_{\text{dop,c-Si}} = (1.4 \pm 0.5) \times 10^{19} \text{ cm}^{-3}$ as determined from ECV measurements. The measured J_0 values are varied in the range of their standard deviation after multiple measurements on the same sample.

The J_0 values of $(5.7 \pm 0.7) \text{ fA/cm}^2$ after annealing can be further improved to $(2.1 \pm 0.8) \text{ fA/cm}^2$ by depositing the two dielectric layers ($\text{Al}_2\text{O}_3/\text{SiN}_y$). Please note that this time, no intermediate annealing step after Al_2O_3 deposition is done. The calculated D_{it} values after annealing are approx. $3.6 \times 10^{12} \text{ cm}^{-2} \text{ eV}^{-1}$ and thus higher than for the samples in Figure 5.9(b) in the same state before firing which were however not processed together. One difference between these batches is the higher annealing temperature of 860°C for the samples in Figure 5.9. In contrast, the samples in Figure 5.22(b) were annealed at 820°C . A possible explanation for the difference in D_{it} could be that annealing at 860°C leads to a stronger restructuring of the bonds at the c-Si/ SiO_x interface.

After the Al_2O_3 and SiN_y deposition and before firing, a slight trend of decreasing

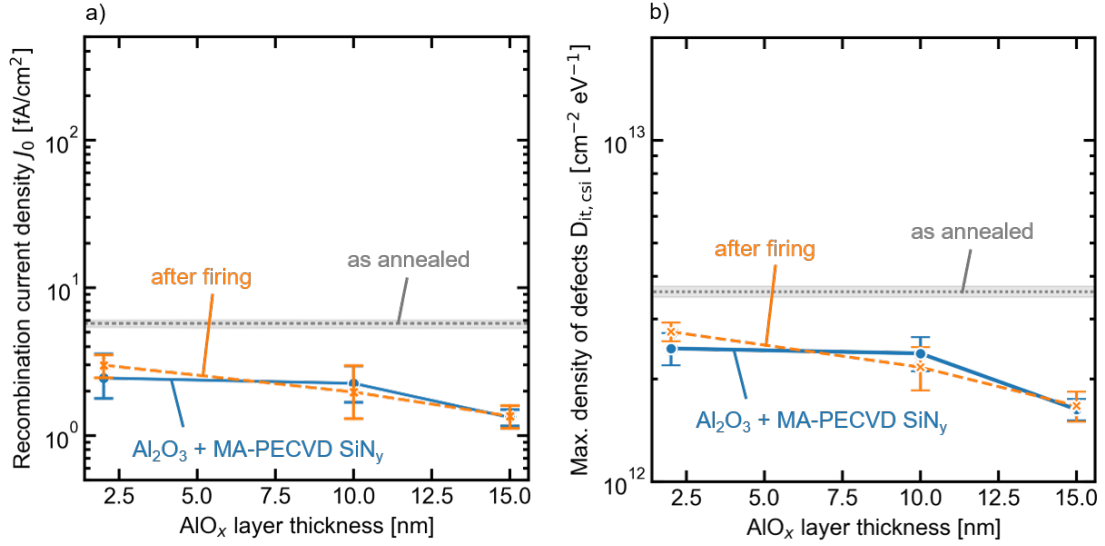


Figure 5.22: a) Recombination current density and (b) maximum interface state density of samples capped with an Al₂O₃/SiN_y stack, fired at $T_{\text{meas,peak}} = (724 \pm 5)^\circ\text{C}$ and varying Al₂O₃ layer thickness measured before (blue) and after firing (orange). The gray interval depicts the results directly after annealing at 820 °C measured on all samples from the respective group of samples. The error bars in (a) denote the 95 % confidence interval of between two and five measurements on different samples, respectively. The error bars in (b) denote the standard deviation of the calculated values determined by a Monte-Carlo analysis. This figure is adapted from Figure 3 in Ref. [105].

J_0 with increasing Al₂O₃ layer thickness can be observed. However, due to the comparatively small changes and the large error bars, process variations during SiN_y deposition, for example, could be responsible. Subsequent firing at 724 °C has little effect on the J_0 and D_{it} values. The samples with 15 nm thick Al₂O₃ layers show particularly good values below 2 fA/cm².

Figures 5.23, 5.24 show hydrogen and deuterium profiles measured by SIMS. Please note that the calibrated values only apply to the poly-Si, SiO_x, and c-Si layers and not to the SiN_y and Al₂O₃ layers because of the c-Si-based calibration used in the analysis. However, the hydrogen concentration in an unfired MA-PECVD SiN_y layer was determined by FTIR measurements and resulted in a concentration of $6 \times 10^{21} \text{ cm}^{-3}$. Comparing the uncalibrated values in Figures 5.23, 5.24 and 5.26 inside the SiN_y layer no measurable hydrogen loss can be detected between the pre- and post-firing states.

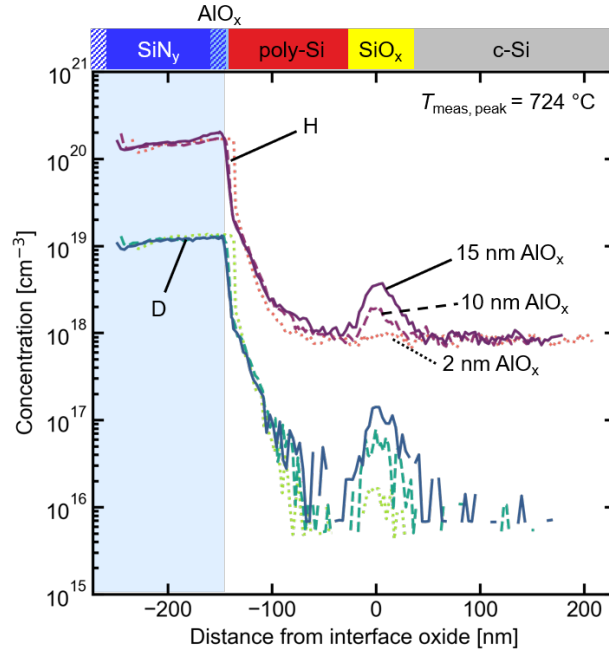


Figure 5.23: Hydrogen and deuterium ToF-SIMS profiles of $\text{Al}_2\text{O}_3/\text{SiN}_y$ capped samples with different Al_2O_3 layer thickness fired at $T_{\text{meas,peak}} = (724 \pm 5)^\circ\text{C}$. The concentrations are only valid for the silicon parts of the sample and are not calibrated within the blue-marked SiN_y and Al_2O_3 regions. This figure is adapted from Figure 5 in Ref. [105].

The peak hydrogen concentration of 1×10^{18} to $3.5 \times 10^{18} \text{ cm}^{-3}$ for hydrogen and $1.5 \times 10^{17} \text{ cm}^{-3}$ down to the detection limit of about $1 \times 10^{16} \text{ cm}^{-3}$ for deuterium at the $\text{SiO}_x/\text{c-Si}$ interface after firing at $T_{\text{meas,peak}} = 724^\circ\text{C}$ in Figure 5.23 are more than three magnitudes lower than the hydrogen concentration of $6 \times 10^{21} \text{ cm}^{-3}$ inside the SiN_y layer. These peak concentrations show an increasing trend with increasing Al_2O_3 layer thickness.

Compared to the J_0 and D_{it} values, these results indicate that there could be a positive influence of an increasing concentration of hydrogen in the range of 1×10^{18} to $3.5 \times 10^{18} \text{ cm}^{-3}$ on the passivation of the poly-Si/ $\text{SiO}_x/\text{c-Si}$ interface states. At the low firing temperature of 724°C used here, the active defect density is slightly reduced with increasing hydrogen content due to an increasing Al_2O_3 layer thickness (cf. Figure 5.22).

The fact that the hydrogen concentration increases with the film thickness of the Al_2O_3 layer does not fit the expectation of the hydrogen blocking property of aluminum oxide reported by Helmich et al. [208] and others [209], [210]. However,

compared to the experiments of Helmich et al., who used SiN_y layers with a refractive index of 2.3 and an approximate hydrogen content of more than 15% [211], we used SiN_y layers with a refractive index of 2.05 and a lower hydrogen content of $(5 \pm 1)\%$. It is, therefore, possible that in our work, the amount of hydrogen introduced from the Al_2O_3 layers contributes a relevant share to the final H concentration at the interface due to the lower H concentration of the 2.05 SiN_y layers as compared to 2.3 SiN_y layers used by Helmich et al.[208]. Moreover, the ratio of the hydrogen-containing species, i.e., Si-H and N-H, changes with the refractive index and therefore differs between both experiments [211]. It is also known that Si-H and N-H bonds exhibit different activation energies for the release of hydrogen [212]. Moreover, it is puzzling at first glance that the deuterium concentration also increases simultaneously. Since deuterium-containing gas (D_2) is only used in the SiN_y deposition, the deuterium cannot directly originate from the Al_2O_3 layer. However, a possible explanation might involve D-H exchange reactions, as proposed in [82].

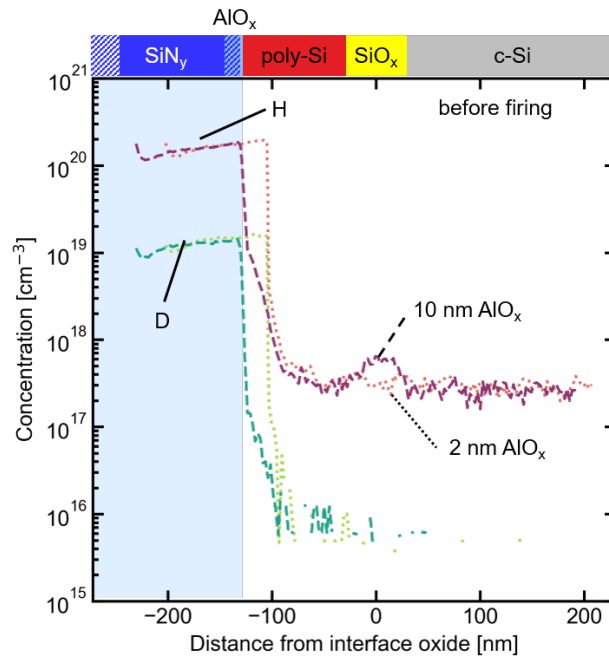


Figure 5.24: Hydrogen and deuterium ToF-SIMS profiles of samples after the deposition of $\text{Al}_2\text{O}_3/\text{SiN}_y$ capping layers for different Al_2O_3 layer thickness. The concentrations are only valid for the silicon parts of the sample and are not calibrated within the SiN_y and Al_2O_3 regions highlighted in blue. This figure is adapted from Figure 4 in Ref. [105].

This trend that the hydrogen concentration at the interface increases with increasing

5.4 Changes in hydrogen concentration and defect state density due to firing

Al_2O_3 thickness and decreasing J_0 values can already be seen directly after the deposition of the dielectric layers, i.e., before firing. Figure 5.24 shows the hydrogen concentration of two samples before firing. The samples with the thicker Al_2O_3 layer (10 nm) have slightly more hydrogen at the poly-Si/ SiO_x /c-Si interface before firing as the sample with 2 nm Al_2O_3 . Since the temperature in the deposition chamber during SiN_y deposition is 500 °C, diffusion of H from the Al_2O_3 layers is likely. The deuterium concentrations of both samples inside poly-Si, SiO_x , and c-Si are below the resolution limit. This indicates that H from the Al_2O_3 layer accumulates at the interface even prior to firing due to the high temperature during nitride deposition. The existing defects are probably already passivated with H from the Al_2O_3 layer during this pre-firing hydrogenation. Upon firing, additional H and D is released from the nitride layer, as shown by the deuterium peaks in Figure 5.23 compared to Figure 5.24. The newly released D likely exchanges with H at the already passivated defects [82], explaining the higher D peaks for thicker Al_2O_3 layers (see Fig. 5.23).

Firing at 863 °C

Figure 5.25 shows the J_0 and $D_{\text{it,max}}$ values of samples before and after firing at 863 °C. At this temperature, samples with just MA-PECVD SiN_y layers show a strong degradation of J_0 up to 20 fA/cm², as shown previously in Figure 5.13. In these samples with a stack of Al_2O_3 and SiN_y layers, the passivation quality also deteriorates as the J_0 values increase to (6 ± 2) fA/cm² and the defect density increases up to 4.2×10^{12} cm⁻² eV⁻¹. The passivation quality shows an optimum at an Al_2O_3 film thickness of 5 nm. Again, the trends should be treated with caution compared to the dispersion of the data. It should also be noted that all samples, except those with 5 nm Al_2O_3 , are suffering from blister formation. Samples with no blisters or as few as possible blisters were selected for the following SIMS measurements.

Figure 5.26 shows the ToF-SIMS measurements after firing at 863 °C. When looking at the H and D concentrations at the interface, it can be seen that the sample with 5 nm Al_2O_3 has the highest H peak concentrations of 5.2×10^{18} cm⁻³. The samples with 10 and 15 nm Al_2O_3 show H peak concentration values of 3.4×10^{18} cm⁻³, which are only slightly below this, whereas the sample with 15 nm Al_2O_3 shows a clearly broader peak and indicating that more H and D is stored in the area around the interface. The sample with the smallest Al_2O_3 thickness of 2 nm again

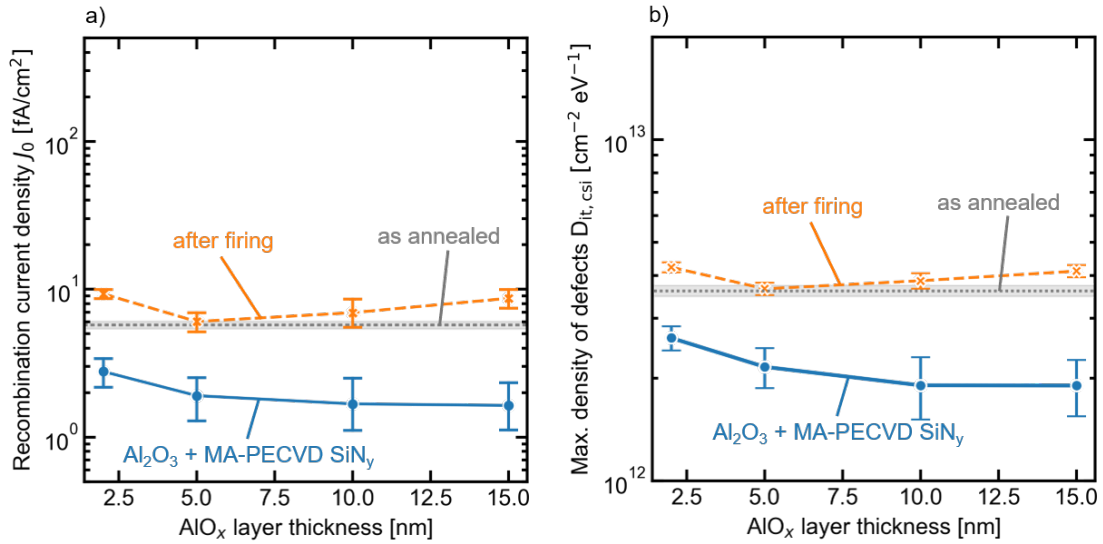


Figure 5.25: a) Recombination current density and (b) D_{it} of samples capped with Al₂O₃/SiN_y stacks, fired at $T_{\text{meas,peak}} = (863 \pm 5)^\circ\text{C}$ and varying Al₂O₃ layer thickness measured before (blue) and after firing (orange). The gray interval depicts the results directly after annealing at 820 °C measured on all samples from that batch. The error bars in (a) denote the 95% confidence interval of five measurements on different samples, respectively. The error bars in (b) denote the standard deviation of the calculated values determined by a Monte-Carlo analysis. This figure is adapted from Figure 6 in Ref. [105].

shows the lowest peak H and D concentrations (H: $1 \times 10^{18} \text{ cm}^{-3}$, D: $8 \times 10^{16} \text{ cm}^{-3}$). Compared to the samples fired at 724 °C (see Figure 5.23), the samples with 10 nm and 15 nm Al₂O₃ show a slight increase in peak concentration, and also the sample with 5 nm Al₂O₃ shows a higher peak concentration than the samples fired at 724 °C with 2 nm and 10 nm. A directly comparable sample with 5 nm Al₂O₃ is not present in this group.

Considering the hydrogen concentration in the poly-Si regions, the two samples with 2 nm and 10 nm Al₂O₃ show concentrations that are about one order of magnitude lower than in all the other fired samples. An explanation could be that strong blistering possibly of the whole poly-Si/Al₂O₃/SiN_y stack, as seen earlier for SiN_y/poly-Si samples, took place in the area of investigation so that a large amount of hydrogen diffused out of the poly-Si and the wafer. This would also explain why the poly-thickness and the Al₂O₃/SiN_y thickness seem to be less thick for these samples.

5.4 Changes in hydrogen concentration and defect state density due to firing

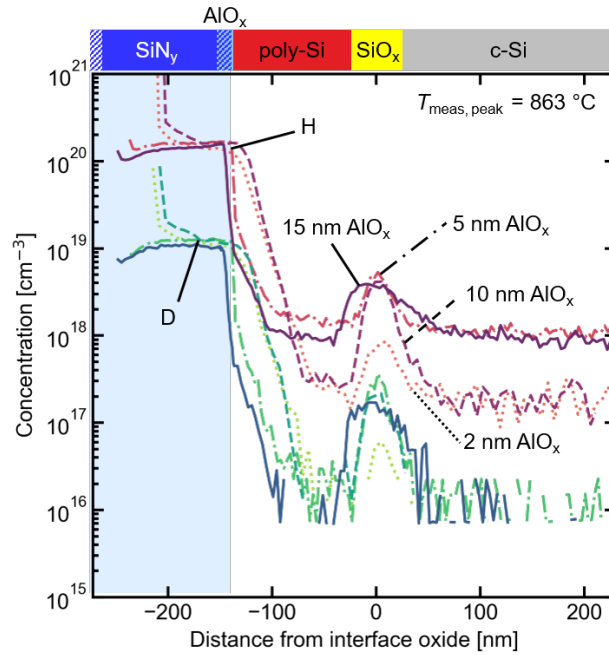


Figure 5.26: Hydrogen and deuterium ToF-SIMS profiles of $\text{Al}_2\text{O}_3/\text{SiN}_y$ capped samples with different Al_2O_3 layer thickness fired at $T_{\text{meas,peak}} = (863 \pm 5)^\circ\text{C}$. The concentrations are only valid for the silicon parts of the sample and are not calibrated within the blue-marked SiN_y and Al_2O_3 regions. This figure is adapted from Figure 7 in Ref. [105].

5.4.2 Comparison of integrated hydrogen concentrations and defect state densities at the interface

Following the hypothesis that hydrogen passivates defect states at the c-Si/ SiO_x /poly-Si interface, the question arises if the hydrogen concentration measured at the interface is large enough to passivate the present defects.

Figure 5.27(a) and (b) show the integrated hydrogen concentrations over an interval of ± 55 nm around the hydrogen peaks at the SiO_x /c-Si interface. The results are shown by gray, blue, orange and red markers (joint by lines) after annealing, after $\text{Al}_2\text{O}_3/\text{SiN}_y$ deposition, after firing at 724°C and 863°C , respectively.

Under the simplifying assumption of a constant distribution of the interface state density across the bandgap, we calculate an aerial defect density by multiplying the $D_{\text{it,max}}$ values with the bandgap energy of 1.13 eV ($D_{\text{it,max}} \times E_g$). The colorized horizontal intervals indicate these results. Figures 5.27(a) and (b) thus allow a rough

comparison between the hydrogen concentration and the interface state density.

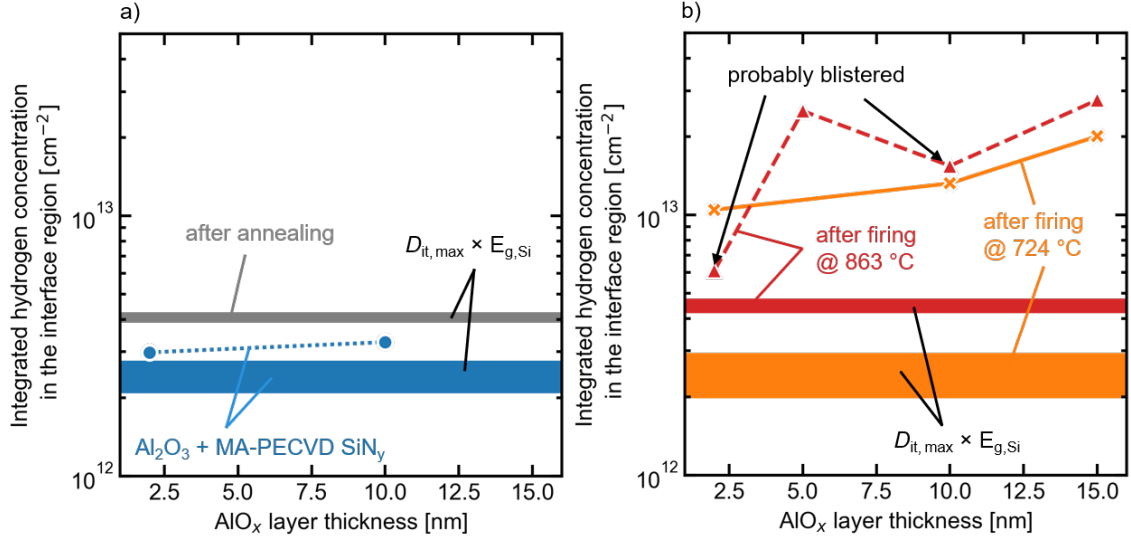


Figure 5.27: Integrated hydrogen concentrations in the SiO_x/c-Si interface region as a function of the Al₂O₃ layer thickness are shown in Figures (a) and (b) indicated by markers joint by lines. The colored bars indicate the intervals of the maximal areal interface state density $D_{it,max} \times E_{g,Si}$ determined under the assumption of a constant D_{it} distribution over the bandgap. In Figure (a) the states after annealing (gray) and after Al₂O₃/SiN_y deposition (blue) are shown. In Figure (b) results after firing at $T_{meas,peak}$ of $(724 \pm 5)^\circ\text{C}$ (orange) and $(863 \pm 5)^\circ\text{C}$ (red) are shown. This figure is adapted from Figure 8 in Ref. [105].

In Figure 5.27(a) results of samples measured after annealing (gray interval) and after Al₂O₃ and SiN_y deposition (blue symbols and interval) are shown. After annealing at 820 °C, the defect concentration is $(4.1 \pm 0.2) \times 10^{12} \text{ cm}^{-2}$, which is reduced to $(2.4 \pm 0.4) \times 10^{12} \text{ cm}^{-2}$ by an induced hydrogen concentration at the interface of $(3.1 \pm 0.2) \times 10^{12} \text{ cm}^{-2}$ due to Al₂O₃ and SiN_y deposition. Assuming that the defects were each passivated by one hydrogen atom, the amount of hydrogen matches quite well.

The results shown in Figure 5.27(b) are measured after firing at 724 °C (orange symbols) and 863 °C (red symbols). The integrated hydrogen concentration at the SiO_x/c-Si interface increases significantly due to firing in accordance with the previous observations. They moreover show an increasing trend with increasing Al₂O₃ layer thickness as already observed in the SIMS profiles. This behavior is not observed for the samples fired at 863 °C. The samples with 2 and 10 nm Al₂O₃ layer

show a deviating behavior of the overall SIMS profiles as compared to all other measurements, which was discussed in Section 5.4.1 and which are thus suspected to be affected by blistering in the measured region. The integrated H concentration of the other two samples with 5 and 15 nm Al_2O_3 layers is 2.51×10^{13} and $2.76 \times 10^{13} \text{ cm}^{-2}$ respectively and thus similar. Firing at 863°C thus drives in more H than firing at 724°C .

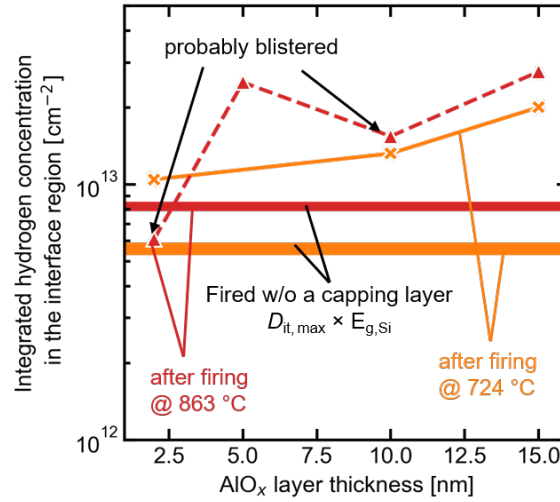


Figure 5.28: Integrated hydrogen concentrations in the $\text{SiO}_x/\text{c-Si}$ interface region as a function of the Al_2O_3 layer thickness (markers joint by lines). The colored bars indicate the intervals of the maximal areal interface state density $D_{\text{it,max}} \times E_{\text{g,Si}}$ of samples fired without a capping layer determined under the assumption of a constant $D_{\text{it,max}}$ distribution over the bandgap. Results after firing at $T_{\text{meas,peak}}$ of $(724 \pm 5)^\circ\text{C}$ (orange) and $(863 \pm 5)^\circ\text{C}$ (red) are shown.

A comparison to the $D_{\text{it}} \times E_{\text{g}}$ values, shown as colored intervals, reveals that the hydrogen concentrations are several times above the measured defect densities according to this rough estimation. This applies to both samples fired at 724°C and 863°C . As shown in Figure 5.28 the H concentrations also exceed the defect concentration of samples fired without hydrogen-containing layers. In this case the defect concentration is 6×10^{12} to $8.8 \times 10^{12} \text{ cm}^{-2}$ fired at 724°C and 863°C respectively, and here no defects are rendered “invisible” by hydrogen passivation. Thus, after firing samples with $\text{Al}_2\text{O}_3/\text{SiN}_y$ stack at 724°C as well as at 863°C , an oversupply of H is present. Despite the oversupply of H, the defect density increases during firing at 863°C . This behavior supports the hypothesis that the excessive hydrogenation of the interface during firing, on the one hand, passivates defects that are

already present or induced by the firing process but, on the other hand, also creates additional defects. When fired at lower $T_{\text{meas,peak}}$, these defects appear to remain passivated. However, with rising thermal activation at a higher firing temperature, the balance between the formation of new defects and hydrogenation of defects likely shifts to more active defects.

In Section 5.2.4, it was hypothesized that thermal stress at the $\text{SiO}_x/\text{c-Si}$ interface plays a role during firing. Thermal stress caused by the mismatch in thermal expansion coefficients between the poly-Si and the SiO_x [213] is believed to promote defect formation with increasing strength at increasing temperatures. Under this hypothesis, in-diffusing hydrogen then likely inserts into these weakened, strained bonds [190] or dangling interfacial bonds and creates additional defect states. There are several examples in the literature of hydrogen causing active recombination defects, such as the formation of structural defects or platelets [214]–[216], or the formation of vacancy-hydrogen complexes [217].

Platelets [214], [218]–[220] are further known to trigger the formation of blisters, especially from hydrogen implanted c-Si and poly-Si [221] and could explain the high concentrations of H accumulated at the interface.

5.4.3 Summary and discussion of Section 5.4

The key findings about the influence of the hydrogen concentration on the defect density at the $\text{SiO}_x/\text{c-Si}$ interface in $\text{SiN}_y/\text{Al}_2\text{O}_3/n^+$ POLO junctions, presented in this section, are:

- After capping layer deposition, the J_0 values show a slightly decreasing trend with an increasing thickness of the Al_2O_3 layer with the applied $\text{Al}_2\text{O}_3/\text{SiN}_y$ stack.
- After firing at 724°C J_0 stays at about the level before firing and slightly decreases while the hydrogen concentration at the interface increases by a factor of 3 to 7.
- After firing at 863°C J_0 increases to above $5\text{ fA}/\text{cm}^2$ for all Al_2O_3 thicknesses, while the hydrogen concentration increases further for samples not suspected of being blistered in the measured region.

The correlation between D_{it} of n^+ POLO junctions featuring a wet-chemical interfacial oxide and $\text{Al}_2\text{O}_3/\text{SiN}_y$ capping layer stacks with varying Al_2O_3 layer thickness and the hydrogen concentration at the interface before and after firing were analyzed. The application of TOF-SIMS measurements to determine the hydrogen concentration at the interface confirmed that the hydrogen concentration at the oxide interface of poly-Si samples increases significantly during firing.

A rough comparison of the hydrogen concentrations and the defect density reduction after annealing, plus capping layer deposition, shows that they have the same order of magnitude. After firing, however, the hydrogen concentration exceeds the defect concentration several times, indicating that the hydrogen is also stored at other sites than former dangling bonds, which are likely hydrogen-induced, newly created defects. A firing temperature of 760°C does not lead to a significant reduction in J_0 despite a significant increase in H concentration. However, firing at 900°C significantly increases the J_0 . This is suspected to be due to thermally induced stress leading to weakened bonds promoting the defect formation [190], which can lead to blistering in the worst case.

The results of Kang et al. [103] as well showed that there is no monotonic relationship between the hydrogen concentration at the interface and the J_0 , which suggests that the hydrogen concentration has a complex effect on the passivation of the interface depending on its amount. Recently Kang et al. [108] have confirmed the suggestion that both too little and too much hydrogen increases the J_0 of n^+ POLO junctions [108].

In summary, this means that each sample has an optimum hydrogen concentration, which probably depends on the intrinsic D_{it} and the D_{it} arising during firing. Both too much and too little H can thus be the reason for an increased D_{it} after firing. Further investigations are necessary to better understand the effects and distinguish between the different simultaneous defect formation and passivation processes.

5.5 Summary and implication of Chapter 5

This chapter aimed to answer why the firing of n^+ POLO junctions negatively affects their passivation quality and how the application of hydrogen-containing capping layers can be used to improve the firing stability.

The exponential relationship between D_{it} and the firing temperature on uncapped n^+ POLO samples indicates a thermally activated defect formation process. This behavior applies to both thin wet-chemical and thicker thermal oxides. The determined low activation energy of 0.3 eV of the defect formation process is, however, not sufficient to explain the breaking of unstrained Si-O or Si-H bonds [180], [222]. This raises the question of why the firing process negatively influences the passivation quality while the tube furnace annealing processes lead to good J_0 values. Here, the heating and cooling rates are found to be the decisive difference between those processes. In both cases, the change in temperature leads to thermal expansion of the various layers of the sample, leading to thermal stress due to the significantly lower CTE of the oxide compared to c-Si and poly-Si. The different behavior upon firing leads to the hypothesis that during the tube furnace annealing, the slow heating and cooling rates of 5 to 10 K/min enable viscose flow of the SiO_x to relieve the arising stress and repair nevertheless created defects by a reorganization of the interfaces during the long plateau phase of 30 min and a slow ramp-down process.

In contrast, the heating and cooling rates during firing are in the range of 50 to 100 K/s, which presumably prevents sufficient relaxation of the stress by viscous flow and thus may lead to stress-induced defect formation. Another amplifying factor for this stress might be faster heating of the poly-Si layer than the c-Si bulk during firing. This is possibly induced by the higher doping and thus increased FCA of the IR radiation compared to the c-Si bulk, which would even enhance the non-uniform expansion of the different layers at the poly-Si/ SiO_x /c-Si interface.

If hydrogen is introduced to the interface during and/or before firing, this can have complex effects on the passivation quality of the samples under investigation. Depending on the capping layer used, the passivation quality tends to be improved by the more or less intense introduction of hydrogen during the layer deposition. Depending on the temperature at which the samples are subsequently fired, a different picture emerges. At temperatures up to 760 °C, a clear improvement of stability is seen for all groups with Al_2O_3 , SiN_y or $\text{Al}_2\text{O}_3/\text{SiN}_y$. Here, firing brings enough hydrogen to the interface to passivate the defects that arise during firing, described in Section 5.2. As shown by the SIMS measurements in Section 5.3, the hydrogen content increases significantly, even exceeding the defect concentration measured during firing without hydrogen. Thus, the hydrogen is stored in places other than former dangling bonds, which are likely hydrogen-induced, newly created defects. These

defects probably mostly stay passivated at lower firing temperatures explaining the simultaneous more or less stable J_0 values. With increasing firing temperature and thus increasing stress at the interface, this balance changes to more unpassivated defects. In the case of especially hydrogen-rich SiN_y capping, a strong increase in J_0 and at the same time strong blistering is seen, which is also often related to hydrogen [223], [224]. Overall, in these experiments, the deterioration of J_0 is significantly lower for samples with only Al_2O_3 or $\text{Al}_2\text{O}_3/\text{SiN}_y$ capping layers. The Al_2O_3 layer located between the poly-Si and SiN_y layer likely acts as a hydrogen in- and out-diffusion barrier regulating the amount of H at the interface.

In summary, this means that there is an optimum hydrogen concentration for each sample, which depends on the intrinsic D_{it} and the D_{it} induced by firing. Both too much and too little H can be the reason for an increased D_{it} after firing. However, further investigations are required for a more detailed understanding of the effects and to discriminate between the different simultaneous defect formation and passivation processes.

From an application perspective, these results indicate that using an $\text{Al}_2\text{O}_3/\text{SiN}_y$ stack rather than a single SiN_y capping layer is advantageous for the passivation quality after firing. With this stack, J_0 values below 4 fA/cm^2 can be achieved even at 900°C . This result is very suitable for the application in POLO-IBC cells, which need the stack of $\text{Al}_2\text{O}_3/\text{SiN}_y$ layers to passivate the base regions on the rear side anyway. However, when considering the entire cell process, it should be noted that this will require adjustment of subsequent processes, e.g., choosing a different Ag paste than for SiN_y alone [225]. Thus for cell concepts where the poly-Si layer is not structured but covers the whole rear side of the wafer, like in TOPCon and POLO-BJ cells, the application of SiN_y single stacks is preferable. However, the results of the single MA-PECVD SiN_y layer and results from literature [102], [109] indicate by an optimization of SiN_y layers in terms of H release similar good results should be possible.

6 IBC solar cells with POLO junctions for one polarity

This chapter describes the fabrication and investigates loss mechanisms of POLO-IBC solar cells. The POLO-IBC cell concept is part of the ISFH cell development roadmap [226] and was presented in 2018 [91]. As described in section 2.4.3 this concept aims to combine the lean process flow of the PERC technology with the high selectivity of a large-area n^+ POLO contact.

The presented POLO-IBC cell concept was invented by Robby Peibst in 2016 [227] and developed by Felix Haase and presented in 2018 [91]. The author took over the cell development from Felix Haase, who established the processes for fabricating the cells with several cell batches. The author supervised the processing of the latest cell batch shown in this chapter. David Sylla did the J - V measurements, and the author analyzed the results and did the simulation.

6.1 Cell structure and processing

The POLO-IBC cell process flow is performed using gallium doped p -type Cz wafers with a resistivity of $(1.3 \pm 0.2) \Omega \text{ cm}$. After a saw-damage etch step in a 50 % KOH solution and an RCA cleaning sequence, the wafers have a thickness of 150 μm . The main process starts with the growth of a $(1.5 \pm 0.2) \text{ nm}$ thick wet-chemically grown interfacial oxide in de-ionized water with diluted ozone. The oxide is subsequently

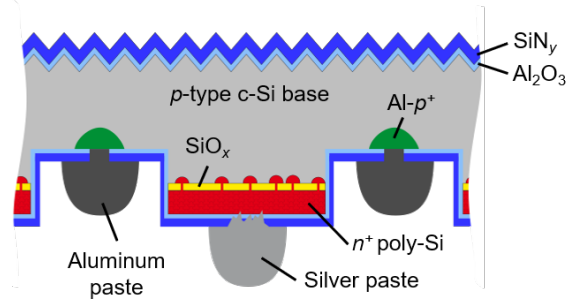


Figure 6.1: Schematic drawing of the POLO-IBC cell structure.

capped by a 200 nm-thick LPCVD in situ phosphorus-doped a-Si layer deposited at 580 °C. During a subsequent high-temperature wet oxidation step in a tube furnace at 860 °C for 30 min, the a-Si is completely crystallized, its surface is oxidized, and the interfacial oxide layer breaks up. Due to oxidation, the thickness of the poly-Si layer decreases to about (120 ± 10) nm. The oxidation step is directly followed by an impurity gettering step at 550 °C for 1 h in N₂ atmosphere [145], [146].

Subsequently, the oxide on the rear side is structured by a laser process to define the base region and the entire front side is laser processed. In this process, twenty one 20×20 mm² cells are defined on an M2 size wafer, as can be seen in Figure 6.2. A PECVD SiN_y layer is applied to protect the rear side from the subsequent texturization step of the front side in a KOH-based solution. After removing the SiN_y layer in an HF solution, the front and rear sides are passivated by a stack of an ALD Al₂O₃ layer and an MA-PECVD SiN_y layer with a refractive index of 2.05. On the textured front side the thicknesses are 10 nm/60 nm for Al₂O₃/SiN_y, respectively. On the planar rear side the thicknesses are either 10 nm/60 nm or 5 nm/85 nm for Al₂O₃/SiN_y, respectively. A laser is used to locally open the dielectric stack to form the laser contact openings in the base region. For the n⁺POLO contacts, we split the cell batch. In one group, the dielectric layer is locally opened by a laser, whereas the other group remains untreated.

The contact metallization is applied by screen printing with aluminum paste for the base metallization and silver paste for the n⁺POLO contact metallization, followed by a co-firing process for contact formation.

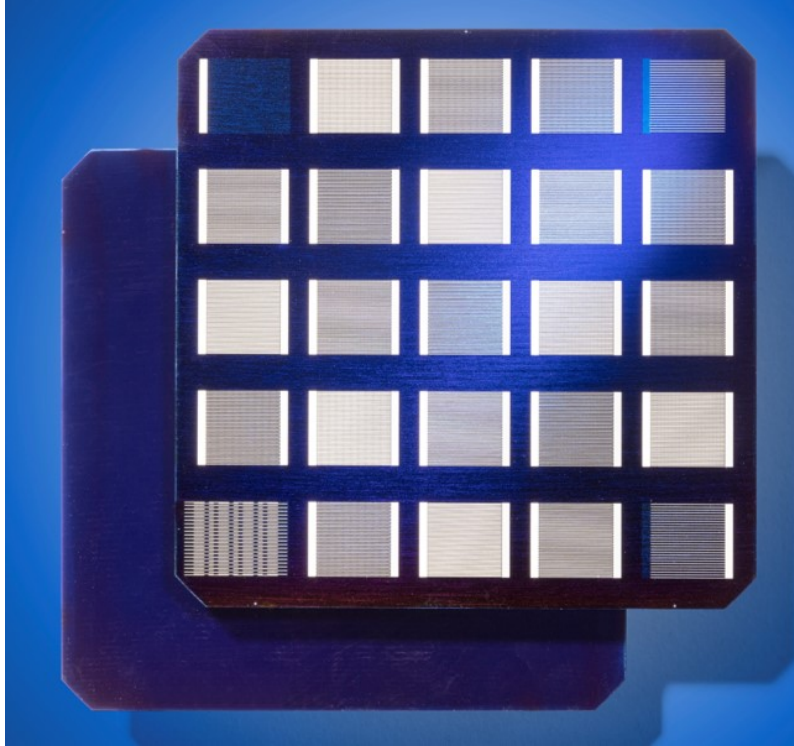


Figure 6.2: Photograph of a POLO-IBC wafer with twenty one $20 \times 20 \text{ mm}^2$ cells and 4 further test structures in the corners.

6.2 Analysis of loss mechanisms

To improve solar cell efficiencies, it is essential to optimize the structural cell parameters. In this case, finger pitch, contact LCO area fractions, and the thickness of the dielectric stack on the rear side are varied. The data obtained from this evaluation helps to identify further potential for improvement.

6.2.1 Evaluation of J - V results of different split groups

The study's main objective is to investigate the effect of different thicknesses of the dielectric stack on the rear surface. This $\text{Al}_2\text{O}_3/\text{SiN}_y$ stack has to fulfill different tasks simultaneously, which leads to opposing requirements concerning its thickness. On the one hand, the stack has to prevent the Al paste from unintentionally spiking through next to the LCOs, forming a very thin and bad contacts; on the other hand, it has to enable the Ag paste to fire through. In addition, the stack has to

provide good rear side passivation, which concerns both the direct passivation of the p -type base regions and the supply of an optimal amount of H during the firing to the n^+ POLO regions. As shown in the previous chapter, an $\text{Al}_2\text{O}_3/\text{SiN}_y$ stack that excellently passivates the base region is also very well suited for application on n^+ POLO junctions. Thus two stacks of 10 nm/60 nm $\text{Al}_2\text{O}_3/\text{SiN}_y$ and 5 nm/85 nm $\text{Al}_2\text{O}_3/\text{SiN}_y$ are compared in this study. A further parameter that is varied is the areal fraction of the $\text{Al-}p^+$ contact region by changing the finger pitch and the pitch of the $\text{Al-}p^+$ LCO dashes. Moreover, different firing temperatures are being tested.

Figure 6.3 shows the results of J - V measurements, done using a LOANA tool, of the different split groups as a function of the firing temperature. On the left hand side of the graph, cell with a 10 nm/60 nm $\text{Al}_2\text{O}_3/\text{SiN}_y$ stack and on the right hand side cells with a 5 nm/85 nm $\text{Al}_2\text{O}_3/\text{SiN}_y$ stack are shown. Their comparison shows that both splits archive cells with excellent efficiencies above 23 %.

The cells with n^+ POLO contact LCOs show great robustness towards the firing temperature as all temperature groups between 780 to 830 °C yield average results over 20 % and maximum values of ≥ 22 %. A comparison of the V_{oc} values with the group without LCOs shows that the fabrication of the n^+ POLO contact LCOs, at least with an SiN_y thickness of 60 nm, was, however, not done without any damage to the n^+ POLO contact. The cells without n^+ POLO contact LCOs clearly show the best V_{oc} values ≥ 718 mV, with an optimum at 800 °C. These high achieved V_{oc} values moreover show the overall good passivation quality, which is confirmed by lifetime measurements on cell precursor structures that are yielding values of $J_{0 \text{ front}} = (4.5 \pm 1.5) \text{ fA/cm}^2$, $J_{0, \text{rear}, n^+ \text{POLO}} = (0.75 \pm 0.55) \text{ fA/cm}^2$ and $J_{0 \text{ rear, base}} = (1.5 \pm 0.5) \text{ fA/cm}^2$.

Furthermore, the cells without n^+ POLO contact LOCs show an advantage of up to 1 to 2 % on average in pFF . The laser contact opening is probably more complicated for these cells than the POLO^2 -IBC cells due to a thinner poly-Si layer and a less homogeneous SiN_y layer instead of a thermally grown oxide.

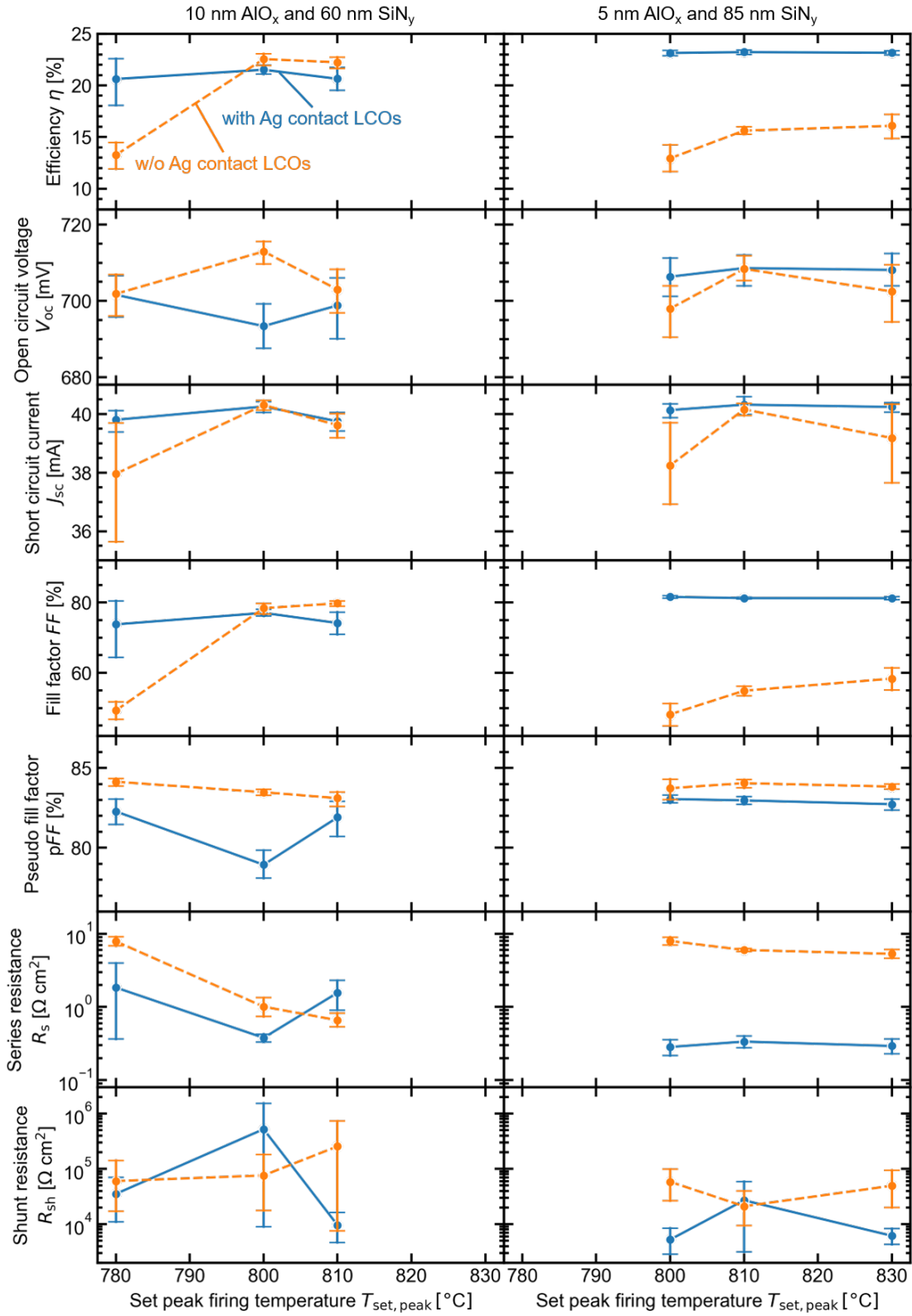


Figure 6.3: J - V parameters as a function of $T_{\text{set,peak}}$, for cells with 10 nm/60 nm $\text{Al}_2\text{O}_3/\text{SiN}_y$ (left column) and 5 nm/85 nm $\text{Al}_2\text{O}_3/\text{SiN}_y$ (right column). The error bars denote the 95 % confidence interval of measurements of 21 to 44 cells per marker.

The V_{oc} values of the samples without n^+ POLO contact LCOs are showing an optimum at 800 °C or 810 °C for the 10 nm/60 nm Al_2O_3/SiN_y and 5 nm/85 nm Al_2O_3/SiN_y group, respectively. At higher and especially lower temperatures, a decreasing trend is visible. Additionally, regarding the FF , it becomes clear that the process window for sufficient penetration of the Ag paste through the Al_2O_3/SiN_y stack is rather small. The series resistances of cells with the 10 nm/60 nm Al_2O_3/SiN_y layers show an increasing trend for lower temperatures, which results in just acceptable values of about $1 \Omega cm^2$ at 800 °C. With the thicker stack, none of the firing temperatures leads to acceptable R_s and thus FF values.

Fortunately, the problem of spiking of the Al paste through the Al_2O_3/SiN_y stack is not or only a marginal problem in this batch of cells regarding both groups. In the previous cell batch, it was a major limiting factor for the cells and could be seen as a decreased lifetime in ILM images by comparing Al printed and plain base regions without LCOs. However, such a difference in lifetime is not seen this time. Additionally, in this cell batch, a comparison of cells having the same Al- p^+ area fraction and different fractions of the area underneath the Al fingers, resulting from varying the two parameters finger pitch and Al- p^+ LCO pitch, does not show a falling trend in V_{oc} with an increasing fraction of area underneath the Al fingers.

The shunt resistances of all groups are large enough to not significantly limit the cell performance. Thus the damage introduced by LCOs on the n^+ POLO contacts is not as severe that it leads to a shunting problem.

Table 6.1: J - V parameters of the best POLO-IBC cells.

Cell name	Cell 1		Cell 2
Measurement	in-house	in-house	ISFH CalTeC
Al- p^+ area fraction	1.21 %		0.77 %
Al_2O_3/SiN_y thickness [nm]	10/60		5/85
n^+ POLO LCOs	no		yes
η [%]	23.82	23.75	23.92
V_{oc} [mV]	717.5	719.2	719.1
J_{sc} [cm^2]	40.67	40.57	41.09
FF [%]	81.63	81.38	80.97
pFF [%]	83.63	83.88	-
R_s [Ωcm^2]	0.43	0.49	-
R_{sh} [$M\Omega cm^2$]	0.1	0.2	-

In conclusion, the two best performing groups are cells with 10 nm Al_2O_3 and 60 nm SiN_y without n^+ POLO contact LOCs and the cells with 5 nm/85 nm of $\text{Al}_2\text{O}_3/\text{SiN}_y$ with n^+ POLO contact LCOs. The overall best cells of both groups can be found in Table 6.1. The best and independently confirmed result of 23.92 % conversion efficiency is achieved with a cell having n^+ POLO contact LOCs and the 5 nm/85 nm $\text{Al}_2\text{O}_3/\text{SiN}_y$ stack, closely followed by a cell with the thinner stack and without n^+ POLO contact LOCs, in-house measured with a LOANA tool with 23.82 % efficiency.

The two best split groups are also shown in Figure 6.4. The J - V parameters are plotted here versus the $\text{Al-}p^+$ area fraction. The markers connected by solid lines represent the measured data. In both groups, an apparent decrease in V_{oc} with increasing $\text{Al-}p^+$ area fraction can be seen, which is the main reason for the decreasing trend in efficiency. This is, however, partly compensated on the right-hand side by a simultaneously decreasing series resistance. However, the fact that the series resistance of the cells without LCOs tends to remain constant indicates that the resistance of the Ag contacts is primarily limiting here. The area fraction of the Ag contacts only double over the entire x-axis and does not increase fivefold as the $\text{Al-}p^+$ area fraction does. This probably has at least some influence on the slope of the R_s versus $T_{\text{set,peak}}$ data.

In addition to the measured data, results of simulations of the unit cell with the tool Quokka3 can also be seen in Figure 6.4 joined by dotted lines. As with the cells, the $\text{Al-}p^+$ LCO and finger pitches were varied for the simulations, resulting in the same $\text{Al-}p^+$ area fractions. In addition, the $J_{0,\text{Al-}p^+}$ is varied. Table 6.2 gives all the other parameters used for the simulation.

Looking at the V_{oc} values, it can be seen that the values simulated with $J_{0,\text{Al-}p^+} = 1500 \text{ fA/cm}^2$ describe the maximum measured V_{oc} values of up to 721.5 mV in the range of up to 2 % $\text{Al-}p^+$ fraction, quite well. However, there are deviations in J_{sc} and FF . The deviations in FF are at least partly due to the series resistance of the metal fingers, which is not considered in the unit cell simulations. A further simulation of a whole 2 cm long finger with otherwise identical parameters and finger line resistances of $0.96 \Omega/\text{cm}^2$ for the Al finger and $0.8 \Omega/\text{cm}^2$ for the Ag finger results in a 1.5 % lower FF . This leaves about 0.5 % difference between simulation and measurement.

6 IBC solar cells with POLO junctions for one polarity

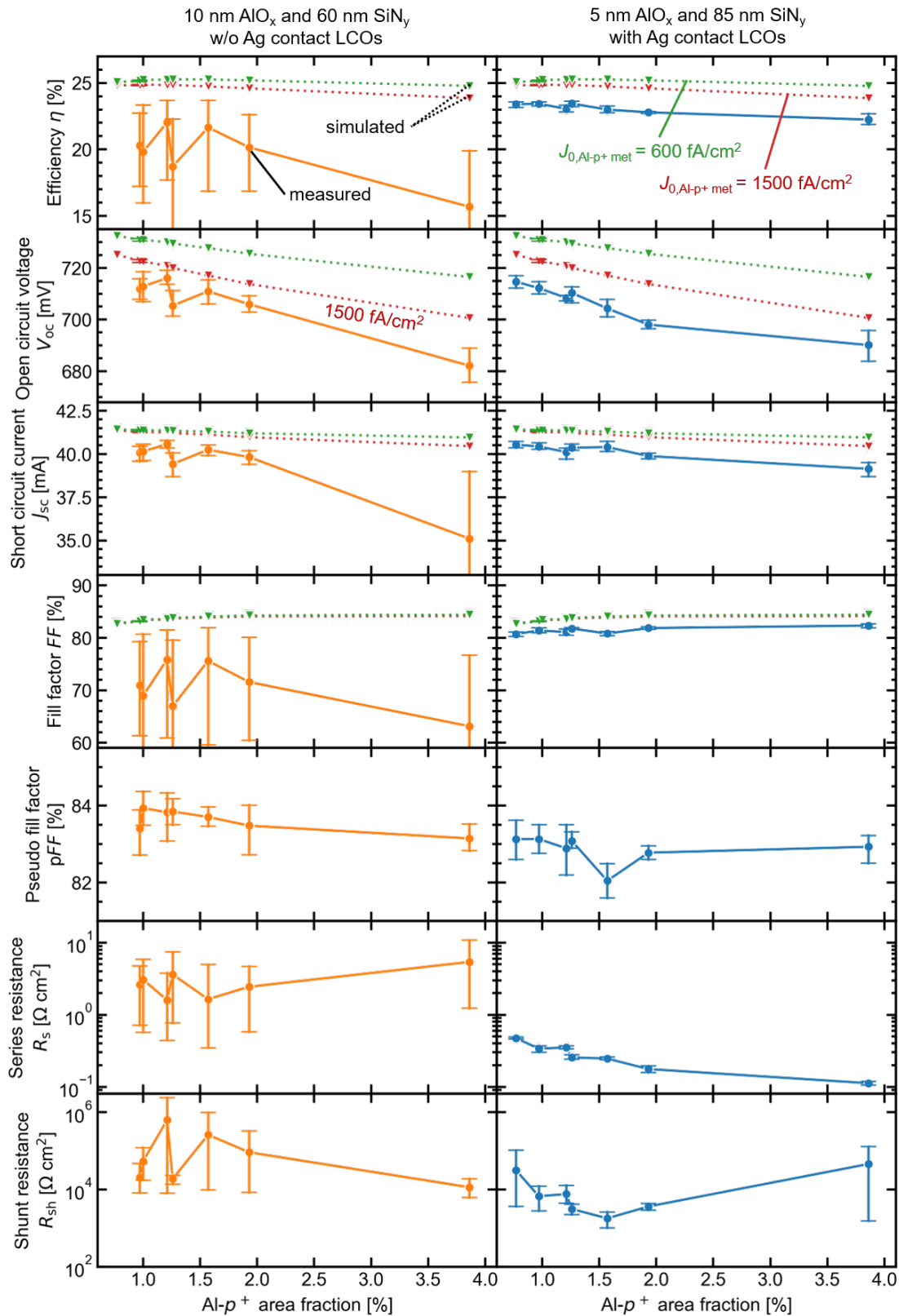


Figure 6.4: J - V parameters as a function of Al-p^+ area fraction. The circles joint by solid lines show measured data while the markers joined by dotted lines show simulation results assuming a $J_{0,\text{Al-p}^+}$ of 1500 fA/cm^2 (red) and 600 fA/cm^2 (green).

Table 6.2: Cell parameters of the processed cells and input parameters for the solar cell simulations.

Cell name			
Bulk doping type	<i>p</i> -type		
Bulk ρ_{bulk} [Ω cm]	0.89 - 1.5		
Cell thickness [μm]	160		
Bulk minority $\tau_{\text{SRH,bulk}}$ [ms]	2		
Base region front surface $J_{0,\text{front}}$ [fA/cm^2]	3		
Base region rear surface $J_{0,\text{rearbase}}$ [fA/cm^2]	1		
n^+ POLO region $J_{0,\text{rear } n^+\text{POLO}}$ [fA/cm^2]	0.2		
Contacted Al- p^+ region $J_{0,\text{Al-}p^+}$ [fA/cm^2]	1500/600		
R_{sheet} n^+ POLO region [Ω]	80		
Ag n^+ POLO contact $\rho_{c,p^+\text{POLO}}$ [$\text{m}\Omega \text{cm}^2$]	0.5		
Al- p^+ contact $\rho_{c,p^+\text{POLO}}$ [$\text{m}\Omega \text{cm}^2$]	0.5		
Finger pitch [μm]	500	750	1000
n^+ POLO region width [μm]	214	475	720
Base region width [μm]	259	275	280
Ag n^+ POLO contact width [μm]	60		
Al- p^+ contact width [μm]	38		
Al- p^+ contact dash length [μm]	250		
Al- p^+ contact pitch [mm]	0.5/0.8/1/1.25		
Ag finger width [μm]	60		
Al finger width [μm]	100		

That the J_{sc} is underestimated by the J - V measurements shown here is indicated by comparison to the calibrated measurement of the best cell at ISFH CalTeC in Table 6.1. This measurement yields a J_{sc} of $41.09 \text{ mA}/\text{cm}^2$, which is $0.52 \text{ mA}/\text{cm}^2$ higher than the J_{sc} measured by the LOANA tool and thus comes within approx. $0.5 \text{ mA}/\text{cm}^2$ of the simulated current. The reason for this may be a non-optimal manual positioning of the cells under the mask in the LOANA tool or a not optimal reference cell.

Overall, it can be concluded that the $J_{0,\text{Al-}p^+}$ of $1500 \text{ fA}/\text{cm}^2$ is a reasonable upper estimate. Whereas perimeter losses occurring during the masked J - V measurements, as shown for the POLO²-IBC cells 4.2.1, which are not taken into account in the simulation, could lead to somewhat lower J_0 values in reality. Nevertheless, this result indicates a significant deterioration compared to previous batches in which a $J_{0,\text{Al-}p^+}$ of $600 \text{ fA}/\text{cm}^2$ was determined using the same method. The simulation

data in green shows an estimation of what improvement would be possible with the excellent passivation of the non-contacted surfaces achieved in this cell batch in combination with a good $J_{0,Al-p^+} = 600 \text{ fA/cm}^2$ from the last one. Here, approx. 10 mV higher V_{oc} values and thus an efficiency potential higher by approx. 0.38 % of up to 25.26 % are determined by the simulation.

6.2.2 Free Energy Loss Analysis

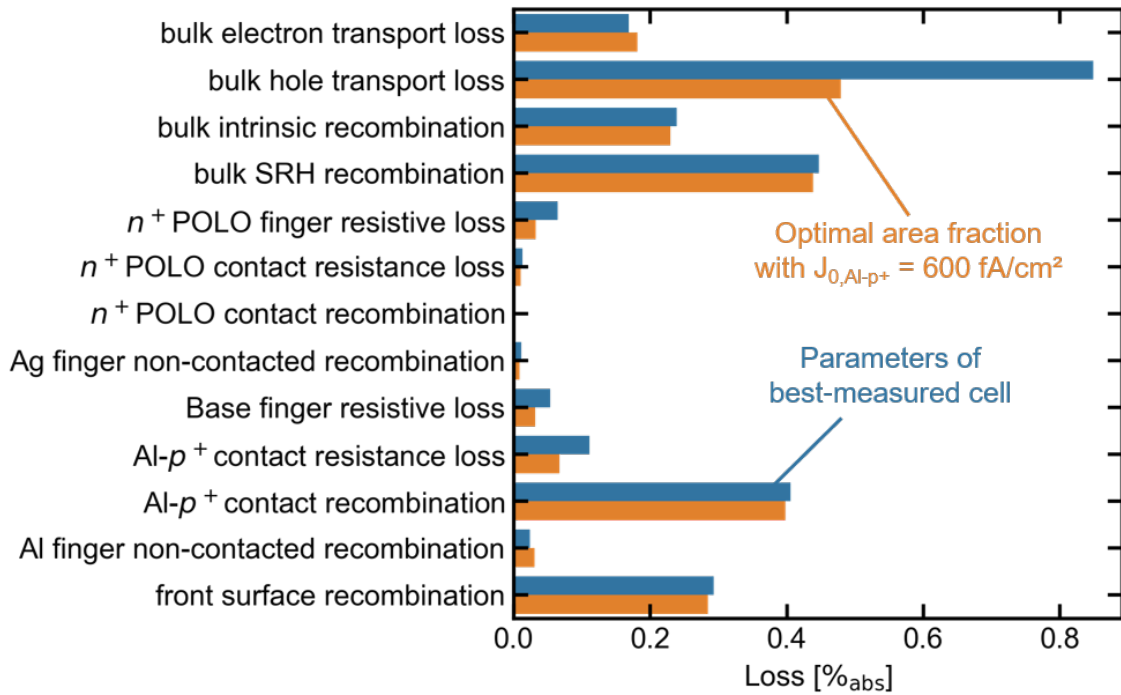


Figure 6.5: FELA analysis of two sets of cell parameters according to a Quokka3 simulation. The losses due to recombination and resistance are given in $\%_{abs}$. The blue data results from a simulated cell with a Al- p^+ contact pitch of 1.25 mm a finger pitch of 1 mm and an $J_{0,Al-p^+} = 1500 \text{ fA/cm}^2$. The cell simulation shown in orange has a finger pitch of 0.75 mm, a Al- p^+ contact pitch of 1 mm and a $J_{0,Al-p^+} = 600 \text{ fA/cm}^2$. For the other simulation parameters please refer to Table 6.2.

Figure 6.5 shows the FELA results of two simulated cells. The data shown in orange correspond to the cell parameters of the best-measured cell (cell 2 in Table 6.1) and shows a simulated potential of 24.82 % for the unit cell assuming $J_{0,Al-p^+} = 1500 \text{ fA/cm}^2$. With the Al- p^+ area fraction of 0.77 %, the cell is slightly below the simulated optimum of 1 % for this case, as shown by the high bulk hole transport

loss. With an $J_{0,\text{Al-p}^+} = 600 \text{ fA/cm}^2$ and an therefore optimal area fraction of 1.26 % (orange bars) a simulated potential of 25.28 % results with otherwise identical parameters.

As can be seen, with increasing passivation quality of the Al- p^+ contacts, a significant increase of the Al- p^+ fraction from 0.77 to 1.26 % is possible with approximately constant Al- p^+ contact recombination, leading to almost a halving of the bulk hole transport loss from 0.87 to 0.48 %. Reducing the finger pitch from 1 to 0.75 mm and the LCO spacing from 1.25 to 1 mm as done between the blue and orange data also decreases the n^+ POLO finger resistive loss, the Al- p^+ contact resistance loss, and the base finger resistive loss. All other losses show very similar magnitudes for the two simulated cells. Besides the bulk hole transport loss and Al- p^+ contact recombination, the bulk SRH recombination loss with about 0.4 % is the third largest loss mechanism, which depends primarily on the selected base material and its quality, which is followed by the 0.28 % loss due to recombination at the front surface with a $J_{0,\text{front}} = 3 \text{ fA/cm}^2$.

6.3 Summary and implications of Chapter 6

In this chapter, the investigations of multiple parameter variations for the design of POLO-IBC cells show the great potential of cells with passivating contacts and give important insights into different parts of the cells.

Regarding the Al- p^+ contacts, it is shown that an optimal Al- p^+ area fraction lies around 1 %, depending on the quality of the Al- p^+ contacts. Furthermore, it becomes clear that the Al- p^+ contacts are not optimally formed in this cell batch and thus fall short of what has already been shown. However, this leaves room for improvement.

Another finding is that n^+ POLO contact LCOs are a working solution to avoid Al spiking problems by thicker SiN_y layers, even though a slight advantage for n^+ POLO contacts without LCOs becomes apparent in V_{oc} and $\text{p}FF$ values.

Finally, simulations of the unit cell and a whole 2 cm long finger show that the finger resistances can lead to losses of up to 1.5 % in FF . Thus, a cell design with significantly shorter fingers would provide benefits here. On large, full-wafer POLO-IBC solar cells, a design with shorter fingers can be implemented by adjusting the

number of busbars accordingly.

Last but not least, the investigations in this chapter impressively show that the excellent passivation quality of n^+ POLO contacts can be successfully transferred to industry-relevant cell concepts. Thus, after firing at $T_{\text{set,peak}}$ 820 °C on precursors $J_{0,\text{rear},n^+\text{POLO}}$ values of down to 0.2 fA/cm² are achieved, enabling very promising efficiencies of up to 23.92 %.

7 Summary

The first part of this work dealt with analyzing POLO²-IBC solar cells, which include POLO junctions for both contact polarities separated by nominally intrinsic poly-Si regions. Despite the achieved world record efficiencies for *p*-type cells of 26.1 %, the goal here was to identify further improvement opportunities. Thus, in Chapter 4, an experimental and simulation study of the efficiency potential of POLO²-IBC cells with *p*⁺ and *n*⁺POLO junctions was presented. Special attention was paid to the comparison of different base materials. A FELA analysis showed that the most significant loss channel of the cells on low resistivity (1.3 Ω cm) *p*-type material is the intrinsic bulk recombination. Thus, at first glance, it seemed apparent that using a lower-doped base material is advantageous. However, both experimental analysis and simulations showed that high resistivity material (80 Ω cm) is significantly more vulnerable to passivation degradation or non-optimal passivation in the (*i*) poly-Si regions. Another major loss channel of 0.3 to 0.6 % efficiency, which also mainly affects cells on 80 Ω cm material, is perimeter recombination. Therefore, despite clear disadvantages in bulk recombination, the cells on the 1.3 Ω cm material ultimately performed better in both simulation and experiment. Furthermore, it was shown that the use of *n*-type material is also a possible option, which, although no adjustments to the process flow were made despite the change of the base doping in this experiment, reached an efficiency of 24.6 %. During the cell process, substantial losses showed up for these cells after the cell metallization. This is attributed to the emitter metallization overlapping with the (*i*) poly-Si-Si region in the case of the *n*-type base, leading to shunting currents through the leaky SiO_x on the rear side.

A distinct feature of the POLO²-IBC cells is a nominally intrinsic poly-Si region, separating the electron-collecting *n*-type poly-Si and the hole-collecting *p*-type poly-Si regions. This charge carrier separating region is an elegant method to avoid a lateral *p*⁺*n*⁺ poly-Si junction between the base and emitter poly-Si fingers. However, as shown in this work, there are a certain number of points that need to be taken

7 Summary

into account for the cell to function optimally. The aim of electrically separating the p^+ and n^+ fingers is to reduce the recombination current over the $p^+(i)n^+$ junction to an acceptable level. However, as the width of the (i) poly-Si regions increases, their poorer passivation quality can limit the cell performance. Another factor that affects this optimization problem is the strong diffusion of dopants into the nominally intrinsic poly-Si domain during the annealing of the POLO junctions. On the one hand, this improves the passivation quality of the (i) poly-Si region. However, on the other hand, it increases the recombination current over the $p^+(i)n^+$ junction and thus shifts the optimum with increasing annealing temperature to larger (i) poly-Si region widths, as shown by experiments. However, the results suggest that the cell concept strongly benefits from the fact that the dopants inside the poly-Si are mainly captured in trapping states at the grain boundaries up to a certain doping level. These trapped dopants are believed to create a potential barrier and thus a transport limitation for charge carriers, limiting the recombination current over the $p^+(i)n^+$ junction. This probably allows for smaller widths of the (i) poly-Si regions, thus improving surface passivation. The gained understanding of the $p^+(i)n^+$ junction will further pave the way for a strongly simplified fabrication of Si solar cells with efficiencies above 26 %.

The second part of this work focused on the firing stability of POLO junctions, which must be provided for implementing POLO junctions in industrial cell concepts. Chapter 5 aimed to answer why the firing of n^+ POLO junctions negatively affects their passivation quality and how applying hydrogen-containing capping layers can be used to improve the firing stability. The determined low activation energy of 0.3 eV of the defect formation process during firing of uncapped n^+ POLO junctions is not sufficient to explain the breaking of unstrained Si-O or Si-H bonds [180], [222]. This raised the question of why the firing process negatively influences the passivation quality while the tube furnace annealing processes lead to good J_0 values. Here, the higher heating and cooling rates during the firing were found to be the striking point. As a change in temperature leads to thermal expansion of the various layers of the sample, the significantly lower CTE of the oxide compared to c-Si and poly-Si leads to thermal stress. During the slower annealing process, viscous flow of the SiO_x is suspected of relieving the arising stress and repairing nevertheless created defects by a reorganization. In contrast, the heating and cooling rates during firing presumably prevent sufficient relaxation of the induced thermal stress by viscous flow.

If hydrogen is introduced during firing by Al_2O_3 , SiN_y , or $\text{Al}_2\text{O}_3/\text{SiN}_y$ layers to the c-Si/ SiO_x /poly-Si interface during and/or before firing, complex effects on the passivation quality are observed. A significant finding is that the deterioration of J_0 is significantly lower for samples with only Al_2O_3 or $\text{Al}_2\text{O}_3/\text{SiN}_y$ capping layers as compared to single SiN_y layers so that excellent J_0 values below 4 fA/cm^2 even at $T_{\text{set,peak}} = 900\text{ }^\circ\text{C}$ can be reached. The Al_2O_3 layer between the poly-Si and SiN_y layer here likely acts as a hydrogen in- and out-diffusion barrier regulating the amount of H at the interface. These results lead to the hypothesis that both too much and too little H can be the reason for an increased D_{it} after firing. Thus, depending on the intrinsic D_{it} and the D_{it} induced by firing, there is an optimum hydrogen concentration to achieve as low as possible J_0 values. Above this concentration, the excess hydrogen, which was found to exceed the D_{it} several times, is suspected of creating additional hydrogen-induced defects. The knowledge gained is essential to optimize an industrially relevant capping layer, which during firing helps to maintain the excellent passivation quality of POLO junctions.

The fact that this excellent passivation by POLO junctions can also be successfully used in an industrial cell process was shown in the last part of the work on POLO-IBC solar cells. Here, further optimization is required for the Al- p^+ contacts, which caused relatively strong recombination with $J_{0,\text{Al-}p^+}$ of about 1500 fA/cm^2 . Still, the excellent passivation quality of the front and rear surfaces enabled an efficiency of 23.92%. Overall, this work successfully implemented and transferred passivating contacts from highly efficient POLO²-IBC laboratory cells to the promising industry-relevant POLO-IBC cell concept.

Looking to the future, we can conclude that the efficiency potential of Si solar cells is still far from being exhausted. This is, for example, demonstrated by POLO²-IBC solar cells with novel light-trapping structures, which could achieve efficiencies of about 28 to 30% [76]. A further alternative for improving efficiency could be using POLO-IBC solar cells as lower subcells in 3-terminal tandem solar cells [228]. A particular advantage here would be that resistance losses play a much smaller role since the current densities are roughly halved, meaning that the area fraction of the previously limiting Al- p^+ contacts could be significantly reduced.

Bibliography

- [1] J. B. J. Fourier, „Remarques Generales sur les Temperatures Du Globe Terrestre et des Espaces Planetaires“, *Annales de Chemie et de Physique*, vol. 27, pp. 136–167, 1824.
- [2] John Tyndall, „On the Absorption and Radiation of Heat by Gaseous Matter.– Second Memoir“, *Proceedings of the Royal Society of London*, vol. 1860-1862, no. 11, pp. 558–561, 1860.
- [3] S. Arrhenius, „On the influence of carbonic acid in the air upon the temperature of the ground“, *The London, Edinburgh, and Dublin Philosophical Magazine and Journal of Science*, vol. 41, no. 251, pp. 237–276, 1896. DOI: 10.1080/14786449608620846.
- [4] G. S. Callendar, „The artificial production of carbon dioxide and its influence on temperature“, *Quarterly Journal of the Royal Meteorological Society*, vol. 64, no. 275, pp. 223–240, 1938. DOI: 10.1002/qj.49706427503.
- [5] *The limits to growth*, 2. ed. New York: Universe Books, 1974, ISBN: 0876631650.
- [6] Houghton J.T., G.J. Jenkins, and J.J. Ephraums, *Climate Change: The IPCC Scientific Assessment*, Cambridge University Press ,In Press, 1990.
- [7] H.-O. Pörtner, D.C. Roberts, M. Tignor, E.S. Poloczanska, K. Mintenbeck, A. Alegría, M. Craig, S. Langsdorf, S. Löschke, V. Möller, A. Okem, B. Rama, *Climate Change 2022: Impacts, Adaptation, and Vulnerability*, IPCC, Ed., Cambridge University Press ,In Press, 2022. [Online]. Available: <https://research.wur.nl/en/publications/climate-change-2022-impacts-adaptation-and-vulnerability>.
- [8] T. M. Lenton, J. Rockström, O. Gaffney, S. Rahmstorf, K. Richardson, W. Steffen, and H. J. Schellnhuber, „Climate tipping points - too risky to bet against“, *Nature*, vol. 575, no. 7784, pp. 592–595, 2019. DOI: 10.1038/d41586-019-03595-0.

Bibliography

- [9] R. S. Ohl, *Light-sensitive electric device*, US Patent 2,402,662, Jun. 1946.
- [10] D. M. Chapin, C. S. Fuller, and G. L. Pearson, „A New Silicon p–n Junction Photocell for Converting Solar Radiation into Electrical Power“, *Journal of Applied Physics*, vol. 25, no. 5, pp. 676–677, 1954. DOI: 10.1063/1.1721711.
- [11] W. Hemetsberger, M. Schmela, G. Chianetta, *Global Market Outlook for Solar Power 2021–2025*, SolarPower Europe, Ed., 2021.
- [12] The International Renewable Energy Agency, Ed., *IRENA, Renewable Energy Statistics 2020*, Abu Dhabi, 2020.
- [13] G. Luderer, C. Kost, and Dominika, *Deutschland auf dem Weg zur Klimaneutralität 2045 - Szenarien und Pfade im Modellvergleich (Ariadne-Report)*, G. Luderer, C. Kost, and D. Sörgel, Eds., Potsdam, 2021. DOI: 10.48485/pik.2021.006. [Online]. Available: <https://elib.dlr.de/147862/>.
- [14] V. Quaschnig, N. Orth, J. Weniger, J. Bergner, B. Siegel, M. Zoll, *Solarstromausbau für den Klimaschutz*, 2021. [Online]. Available: <https://pvspeicher.htw-berlin.de/solarstromausbau>.
- [15] Emiliano Bellini, *Longi achieves 25.21% efficiency for TOPCon solar cell*, pv magazine, Ed., 2020. [Online]. Available: <https://www.pv-magazine-india.com/2021/06/07/longi-achieves-25-21-efficiency-for-topcon-solar-cell/>.
- [16] JinkoSolar Holding Co., Ltd., *JinkoSolar’s High-efficiency N-Type Monocrystalline Silicon Solar Cell Sets New World Record with Highest Conversion Efficiency of 25.4%*, JinkoSolar, Ed., SHANGRAO, China, 2021. [Online]. Available: <https://ir.jinkosolar.com/news-releases/news-release-details/jinkosolars-high-efficiency-n-type-monocrystalline-silicon-solar%20https://www.pvtech..>
- [17] VDMA, *International Technology Roadmap for Photovoltaics: Results 2019 - 10th Edition 2020*.
- [18] A. B. Sproul and M. A. Green, „Improved value for the silicon intrinsic carrier concentration from 275 to 375 K“, *Journal of Applied Physics*, vol. 70, no. 2, pp. 846–854, 1991. DOI: 10.1063/1.349645.

- [19] P. P. Altermatt, A. Schenk, F. Geelhaar, and G. Heiser, „Reassessment of the intrinsic carrier density in crystalline silicon in view of band-gap narrowing“, *Journal of Applied Physics*, vol. 93, no. 3, pp. 1598–1604, 2003. DOI: 10.1063/1.1529297.
- [20] A. Richter, S. W. Glunz, F. Werner, J. Schmidt, and A. Cuevas, „Improved quantitative description of Auger recombination in crystalline silicon“, *Physical Review B*, vol. 86, no. 16, p. 187, 2012. DOI: 10.1103/PhysRevB.86.165202.
- [21] B. A. Veith-Wolf, S. Schäfer, R. Brendel, and J. Schmidt, „Reassessment of intrinsic lifetime limit in n-type crystalline silicon and implication on maximum solar cell efficiency“, *Solar Energy Materials and Solar Cells*, vol. 186, pp. 194–199, 2018. DOI: 10.1016/j.solmat.2018.06.029.
- [22] U. Würfel, A. Cuevas, and P. Würfel, „Charge carrier separation in solar cells“, *IEEE Journal of Photovoltaics*, vol. 5, no. 1, pp. 461–469, 2015.
- [23] R. Brendel and R. Peibst, „Contact Selectivity and Efficiency in Crystalline Silicon Photovoltaics“, *IEEE Journal of Photovoltaics*, vol. 6, no. 6, pp. 1413–1420, 2016. DOI: 10.1109/JPHOTOV.2016.2598267.
- [24] K. Yoshikawa, H. Kawasaki, W. Yoshida, T. Irie, K. Konishi, K. Nakano, T. Uto, D. Adachi, M. Kanematsu, H. Uzu, and K. Yamamoto, „Silicon heterojunction solar cell with interdigitated back contacts for a photoconversion efficiency over 26%“, *Nature Energy*, vol. 2, no. 5, p. 1552, 2017. DOI: 10.1038/nenergy.2017.32.
- [25] F. Haase, C. Hollemann, S. Schäfer, A. Merkle, M. Rienäcker, J. Krügener, R. Brendel, and R. Peibst, „Laser contact openings for local poly-Si-metal contacts enabling 26.1%-efficient POLO-IBC solar cells“, *Solar Energy Materials and Solar Cells*, vol. 186, pp. 184–193, 2018. DOI: 10.1016/j.solmat.2018.06.020.
- [26] M. A. Green, E. D. Dunlop, J. Hohl–Ebinger, M. Yoshita, N. Kopidakis, and X. Hao, „Solar cell efficiency tables (version 59)“, *Progress in Photovoltaics: Research and Applications*, vol. 30, no. 1, pp. 3–12, 2022. DOI: 10.1002/pip.3506.

Bibliography

- [27] V. Titova and J. Schmidt, „Selectivity of TiO_x –Based Electron–Selective Contacts on n–Type Crystalline Silicon and Solar Cell Efficiency Potential“, *physica status solidi (RRL) – Rapid Research Letters*, vol. 15, no. 9, p. 2100246, 2021. DOI: 10.1002/pssr.202100246.
- [28] G. Yang, A. Ingenito, O. Isabella, and M. Zeman, „IBC c-Si solar cells based on ion-implanted poly-silicon passivating contacts“, *Solar Energy Materials and Solar Cells*, vol. 158, pp. 84–90, 2016. DOI: 10.1016/j.solmat.2016.05.041.
- [29] C. Battaglia, S. M. de Nicolás, S. de Wolf, X. Yin, M. Zheng, C. Ballif, and A. Javey, „Silicon heterojunction solar cell with passivated hole selective MoO_x contact“, *Applied Physics Letters*, vol. 104, no. 11, p. 113902, 2014. DOI: 10.1063/1.4868880.
- [30] M. Bivour, J. Temmler, F. Zahringer, S. Glunz, and M. Hermle, „High work function metal oxides for the hole contact of silicon solar Cells“, in *Proceedings of the 2016 IEEE 43rd Photovoltaic Specialists Conference (PVSC)*, IEEE, 2016. DOI: 10.1109/PVSC.2016.7749581.
- [31] L. G. Gerling, G. Masmitja, C. Voz, P. Ortega, J. Puigdollers, and R. Alcubilla, „Back Junction n-type Silicon Heterojunction Solar Cells with V_2O_5 Hole-selective Contact“, *Energy Procedia*, vol. 92, pp. 633–637, 2016. DOI: 10.1016/j.egypro.2016.07.029.
- [32] S. Avasthi, S. Lee, Y.-L. Loo, and J. C. Sturm, „Role of majority and minority carrier barriers silicon/organic hybrid heterojunction solar cells“, *Advanced materials (Deerfield Beach, Fla.)*, vol. 23, no. 48, pp. 5762–5766, 2011. DOI: 10.1002/adma.201102712.
- [33] D. Zielke, C. Niehaves, W. Lövenich, A. Elschner, M. Hörteis, and J. Schmidt, „Organic-silicon Solar Cells Exceeding 20% Efficiency“, *Energy Procedia*, vol. 77, pp. 331–339, 2015. DOI: 10.1016/j.egypro.2015.07.047.
- [34] M.-U. Halbich, R. Sauer-Stieglitz, W. Lövenich, and J. Schmidt, „Improving Organic-Silicon Heterojunction Solar Cells through the Admixture of Sorbitol to PEDOT:PSS“, in *Proceedings of the 36th European Photovoltaic Solar Energy Conference and Exhibition*, Munich, Germany: WIP, 2019. DOI: 10.4229/EUPVSEC20192019-2C0.9.6.

- [35] J. Graul, A. Glasl, and H. Murrmann, „Ion implanted bipolar high performance transistors with polysil emitter“, in *1975 International Electron Devices Meeting*, IEEE, 1975. DOI: 10.1109/IEDM.1975.188920.
- [36] J. G. Fossum and M. A. Shibib, „A minority-carrier transport model for polysilicon contacts to silicon bipolar devices, including solar cells“, in *1980 International Electron Devices Meeting*, 1980. DOI: 10.1109/IEDM.1980.189814.
- [37] M. A. Green and A. W. Blakers, „Advantages of metal-insulator-semiconductor structures for silicon solar cells“, *Solar Cells*, vol. 8, no. 1, pp. 3–16, 1983. DOI: 10.1016/0379-6787(83)90036-4.
- [38] U. Römer, R. Peibst, T. Ohrdes, B. Lim, J. Krügener, E. Bugiel, T. Wietler, and R. Brendel, „Recombination behavior and contact resistance of n^+ and p^+ poly-crystalline Si/mono-crystalline Si junctions“, *Solar Energy Materials and Solar Cells*, vol. 131, pp. 85–91, 2014.
- [39] F. Feldmann, M. Bivour, C. Reichel, M. Hermle, and S. W. Glunz, „Passivated rear contacts for high-efficiency n-type Si solar cells providing high interface passivation quality and excellent transport characteristics“, *Solar Energy Materials and Solar Cells*, vol. 120, pp. 270–274, 2014. DOI: 10.1016/j.solmat.2013.09.017.
- [40] D. D. Smith, *Backside contact solar cell with formed polysilicon doped regions*, US Patent 8,242,354, Aug. 2012.
- [41] D. D. Smith, P. J. Cousins, A. Masad, A. Waldhauer, S. Westerberg, M. Johnson, X. Tu, T. Dennis, G. Harley, G. Solomon, S. Rim, M. Shepherd, S. Harrington, M. Defensor, A. Leygo, P. Tomada, J. Wu, T. Pass, L. Ann, L. Smith, N. Bergstrom, C. Nicdao, P. Tipones, and D. Vicente, „Generation III high efficiency lower cost technology: Transition to full scale manufacturing“, in *Proceedings of the 2012 IEEE 38th Photovoltaic Specialists Conference (PVSC)*, 2012, pp. 001 594–001 597. DOI: 10.1109/PVSC.2012.6317899.
- [42] D. Crafts and O. Schultz-Wittman, *Shielded electrical contact and doping through a passivating dielectric layer in a high-efficiency crystalline solar cell, including structure and methods of manufacture*, US Patent 9,184,314, Nov. 2015.

Bibliography

- [43] O. Schultz-Wittmann, A. Turner, B. Eggleston, D. de Ceuster, D. Suwito, E. van Kerschaver, S. Baker-Finch, and V. Prajapati, „High Volume Manufacturing of High Efficiency Crystalline Silicon Solar Cells with Shielded Metal Contacts“, in *Proceedings of the 32nd European Photovoltaic Solar Energy Conference and Exhibition*, Munich, Germany: WIP, 2016, pp. 456–459, ISBN: 3936338418. DOI: 10.4229/EUPVSEC20162016-2C0.4.5.
- [44] D. Chen, Y. Chen, Z. Wang, J. Gong, C. Liu, Y. Zou, Y. He, Y. Wang, L. Yuan, W. Lin, R. Xia, L. Yin, X. Zhang, G. Xu, Y. Yang, H. Shen, Z. Feng, P. P. Altermatt, and P. J. Verlinden, „24.58% total area efficiency of screen-printed, large area industrial silicon solar cells with the tunnel oxide passivated contacts (i-TOPCon) design“, *Solar Energy Materials and Solar Cells*, vol. 206, p. 110258, 2020. DOI: 10.1016/j.solmat.2019.110258.
- [45] M. Choi, P. Hyunjung, J. Choi, and Y. Choe, *Solar cell and method for manufacturing the same*, US Patent 10,566,484, Feb. 2020.
- [46] A. Bhambhani, *LONGi Reports 25.09% N-Type TOPCon Cell Efficiency*, TaiyangNews. [Online]. Available: <https://taiyangnews.info/technology/longi-reports-25-09-n-type-topcon-cell-efficiency/>.
- [47] Y. Chen, D. Chen, C. Liu, Z. Wang, Y. Zou, Y. He, Y. Wang, L. Yuan, J. Gong, W. Lin, X. Zhang, Y. Yang, H. Shen, Z. Feng, P. P. Altermatt, and P. J. Verlinden, „Mass production of industrial tunnel oxide passivated contacts (i-TOPCon) silicon solar cells with average efficiency over 23% and modules over 345 W“, *Progress in Photovoltaics: Research and Applications*, vol. 27, no. 10, pp. 827–834, 2019. DOI: 10.1002/pip.3180.
- [48] W. Wu, J. Bao, L. Ma, C. Chen, R. Liu, Z. Qiao, J. Chen, and Z. Liu, „Development of Industrial n-Type Bifacial TOPCon Solar Cells and Modules“, in *Proceedings of the 36th European Photovoltaic Solar Energy Conference and Exhibition*, F. Lambert, R. Kenny, and P. Helm, Eds., München and Florence: WIP, 2019, pp. 100–102. DOI: 10.4229/EUPVSEC20192019-2BP.1.5.
- [49] J. Bao, C. Chen, L. Ma, C. Huang, X. Zhang, Z. Wang, S. Zhan, R. Liu, Z. Qiao, Z. Du, Z. Liu, and J. Chen, „Towards 24% Efficiency for Industrial n-Type Bifacial Passivating-Contact Solar Cells with Homogeneous Emitter“, in *Proceedings of the 37th European Photovoltaic Solar Energy Conference and Exhibition*, N. Pearsall, R. P. Kenny, and P. Helm, Eds., München and Florence: WIP, 2020. DOI: 10.4229/EUPVSEC20202020-2A0.6.1.

- [50] A. Moldovan, F. Feldmann, M. Zimmer, J. Rentsch, J. Benick, and M. Hermle, „Tunnel oxide passivated carrier-selective contacts based on ultra-thin SiO₂ layers“, *Solar Energy Materials and Solar Cells*, vol. 142, pp. 123–127, 2015. DOI: 10.1016/j.solmat.2015.06.048.
- [51] F. Feldmann, M. Simon, M. Bivour, C. Reichel, M. Hermle, and S. W. Glunz, „Carrier-selective contacts for Si solar cells“, *Applied Physics Letters*, vol. 104, no. 18, p. 181105, 2014. DOI: 10.1063/1.4875904.
- [52] R. Peibst, Y. Larionova, S. Reiter, M. Turcu, R. Brendel, D. Tetzlaff, J. Krügener, T. Wietler, U. Höhne, J.-D. Kähler, H. Mehlich, and S. Frigge, „Implementation of n⁺ and p⁺ Poly Junctions on Front and Rear Side of Double-Side Contacted Industrial Silicon Solar Cells“, in *Proceedings of the 32nd European Photovoltaic Solar Energy Conference and Exhibition*, Munich, Germany: WIP, 2016, pp. 323–327. DOI: 10.4229/EUPVSEC20162016-2B0.3.2.
- [53] S. Choi, K. H. Min, M. S. Jeong, J. in Lee, M. G. Kang, H.-E. Song, Y. Kang, H.-S. Lee, D. Kim, and K.-H. Kim, „Structural evolution of tunneling oxide passivating contact upon thermal annealing“, *Scientific Reports*, vol. 7, no. 1, p. 12853, 2017. DOI: 10.1038/s41598-017-13180-y.
- [54] U. Römer, R. Peibst, T. Ohrdes, B. Lim, J. Krugener, T. Wietler, and R. Brendel, „Ion Implantation for Poly-Si Passivated Back-Junction Back-Contacted Solar Cells“, *IEEE Journal of Photovoltaics*, vol. 5, no. 2, pp. 507–514, 2015. DOI: 10.1109/JPHOTOV.2014.2382975.
- [55] J.Y. Gan and R.M. Swanson, „Polysilicon emitters for silicon concentrator solar cells“, in *IEEE Conference on Photovoltaic Specialists*, IEEE Conference on Photovoltaic Specialists, Ed., 1990.
- [56] J.-I. Polzin, S. Lange, S. Richter, A. Moldovan, M. Bivour, C. Hagendorf, M. Hermle, S. W. Glunz, and F. Feldmann, „Temperature-induced stoichiometric changes in thermally grown interfacial oxide in tunnel-oxide passivating contacts“, *Solar Energy Materials and Solar Cells*, vol. 218, p. 110713, 2020. DOI: 10.1016/j.solmat.2020.110713.
- [57] F. Feldmann, J. Schön, J. Niess, W. Lerch, and M. Hermle, „Studying dopant diffusion from Poly-Si passivating contacts“, *Solar Energy Materials and Solar Cells*, vol. 200, p. 109978, 2019. DOI: 10.1016/j.solmat.2019.109978.

Bibliography

- [58] M. Stöhr, J. Aprojanz, R. Brendel, and T. Dullweber, „Firing-Stable PECVD SiO_xN_y /n-Poly-Si Surface Passivation for Silicon Solar Cells“, *ACS Applied Energy Materials*, vol. 4, no. 5, pp. 4646–4653, 2021. DOI: 10.1021/acsaem.1c00265.
- [59] M. K. Stodolny, J. Anker, B. L. Geerligs, G. J. Janssen, B. W. van de Loo, J. Melskens, R. Santbergen, O. Isabella, J. Schmitz, M. Lenes, J.-M. Luchies, W. M. Kessels, and I. Romijn, „Material properties of LPCVD processed n-type polysilicon passivating contacts and its application in PERPoly industrial bifacial solar cells“, *Energy Procedia*, vol. 124, pp. 635–642, 2017. DOI: 10.1016/j.egypro.2017.09.250.
- [60] S. Mack, J. Schube, T. Fellmeth, F. Feldmann, M. Lenes, and J.-M. Luchies, „Metallisation of Boron-Doped Polysilicon Layers by Screen Printed Silver Pastes“, *physica status solidi (RRL) - Rapid Research Letters*, vol. 11, no. 12, p. 1700334, 2017. DOI: 10.1002/pssr.201700334.
- [61] A. Merkle, S. Seren, H. Knauss, B. Min, J. Steffens, B. Terheiden, R. Brendel, and R. Peibst, „Atmospheric Pressure Chemical Vapor Deposition of In-Situ Doped Amorphous Silicon Layers for Passivating Contacts“, in *Proceedings of the 35th European Photovoltaic Solar Energy Conference and Exhibition*, Munich, Germany, 2018. DOI: 10.4229/35THEUPVSEC20182018-2DV.3.49.
- [62] G. Nogay, J. Stuckelberger, P. Wyss, E. Rucavado, C. Allebé, T. Koida, M. Morales-Masis, M. Despeisse, F.-J. Haug, P. Löper, and C. Ballif, „Interplay of annealing temperature and doping in hole selective rear contacts based on silicon-rich silicon-carbide thin films“, *Solar Energy Materials and Solar Cells*, vol. 173, pp. 18–24, 2017. DOI: 10.1016/j.solmat.2017.06.039.
- [63] Di Yan, A. Cuevas, S. P. Phang, Y. Wan, and D. Macdonald, „23% efficient p-type crystalline silicon solar cells with hole-selective passivating contacts based on physical vapor deposition of doped silicon films“, *Applied Physics Letters*, vol. 113, no. 6, p. 061603, 2018. DOI: 10.1063/1.5037610.
- [64] L. Nasebandt, B. Min, S. Hübner, T. Dippell, P. Wohlfart, R. Peibst, and R. Brendel, „Controlling Doping Density in DC-Sputtered In-Situ Phosphorous-Doped Polysilicon Layers for Passivating Contacts“, in *Proceedings of the 38th European Photovoltaic Solar Energy Conference and Exhibition*, J. Serra, R. P. Kenny, and P. Helm, Eds., München, Germany: WIP, 2021. DOI: 10.4229/EUPVSEC20212021-2B0.11.5.

- [65] A. Morisset, T. Famprakis, F.-J. Haug, A. Ingenito, C. Ballif, and L. J. Banenberg, „In Situ Reflectometry and Diffraction Investigation of the Multiscale Structure of p-Type Polysilicon Passivating Contacts for c-Si Solar Cells“, *ACS Applied Materials & Interfaces*, vol. 14, no. 14, pp. 16 413–16 423, 2022. DOI: 10.1021/acsami.2c01225.
- [66] R. Peibst, U. Römer, Y. Larionova, M. Rienäcker, A. Merkle, N. Folchert, S. Reiter, M. Turcu, B. Min, J. Krügener, D. Tetzlaff, E. Bugiel, T. Wietler, and R. Brendel, „Working principle of carrier selective poly-Si/c-Si junctions: Is tunnelling the whole story?“, *Solar Energy Materials and Solar Cells*, vol. 158, pp. 60–67, 2016. DOI: 10.1016/j.solmat.2016.05.045.
- [67] D. Tetzlaff, J. Krügener, Y. Larionova, S. Reiter, M. Turcu, F. Haase, R. Brendel, R. Peibst, U. Höhne, J.-D. Kähler, and T. Wietler, „A simple method for pinhole detection in carrier selective POLO-junctions for high efficiency silicon solar cells“, *Solar Energy Materials and Solar Cells*, 2017. DOI: 10.1016/j.solmat.2017.05.041.
- [68] A. Harter, J.-I. Polzin, L. Tutsch, J. Temmler, M. Hofmann, A. Moldovan, and F. Feldmann, „Influence of Intrinsic Silicon Layer and Intermediate Silicon Oxide Layer on the Performance of Inline PECVD Deposited Boron-Doped TOPCon“, *IEEE Journal of Photovoltaics*, vol. 11, no. 4, pp. 936–943, 2021. DOI: 10.1109/JPHOTOV.2021.3071220.
- [69] A. Ingenito, G. Nogay, J. Stuckelberger, P. Wyss, L. Gnocchi, C. Allebe, J. Horzel, M. Despeisse, F.-J. Haug, P. Loper, and C. Ballif, „Phosphorous-Doped Silicon Carbide as Front-Side Full-Area Passivating Contact for Double-Side Contacted c-Si Solar Cells“, *IEEE Journal of Photovoltaics*, vol. 9, no. 2, pp. 346–354, 2019. DOI: 10.1109/JPHOTOV.2018.2886234.
- [70] A. Ingenito, G. Nogay, Q. Jeangros, E. Rucavado, C. Allebé, S. Eswara, N. Valle, T. Wirtz, J. Horzel, T. Koida, M. Morales-Masis, M. Despeisse, F.-J. Haug, P. Löper, and C. Ballif, „A passivating contact for silicon solar cells formed during a single firing thermal annealing“, *Nature Energy*, vol. 3, no. 9, pp. 800–808, 2018. DOI: 10.1038/s41560-018-0239-4.
- [71] L. Galleni, M. Firat, H. S. Radhakrishnan, F. Duerinckx, L. Tous, and J. Poortmans, „Mechanisms of charge carrier transport in polycrystalline silicon passivating contacts“, *Solar Energy Materials and Solar Cells*, vol. 232, p. 111 359, 2021. DOI: 10.1016/j.solmat.2021.111359.

Bibliography

- [72] F. Feldmann, G. Nogay, P. Löper, D. L. Young, B. G. Lee, P. Stradins, M. Hermle, and S. W. Glunz, „Charge carrier transport mechanisms of passivating contacts studied by temperature-dependent J-V measurements“, *Solar Energy Materials and Solar Cells*, vol. 178, pp. 15–19, 2018. DOI: 10.1016/j.solmat.2018.01.008.
- [73] N. Folchert, R. Peibst, and R. Brendel, „Modeling recombination and contact resistance of poly-Si junctions“, *Progress in Photovoltaics: Research and Applications*, vol. 28, no. 12, pp. 1289–1307, 2020. DOI: 10.1002/pip.3327.
- [74] T. Niewelt, A. Richter, T. C. Kho, N. E. Grant, R. S. Bonilla, B. Steinhauser, J.-I. Polzin, F. Feldmann, M. Hermle, J. D. Murphy, S. P. Phang, W. Kwapil, and M. C. Schubert, „Taking monocrystalline silicon to the ultimate lifetime limit“, *Solar Energy Materials and Solar Cells*, vol. 185, pp. 252–259, 2018. DOI: 10.1016/j.solmat.2018.05.040.
- [75] B. Steinhauser, J.-I. Polzin, F. Feldmann, M. Hermle, and S. W. Glunz, „Excellent Surface Passivation Quality on Crystalline Silicon Using Industrial-Scale Direct-Plasma TOPCon Deposition Technology“, *Solar RRL*, vol. 2, no. 7, p. 1800068, 2018. DOI: 10.1002/solr.201800068.
- [76] R. Peibst, M. Rienäcker, Y. Larionova, N. Folchert, F. Haase, C. Hollemann, S. Wolter, J. Krügener, P. Bayerl, J. Bayer, M. Dzinnik, R. J. Haug, and R. Brendel, „Towards 28 %-efficient Si single-junction solar cells with better passivating POLO junctions and photonic crystals“, *Solar Energy Materials and Solar Cells*, vol. 238, p. 111560, 2022. DOI: 10.1016/j.solmat.2021.111560.
- [77] A. G. Aberle, *Crystalline silicon solar cells*, Reprinted. Sydney: Centre for Photovoltaic Engineering Univ. of NSW, 2000, ISBN: 0733406459.
- [78] M. K. Stodolny, M. Lenes, Y. Wu, G. Janssen, I. G. Romijn, J. Luchies, and L. J. Geerligs, „n-Type polysilicon passivating contact for industrial bifacial n-type solar cells“, *Solar Energy Materials and Solar Cells*, vol. 158, pp. 24–28, 2016. DOI: 10.1016/j.solmat.2016.06.034.
- [79] M. Lehmann, N. Valle, J. Horzel, A. Pshenova, P. Wyss, M. Döbeli, M. Despeisse, S. Eswara, T. Wirtz, Q. Jeangros, A. Hessler-Wyser, F.-J. Haug, A. Ingenito, and C. Ballif, „Analysis of hydrogen distribution and migration in fired passivating contacts (FPC)“, *Solar Energy Materials and Solar Cells*, vol. 200, p. 110018, 2019. DOI: 10.1016/j.solmat.2019.110018.

- [80] T. N. Truong, Di Yan, C. Samundsett, A. Liu, S. P. Harvey, M. Young, Z. Ding, M. Tebyetekerwa, F. Kremer, M. Al-Jassim, A. Cuevas, D. Macdonald, and H. T. Nguyen, „Hydrogen-Assisted Defect Engineering of Doped Poly-Si Films for Passivating Contact Solar Cells“, *ACS Applied Energy Materials*, vol. 2, no. 12, pp. 8783–8791, 2019. DOI: 10.1021/acsaem.9b01771.
- [81] B. Nemeth, D. L. Young, M. R. Page, V. LaSalvia, S. Johnston, R. Reedy, and P. Stradins, „Polycrystalline silicon passivated tunneling contacts for high efficiency silicon solar cells“, *Journal of Materials Research*, vol. 31, no. 6, pp. 671–681, 2016. DOI: 10.1557/jmr.2016.77.
- [82] M. Schnabel, B. W. H. van de Loo, W. Nemeth, B. Macco, P. Stradins, W. M. M. Kessels, and D. L. Young, „Hydrogen passivation of poly-Si/SiO_x contacts for Si solar cells using Al₂O₃ studied with deuterium“, *Applied Physics Letters*, vol. 112, no. 20, p. 203901, 2018. DOI: 10.1063/1.5031118.
- [83] M. Rienäcker, A. Merkle, U. Römer, H. Kohlenberg, J. Krügener, R. Brendel, and R. Peibst, „Recombination Behavior of Photolithography-free Back Junction Back Contact Solar Cells with Carrier-selective Polysilicon on Oxide Junctions for Both Polarities“, *Energy Procedia*, vol. 92, pp. 412–418, 2016. DOI: 10.1016/j.egypro.2016.07.121.
- [84] D. L. Young, W. Nemeth, V. LaSalvia, R. Reedy, S. Essig, N. Bateman, and P. Stradins, „Interdigitated Back Passivated Contact (IBPC) Solar Cells Formed by Ion Implantation“, *IEEE Journal of Photovoltaics*, vol. 6, no. 1, pp. 41–47, 2016. DOI: 10.1109/JPHOTOV.2015.2483364.
- [85] F. Haase, F. Kiefer, S. Schäfer, C. Kruse, J. Krügener, R. Brendel, and R. Peibst, „Interdigitated back contact solar cells with polycrystalline silicon on oxide passivating contacts for both polarities“, *Japanese Journal of Applied Physics*, vol. 56, no. 8S2, 08MB15, 2017. DOI: 10.7567/JJAP.56.08MB15.
- [86] C. Reichel, R. Müller, F. Feldmann, A. Richter, M. Hermle, and S. W. Glunz, „Influence of the transition region between p- and n-type polycrystalline silicon passivating contacts on the performance of interdigitated back contact silicon solar cells“, *Journal of Applied Physics*, vol. 122, no. 18, p. 184502, 2017. DOI: 10.1063/1.5004331.
- [87] VDMA, *International Technology Roadmap for Photovoltaics: Results 2020 - 11th Edition 2021*.

Bibliography

- [88] S. W. Glunz, B. Steinhauser, J.-I. Polzin, C. Luderer, B. Gröbel, T. Niewelt, A. M. O. M. Okasha, M. Bories, H. Nagel, K. Krieg, F. Feldmann, A. Richter, M. Bivour, and M. Hermle, „Silicon-based passivating contacts: The TOP-Con route“, *Progress in Photovoltaics: Research and Applications*, 2021. DOI: 10.1002/pip.3522.
- [89] Y. Tao, V. Upadhyaya, C.-W. Chen, A. Payne, E. L. Chang, A. Upadhyaya, and A. Rohatgi, „Large area tunnel oxide passivated rear contact n-type Si solar cells with 21.2% efficiency“, *Progress in Photovoltaics: Research and Applications*, vol. 24, no. 6, pp. 830–835, 2016. DOI: 10.1002/pip.2739.
- [90] S. Duttagupta, N. Nandakumar, P. Padhamnath, J. K. Buatis, R. Stangl, and A. G. Aberle, „monoPoly™ cells: Large-area crystalline silicon solar cells with fire-through screen printed contact to doped polysilicon surfaces“, *Solar Energy Materials and Solar Cells*, vol. 187, pp. 76–81, 2018. DOI: 10.1016/j.solmat.2018.05.059.
- [91] F. Haase, C. Hollemann, S. Schafer, J. Krugener, R. Brendel, and R. Peibst, „Transferring the Record p-type Si POLO-IBC Cell Technology Towards an Industrial Level“, in *2019 IEEE 46th Photovoltaic Specialists Conference (PVSC)*, IEEE, 2019. DOI: 10.1109/pvsc40753.2019.8980960.
- [92] R. Peibst, C. Kruse, S. Schäfer, V. Mertens, S. Bordihn, T. Dullweber, F. Haase, C. Hollemann, B. Lim, B. Min, R. Niepelt, H. Schulte-Huxel, and R. Brendel, „For none, one, or two polarities—How do POLO junctions fit best into industrial Si solar cells?“, *Progress in Photovoltaics: Research and Applications*, vol. 28, no. 6, pp. 503–516, 2020. DOI: 10.1002/pip.3201.
- [93] R. Peibst, F. Haase, B. Min, C. Hollemann, T. Brendemühl, K. Bothe, and R. Brendel, „On the chances and challenges of combining electron-collecting nPOLO and hole-collecting Al- p^+ contacts in highly efficient p-type c-Si solar cells“, *Progress in Photovoltaics: Research and Applications*, 2022. DOI: 10.1002/pip.3545.
- [94] T. Dullweber, C. Kranz, R. Peibst, U. Baumann, H. Hannebauer, A. Fülle, S. Steckemetz, T. Weber, M. Kutzer, M. Müller, G. Fischer, P. Palinginis, and H. Neuhaus, „PERC+: industrial PERC solar cells with rear Al grid enabling bifaciality and reduced Al paste consumption“, *Progress in Photovoltaics: Research and Applications*, vol. 24, no. 12, pp. 1487–1498, 2016. DOI: 10.1002/pip.2712.

- [95] H. E. Çiftçinar, M. K. Stodolny, Y. Wu, G. J. Janssen, J. Löffler, J. Schmitz, M. Lenes, J.-M. Luchies, and L. J. Geerligs, „Study of screen printed metalization for polysilicon based passivating contacts“, *Energy Procedia*, vol. 124, pp. 851–861, 2017. DOI: 10.1016/j.egypro.2017.09.242.
- [96] A. Mewe, M. Stodolny, J. Anker, M. Lenes, X. Pagès, Y. Wu, K. Tool, B. Geerligs, and I. Romijn, „Full wafer size IBC cell with polysilicon passivating contacts“, in *Proceeding of the SiliconPV 2018, the 8th International Conference on Crystalline Silicon Photovoltaics*, ser. AIP Conference Proceedings, Melville, New York: AIP Publishing, 2018, p. 040014. DOI: 10.1063/1.5049277.
- [97] P. Padhamnath, J. Wong, B. Nagarajan, J. K. Buatis, L. M. Ortega, N. Nandakumar, A. Khanna, V. Shanmugam, and S. Duttagupta, „Metal contact recombination in monoPoly™ solar cells with screen-printed & fire-through contacts“, *Solar Energy Materials and Solar Cells*, vol. 192, pp. 109–116, 2019. DOI: 10.1016/j.solmat.2018.12.026.
- [98] M. K. Stodolny, J. Anker, C. Tool, M. Koppes, A. A. Mewe, P. Manshanden, M. Lenes, and I. G. Romijn, „Novel schemes of P^+ poly-Si hydrogenation implemented in industrial 6 "bifacial front-and-rear passivating contacts solar cells“, in *Proceedings of the 35th European Photovoltaic Solar Energy Conference and Exhibition*, Munich, Germany, 2018.
- [99] M. Stodolny, K. Tool, B. Geerligs, J. Löffler, A. Weeber, Y. Wu, J. Anker, X. Lu, J. Liu, P. Bronsveld, A. Mewe, G. Janssen, and G. Coletti, „PolySi Based Passivating Contacts Enabling Industrial Silicon Solar Cell Efficiencies up to 24%“, in *Proceedings of the Photovoltaic Specialists (PVSC), IEEE Conference*, IEEE Xplore, 2019, pp. 1456–1459. DOI: 10.1109/PVSC40753.2019.8980806.
- [100] C. Hollemann, F. Haase, J. Krugener, R. Brendel, and R. Peibst, „Firing stability of n-type poly-Si on oxide junctions formed by quartz tube annealing“, in *Proceedings of the 2020 IEEE 44th Photovoltaic Specialist Conference (PVSC)*, IEEE, 2020, pp. 1274–1278. DOI: 10.1109/PVSC45281.2020.9300849.
- [101] B. W. van de Loo, B. Macco, M. Schnabel, M. K. Stodolny, A. A. Mewe, D. L. Young, W. Nemeth, P. Stradins, and W. M. Kessels, „On the hydrogenation of Poly-Si passivating contacts by Al_2O_3 and SiN thin films“, *Solar Energy*

Bibliography

- Materials and Solar Cells*, vol. 215, p. 110 592, 2020. DOI: 10 . 1016 / j . solmat . 2020 . 110592.
- [102] B. Steinhauser, F. Feldmann, D. Ourinson, H. Nagel, T. Fellmeth, and M. Hermle, „On the Influence of the SiN_x Composition on the Firing Stability of Poly-Si/SiN_x Stacks“, *physica status solidi (a)*, vol. 217, no. 21, p. 2 000 333, 2020. DOI: 10 . 1002 / pssa . 202000333.
- [103] D. Kang, H. C. Sio, D. Yan, W. Chen, J. Yang, J. Jin, X. Zhang, and D. Macdonald, „Long-term stability study of the passivation quality of polysilicon-based passivation layers for silicon solar cells“, *Solar Energy Materials and Solar Cells*, vol. 215, no. 6, p. 110 691, 2020. DOI: 10 . 1016 / j . solmat . 2020 . 110691.
- [104] C. Hollemann, M. Rienäcker, A. Soeriyadi, C. Madumelu, F. Haase, J. Krügener, B. Hallam, R. Brendel, and R. Peibst, „Firing stability of tube furnace-annealed n-type poly-Si on oxide junctions“, *Progress in Photovoltaics: Research and Applications*, 2021. DOI: 10 . 1002 / pip . 3459.
- [105] C. Hollemann, N. Folchert, S. P. Harvey, P. Stradins, D. L. Young, C. L. Salles de Souza, M. Rienäcker, F. Haase, R. Brendel, and R. Peibst, „Changes in hydrogen concentration and defect state density at the poly-Si/SiO_x/c-Si interface due to firing“, *Solar Energy Materials and Solar Cells*, vol. 231, p. 111 297, 2021. DOI: 10 . 1016 / j . solmat . 2021 . 111297.
- [106] D. Kang, H. C. Sio, J. Stuckelberger, D. Yan, H. T. Nguyen, T. N. Truong, R. Liu, and D. Macdonald, „Firing Stability of Polysilicon Passivating Contacts: The Role of Hydrogen“, in *2021 IEEE 48th Photovoltaic Specialists Conference (PVSC)*, IEEE, 2021, pp. 0701–0705. DOI: 10 . 1109 / PVSC43889 . 2021 . 9519080.
- [107] J.-I. Polzin, B. Hammann, T. Niewelt, W. Kwapil, M. Hermle, and F. Feldmann, „Thermal activation of hydrogen for defect passivation in poly-Si based passivating contacts“, *Solar Energy Materials and Solar Cells*, vol. 230, p. 111 267, 2021. DOI: 10 . 1016 / j . solmat . 2021 . 111267.
- [108] D. Kang, H. C. Sio, J. Stuckelberger, R. Liu, Di Yan, X. Zhang, and D. Macdonald, „Optimum Hydrogen Injection in Phosphorus-Doped Polysilicon Passivating Contacts“, *ACS Applied Materials & Interfaces*, 2021. DOI: 10 . 1021 / acsami . 1c17342.

- [109] D. Kang, H. C. Sio, Di Yan, J. Stuckelberger, X. Zhang, and D. Macdonald, „Firing stability of phosphorus-doped polysilicon passivating contacts: Factors affecting the degradation behavior“, *Solar Energy Materials and Solar Cells*, vol. 234, p. 111 407, 2022. DOI: 10.1016/j.solmat.2021.111407.
- [110] Di Kang, H. C. Sio, J. Stuckelberger, Di Yan, S. P. Phang, R. Liu, T. N. Truong, T. Le, H. T. Nguyen, X. Zhang, and D. Macdonald, „Comparison of firing stability between p- and n-type polysilicon passivating contacts“, *Progress in Photovoltaics: Research and Applications*, 2022. DOI: 10.1002/pip.3544.
- [111] B. Min, L. Nasebandt, C. Hollemann, D. Bredemeier, L. Thiemann, T. Brendemühl, K. Bothe, R. Peibst, R. Brendel, „Recent progress of POLO back junction solar cells“, in *submitted for 8th World Conference on Photovoltaic Energy Conversion*, München, Germany: WIP, 2022.
- [112] R. A. Sinton and A. Cuevas, „Contactless determination of current–voltage characteristics and minority–carrier lifetimes in semiconductors from quasi–steady–state photoconductance data“, *Applied Physics Letters*, vol. 69, no. 17, pp. 2510–2512, 1996. DOI: 10.1063/1.117723.
- [113] Lailah Helmich, „Improved understanding of boron-oxygen-related carrier lifetime degradation and regeneration in crystalline silicon solar cells“, doctoral dissertation, Leibniz Universität Hannover, Hannover, 2022.
- [114] D. Klaassen, „A unified mobility model for device simulation—II. Temperature dependence of carrier mobility and lifetime“, *Solid-state electronics*, vol. 35, no. 7, pp. 961–967, 1992. DOI: 10.1016/0038-1101(92)90326-8.
- [115] D. E. Kane, R. M. Swanson, „Measurement of the Emitter Saturation Current by a Contactless Photoconductivity Decay Method“, in *18th IEEE photovoltaic specialists conference*, 1985, pp. 578–583.
- [116] A. L. Blum, J. S. Swirhun, R. A. Sinton, and A. Kimmerle, „An Updated Analysis to the WCT-120 QSSPC Measurement System Using Advanced Device Physics“, in *Proceedings of the 28th European Photovoltaic Solar Energy Conference and Exhibition*, A. Mine, Ed., München: WIP, 2013. DOI: 10.4229/28thEUPVSEC2013-2CV.3.3.

Bibliography

- [117] A. Kimmerle, P. Rothhardt, A. Wolf, and R. A. Sinton, „Increased Reliability for J_0 -analysis by QSSPC“, *Energy Procedia*, vol. 55, pp. 101–106, 2014. DOI: 10.1016/j.egypro.2014.08.087.
- [118] E. K. Banghart and J. L. Gray, „Extension of the open-circuit voltage decay technique to include plasma-induced bandgap narrowing“, *IEEE Transactions on Electron Devices*, vol. 39, no. 5, pp. 1108–1114, 1992. DOI: 10.1109/16.129090.
- [119] T. Otaredian, „Separate contactless measurement of the bulk lifetime and the surface recombination velocity by the harmonic optical generation of the excess carriers“, *Solid-State Electronics*, vol. 36, no. 2, pp. 153–162, 1993. DOI: 10.1016/0038-1101(93)90134-c.
- [120] M. Bail, J. Kentsch, R. Brendel, and M. Schulz, „Lifetime mapping of Si wafers by an infrared camera [for solar cell production]“, in *Conference Record of the Twenty-Eighth IEEE Photovoltaic Specialists Conference - 2000*, IEEE, 2000, pp. 99–103. DOI: 10.1109/PVSC.2000.915763.
- [121] K. Ramspeck, „Characterization of solar cells and material using Infrared Imaging techniques“, doctoral dissertation, Leibniz Universität Hannover, Hannover, 2009.
- [122] K. Ramspeck, S. Reissenweber, J. Schmidt, K. Bothe, and R. Brendel, „Dynamic carrier lifetime imaging of silicon wafers using an infrared-camera-based approach“, *Applied Physics Letters*, vol. 93, no. 10, p. 102104, 2008. DOI: 10.1063/1.2972122.
- [123] O. Breitenstein, *Lock-in Thermography*. Berlin and Heidelberg: Springer, 2003, vol. 10, ISBN: 978-3-642-07785-2. DOI: 10.1007/978-3-662-08396-3.
- [124] S. Herlufsen, „Characterization of crystalline silicon based on measurements of the photoluminescence emission“, doctoral dissertation, Leibniz Universität Hannover, Hannover, 2013.
- [125] W. van Roosbroeck and W. Shockley, „Photon-Radiative Recombination of Electrons and Holes in Germanium“, *Physical Review*, vol. 94, no. 6, pp. 1558–1560, 1954. DOI: 10.1103/physrev.94.1558.

- [126] Z. Yin and F. W. Smith, „Optical dielectric function and infrared absorption of hydrogenated amorphous silicon nitride films: Experimental results and effective-medium-approximation analysis“, *Physical Review B*, vol. 42, no. 6, pp. 3666–3675, 1990. DOI: 10.1103/physrevb.42.3666.
- [127] A. W. Weeber, H. C. Rieffe, I. G. Romijn, W. C. Sinke, and W. J. Soppe, „The fundamental properties of SiN_x:H that determine its passivating qualities“, in *Conference Record of the Thirty-first IEEE Photovoltaic Specialists Conference, 2005*, IEEE, 2005, pp. 1043–1046. DOI: 10.1109/PVSC.2005.1488312.
- [128] E. H. Nicollian and A. Goetzberger, „MOS Conductance Technique for Measuring Surface State Parameters“, *Applied Physics Letters*, vol. 7, no. 8, pp. 216–219, 1965. DOI: 10.1063/1.1754385.
- [129] J. R. Brews, „Rapid interface parameterization using a single MOS conductance curve“, *Solid-state electronics*, vol. 26, no. 8, pp. 711–716, 1983. DOI: 10.1016/0038-1101(83)90030-8.
- [130] E. H. Nicollian and J. R. Brews, *MOS (metal oxide semiconductor) physics and technology*. Wiley New York, 1982.
- [131] L. M. Terman, „An investigation of surface states at a silicon/silicon oxide interface employing metal-oxide-silicon diodes“, *Solid-state electronics*, vol. 5, no. 5, pp. 285–299, 1962.
- [132] R. Girisch, R. P. Mertens, and R. F. de Keersmaecker, „Determination of Si-SiO₂ interface recombination parameters using a gate-controlled point-junction diode under illumination“, *IEEE Transactions on Electron Devices*, vol. 35, no. 2, pp. 203–222, 1988. DOI: 10.1109/16.2441.
- [133] N. Folchert, S. Bordihn, R. Peibst, and R. Brendel, „Modelling the annealing of poly-Si/SiO_x/c-Si junctions“, in *Proceedings of the Silicon PV 2021, the 11th International Conference on Crystalline Silicon Photovoltaics*, ser. AIP Conference Proceedings, AIP Conference Proceedings, 2021, p. 020 006. DOI: 10.1063/5.0089597.
- [134] K. R. McIntosh and P. P. Altermatt, „A freeware 1D emitter model for silicon solar cells“, in *Proceedings of the 2010 35th IEEE Photovoltaic Specialists Conference*, IEEE, 2010, pp. 002 188–002 193. DOI: 10.1109/PVSC.2010.5616124.

Bibliography

- [135] R. Peibst, U. Römer, K. R. Hofmann, B. Lim, T. F. Wietler, J. Krugener, N.-P. Harder, and R. Brendel, „A Simple Model Describing the Symmetric I - V Characteristics of p Polycrystalline Si/n Monocrystalline Si, and n Polycrystalline Si/p Monocrystalline Junctions“, *IEEE Journal of Photovoltaics*, vol. 4, no. 3, pp. 841–850, 2014. DOI: 10.1109/JPHOTOV.2014.2310740.
- [136] N. Folchert, „Modeling poly-Si/SiO_x/c-Si junctions for solar cells“, doctoral dissertation, Leibniz Universität Hannover, Hannover, to be published.
- [137] R. Brendel, S. Dreissigacker, N.-P. Harder, and P. P. Altermatt, „Theory of analyzing free energy losses in solar cells“, *Applied Physics Letters*, vol. 93, no. 17, p. 173 503, 2008. DOI: 10.1063/1.3006053.
- [138] A. Fell, „A Free and Fast Three-Dimensional/Two-Dimensional Solar Cell Simulator Featuring Conductive Boundary and Quasi-Neutrality Approximations“, *IEEE Transactions on Electron Devices*, vol. 60, no. 2, pp. 733–738, 2013. DOI: 10.1109/TED.2012.2231415.
- [139] A. Fell, K. R. McIntosh, M. Abbott, and D. Walter, „Quokka version 2: selective surface doping, luminescence modeling and data fitting“, in *Proceedings of the 23rd International Photovoltaic Science and Engineering Conference 2013*, 2013.
- [140] Andreas Fell, *Quokka 3*. [Online]. Available: <https://www.quokka3.com>.
- [141] R. Brendel, „Modeling solar cells with the dopant-diffused layers treated as conductive boundaries“, *Progress in Photovoltaics: Research and Applications*, vol. 20, no. 1, pp. 31–43, 2012. DOI: 10.1002/pip.954.
- [142] F. Haase, S. Schafer, C. Klamt, F. Kiefer, J. Krugener, R. Brendel, and R. Peibst, „Perimeter Recombination in 25%-Efficient IBC Solar Cells With Passivating POLO Contacts for Both Polarities“, *IEEE Journal of Photovoltaics*, vol. 8, no. 1, pp. 23–29, 2018. DOI: 10.1109/JPHOTOV.2017.2762592.
- [143] C. Hollemann, F. Haase, S. Schäfer, J. Krügener, R. Brendel, and R. Peibst, „26.1%-efficient POLO-IBC cells: Quantification of electrical and optical loss mechanisms“, *Progress in Photovoltaics: Research and Applications*, vol. 26, no. 1, p. 3, 2019. DOI: 10.1002/pip.3098.

- [144] C. Hollemann, F. Haase, M. Rienäcker, V. Barnscheidt, J. Krügener, N. Folchert, R. Brendel, S. Richter, S. Großer, E. Sauter, J. Hübner, M. Oestreich, and R. Peibst, „Separating the two polarities of the POLO contacts of an 26.1%-efficient IBC solar cell“, *Scientific Reports*, vol. 10, no. 1, p. 658, 2020. DOI: 10.1038/s41598-019-57310-0.
- [145] J. Krügener, F. Haase, M. Rienäcker, R. Brendel, H. Osten, and R. Peibst, „Improvement of the SRH bulk lifetime upon formation of n-type POLO junctions for 25% efficient Si solar cells“, *Solar Energy Materials and Solar Cells*, 2017. DOI: 10.1016/j.solmat.2017.05.055.
- [146] Z. Yang, J. Krügener, F. Feldmann, J.-I. Polzin, B. Steinhauser, T. T. Le, D. Macdonald, and A. Liu, „Impurity Gettering in Polycrystalline-Silicon Based Passivating Contacts—The Role of Oxide Stoichiometry and Pinholes“, *Advanced Energy Materials*, p. 2103773, 2022. DOI: 10.1002/aenm.202103773.
- [147] F. Haase, T. Neubert, R. Horbelt, B. Terheiden, K. Bothe, and R. Brendel, „Local aluminum-silicon contacts by layer selective laser ablation“, *Solar Energy Materials and Solar Cells*, vol. 95, no. 9, pp. 2698–2700, 2011. DOI: 10.1016/j.solmat.2011.05.015.
- [148] U. Römer, R. Peibst, T. Ohrdes, B. Lim, J. Krügener, T. Wietler, and R. Brendel, „Ion Implantation for Poly-Si Passivated Back-Junction Back-Contacted Solar Cells“, *IEEE Journal of Photovoltaics*, vol. 5, no. 2, pp. 507–514, 2015.
- [149] P. P. Altermatt, „Models for numerical device simulations of crystalline silicon solar cells—a review“, *Journal of computational electronics*, vol. 10, no. 3, p. 314, 2011.
- [150] G. R. Wolstenholme, N. Jorgensen, P. Ashburn, and G. R. Booker, „An investigation of the thermal stability of the interfacial oxide in polycrystalline silicon emitter bipolar transistors by comparing device results with high-resolution electron microscopy observations“, *Journal of Applied Physics*, vol. 61, no. 1, pp. 225–233, 1987. DOI: 10.1063/1.338861.
- [151] B. Fischer, „Loss analysis of crystalline silicon solar cells using photoconductance and quantum efficiency measurements“, doctoral dissertation, University of Konstanz, Konstanz, 2003.

Bibliography

- [152] F. H. Spit and H. Bakker, „Diffusion of donor elements (125Sb, 82P, 74 (73) As) in polycrystalline silicon“, *physica status solidi (a)*, vol. 97, no. 1, pp. 135–142, 1986.
- [153] A. Merabet and C. Gontrand, „Dopant Redistribution during Rapid Thermal Annealing in a Self–Aligned Polysilicon Emitter Bipolar Structure Compatible with a Complementary Metal–Oxide–Semiconductor Technology“, *physica status solidi (a)*, vol. 145, no. 1, pp. 77–88, 1994.
- [154] S. Solmi, F. Baruffaldi, and R. Canteri, „Diffusion of boron in silicon during post–implantation annealing“, *Journal of Applied Physics*, vol. 69, no. 4, pp. 2135–2142, 1991. DOI: 10.1063/1.348740.
- [155] U. Römer, „Polycrystalline silicon/monocrystalline silicon junctions and their application as passivated contacts for Si solar cells“, doctoral dissertation, Leibniz Universität Hannover, Hannover, 2015.
- [156] T. Matsuura, „Diffusion of As, P, and B from Doped Polysilicon through Thin SiO₂ Films into Si Substrates“, *Journal of The Electrochemical Society*, vol. 138, no. 11, p. 3474, 1991. DOI: 10.1149/1.2085437.
- [157] R. Brendel, T. Dullweber, R. Peibst, C. Kranz, A. Merkle, and D. Walter, „Breakdown of the efficiency gap to 29% based on experimental input data and modeling“, *Progress in Photovoltaics: Research and Applications*, vol. 24, no. 12, pp. 1475–1486, 2016. DOI: 10.1002/pip.2696. (visited on).
- [158] C. H. Seager and D. S. Ginley, „Passivation of grain boundaries in polycrystalline silicon“, *Applied Physics Letters*, vol. 34, no. 5, pp. 337–340, 1979. DOI: 10.1063/1.90779.
- [159] T. I. Kamins, „Hall Mobility in Chemically Deposited Polycrystalline Silicon“, *Journal of Applied Physics*, vol. 42, no. 11, pp. 4357–4365, 1971. DOI: 10.1063/1.1659780.
- [160] J. Y. W. Seto, „The electrical properties of polycrystalline silicon films“, *Journal of Applied Physics*, vol. 46, no. 12, pp. 5247–5254, 1975. DOI: 10.1063/1.321593.
- [161] G. Baccarani, B. Riccò, and G. Spadini, „Transport properties of polycrystalline silicon films“, *Journal of Applied Physics*, vol. 49, no. 11, pp. 5565–5570, 1978. DOI: 10.1063/1.324477.

- [162] N.-C. Lu, L. Gerzberg, C.-Y. Lu, and J. D. Meindl, „A conduction model for semiconductor-grain-boundary-semiconductor barriers in polycrystalline-silicon films“, *IEEE Transactions on Electron Devices*, vol. 30, no. 2, pp. 137–149, 1983. DOI: 10.1109/t-ed.1983.21087.
- [163] D. P. Joshi and R. S. Srivastava, „Mobility and carrier concentration in polycrystalline silicon“, *Solar Cells*, vol. 12, no. 3, pp. 337–344, 1984. DOI: 10.1016/0379-6787(84)90112-1.
- [164] H. Ikeda, „Evaluation of grain boundary trap states in polycrystalline-silicon thin-film transistors by mobility and capacitance measurements“, *Journal of Applied Physics*, vol. 91, no. 7, pp. 4637–4645, 2002. DOI: 10.1063/1.1454202.
- [165] D. P. Joshi and R. S. Srivastava, „A model of electrical conduction in polycrystalline silicon“, *IEEE Transactions on Electron Devices*, vol. 31, no. 7, pp. 920–927, 1984. DOI: 10.1109/T-ED.1984.21631.
- [166] M. B. Hartenstein, C. Stetson, W. Nemeth, V. LaSalvia, S. P. Harvey, S. Theingi, M. Page, C.-S. Jiang, M. M. Al-Jassim, D. L. Young, S. Agarwal, and P. Stradins, „Trap-Assisted Dopant Compensation Prevents Shunting in Poly-Si Passivating Interdigitated Back Contact Silicon Solar Cells“, *ACS Applied Energy Materials*, vol. 4, no. 10, pp. 10774–10782, 2021. DOI: 10.1021/acsaem.1c01775.
- [167] C. H. Seager, D. S. Ginley, and J. D. Zook, „Improvement of polycrystalline silicon solar cells with grain-boundary hydrogenation techniques“, *Applied Physics Letters*, vol. 36, no. 10, pp. 831–833, 1980. DOI: 10.1063/1.91339.
- [168] U. Römer, R. Peibst, T. Ohrdes, Y. Larionova, N.-P. Harder, R. Brendel, A. Grohe, D. Stichtenoth, T. Wutherich, C. Schollhorn, H.-J. Krokoszinski, and J. Graff, „Counterdoping with patterned ion implantation“, in *Proceedings of the 2013 IEEE 39th Photovoltaic Specialists Conference (PVSC)*, IEEE, 2013, pp. 1280–1284. DOI: 10.1109/PVSC.2013.6744375.
- [169] F. Haase, B. Lim, A. Merkle, T. Dullweber, R. Brendel, C. Günther, M. H. Holthausen, C. Mader, O. Wunnicke, and R. Peibst, „Printable liquid silicon for local doping of solar cells“, *Solar Energy Materials and Solar Cells*, vol. 179, pp. 129–135, 2018. DOI: 10.1016/j.solmat.2017.11.003.

Bibliography

- [170] G. Scardera, D. Inns, G. Wang, S. Dugan, J. Dee, T. Dang, K. Bendimerad, F. Lemmi, and H. Antoniadis, „All-screen-printed Dopant Paste Interdigitated Back Contact Solar Cell“, *Energy Procedia*, vol. 77, pp. 271–278, 2015. DOI: 10.1016/j.egypro.2015.07.038.
- [171] Y. Larionova, F. Haase, A. Raugewitz, M. Rienäcker, R. Brendel and R. Peibst, „Screen print - based metallization schemes for POLO junctions“, in *7th Workshop on Metallization & Interconnection for Crystalline Silicon Solar Cells*, vol. 7th Workshop on Metallization & Interconnection, 2017.
- [172] B. Min, A. Dastgheib-Shirazi, P. P. Altermatt, and H. Kurz, „Accurate Determination of the Emitter Saturation Current Density for Industrial p-Diffused Emitters“, in *Proceedings of the 29th European Photovoltaic Solar Energy Conference and Exhibition*, 2014, pp. 463–466. DOI: 10.4229/EUPVSEC20142014-2B0.3.6.
- [173] F. Haase, B. Min, C. Hollemann, J. Krügener, R. Brendel, and R. Peibst, „Fully screen-printed silicon solar cells with local Al-p⁺ and n-type POLO interdigitated back contacts with a V_{OC} of 716 mV and an efficiency of 23%“, *Progress in Photovoltaics: Research and Applications*, vol. 212, no. 2, p. 110586, 2021. DOI: 10.1002/pip.3399.
- [174] B. Min, N. Wehmeier, T. Brendemuehl, F. Haase, Y. Larionova, L. Nasebandt, H. Schulte-Huxel, R. Peibst, and R. Brendel, „716 mV Open-Circuit Voltage with Fully Screen-Printed p-Type Back Junction Solar Cells Featuring an Aluminum Front Grid and a Passivating Polysilicon on Oxide Contact at the Rear Side“, *Solar RRL*, vol. 5, no. 1, p. 2000703, 2021. DOI: 10.1002/solr.202000703.
- [175] F. A. Stevie, C. Zhou, M. Hopstaken, M. Saccomanno, Z. Zhang, and A. Turansky, „SIMS measurement of hydrogen and deuterium detection limits in silicon: Comparison of different SIMS instrumentation“, *Journal of Vacuum Science & Technology B, Nanotechnology and Microelectronics: Materials, Processing, Measurement, and Phenomena*, vol. 34, no. 3, 03H103, 2016. DOI: 10.1116/1.4940151.
- [176] E. Schneiderlöchner, R. Preu, R. Lüdemann, and S. W. Glunz, „Laser-fired rear contacts for crystalline silicon solar cells“, *Progress in Photovoltaics: Research and Applications*, vol. 10, no. 1, pp. 29–34, 2002. DOI: 10.1002/pip.422.

- [177] C.-H. Lin, S.-P. Hsu, and W.-C. Hsu, „Silicon Solar Cells: Structural Properties of Ag-Contacts/Si-Substrate“, in *Solar Cells*, L. A. Kosyachenko, Ed., Erscheinungsort nicht ermittelbar: IntechOpen, 2011. DOI: 10.5772/19687.
- [178] B. J. O’Sullivan, P. K. Hurley, C. Leveugle, and J. H. Das, „Si(100)–SiO₂ interface properties following rapid thermal processing“, *Journal of Applied Physics*, vol. 89, no. 7, pp. 3811–3820, 2001. DOI: 10.1063/1.1343897.
- [179] A. G. Aberle, S. Glunz, and W. Warta, „Impact of illumination level and oxide parameters on Shockley–Read–Hall recombination at the Si–SiO₂ interface“, *Journal of Applied Physics*, vol. 71, no. 9, pp. 4422–4431, 1992. DOI: 10.1063/1.350782.
- [180] A. Stesmans, „Dissociation kinetics of hydrogen-passivated Pb defects at the (111)Si/SiO₂ interface“, *Physical Review B*, vol. 61, no. 12, pp. 8393–8403, 2000. DOI: 10.1103/PhysRevB.61.8393.
- [181] P. K. Hurley, C. Leveugle, A. Mathewson, D. Doyle, S. Whiston, J. Prendergast, and P. Lundgren, „The Impact of Rapid Thermal Annealing on the Properties of the Si (100)-SiO₂ Interface“, *MRS Proceedings*, vol. 510, 1998. DOI: 10.1557/PROC-510-659.
- [182] J. H. Stathis, „Dissociation kinetics of hydrogen-passivated (100) Si/SiO₂ interface defects“, *Journal of Applied Physics*, vol. 77, no. 12, pp. 6205–6207, 1995. DOI: 10.1063/1.359148.
- [183] R. A. Street, C. C. Tsai, J. Kakalios, and W. B. Jackson, „Hydrogen diffusion in amorphous silicon“, *Philosophical Magazine B*, vol. 56, no. 3, pp. 305–320, 1987. DOI: 10.1080/13642818708221319.
- [184] T. N. Truong, Di Yan, W. Chen, M. Tebyetekerwa, M. Young, M. Al-Jassim, A. Cuevas, D. Macdonald, and H. T. Nguyen, „Hydrogenation Mechanisms of Poly-Si/SiO_x Passivating Contacts by Different Capping Layers“, *Solar RRL*, vol. 4, no. 3, p. 1900476, 2020. DOI: 10.1002/solr.201900476.
- [185] Y. Ohji, Y. Nishioka, K. Yokogawa, K. Mukai, Q. Qiu, E. Arai, and T. Sugano, „Effects of minute impurities (H, OH, F) on SiO₂/Si interface as investigated by nuclear resonant reaction and electron spin resonance“, *IEEE Transactions on Electron Devices*, vol. 37, no. 7, pp. 1635–1642, 1990. DOI: 10.1109/16.55750.

Bibliography

- [186] H. Tada, A. E. Kumpel, R. E. Lathrop, J. B. Slanina, P. Nieva, P. Zavracky, I. N. Miaoulis, and P. Y. Wong, „Thermal expansion coefficient of polycrystalline silicon and silicon dioxide thin films at high temperatures“, *Journal of Applied Physics*, vol. 87, no. 9, pp. 4189–4193, 2000. DOI: 10.1063/1.373050.
- [187] I. Blech and U. Cohen, „Effects of humidity on stress in thin silicon dioxide films“, *Journal of Applied Physics*, vol. 53, no. 6, pp. 4202–4207, 1982. DOI: 10.1063/1.331244.
- [188] C.-L. Yu, P. A. Flinn, and J. C. Bravman, „In-situ Measurement of Viscous Flow of Thermal Silicon Dioxide Thin Films at High Temperature“, *MRS Proceedings*, vol. 446, 1996. DOI: 10.1557/PROC-446-261.
- [189] I. Kurachi, H. Takano, and H. Kanie, „Study of oxide-silicon interface state generation and annihilation by rapid thermal processing“, *Japanese Journal of Applied Physics*, vol. 54, no. 8, p. 086 501, 2015. DOI: 10.7567/JJAP.54.086501.
- [190] A.-M. El-Sayed, M. B. Watkins, T. Grasser, V. V. Afanas'ev, and A. L. Shluger, „Hydrogen-induced rupture of strained Si-O bonds in amorphous silicon dioxide“, *Physical review letters*, vol. 114, no. 11, p. 115 503, 2015. DOI: 10.1103/PhysRevLett.114.115503.
- [191] Y. Okada and Y. Tokumaru, „Precise determination of lattice parameter and thermal expansion coefficient of silicon between 300 and 1500 K“, *Journal of Applied Physics*, vol. 56, no. 2, pp. 314–320, 1984. DOI: 10.1063/1.333965.
- [192] J.-H. Chae, J.-Y. Lee, and S.-W. Kang, „Measurement of thermal expansion coefficient of poly-Si using microgauge sensors“, *Sensors and Actuators A: Physical*, vol. 75, no. 3, pp. 222–229, 1999. DOI: 10.1016/S0924-4247(98)00279-9.
- [193] H. Liu and L. Wang, „Measurements of thermal conductivity and the coefficient of thermal expansion for polysilicon thin films by using double-clamped beams“, *Journal of Micromechanics and Microengineering*, vol. 28, no. 1, p. 015 010, 2018. DOI: 10.1088/1361-6439/aa9d29.
- [194] F. Jansen, M. A. Machonkin, N. Palmieri, and D. Kuhman, „Thermomechanical properties of amorphous silicon and nonstoichiometric silicon oxide films“, *Journal of Applied Physics*, vol. 62, no. 12, pp. 4732–4736, 1987. DOI: 10.1063/1.339026.

- [195] I. R. McKerracher, L. Fu, H. H. Tan, and C. Jagadish, „Thermal expansion coefficients and composition of sputter-deposited silicon oxynitride thin films“, *Journal of Physics D: Applied Physics*, vol. 43, no. 33, p. 335104, 2010. DOI: 10.1088/0022-3727/43/33/335104.
- [196] E. E. Bende and J. Anker, „Doping Level Effect on Sample Temperatures in Infrared Belt Furnace Firing“, *Energy Procedia*, vol. 77, pp. 665–676, 2015. DOI: 10.1016/j.egypro.2015.07.096.
- [197] P. K. Hurley, A. Stesmans, V. V. Afanas'ev, B. J. O'Sullivan, and E. O'Callaghan, „Analysis of P_b centers at the Si(111)/SiO₂ interface following rapid thermal annealing“, *Journal of Applied Physics*, vol. 93, no. 7, pp. 3971–3973, 2003. DOI: 10.1063/1.1559428.
- [198] A. Kamgar and S. J. Hillenius, „Rapid thermal anneal induced effects in polycrystalline silicon gate structures“, *Applied Physics Letters*, vol. 51, no. 16, pp. 1251–1253, 1987. DOI: 10.1063/1.98695.
- [199] G. J. Gerardi, E. H. Poindexter, P. J. Caplan, and N. M. Johnson, „Interface traps and P_b centers in oxidized (100) silicon wafers“, *Applied Physics Letters*, vol. 49, no. 6, pp. 348–350, 1986. DOI: 10.1063/1.97611.
- [200] J. P. Campbell and P. M. Lenahan, „Density of states of P_{b1} Si/SiO₂ interface trap centers“, *Applied Physics Letters*, vol. 80, no. 11, pp. 1945–1947, 2002. DOI: 10.1063/1.1461053.
- [201] D. Kang, H. C. Sio, D. Yan, J. Stuckelberger, R. Liu, and D. Macdonald, „Firing Stability of Doped Polysilicon Passivation Layers“, in *Proceedings of the 37th European Photovoltaic Solar Energy Conference and Exhibition*, N. Pearsall, R. P. Kenny, and P. Helm, Eds., München and Florence: WIP, 2020, pp. 188–192. DOI: 10.4229/EUPVSEC20202020-2B0.1.4.
- [202] A. G. Aberle, S. W. Glunz, A. W. Stephens, and M. A. Green, „High-efficiency silicon solar cells: Si/SiO₂, interface parameters and their impact on device performance“, *Progress in Photovoltaics: Research and Applications*, vol. 2, no. 4, pp. 265–273, 1994. DOI: 10.1002/pip.4670020402.
- [203] S. Mack, A. Wolf, C. Brosinsky, S. Schmeisser, A. Kimmerle, P. Saint-Cast, M. Hofmann, and D. Biro, „Silicon Surface Passivation by Thin Thermal Oxide/PECVD Layer Stack Systems“, *IEEE Journal of Photovoltaics*, vol. 1, no. 2, pp. 135–145, 2011. DOI: 10.1109/JPHOTOV.2011.2173299.

Bibliography

- [204] W. Beyer and H. Dekkers, „Microstructure Characterization of Amorphous Silicon-Nitride Films by Effusion Measurements“, *MRS Proceedings*, vol. 910, 2006. DOI: 10.1557/PROC-0910-A06-05.
- [205] D. Bredemeier, D. C. Walter, R. Heller, and J. Schmidt, „Impact of Hydrogen-Rich Silicon Nitride Material Properties on Light-Induced Lifetime Degradation in Multicrystalline Silicon“, *physica status solidi (RRL) – Rapid Research Letters*, vol. 13, no. 8, p. 1900201, 2019. DOI: 10.1002/pssr.201900201.
- [206] G. Dingemans, F. Einsele, W. Beyer, M. C. M. van de Sanden, and W. M. M. Kessels, „Influence of annealing and Al₂O₃ properties on the hydrogen-induced passivation of the Si/SiO₂ interface“, *Journal of Applied Physics*, vol. 111, no. 9, p. 093713, 2012. DOI: 10.1063/1.4709729.
- [207] A. Richter, J. Benick, M. Hermle, and S. W. Glunz, „Reaction kinetics during the thermal activation of the silicon surface passivation with atomic layer deposited Al₂O₃“, *Applied Physics Letters*, vol. 104, no. 6, p. 061606, 2014. DOI: 10.1063/1.4865901.
- [208] L. Helmich, D. C. Walter, D. Bredemeier, and J. Schmidt, „Atomic-Layer-Deposited Al₂O₃ as Effective Barrier against the Diffusion of Hydrogen from SiN_x:H Layers into Crystalline Silicon during Rapid Thermal Annealing“, *physica status solidi (RRL) – Rapid Research Letters*, vol. 96, p. 2000367, 2020. DOI: 10.1002/pssr.202000367.
- [209] A. Schmid, C. Fischer, D. Skorka, A. Herguth, C. Winter, A. Zuschlag, and G. Hahn, „On the Role of AlO_x Thickness in AlO_x/SiN_y:H Layer Stacks Regarding Light- and Elevated Temperature-Induced Degradation and Hydrogen Diffusion in c-Si“, *IEEE Journal of Photovoltaics*, vol. 11, no. 4, pp. 967–973, 2021. DOI: 10.1109/JPHOTOV.2021.3075850.
- [210] U. Varshney, B. Hallam, P. Hamer, A. Ciesla, D. Chen, S. Liu, C. Sen, A. Samadi, M. Abbott, C. Chan, and B. Hoex, „Controlling Light- and Elevated-Temperature-Induced Degradation With Thin Film Barrier Layers“, *IEEE Journal of Photovoltaics*, vol. 10, no. 1, pp. 19–27, 2020. DOI: 10.1109/JPHOTOV.2019.2945199.
- [211] D. Bredemeier, D. Walter, and J. Schmidt, „Impact of silicon nitride film properties on hydrogen in-diffusion into crystalline silicon“, in *Proceedings of the 36th European Photovoltaic Solar Energy Conference and Exhibition*, F. Lambert, R. Kenny, and P. Helm, Eds., München and Florence: WIP, 2019.

- [212] F. L. Martínez, A. del Prado, I. Mártil, G. González-Díaz, W. Bohne, W. Fuhs, J. Röhrich, B. Selle, and I. Sieber, „Molecular models and activation energies for bonding rearrangement in plasma-deposited a-SiN_x:H dielectric thin films treated by rapid thermal annealing“, *Physical Review B*, vol. 63, no. 24, 2001. DOI: 10.1103/PhysRevB.63.245320.
- [213] S. M. Hu, „Stress-related problems in silicon technology“, *Journal of Applied Physics*, vol. 70, no. 6, R53–R80, 1991. DOI: 10.1063/1.349282.
- [214] N. M. Johnson, F. Ponce, R. Street, and R. Nemanich, „Defects in single-crystal silicon induced by hydrogenation“, *Physical Review B*, vol. 35, no. 8, pp. 4166–4169, 1987. DOI: 10.1103/physrevb.35.4166.
- [215] N. H. Nickel, G. B. Anderson, and J. Walker, „Hydrogen-induced platelets in disordered silicon“, *Solid State Communications*, vol. 99, no. 6, pp. 427–431, 1996. DOI: 10.1016/0038-1098(96)00283-9.
- [216] J. Weber, „Hydrogen in semiconductors: From basic physics to technology“, *physica status solidi (c)*, vol. 5, no. 2, pp. 535–538, 2008. DOI: 10.1002/pssc.200776819.
- [217] Roberson and Estreicher, „Vacancy and vacancy-hydrogen complexes in silicon“, *Physical Review B*, vol. 49, no. 24, pp. 17 040–17 049, 1994.
- [218] N. Nickel, G. Anderson, N. Johnson, and J. Walker, „Nucleation mechanism of hydrogen-induced platelets in single crystal and polycrystalline silicon“, *Physica B: Condensed Matter*, vol. 273-274, pp. 212–215, 1999. DOI: 10.1016/S0921-4526(99)00452-4.
- [219] N. H. Nickel, W. B. Jackson, and J. Walker, „Hydrogen migration in polycrystalline silicon“, *Physical Review B*, vol. 53, no. 12, pp. 7750–7761, 1996. DOI: 10.1103/physrevb.53.7750.
- [220] N. M. Johnson, C. Doland, F. Ponce, J. Walker, and G. Anderson, „Hydrogen in crystalline semiconductors“, *Physica B: Condensed Matter*, vol. 170, no. 1-4, pp. 3–20, 1991. DOI: 10.1016/0921-4526(91)90104-M.
- [221] R.-S. Huang, C.-H. Cheng, J. C. Liu, M. K. Lee, and C. T. Chen, „Electrical measurements on ion-implanted LPCVD polycrystalline silicon films“, *Solid-state electronics*, vol. 26, no. 7, pp. 657–665, 1983. DOI: 10.1016/0038-1101(83)90021-7.

Bibliography

- [222] M. Jech, A.-M. El-Sayed, S. Tyaginov, A. L. Shluger, and T. Grasser, „Abinitio treatment of silicon-hydrogen bond rupture at Si/SiO₂ interfaces“, *Physical Review B*, vol. 100, no. 19, 2019. DOI: 10.1103/PhysRevB.100.195302.
- [223] L.-J. Huang, Q.-Y. Tong, Y.-L. Chao, T.-H. Lee, T. Martini, and U. Gösele, „Onset of blistering in hydrogen-implanted silicon“, *Applied Physics Letters*, vol. 74, no. 7, p. 982, 1999. DOI: 10.1063/1.123430.
- [224] B. Terreault, „Hydrogen blistering of silicon: Progress in fundamental understanding“, *physica status solidi (a)*, vol. 204, no. 7, pp. 2129–2184, 2007. DOI: 10.1002/pssa.200622520.
- [225] D. Ourinson, T. Fellmeth, S. Tepner, T. Javaid, M. Dhamrin, C. Turney, G. Emanuel, S. W. Glunz, M. Pospischil, and F. Clement, „Optimization of Al Fire-Through Contacts for AlO_x-SiN_x Rear Passivated Bifacial *p*-PERC“, *IEEE Journal of Photovoltaics*, vol. 10, no. 6, pp. 1523–1531, 2020. DOI: 10.1109/JPHOTOV.2020.2983006.
- [226] C. N. Kruse, S. Schäfer, F. Haase, V. Mertens, H. Schulte-Huxel, B. Lim, B. Min, T. Dullweber, R. Peibst, and R. Brendel, „Simulation-based roadmap for the integration of poly-silicon on oxide contacts into screen-printed crystalline silicon solar cells“, *Scientific reports*, vol. 11, no. 1, p. 996, 2021. DOI: 10.1038/s41598-020-79591-6.
- [227] R. Peibst, N. Folchert, F. Haase, C. Klamt, Y. Larionova, J. Krügener, A. Merkle, B. Min, M. Rienäcker, U. Römer, S. Schäfer, D. Tetzlaff, T. Wietler, and R. Brendel, „In-Depth Study of poly-Si / Oxide / c -Si Junctions and p+ poly-Si / n+ poly-Si Tunneling Junctions for Applications in Si Single Junction and Si- Based Tandem Cells“, in *presented at 2018 MRS Fall Meeting and Exhibit*, Boston, MA, USA, Nov. 26, 2018.
- [228] M. Rienäcker, „Three-terminal tandem solar cells enabled by back-contacted bottom cells featuring passivating, carrier-selective polysilicon based junctions“, doctoral dissertation, Leibniz Universität Hannover, Hannover, 2022. DOI: 10.15488/11835.

List of publications

Peer-reviewed journal papers

1. R. Peibst, F. Haase, B. Min, C. Hollemann, T. Brendemühl, K. Bothe, and R. Brendel, „On the chances and challenges of combining electron-collecting n POLO and hole-collecting Al- p^+ contacts in highly efficient p-type c-Si solar cells“, *Progress in Photovoltaics: Research and Applications*, 2022. DOI: 10.1002/pip.3545
2. R. Peibst, M. Rienäcker, Y. Larionova, N. Folchert, F. Haase, C. Hollemann, S. Wolter, J. Krügener, P. Bayerl, J. Bayer, M. Dzinnik, R. J. Haug, and R. Brendel, „Towards 28 %-efficient Si single-junction solar cells with better passivating POLO junctions and photonic crystals“, *Solar Energy Materials and Solar Cells*, vol. 238, p. 111560, 2022. DOI: 10.1016/j.solmat.2021.111560
3. L. Nasebandt, B. Min, C. Hollemann, S. Hübner, T. Dippell, R. Peibst, and R. Brendel, „Sputtered phosphorus-doped poly-Si on oxide contacts for screen-printed Si solar cells“, *Solar RRL*, 2022. DOI: 10.1002/solr.202200409
4. C. Hollemann, N. Folchert, S. P. Harvey, P. Stradins, D. L. Young, C. L. Salles de Souza, M. Rienäcker, F. Haase, R. Brendel, and R. Peibst, „Changes in hydrogen concentration and defect state density at the poly-Si/SiO_x/c-Si interface due to firing“, *Solar Energy Materials and Solar Cells*, vol. 231, p. 111297, 2021. DOI: 10.1016/j.solmat.2021.111297
5. C. Hollemann, M. Rienäcker, A. Soeriyadi, C. Madumelu, F. Haase, J. Krügener, B. Hallam, R. Brendel, and R. Peibst, „Firing stability of tube furnace-annealed n-type poly-Si on oxide junctions“, *Progress in Photovoltaics: Research and Applications*, 2021. DOI: 10.1002/pip.3459

6. P. Bayerl, N. Folchert, J. Bayer, M. Dzinnik, C. Hollemann, R. Brendel, R. Peibst, and R. J. Haug, „Contacting a single nanometer-sized pinhole in the interfacial oxide of a poly-silicon on oxide (POLO) solar cell junction“, *Progress in Photovoltaics: Research and Applications*, vol. 6, no. 6, p. 1413, 2021. DOI: 10.1002/pip.3417
7. R. Peibst, H. Fischer, M. Brunner, A. Schießl, S. Wöhe, R. Wecker, F. Haase, H. Schulte-Huxel, S. Blankemeyer, M. Köntges, C. Hollemann, R. Brendel, G. Wetzels, J. Krügener, H. Nonnenmacher, H. Mehlich, A. Salavei, K. Ding, A. Lambertz, B. Pieters, S. Janke, B. Stannowski, and L. Korte, „Demonstration of Feeding Vehicle-Integrated Photovoltaic-Converted Energy into the High-Voltage On-Board Network of Practical Light Commercial Vehicles for Range Extension“, *Solar RRL*, p. 2100516, 2021. DOI: 10.1002/solr.202100516
8. R. Peibst, M. Rienacker, B. Min, C. Klamt, R. Niepelt, T. F. Wietler, T. Dullweber, E. Sauter, J. Hubner, M. Oestreich, and R. Brendel, „From PERC to Tandem: POLO- and p⁺/n⁺Poly-Si Tunneling Junction as Interface Between Bottom and Top Cell“, *IEEE Journal of Photovoltaics*, vol. 9, no. 1, pp. 49–54, 2019. DOI: 10.1109/JPHOTOV.2018.2876999
9. C. Hollemann, F. Haase, S. Schäfer, J. Krügener, R. Brendel, and R. Peibst, „26.1%-efficient POLO-IBC cells: Quantification of electrical and optical loss mechanisms“, *Progress in Photovoltaics: Research and Applications*, vol. 26, no. 1, p. 3, 2019. DOI: 10.1002/pip.3098
10. S. Schäfer, F. Haase, C. Hollemann, J. Hensen, J. Krügener, R. Brendel, and R. Peibst, „26%-efficient and 2 cm narrow interdigitated back contact silicon solar cells with passivated slits on two edges“, *Solar Energy Materials and Solar Cells*, vol. 200, p. 110021, 2019. DOI: 10.1016/j.solmat.2019.110021
11. F. Haase, S. Schafer, C. Klamt, F. Kiefer, J. Krugener, R. Brendel, and R. Peibst, „Perimeter Recombination in 25%-Efficient IBC Solar Cells With Passivating POLO Contacts for Both Polarities“, *IEEE Journal of Photovoltaics*, vol. 8, no. 1, pp. 23–29, 2018. DOI: 10.1109/JPHOTOV.2017.2762592
12. F. Haase, C. Hollemann, S. Schäfer, A. Merkle, M. Rienacker, J. Krügener, R. Brendel, and R. Peibst, „Laser contact openings for local poly-Si-metal contacts enabling 26.1%-efficient POLO-IBC solar cells“, *Solar Energy Materials*

and Solar Cells, vol. 186, pp. 184–193, 2018. DOI: 10.1016/j.solmat.2018.06.020

13. C. Klamt, A. Dittrich, B. Jaquet, C. Eberl, F. Döring, and H.-U. Krebs, „Largest possible deviations from stoichiometry transfer during pulsed laser deposition“, *Applied Physics A*, vol. 122, no. 7, pp. 1–5, 2016. DOI: 10.1007/s00339-016-0234-1

Conference proceedings

1. L. David, S. Hübner, B. Min, C. Hollemann, T. Dippell, P. Wohlfart, R. Peibst, and R. Brendel, „Fired-Only Passivating Poly-Si on Oxide Contacts with DC-Sputtered In-Situ Phosphorous-Doped Silicon Layers“, 2020. DOI: 10.4229/EUPVSEC20202020-2B0.1.3
2. C. Hollemann, F. Haase, J. Krugener, R. Brendel, and R. Peibst, „Firing stability of n-type poly-Si on oxide junctions formed by quartz tube annealing“, in *Proceedings of the 2020 IEEE 44th Photovoltaic Specialist Conference (PVSC)*, IEEE, 2020, pp. 1274–1278. DOI: 10.1109/PVSC45281.2020.9300849
3. F. Haase, C. Hollemann, S. Schafer, J. Krugener, R. Brendel, and R. Peibst, „Transferring the Record p-type Si POLO-IBC Cell Technology Towards an Industrial Level“, in *2019 IEEE 46th Photovoltaic Specialists Conference (PVSC)*, IEEE, 2019. DOI: 10.1109/pvsc40753.2019.8980960
4. R. Peibst, M. Rienacker, B. Min, C. Klamt, R. Niepelt, T. Wietler, T. Dullweber, E. Sauter, J. Hibner, M. Oestreich, and R. Brendel, „p+/n+ polysilicon-on-oxide tunneling junctions as an interface of p-type PERC cells for tandem applications“, in *2018 IEEE 7th World Conference on Photovoltaic Energy Conversion (WCPEC)*, Piscataway, NJ: IEEE, 2018, pp. 2635–2637. DOI: 10.1109/PVSC.2018.8548032

Given Talks

1. Christina Hollemann, Felix Haase, Nadine Wehmeier, Byungsul Min, Karsten Bothe, Jan Krügener, Rolf Brendel, Robby Peibst, *Analysis of Losses in POLO-IBC Cells in the Constraints of Module Integration*, accepted for presentation at World Conference on Photovoltaic Energy Conversion (WCPEC-8), Milano, Italy, 2022
2. C. Hollemann, M. Rienäcker, F. Haase, J. Krügener, R. Brendel, R. Peibst, *Influence of Firing on the Interface State Density of n-Type Poly-Si Passivating Contacts*, presented at SiliconPV 2021 - 11th International Conference on Silicon Photovoltaics, Online Event, 2021, **SiliconPV-Award**
3. C. Hollemann, F. Haase, M. Rienäcker, V. Barnscheidt, J. Krügener, N. Folchert, R. Brendel, S. Richter, S. Großer, and R. Peibst, *Optimization and characterization of POLO-IBC solar cells*, presented at 29th Annual NREL Silicon Workshop, Winter Park, Colorado, USA, 2019
4. C. Klamt, V. Krausse, M. Rienäcker, F. Haase, J. Krügener, N. Folchert, R. Brendel and R. Peibst, *Intrinsic poly-crystalline silicon region in between the p^+ and n^+ POLO contacts of an 26.1%-efficient IBC solar cell*, presented at 35th European Photovoltaic Solar Energy Conference and Exhibition, Brussels, Belgium, 2018, **EU PVSEC Student Awards**

Lebenslauf

Persönliche Daten:

Name: Christina Hollemann
Anschrift: Falkestraße 17
31785 Hameln

Studium der Physik:

Seit 04.2017 Promotionsstudium an der Leibniz Universität Hannover, Institut für Solarenergieforschung GmbH, Hameln/Emmerthal

04.2015 – 04.2017 Masterstudium Physik an der Georg-August-Universität Göttingen mit dem Schwerpunkt Festkörper- und Materialphysik, Abschluss: Master of Science

08.2011 – 04.2015 Bachelorstudium Physik an der Georg-August- Universität Göttingen, Abschluss: Bachelor of Science

Schulische Ausbildung:

08.2002 – 07.2011 Besuch des Gymnasium Marienschule in Hildesheim
Abschluss: Abitur

Berufserfahrung:

Seit 04.2017 Wissenschaftliche Mitarbeiterin am Institut für Solarenergieforschung GmbH, Hameln/Emmerthal

Danksagung

Abschließend möchte ich mich bei den Menschen bedanken, die zum Gelingen dieser Arbeit beigetragen haben.

Das sind Prof. Dr. Robby Peibst, Prof. Dr. Jan Schmidt und Prof. Dr. Stefan Glunz, die die Begutachtung meiner Arbeit übernehmen und Herrn Prof. Dr. Bernd Wicht, der den Prüfungsvorsitz übernimmt.

Vielen Dank Robby Peibst, für die hervorragende Betreuung meiner Doktorarbeit und die erfolgreiche Zusammenarbeit. Ich möchte mich insbesondere für die wertschätzenden und bestärkenden Gespräche bedanken, die mir auch nach Problemen und Zweifeln immer wieder ein gutes Gefühl gegeben haben. Danke für die Möglichkeit, ganz viel zu lernen und an den Aufgaben zu wachsen. Vielen Dank für deinen Rat zu vielen wissenschaftlichen Fragen und deine gezielten Fragen und Denkanstöße, die mich immer wieder weitergebracht haben.

Danke Felix Haase für die tolle Einarbeitung in die Welt der POLO²-IBC Zellen zu Beginn am ISFH, die intensive und großartige Zusammenarbeit in nun schon über 5 Jahren und insbesondere deine riesige Hilfsbereitschaft immer wieder ganz viele meiner Fragen zu beantworten und verständnisfördernde Diskussionen zu führen. Mit dir hatte und habe ich immer einen verständnisvollen Ansprechpartner für alle kleineren und größeren Fragen.

Dann sind natürlich die gesamten Teams der Projekte *26+*, *Street* und *Highlite* zu nennen. Ich bedanke mich für die tolle und konstruktive Zusammenarbeit, bei der ich viel lernen und gemeinsam mit euch tolle Ergebnisse erzielen konnte. Danke an Anja Christ, Annika Raugewitz, Hilke Fischer, Mirjam Berger und Sabine Schmidt für eure stete Hilfsbereitschaft und unschätzbar wertvolle Arbeit im Reinraum bei der Prozessierung vieler exzellenter POLO²-IBC und POLO-IBC Zellen und unzähliger n^+ POLO Proben. Außerdem geht mein Dank an David Sylla für die kompetente La-

Bibliography

serbearbeitung verschiedenster Proben und die Messung der fertigen Zellen. Vielen Dank Magalie Pollmann und Nadine Wehmeier für den höchstpräzisen Siebdruck. Danke an Manuel Stratmann für das selektive Ätzen mit TMAH und an Annika Raugewitz und Bettina Wolpensinger für viele aufschlussreiche und erstklassige REM-Bilder. Danke Magalie Pollmann und Michael Weiß für die gute Zusammenarbeit am LPCVD-Ofen.

Auch dem Team am MBE danke ich für die gute Zusammenarbeit. Vielen Dank Jan Krügener, Guido Glowatzki und Raymond Zieseniß für die unzähligen n^+ Polyscheidungen. Danke Guido für deinen stets sehr engagierten und schnellen Einsatz, uns hochqualitative Polyschichten zu liefern und die Weitergabe deiner langjährigen Erfahrung. Danke Raymond Zieseniß für das RIE Ätzen meiner $C-V$ -Proben, die ich bei euch vermessen konnte. Danke Verena Barnscheidt für deine engagierte Arbeit zu den $p^+(i)n^+$ -Dioden und die zahlreichen hilfreichen Messungen im Rahmen deiner Masterarbeit und an Jan Krügener für die aufschlussreichen Simulationen dazu.

Ein ganz besonderer Dank gilt auch meinem langjährigen direkten Schreibtischkollegen Nils Folchert, mit dem ich auf ganz kurzem Weg immer wieder alle möglichen wissenschaftlichen Fragen diskutieren konnte. So hast du insbesondere mein Verständnis der POLO Kontakte extrem gefördert.

Mein Dank gilt außerdem Prof. Brett Hallam, Anastasia Soeriyadi, Chukwuka Madumelu und Udo Römer, die meinen Aufenthalt an der UNSW in Sydney ermöglicht haben, der zwar auf Grund der Coronapandemie leider sehr kurz, aber dennoch spannend und eine bereichernde Erfahrung war.

Außerdem geht ein großer Dank an Felix Haase, Nils Folchert und Stefan Bordihn, denen ich meine Arbeit zum Korrekturlesen geben durfte.

Vielen Dank Henning Schulte-Huxel, Lasse Nasebandt und Timo Gewohn für die gemeinsame erfolgreiche Organisation der SilivonPV2021.

Weiterhin möchte ich mich bei Bettina Wolpensinger, Valeriya Titova, Lailah Helmich und Catherin Gemmel für die gemütlichen Mittagsrunden am ISFH und auch Unternehmungen außerhalb des ISFHs bedanken. Das gilt auch für Arne Dittrich, dem ich aus der Materialphysik in Göttingen ans ISFH gefolgt bin, worüber ich sehr froh bin.

Wichtig waren in jedem Fall auch meine Bürokollegen Manuel Stratmann, Fabian Kiefer, Nils Folchert, Carsten Schinke, Christian Kruse, Timo Gewohn, Thomas Daschinger, Benjamin Grimm und Chencheng Xu, die in den 5 Jahren mehrfach gewechselt haben, aber immer zu einer sehr guten Atmosphäre und interessanten Gesprächen im Büro 632 beigetragen haben. Danke Manuel Stratmann für die spannenden Gespräche bzw. Fragestunden mit Fragen zu allen möglichen Themen rund um die Energiewende mit denen ich dich löchern durfte.

Ein großer Dank gilt auch meinen Eltern Kerstin und Werner, die mein naturwissenschaftliches Interesse stets gefördert haben und die in allen Lebenslagen immer für mich da sind und meinen Geschwistern Hanna, Sebastian und Daniel, die sowohl bei persönlichen als auch IT-Problemen immer hilfsbereite und geduldige Ansprechpartner*innen sind.

Und zum Schluss möchte ich meinem Mann Bastian danken, der mich in der ganzen Zeit immer liebevoll unterstützt, motiviert und bestärkt hat, auch wenn es mal stressig wurde.